EVALUATION OF DISPERSION STRENGTHENED NICKEL-BASE ALLOY HEAT SHIELDS FOR SPACE SHUTTLE APPLICATION

Phase I Summary Report

May 1973

MDC G4705

Prepared under Contract No. NAS1-11654
McDonnell Douglas Astronautics Company
Huntington Beach, California
for
NATIONAL AERONAUTICS AND SPACE ADMINISTRATION
Langley Research Center
Hampton, Virginia 23365

EVALUATION OF DISPERSION STRENGTHENED NICKEL-BASE ALLOY HEAT SHIELDS FOR SPACE SHUTTLE APPLICATION

Phase I Summary Report
May 1973
MDC G4705

R. Johnson, Jr.
D. H. Killpatrick

/

ABSTRACT

The work conducted from 15 June 1972 through 15 May 1973 in a program to evaluate dispersion-strengthened nickel base alloy heat shields for Space Shuttle application is described. The work reported constitutes the first phase of a two-phase program. Vehicle environments having critical effects on the thermal protection system are defined; TD Ni-20Cr material characteristics are reviewed and compared with TD Ni-20Cr produced in previous development efforts; cyclic load, temperature, and pressure effects on TD Ni-20Cr sheet material are investigated; the effects of braze reinforcement in improving the efficiency of spotwelded, diffusion-bonded, or seam-welded joints are evaluated through tests of simple lap-shear joint samples; parametric studies of metallic radiative thermal protection systems are reported; and the design, instrumentation, and testing of full-scale subsize heat shield panels are described. Tests of full-scale subsize panels included simulated meteoroid impact tests; simulated entry flight aerodynamic heating in an arc-heated plasma stream; programmed differential pressure loads and temperatures simulating mission conditions; and acoustic tests simulating sound levels experienced by heat shields during boost flight. Results of material evaluations show recently produced TD Ni-20Cr sheet material to have characteristics similar to material produced in earlier development programs with the exception that the latest material exhibits lower elongation at failure in the temperature range of 921°K (1,200°F) to 1,368°K (2,000°F). Results of Phase I show TD Ni-20Cr heat shields to be capable of sustaining 100 simulated Shuttle Orbiter mission cycles. Meteoroid impact tests indicate that, with the criteria employed, a single 0.0254-cm (0.010-in) sheet of TD Ni-20Cr will be penetrated, whereas two thicknesses of 0.0254-cm (0.010-in) sheet material (e.g., stiffener and face sheet interface areas) will be cratered on the outer sheet but not penetrated. Simulated entry tests of panel edge closure designs show that either overlap or closure strip design approaches effectively prevent severe ingestion of hot gases at panel edges. Test results are described, and the performances of two heat shield designs are compared and evaluated.

FOREWORD

This report presents results of Phase I work that was performed between 15 June 1972 and 15 May 1973 under Contract NAS1-11654. The program described herein is being performed by the McDonnell Douglas Astronautics Company of the McDonnell Douglas Corporation for the National Aeronautics and Space Administration, Langley Research Center, Hampton, Virginia. Technical direction of the contract is being performed by Mr. W. B. Lisagor of the Materials Division, Materials Application Branch, Metals Section.

The program is being managed by Read Johnson, Jr. under the direction of Dr. J. F. Garibotti, Chief Structures Engineer, Research and Development, Structures, Development Engineering. Major contributions were made to the program by Dr. D. H. Killpatrick, Material and Process, Development Engineering. Others who contributed to the program and to the preparation of this report are: B. G. Fitzgerald, coordination of tests conducted at the McDonnell Douglas Research Laboratories; Ralph Lilienkamp, in charge of Space Simulation Chamber tests; John Hill, Space Simulation Test Engineer; W. B. Shelton, Acoustic Test Engineer; W. A. Rinehart, in charge of Plasma Arc Tunnel tests; B. A. Cramer, analysis of cumulative creep effects.

CONTENTS

FIGURES

xiii

TABLES

Section 1
INTRODUCTION AND SUMMARY

The objective of this program is to evaluate TD Ni-20Cr material for application in reusable radiative metallic heat shields as part of a Space Shuttle thermal protection system (TPS). These evaluations encompass analytical and experimental efforts designed to assess the potential of TD Ni-20Cr heat shields in terms of reuse capability, refurbishment requirements, TPS weight, and TPS costs.

TD Ni-20Cr, a dispersion-strengthened metal for which production techniques were recently improved (Reference 1), was selected for this evaluation program because it extends the service temperature limits for uncoated metallic structures by $111^{\circ}K$ to $333^{\circ}K$ ($200^{\circ}F$ to $600^{\circ}F$) above those of current superalloys. Thus, a maximum reuse temperature of $1477^{\circ}K$ ($2,200^{\circ}F$) has been projected for TD Ni-20Cr heat shields.

To achieve program goals efficiently, the work was organized into two sequential phases covering a total time span of 23-1/2 months. Phase I efforts, covering the first 11 months, are reported herein.

The work conducted under this program is part of an overall effort by the NASA to evaluate advanced thermal protection systems for application in reusable space vehicles capable of entry from earth-orbital missions, maneuvering flight after entry, and horizontal landing. Such advanced thermal protection systems are also projected as being applicable to vehicles capable of sustained hypersonic flight within the earth's atmosphere at speeds ranging from Mach 6 to 12. A reusable space vehicle having the capabilities mentioned above is currently under development as a key part of the NASA Space Shuttle Program (SSP). This vehicle, designated the

Orbiter, will be capable of at least 100 missions to earth orbit followed by entry flight and return to a designated landing site.

The Orbiter TPS has been recognized as a key system in determining the vehicle weight. Durability of the TPS will also be a significant factor in refurbishment requirements; hence, costs associated with refurbishment will be directly affected by the TPS performance in terms of reuse capability. A third design goal, TPS reliability, is a primary requirement for successful operational service of the Space Shuttle. The goal of improving these key TPS performance requirements—weight, cost, and reliability—resulted in establishment of the current program to evaluate TD Ni-20Cr heat shields. The evaluations undertaken in this two-phase program are based upon a coordinated analytical and experimental approach that will culminate in Phase II by demonstration of the performance and behavior of a full-size TD Ni-20Cr heat shield array when tested under simulated Space Shuttle TPS environmental conditions.

An initial task in Phase I defined the Orbiter trajectories critical for the design of a metallic TPS and the associated environmental parameters that must be simulated in tests of material samples and heat shields. A second task in Phase I was directed toward evaluation of material properties and characteristics typical of recently produced TD Ni-20Cr sheet and rod. While a majority of the required material data were available from concurrent or recently completed programs, a limited number of supplementary material tests were conducted in this program to provide needed design information. The required supplementary tests consisted of multiparameter cyclic tests to (1) define creep strain as a function of number of simulated missions and (2) determine residual strength of TD Ni-20Cr after 100 simulated missions. In addition to the multiparameter cyclic tests, braze reinforcement was evaluated as a method of improving the efficiency of spot-welded, diffusion-bonded, or seam-welded joints in thin-gage TD Ni-20Cr sheets. Parametric studies of TPS design approaches were also conducted during Phase I to evaluate analytically the most promising concepts for use with TD Ni-20Cr. These studies provided a basis for selecting two competing designs that were subsequently tested in Phase I as full-scale subsize heat-shield panels.

Full-scale subsize panels were used in several tests to (1) evaluate the two selected designs, (2) evaluate two panel edge joint designs, and (3) evaluate simulated meteoroid impact effects on the TD Ni-20Cr panel designs. Panels with full-scale cross sections but subsize in planform area were designed and fabricated into test components having a 45.7-cm (18-in.) length and a width of approximately 17.3 cm (6.8 in.). Panels of this size, the largest fabricated for Phase I tests, were subjected to cyclic tests consisting of programmed differential pressure loads, temperature profiles, and environmental pressures that simulated boost and entry flight environments applicable to TD Ni-20Cr metallic radiative heat shields. Acoustic exposures were interspersed at intervals to simulate critical acoustic loads imposed on the TPS during boost flight.

Phase I results of TD Ni-20Cr material evaluations showed current sheet material being used in this program to have essentially the same properties and characteristics as material produced in earlier development programs, with the exception that the current material exhibits lower elongation at failure in the temperature range of 921°K (1,200°F) to 1,368°K (2,000°F). Parametric studies of six different heat shield designs resulted in the selection of two TPS configurations for competitive tests in Phase I. The two designs were (1) a corrugation-stiffened single-face heat shield panel with metallic-foil packaged insulation underneath it and (2) a zee-stiffened single-face panel with the same type of insulation package.

Phase I simulated mission tests using the selected heat shield designs showed the TD Ni-20Cr heat shields to be capable of sustaining 100 simulated mission profiles. However, reinforcement of heat shield attach points was required to complete the full 100 test cycles. Simulated meteoroid impact tests with sample panels showed that, with the criteria used, penetration occurred when impact was made on a single 0.0254-cm (0.010-in.) thick sheet, but impact in the region of a double thickness of 0.0254-cm (0.010-in.) material resulted in cratering of the outer sheet without penetration. Subsequent exposures in a plasma-arc stream that simulated entry airflow conditions resulted in no additional degradation of either type of impact point.

Panel edge joint designs subjected to cyclic exposures in a plasma-arc stream simulating repeated entry flights showed that either of the two designs tested was effective in preventing severe ingestion of hot gases at the panel edges. One of the edge closeouts was a simple overlap design, and the second utilized a closure strip that covered both edges of adjoining panels.

Section 2

STUDY VEHICLE SELECTION AND
THERMAL PROTECTION SYSTEM ENVIRONMENT

The initial efforts in Phase I were devoted to (1) selection of a representative
Shuttle Orbiter configuration, (2) selection of a typical location on the Orbiter
for application of a TD Ni-20Cr TPS, and (3) review of critical trajectories,
TPS environments, and simulation requirements for use in material and
panel tests. Results of the initial work are summarized in this section, and
more detailed discussions of entry trajectories and TPS criteria are pre-
sented in Appendix A.

2.1 TRAJECTORY AND TEST SIMULATION EVALUATION

A review of the Orbiter boost, entry, and cruise flight trajectories was
conducted with the objectives of establishing TPS performance requirements
for vehicle regions where TD Ni-20Cr may be utilized effectively and estab-
lishing simulation requirements to be used in material characterization tests
and TPS component tests.

To meet those objectives, the most recent Shuttle Orbiter ascent and entry
trajectories available at the start of Phase I of this contract were reviewed
and compared with similar data from Shuttle Phase B studies. During a
majority of the Phase B study, the vehicle configuration was a two-stage
Shuttle with both Booster and Orbiter being capable of lifting entry flight,
horizontal landing, and subsequent reuse.

Near the end of Phase B, a redefinition of study guidelines changed the
Shuttle configuration by eliminating a horizontal landing Booster, requiring
external tankage for the Orbiter, and using solid rocket motors (SRM)
attached to the external tank. In this later configuration the Orbiter liquid-
fueled engines are fed from the external tank, and a parallel burn of SRM's

5

and Orbiter main engines is employed during the initial portion of boost flight. Staging occurs when the SRM's are expended and separated from the mated Orbiter and its external tank. The Orbiter main engines continue burning until orbit insertion is achieved at which time separation of the Orbiter and the external tank occurs. The later Shuttle mated configuration is shown in Figure 2-1. The configuration shown in Figure 2-1 was selected as the baseline vehicle for use in this program; details of the Orbiter are presented in Figure 2-2. The Orbiter configuration, developed as a proposed Phase C/D configuration, was designated the MDAC 101/E Orbiter. Detailed trajectories, lower surface temperature time-histories, and reference heating rate time-histories are presented in Appendix A for the 101/E Orbiter. The data of Appendix A are presented as reference material, while discussions of the selected performance and test simulation requirements are presented in Section 5. Critical trajectory and environmental conditions are presented in the remainder of this section.

2. 1. 1 Boost, Entry, and Cruise Trajectories

The basic design pressures and temperatures experienced by the TPS surface panels are determined by the vehicle trajectories during boost, entry, and terminal approach phases of the mission. The trajectories for the 101/E Orbiter were reviewed to select critical pressure and temperature histories applicable to a metallic heat-shield design. Detailed time-histories for critical trajectory parameters during boost, entry, and cruise flight phases are shown in Figure 2-3. Selection of a specific area on the lower surface of the Orbiter was considered as a next step in deriving time-histories of TPS temperatures, differential pressures, and ambient pressures to be used in design studies and in Phase I tests.

As a criterion for initial selection of a typical surface area for a TD Ni-20Cr TPS, a maximum reuse temperature of $1,477^{\circ}$K ($2,200^{\circ}$F) was chosen, along with 100 entry flights as the nominal number of missions. Thermal analyses of the 101/E Orbiter showed maximum lower surface temperatures to range from $1,368^{\circ}$K to $1,699^{\circ}$K ($2,000^{\circ}$F to $2,600^{\circ}$F) during entry flight. The maximum temperature isotherms for the 101/E Orbiter configuration are shown in Figure 2-4. A position on the lower surface centerline at X/L = 0. 35 was chosen to define panel design parameters since this position

6
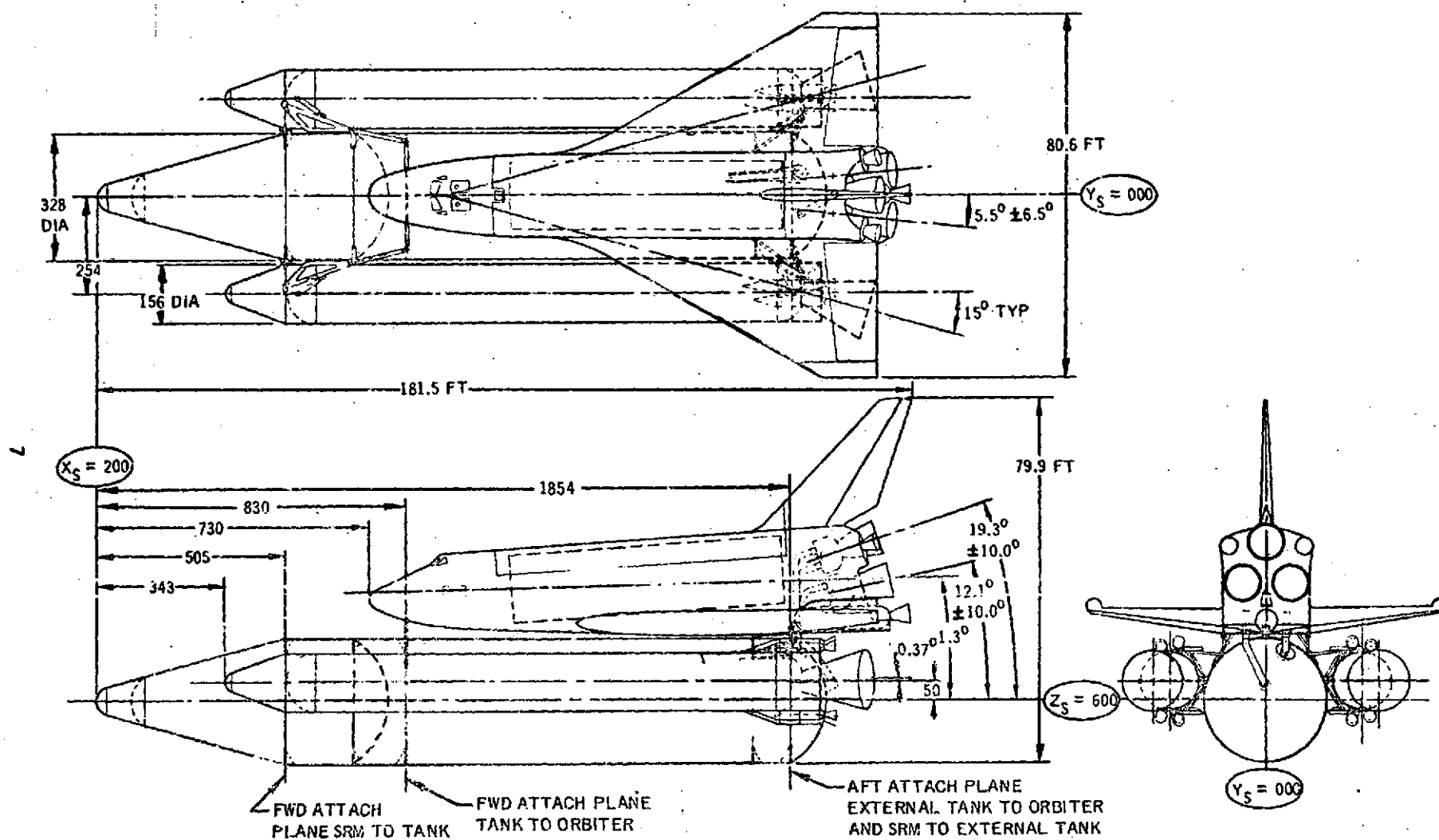
Figure 2-1. Shuttle Mated Configuration — Phase C/D Proposal
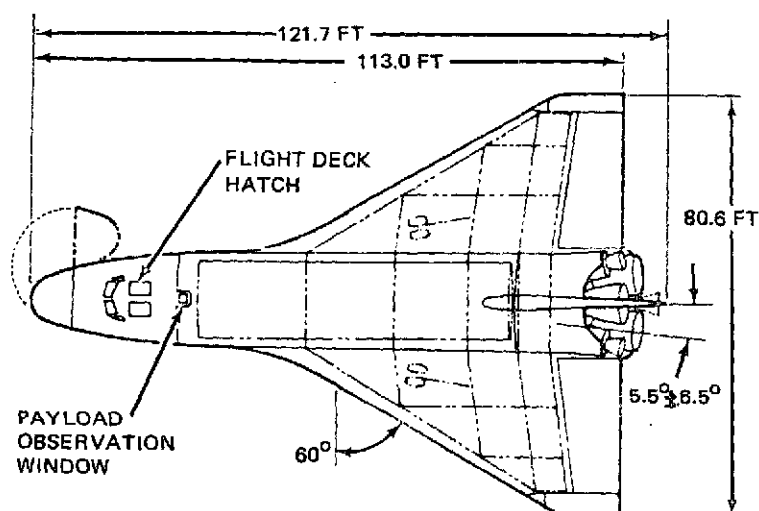
WING		TOTAL VEHICLE	
THEO AREA	$3,800 \text{ FT}^2$	WETTED AREA	$13,258 \text{ FT}^2$
EXPOSED AREA	$2,416 \text{ FT}^2$	PROJECTED PLANFORM	$4,406 \text{ FT}^2$
AR	1.71	ML VOLUME	$40,745 \text{ FT}^3$
ELEVON AREA	548 FT^2		
WETTED AREA W PODS	$5,074 \text{ FT}^2$	FUSELAGE	
WING BODY INTERSECTION	462 FT^2	WETTED AREA FT^2	
ML VOLUME W PODS	$5,988 \text{ FT}^2$	FWD	$1,382 \text{ FT}^2$
AIRFOIL	NACA 0008–64	MID	$4,450 \text{ FT}^2$
TAIL		AFT W OMS AND BODY FLAP	$1,585 \text{ FT}^2$
THEO AREA	450 FT^2	BASE	371 FT^2
EXPOSED AREA	432 FT^2	TOTAL	$7,788 \text{ FT}^2$
ASPECT RATIO	1.74	ML VOLUME FT^3	$34,347 \text{ FT}^3$
RUDDER AREA	161 FT^2	PROJECTED PLANFORM	$1,990 \text{ FT}^2$
WETTED AREA	888 FT^2		
TAIL BODY INTERSECTION	30 FT^2		
ML VOLUME	410 FT^3		
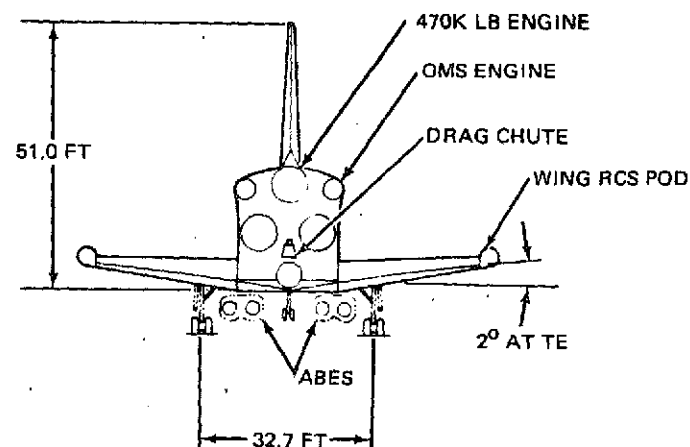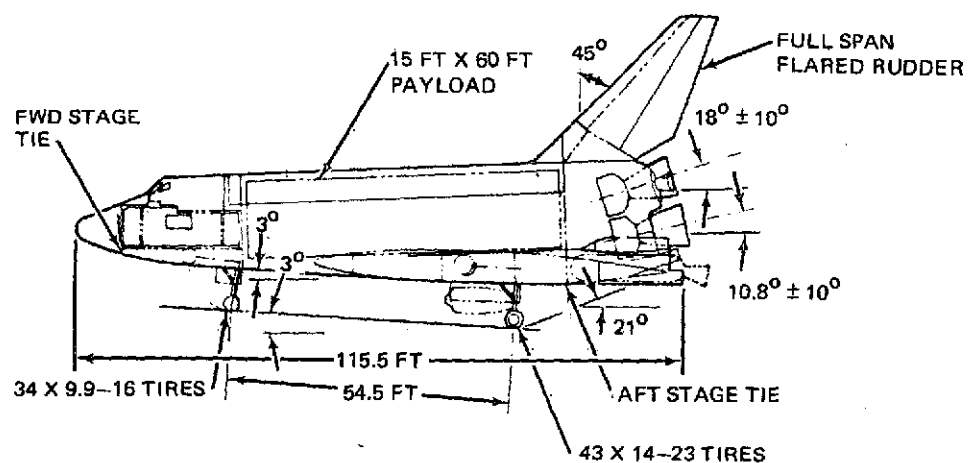
Figure 2-2. 101/E Orbiter Configuration
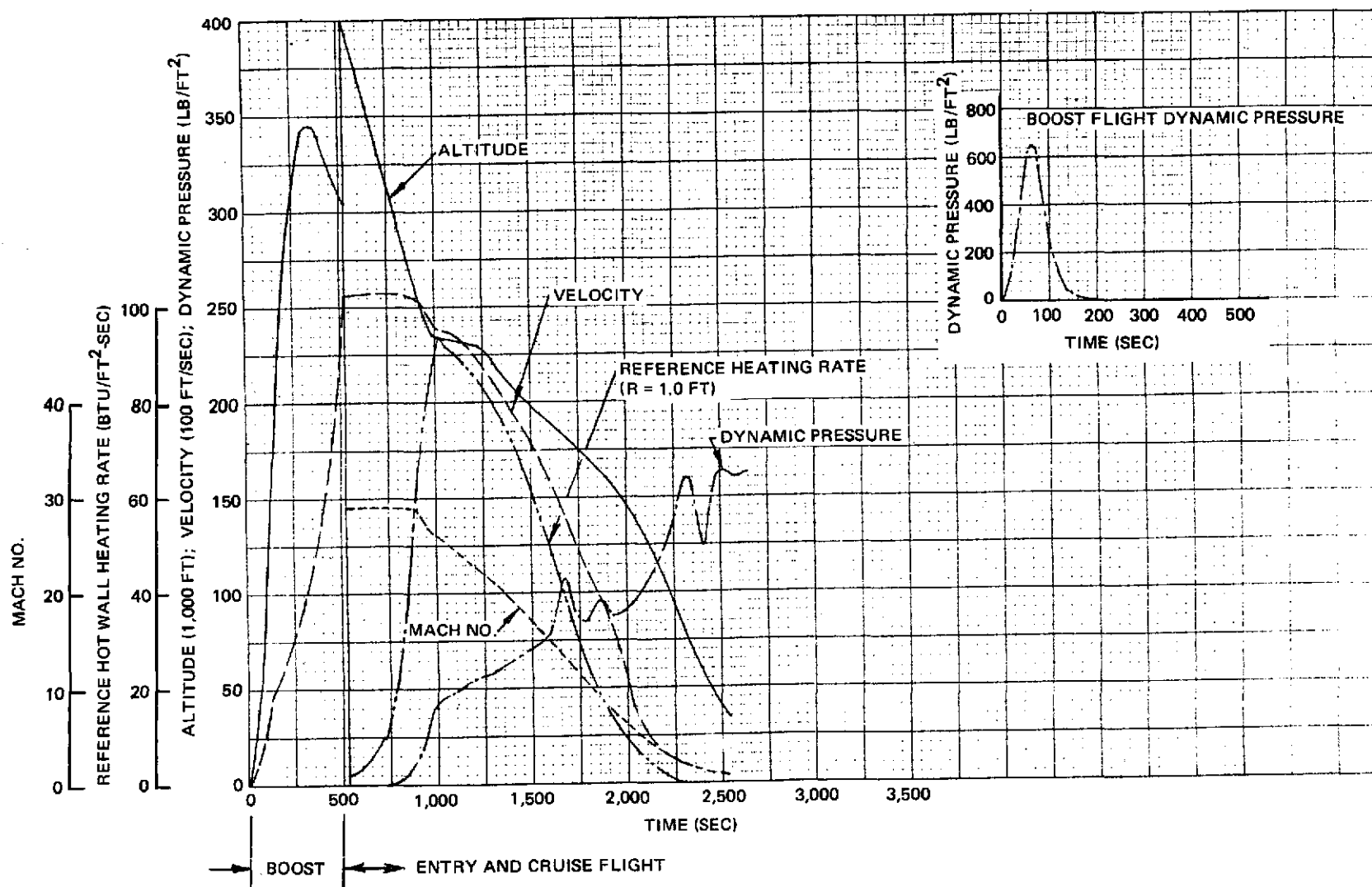
Figure 2-3. 101/E Orbiter Flight Parameters

- MISSION 3 TRAJECTORY WITH ± 200 NMI DOWN-RANGE MANEUVERING MARGIN
- 4° DOWN ELEVON
- MAXIMUM BOTTOM TEMPERATURES RESULT FROM TURBULENT HEATING AFT OF X/L = 0.10

MAXIMUM TEMPERATURES – °F ϵ = 0.90
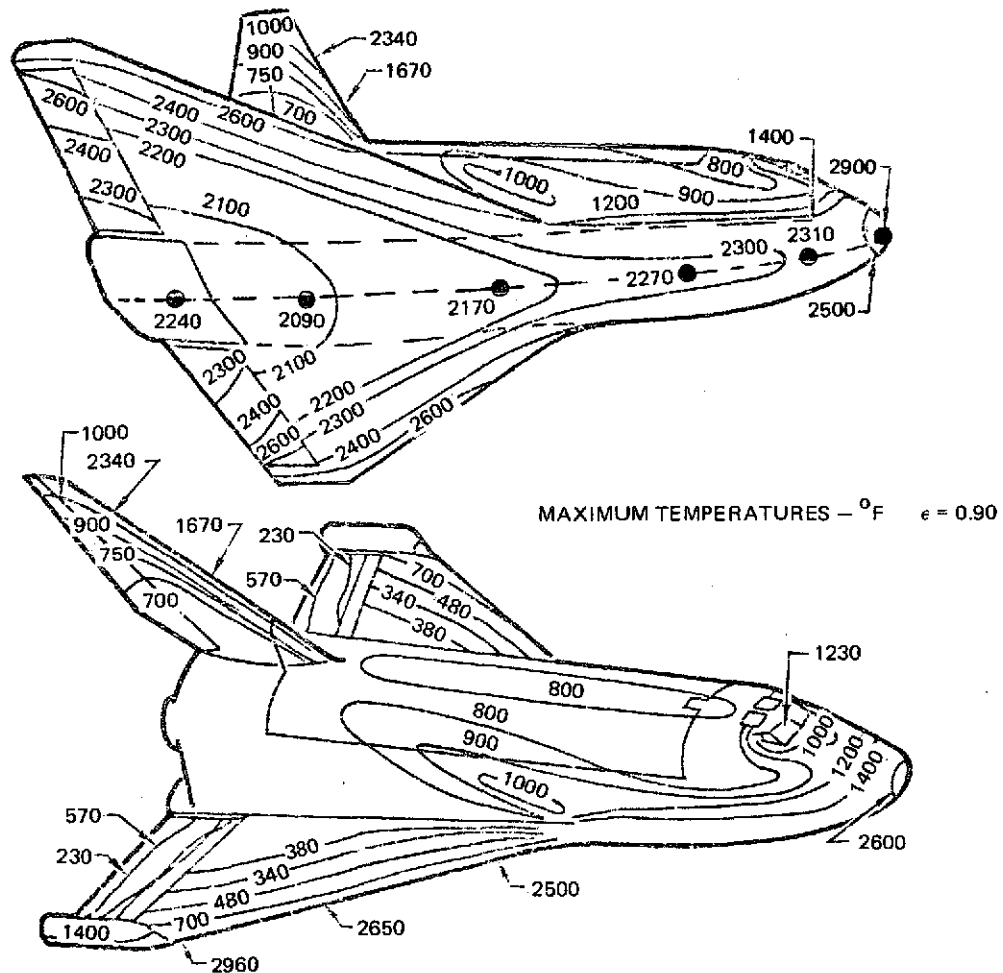
- 101/E ORBITER CONFIGURATION
- SEE APPENDIX A FOR DETAILED TRAJECTORY DATA

Figure 2-4. Maximum Temperatures During Critical Entry Trajectory

10

sustains a maximum temperature of $1,477^O$K $(2,200^O$F). It also maintains maximum temperatures for a significant portion of the entry period due to the early initiation of turbulent flow. This latter characteristic, which may be noted in the data of Appendix A, causes maximum surface temperatures to occur early in the entry flight and consequently produces a high total heat pulse at X/L = 0.35. Figure 2-5 shows the selected position on the vehicle while Figure 2-6 shows the time-histories of temperature, differential pressure, and ambient pressure from lift-off to cruise flight after entry. The entry time-history at X/L = 0.10 is shown in Figure 2-6 for comparison, and the effects of early transition to turbulent flow at the selected position (X/L = 0.35) may be seen.

The parameters shown in Figure 2-6 were used to develop test profiles for programmed multiple-parameter cyclic tests of TD Ni-20Cr material samples and for load and temperature profiles used in the full-scale sub-size panel tests. Such test profiles are discussed subsequently in Sections 3 and 5 when describing material property tests and subsize panel tests respectively.

2.1.2 Acoustic Environment
The overall sound pressure levels predicted for the 101/E Orbiter config-uration are shown in Figure 2-7 for launch and ascent conditions. The full-scale subsize panel designs (Section 5) were analyzed for resistance to fatigue failures at a maximum overall sound pressure level (OASPL) of 160 db in accordance with the predicted values for the Orbiter forward lower surface shown in Figure 2-7. Fatigue analyses were based on 100 missions and a life factor of 10. Preliminary acoustic tests of the panels were conducted up to a maximum OASPL of 165 db for a duration of one minute, however, to determine stress responses at the center of each panel (Section 5).
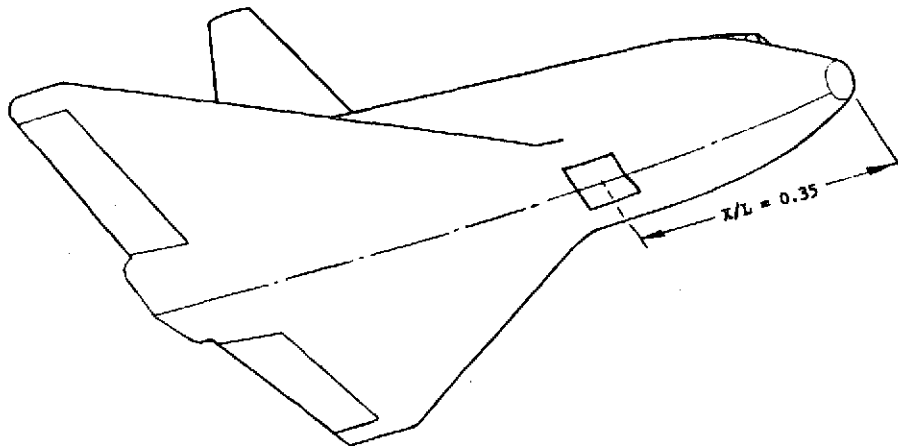
Figure 2-5. Orbiter Surface Area for TPS Parametric Study

2. 1. 3 Meteoroid Environment

The meteoroid environment selected for use in determining simulated meteoroid impact test conditions is taken from Reference 2. References 2 and 3 formed the basis for selecting criteria for the meteoroid environment in the near-earth and cislunar regions and for penetrations of metallic TPS panels. In Reference 2, a model of the average cumulative total meteoroid flux-mass was developed for the region of 1 astronomical unit (1 A. U.) from the sun near the ecliptic plane. This model is shown in Figure 2-8, which also shows data from various sources in comparison to the adopted model. The probability-velocity distribution developed in Reference 2 gives an average velocity of 20 km/s for sporadic meteoroids in the near-earth region.

The meteoroid environment criteria specified in the Space Shuttle Request for Proposal (Reference 4) and in Reference 5 were also reviewed, and meteoroid
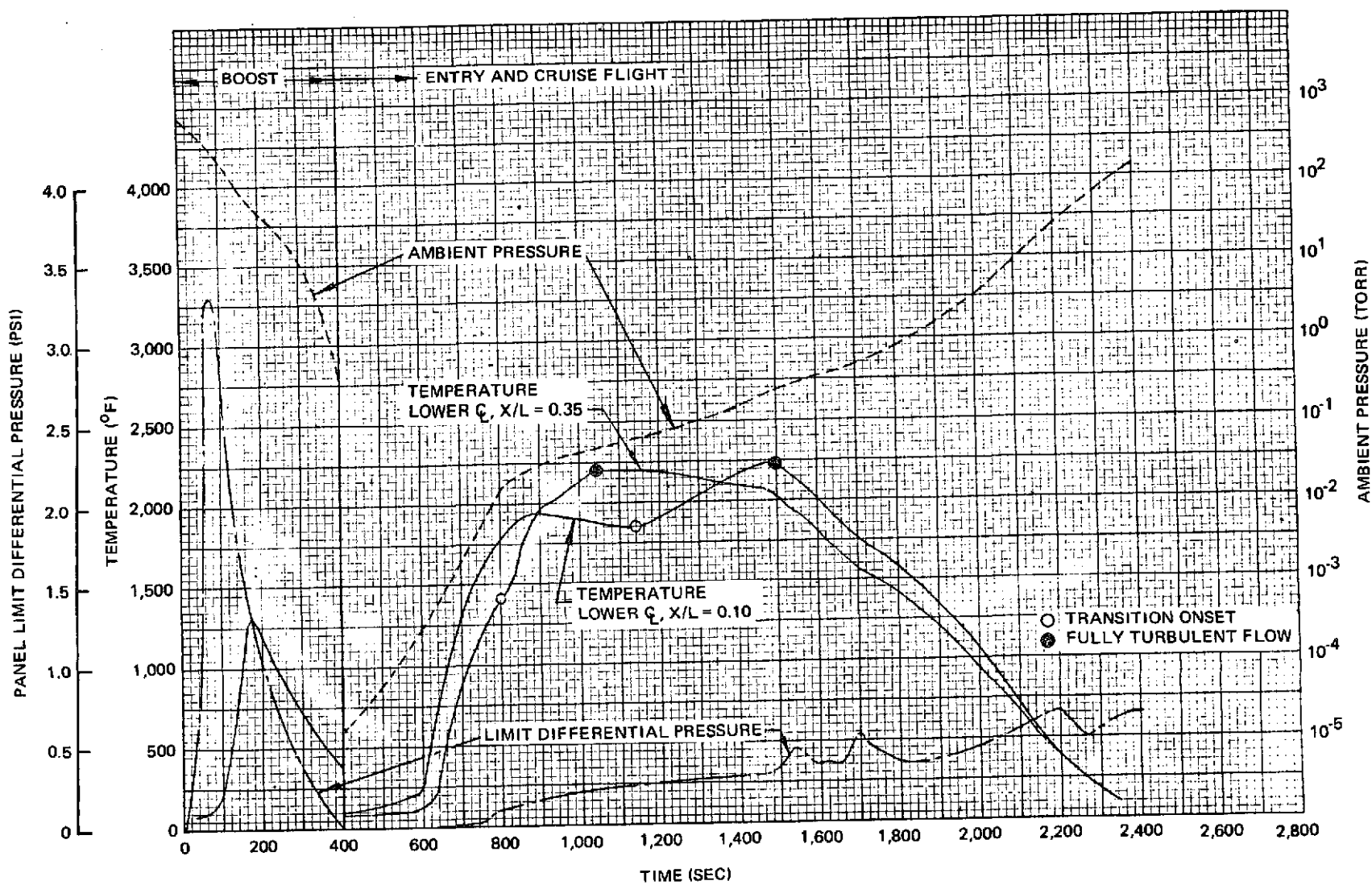
Figure 2-6. Temperature, Panel Differential Pressure, and Ambient Pressure Time-Histories

(ON TANK ₵)
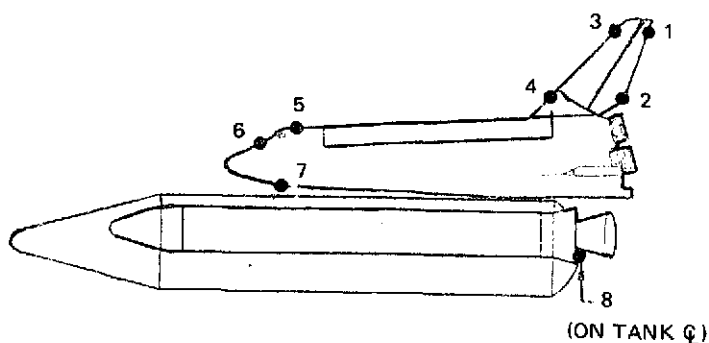
OVERALL SOUND PRESSURE LEVEL (dB)

	LAUNCH*	ASCENT**	
1	164.6	161	
2	165.9	161	*BASED ON TEST
3	163.6	155	FIRINGS OF SATURN
4	163.3	146	J-2 ENGINES AT
5	158.2	161	NASA-MSFC
6	157.6	148	
7	158.0	160	**BASED ON AMES WIND
8	165.0	153	TUNNEL TEST DATA

Figure 2-7. Orbiter Overall Sound Pressure Levels
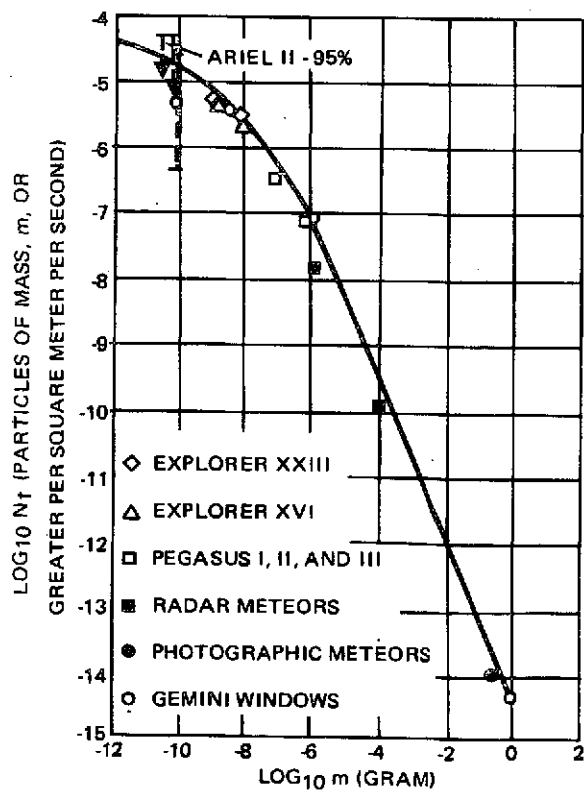
Figure 2-8. Meteoroid Flux-Mass Model

environments specified in References 4 and 5 were found to agree with those
of References 2 and 3. The meteoroid flux-mass model shown in Figure 2-8 is
the same as specified in Reference 5, this model being expressed by the
equations:

$$10^{-6} \leq m \leq 10^{0}: \log N_t = -14.37 - 1.213 \log m$$

$$(1)$$

$$10^{-12} \leq m \leq 10^{-6}: \log N_t = -14.339 - 1.584 \log m - 0.063 (\log m)^2$$

where

    m = meteoroid mass, g

    N_t = particles of mass, m, or greater per square meter per second

Also, Reference 5 specifies an average meteoroid velocity of 20 km/s and a
mass density of 0.5 g/cm^3. The criteria of Reference 4 stipulate that the
Space Shuttle shall be designed for at least a 0.95 probability of no puncture
during the maximum total time (100 to 500 missions) in orbit using the
meteoroid model defined in Figure 2-8 combined with the mass and velocity
values quoted above from Reference 5. The penetration criterion of a 0.95
probability of no puncture was reviewed in greater depth during full-scale
subsize panel design efforts. Findings from that review are discussed in
Section 5 and in Appendix E.

2.2 TPS PERFORMANCE REQUIREMENTS AND DESIGN CRITERIA

A review of the Space Shuttle RFP (Reference 4) was also made to determine
additional performance requirements for the Orbiter TPS. A summary of the
pertinent requirements for TPS design are presented in Appendix A as the
basic set of requirements used in analytical comparisons of candidate designs,
in design of full-scale subsize test components, and in determining objectives
in Phase I tests of TPS designs.

The criteria of Reference 4 specify that materials shall not exhibit cumulative
creep strain leading to rupture, detrimental deformation, or creep buckling
during their service life. However, a specific amount of allowable deformation

in metallic TPS panels is not stipulated; in lieu of such a specified amount, the following equation for maximum cumulative panel deformation during the life of the vehicle was used:

$$\delta = 0.25 + 0.025L \text{ (cm)}$$

$$(\delta = 0.1 + 0.01L \text{ (in.)})$$

(2)

where

δ = maximum normal panel deflection, cm (in.)

L = distance between panel supports, cm (in.)

The criterion expressed by Equation (2) was developed in previous TPS studies on the basis that such a deflection would not cause significant incremental aerodynamic heating. In subsequent creep deflection analyses (Appendix D), the computed panel deflections from cumulative creep, based on cyclic creep tests of TD Ni-20Cr samples, were significantly smaller than the criterion of Equation (2). For example, in using Equation (2), the maximum midspan deflection allowable for a panel of 45.7-cm (18.0-in.) length would be 0.71 cm (0.28 in.). In comparison, the computed mid-span deflection, using the design loads of Appendix D, was 0.0133 cm (0.00524 in.) for a corrugation-stiffened panel design and 0.0167 cm (0.00655 in.) for a zee-stiffened panel configuration (Table D-1). In actual tests simulating 100 missions, the panel midspan average deflection measured at the conclusion of the tests was 0.0203 cm (0.008 in.) for a 45.7-cm (18.0-in.) single-face, corrugation-stiffened design and 0.0305 cm (0.012 in.) for a single-face, zee-stiffened panel of the same length.

Other criteria presented in Appendix A are specific with respect to flight conditions, loads, design factors of safety, internal temperatures that are to be maintained, and duration of missions. These criteria were used in parametric studies and in the design of test components.

Section 3
MATERIAL PROPERTIES

A majority of TD Ni-20Cr sheet characterization tests to evaluate current
material properties have been conducted under existing or recently completed
contracts sponsored by the Lewis Research Center (LeRC) of the NASA. The
two evaluation programs sponsored by LeRC are (1) NAS3-15558, Character-
ization of TD NiCr Material, and (2) NAS3-15567, Forming and Joining of TD
NiCr. The program for characterization of material properties (NAS3-15558)
provided all necessary material property data with the exception of cumula-
tive creep and residual strength characteristics. The latter properties were
evaluated in this program through multiple-parameter tests of tensile sam-
ples. Such tests were conducted using a modified Astrofurnace chamber in
which the samples were subjected to programmed cycles of stress, temper-
ature, and pressure that simulated critical Orbiter mission conditions for a
metallic radiative heat shield. In addition to the multiple-parameter tests,
single lap-shear joint specimens were tested to evaluate the improvements
in joint efficiency resulting from braze-reinforcement of spot-welded, spot
diffusion-bonded, and seam-welded joints. Braze-reinforcement of joint
areas in thin-gage heat shields was considered a promising technique to
improve both the panel's fatigue strength under boost flight acoustic loads
and panel resistance to joint degradation from long-term thermal and load
conditions of repeated entry flights. The multiple-parameter tests of tensile
samples and the braze-reinforced joint tests are discussed in the remainder
of this section while the results from material property tests conducted under
NAS3-15558 are presented in Appendix B.

Strength levels used for design of the full-scale subsize panels were selected
from the data contained in Appendix B which were then modified to account for
degradation effects of exposure to the elevated-temperature, low-pressure
environment projected for Orbiter entry flights. The analysis used in reducing
strength levels to account for such environmental degradation is presented in

17

Appendix C, which also contains comparisons of the analytical values with results obtained in residual strength tests of TD Ni-20Cr samples subjected to simulated mission environments. Results of the cyclic multiparameter tests were also reviewed and compared with the computed strength degradations used in design allowables.

3. 1 CYCLIC MULTIPLE-PARAMETER TESTS

The multiple-parameter test series consisted of repeated cycles of stress, ambient pressure, and temperature profiles that were designed to simulate mission conditions on a Shuttle Orbiter metallic heat shield. Prior to the start of testing, all TD Ni-20Cr specimens were heat oxidized at 1,451 °K (2, 150 °F) for 1 hour at 1 atmosphere to produce a dark, high-emittance surface oxide. The basic test profile of chamber pressure, temperature, and stress are shown in Figure 3-1. Temperature and chamber pressure profiles were maintained as shown in Figure 3-1 for all test samples, but the stress profiles were ratioed for different sets of test specimens. The ratios used in varying the stress profiles are given in Table 3-1, which also shows the peak stress applied to the samples at 1,368 °K (2, 000 °F) during simulated entry flight. The tensile sample configuration used in the tests is also shown in Table 3-1. A sheet thickness of 0.0254 cm (0.010 in.) was used for all samples since it is representative of the thin sheet to be used in radiative metallic heat shields.

A maximum stress level of 34. 4 MN/m^2 (5,000 psi) was selected for the longitudinal samples at elevated temperature conditions based on a review of data from Reference 6 that defines cumulative creep at 100 hr as a function of stress. As a result of the review of cumulative creep data, it was judged that 34.4 MN/m^2 was an upper stress limit at 1,368°K (2, 000°F) beyond which large creep deformations and an accompanying severe strength degradation might be expected for 0.0254-cm (0.010-in.) thick TD Ni-20Cr material. Similarly, a stress level of 27.6 MN/m^2 (4,000 psi) was selected as a peak stress at elevated temperatures for transverse samples. To obtain data over a range of stresses, the samples were divided into three sets each for longitudinal and transverse samples. Maximum stresses were reduced to 30.9 MN/m^2 (4,500 psi) and 27.6 MN/m^2 (4,000 psi) for the additional sets
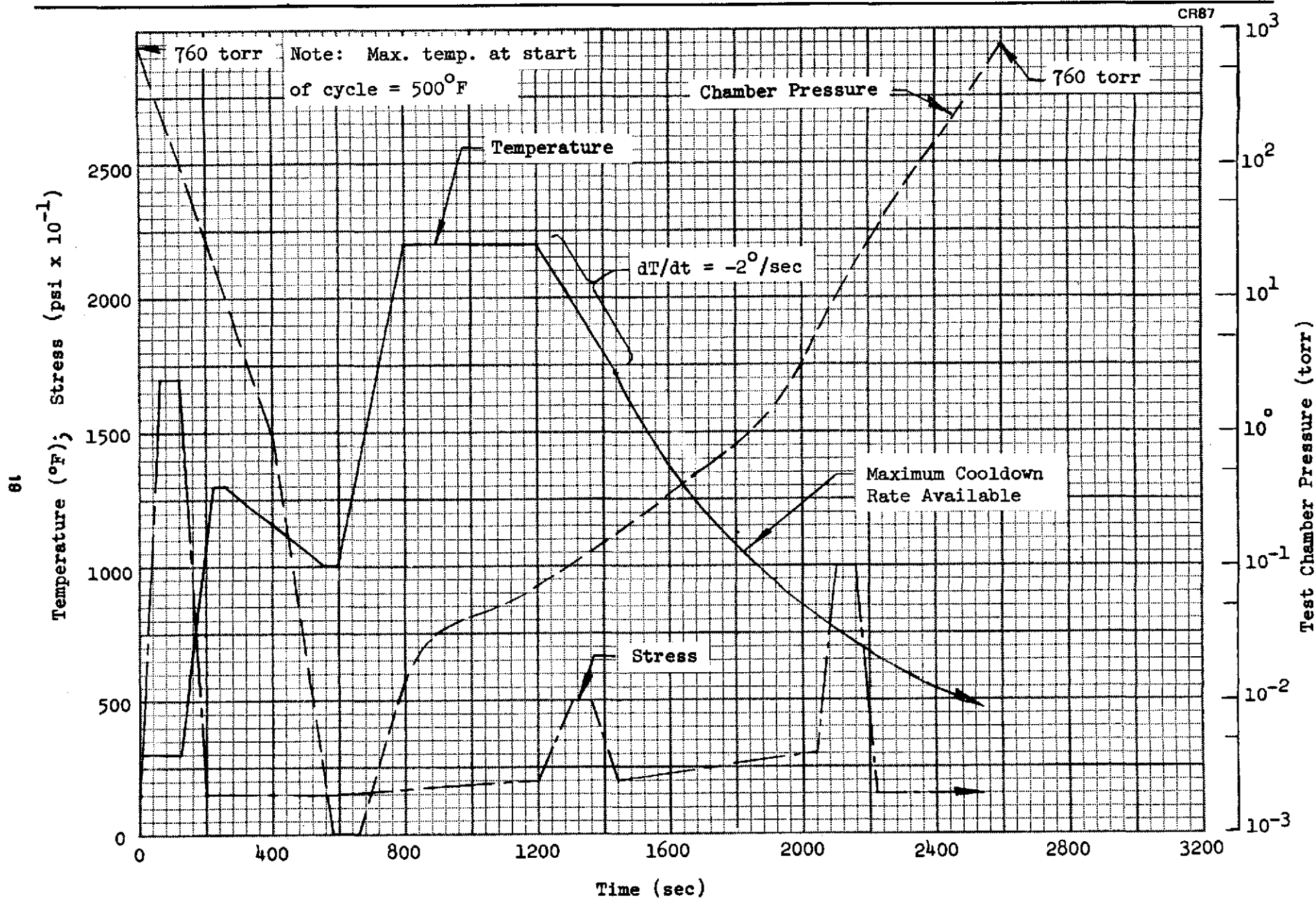
Figure 3-1. Cyclic Multiple Parameter Test Profiles

Table 3-1

TEST MATRIX FOR CYCLIC CREEP STRAIN SPECIMENS

Test Set No.	Specimen Number	Specimen Orientation	Stress Profile	Max. Stress At 1,368°K; MN/m^2 (psi)	No. of Cycles
I	1	L [1]	Basic [3]	34.4 (5,000)	100
	2	L	Basic	34.4 (5,000)	
II	3	T [2]	0.8 x Basic	27.6 (4,000)	100
	4	T	0.8 x Basic	27.6 (4,000)	
III	5	L	0.9 x Basic	31.0 (4,500)	100
	6	L	0.9 x Basic	31.0 (4,500)	
IV	7	T	0.7 x Basic	24.1 (3,500)	100
	8	T	0.7 x Basic	24.1 (3,500)	
V	9	L	0.8 x Basic	27.6 (4,000)	75
	10	L	0.8 x Basic	27.6 (4,000)	
VI	11	T	0.7 x Basic	24.1 (3,500)	75
	12	T	0.7 x Basic	24.1 (3,500)	

[1] Longitudinal

[2] Transverse

[3] See Figure 3-1

SPOTWELD DBLRS 4 PLCS EACH END

ALL DIMENSIONS IN CM (IN.)

20.3 (8.00)

6.35 (2.50)

6.99 (2.75)

1.42 (0.56)

3.18 (1.25)

2.84 (1.12)

A

A

$1.27 {}^{+000}_{-0.013}$
$\left(0.500 {}^{+000}_{-0.005}\right)$

$0.952 {}^{+0.005}_{-000}$ DIA
$\left(0.375 {}^{+0.002}_{-0.000}\ DIA\right)$
(2 PLCS)

7.61 ± 0.15
(3.00 ± 0.06R)
(TYP)

ALL MATL 0.010-IN. TD Ni-20Cr

A-A
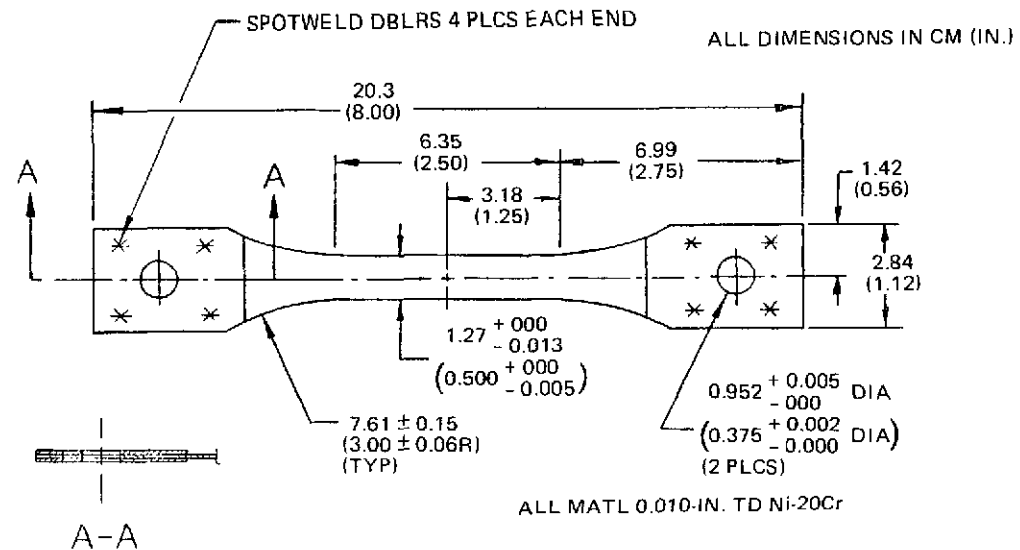
of longitudinal samples, while a similar reduction to 24.1 MN/m^2 (3,500 psi) was made for the remaining sets of transverse samples.

The multiple-parameter tests were conducted in a modified Astrofurnace unit at the McDonnell Douglas Research Laboratories at St. Louis. Figure 3-2 shows an overall view of the Astrofurnace, including the furnace extension chamber modification that permits force transducers to be located inside the chamber. This modification is shown in the schematic diagram of Figure 3-3, which illustrates the use of a force transducer for each test specimen. Such an arrangement provides direct measurement of the load in each specimen and, by locating the transducers internally, avoids unaccounted-for pressurization effects on the sample caused by pressure differences between the low chamber pressure and the one-atmosphere pressure outside the chamber.

3.1.1 Cumulative Creep Strains

A total of 100 cycles was applied to each tensile sample in test sets I, II, III, and IV while each sample of sets V and VI received 75 cycles (Table 3-1). The cumulative creep strain of each specimen was determined at 25-cycle intervals. The method employed to determine strain involved measuring the change in distance between reference marks placed on each specimen in the center of the gage length. The reference marks were approximately 0.0005-cm (0.0002-in.) deep, 0.0025 to 0.010-cm (0.001 to 0.004-in.) wide, 0.159-cm (0.0625-in.) long, and were spaced 2.54 cm (1 in.) apart. The reference marks were scribed in each specimen using a special tool and a jig bore machine. Distance between the scribe marks was measured using a Unitron Measuring Microscope, which is shown in Figure 3-4. This technique of measuring strain does not allow accurate measurement to less than 0.001 in., since the scribe marks have a width of 0.0025 to 0.010 cm (0.001 to 0.004 in.). Hence, strains of less than 0.1 percent (0.001 cm per cm) result in some scatter of data. Four separate measurements of distance between scribe marks were made on each specimen at each 25-cycle interval. The maximum range for any one group was 0.00228 cm (0.0009 in.), indicating that the technique used can provide accuracy within ±0.00114 cm (±0.00045 in.).
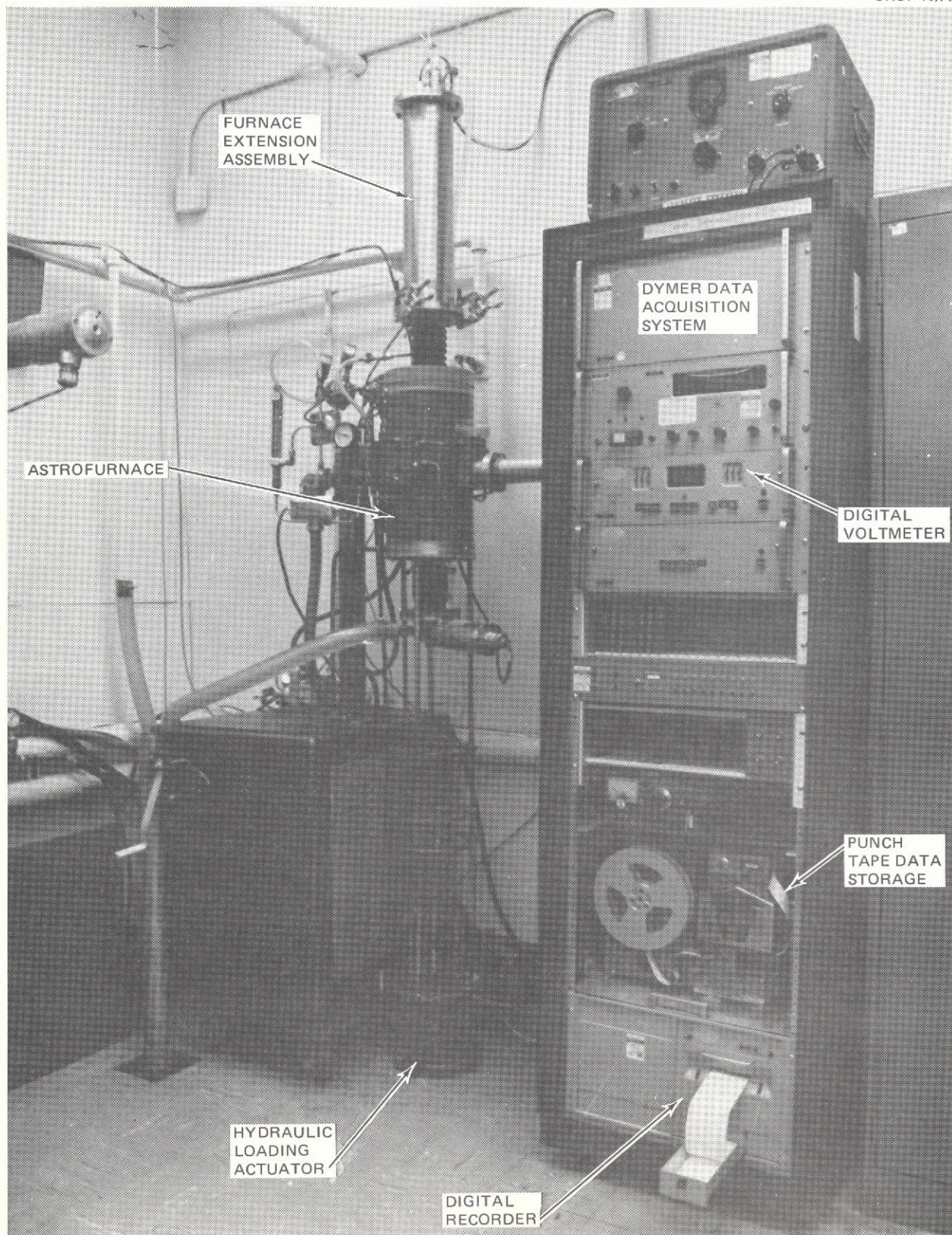
Figure 3-2. Modified Astrofurnace Test Equipment
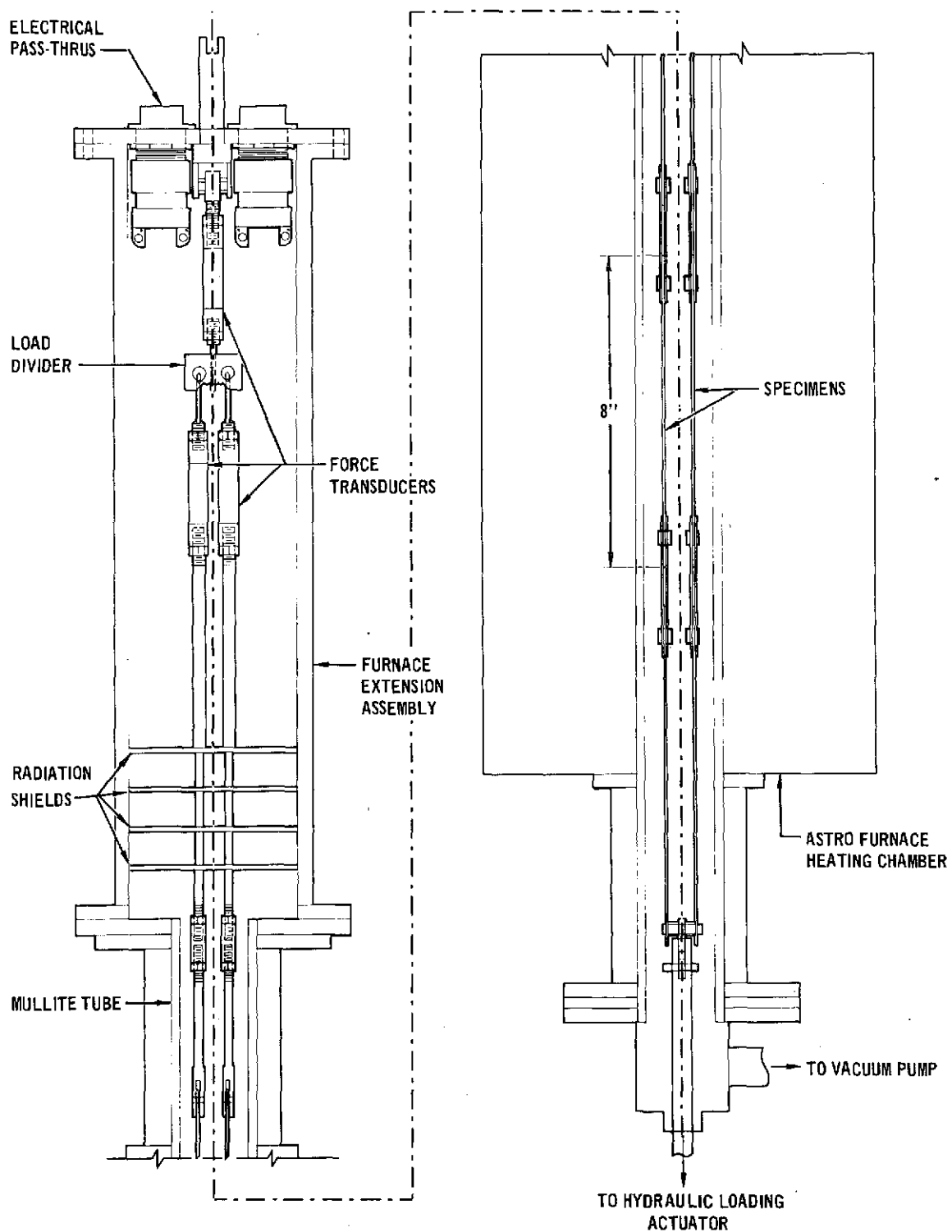
Figure 3-3. Schematic of Astrofurnace Test Chamber
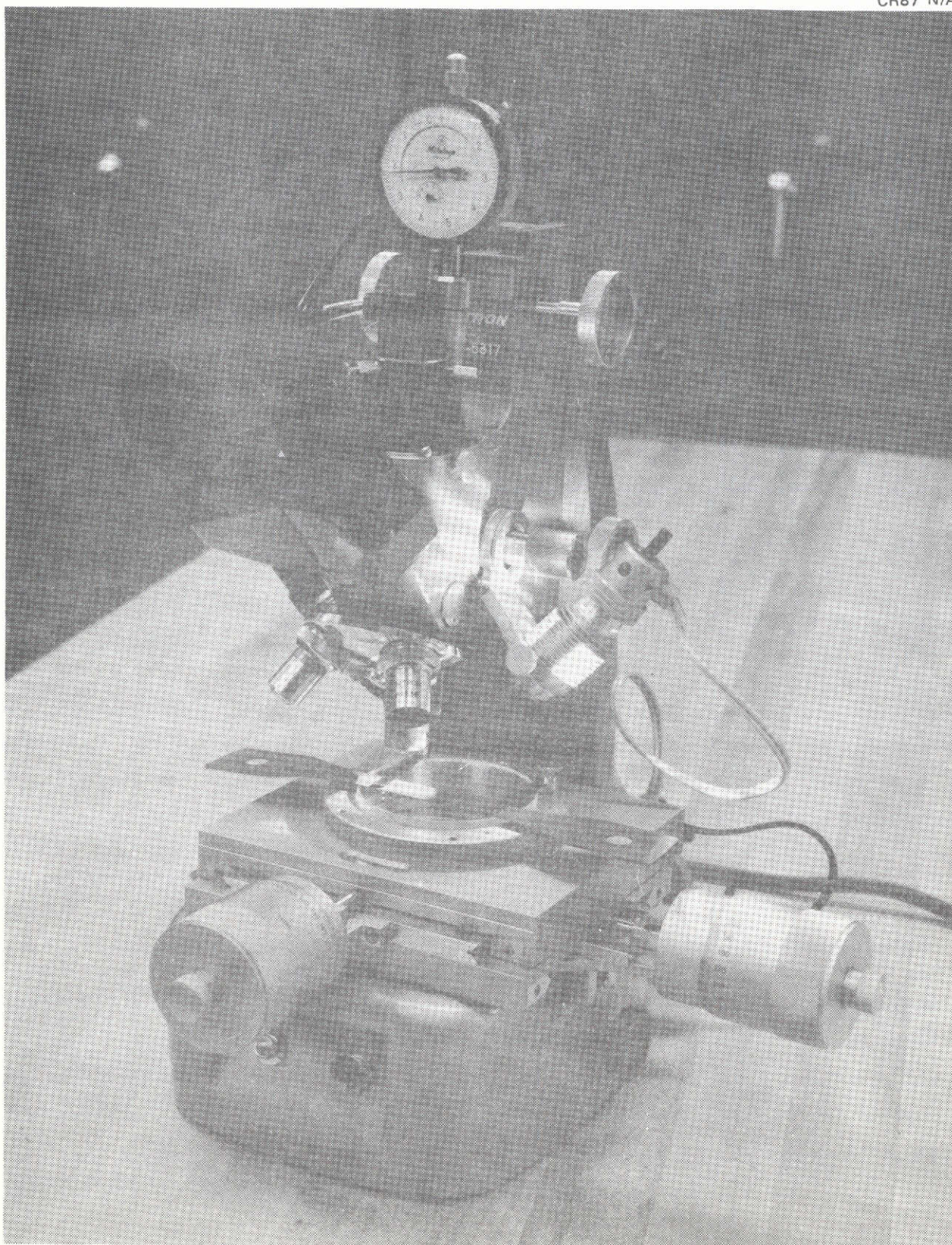
Figure 3-4. Unitron Measuring Microscope

Typical cumulative strain data are shown in Figure 3-5 as a function of number of test cycles. The very low strains experienced by the samples, combined with the accuracy limits of the measuring technique, yielded scatter in the data that is especially evident in Figures 3-5d and 3-5e. The maximum average cumulative strain developed from tensile stresses in the cyclic tests was approximately 0.04 percent, a magnitude that is not expected to be critical in design of TD Ni-20Cr heat shields. However, permanent deformations may also occur from cyclic thermal stresses occurring in builtup heat shields; deformations from thermal cycles are discussed subsequently in Section 5.

Cumulative strains generated in the multiple-parameter cyclic tests are compared in Figure 3-6 with strains recorded on other samples tested in constant-load and temperature tests that are reported in Reference 6. The stress levels used for the cyclic test points plotted in Figure 3-6 were the maximum stresses at elevated temperature (Figure 3-1), and as such represent a somewhat shorter total time at those stresses than shown for the constant-load specimens reported in Reference 6. Despite the differences in stress and temperature histories between the two test series, relatively low total strains are shown by the TD Ni-20Cr samples subjected to either cyclic multiple-parameter tests or to constant-load and temperature tests at maximum stress levels in the range of 24.1 to 31.0 MN/m^2 (3,500 to 4,500 psi).

Figure 3-6 illustrates the typical elevated temperature characteristic of TD Ni-20Cr in which strains are exceptionally low ($\epsilon \leq 0.1$ percent) in either cyclic or constant tensile load conditions until a critical stress level is applied, such a level being dependent on direction of applied stress (longitudinal or transverse) and temperature. Stresses above the critical level produced rapidly increasing cumulative strains and the samples generally failed at total strains ranging from 1 to 2 percent. Such behavior is further reflected in the data of Appendix B.

None of the cyclic test samples was stressed above the critical level, and consequently maximum cumulative strains were less than 0.05 percent. Also, none of the test samples failed and all were available for residual strength evaluations.

TD Ni-20Cr Matl., 0.010 in. Longitudinal Samples

Maximum Stress at 2,000°F: 5,000 psi

⊙ Specimen 1, Set I

▦ Specimen 2, Set I

Cumulative Strain (Percent)

Test Cycles

a. SET I, LONGITUDINAL SAMPLES

TD Ni-20Cr Matl., 0.010-in. Transverse Samples

△ Specimen 1, Set II (Max. Stress at 2,000°F: 4,000 psi)

◉ Specimen 1, Set VI (Max. Stress at 2,000°F: 3,500 psi)

▢ Specimen 2, Set II (Max. Stress at 2,000°F: 4,000 psi)

◁ Specimen 2, Set VI (Max. Stress at 2,000°F; 3,500 psi)

Cumulative Strain (Percent)

Test Cycles

b. TRANSVERSE SAMPLES

Figure 3-5. Cumulative Average Strain Versus Test Cycles (Page 1 of 3)
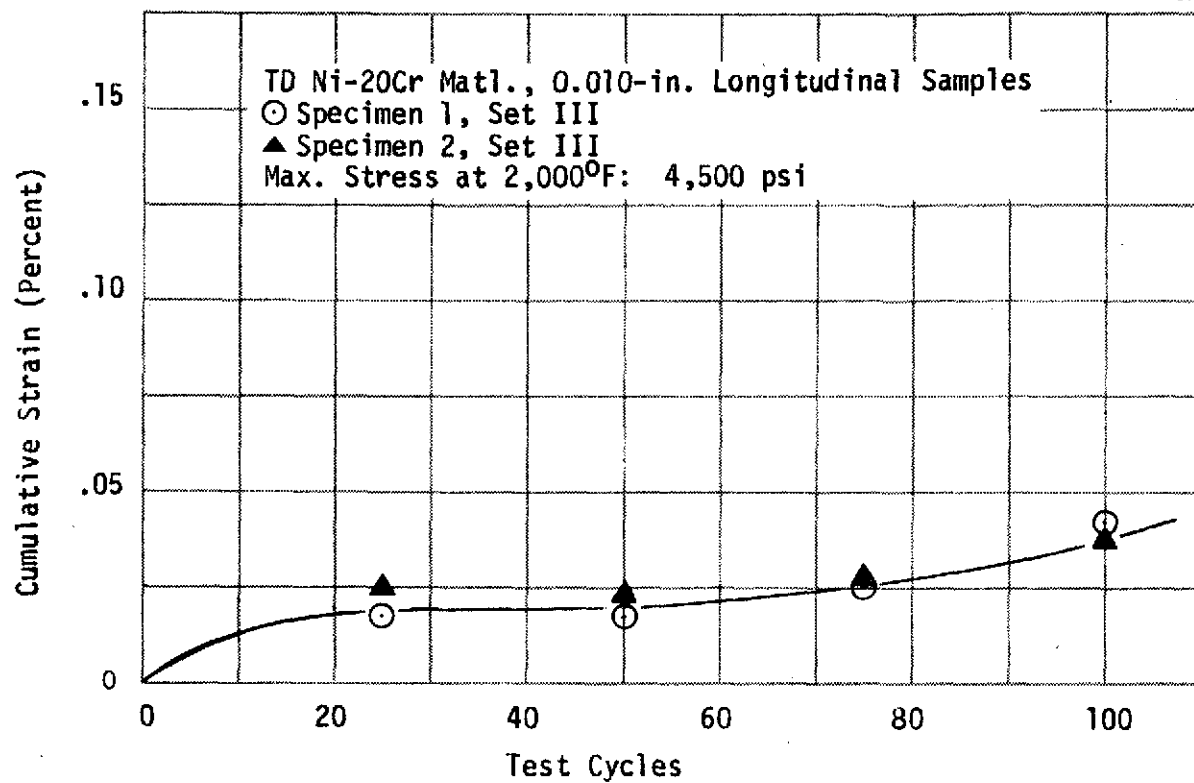
c. SET III, LONGITUDINAL SAMPLES
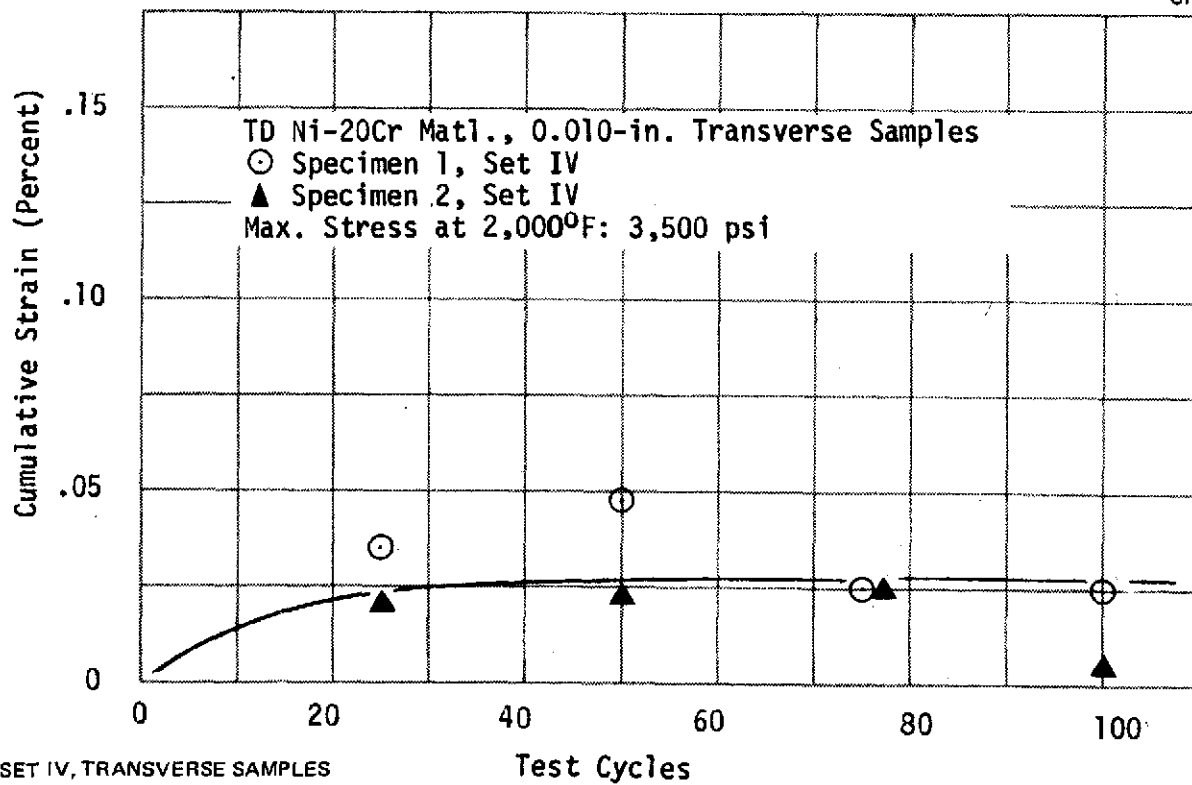
d. SET IV, TRANSVERSE SAMPLES

Figure 3-5. (Page 2 of 3)

TD Ni-20Cr Matl., 0.010-in. Longitudinal Samples
⊙ Specimen 1, Set V
▲ Specimen 2, Set V
Max. Stress at 2,000°F: 4,000 psi

e. SET V, LONGITUDINAL SAMPLES

Test Cycles
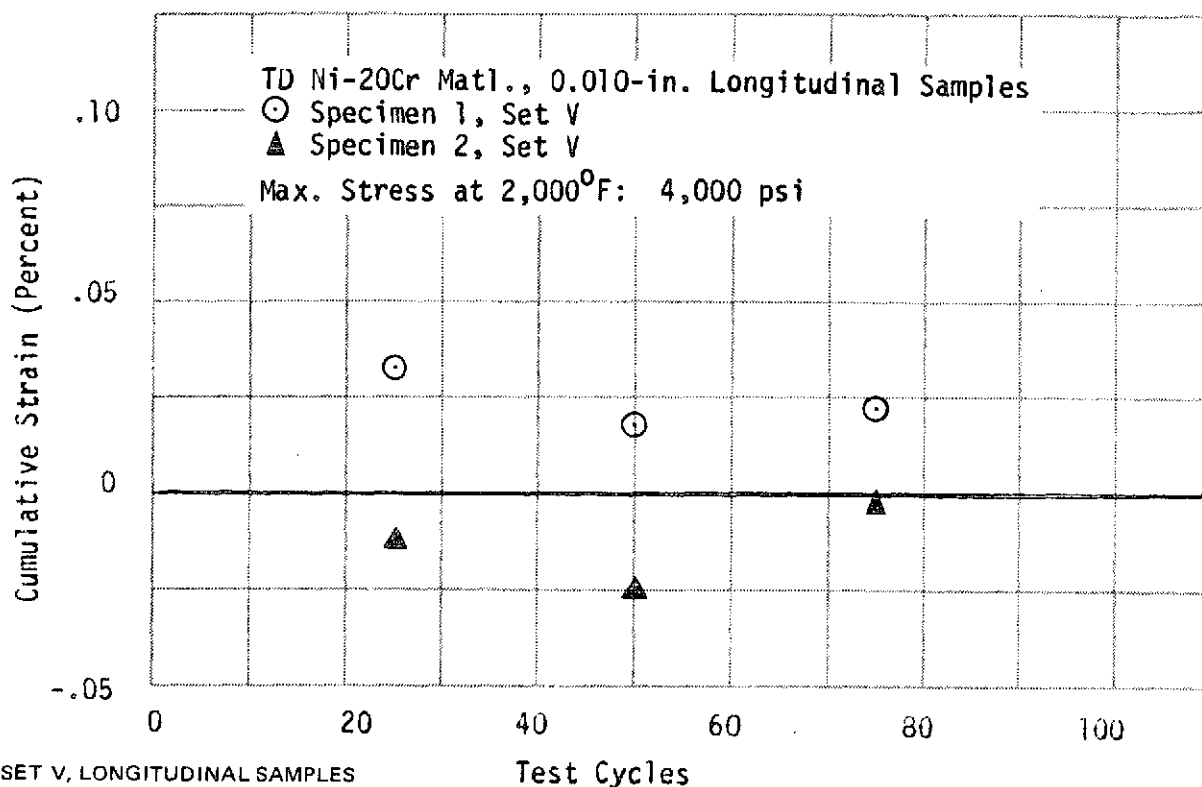
Figure 3-5. (Page 3 of 3)

3.1.2 Residual Strength Tests

Residual strength characteristics were evaluated at room temperature and 1,368°K (2,000°F), half the samples being tested at room temperature and the remainder at 1,368°K (2,000°F). Ultimate tensile strength, yield strength, and elongation at failure were measured during residual strength tests.

Results of all residual strength tests conducted with cyclic creep samples are summarized in Table 3-2. Test results showed a significant loss of elongation at room temperature as well as reductions in ultimate and yield strengths.

It was desired to compare the degradation effects of low pressures and elevated temperatures only with the effects of stress cycles combined with pressure and temperature cycles. Thus, data from residual strength tests of both types of samples were used in comparisons of ultimate strength
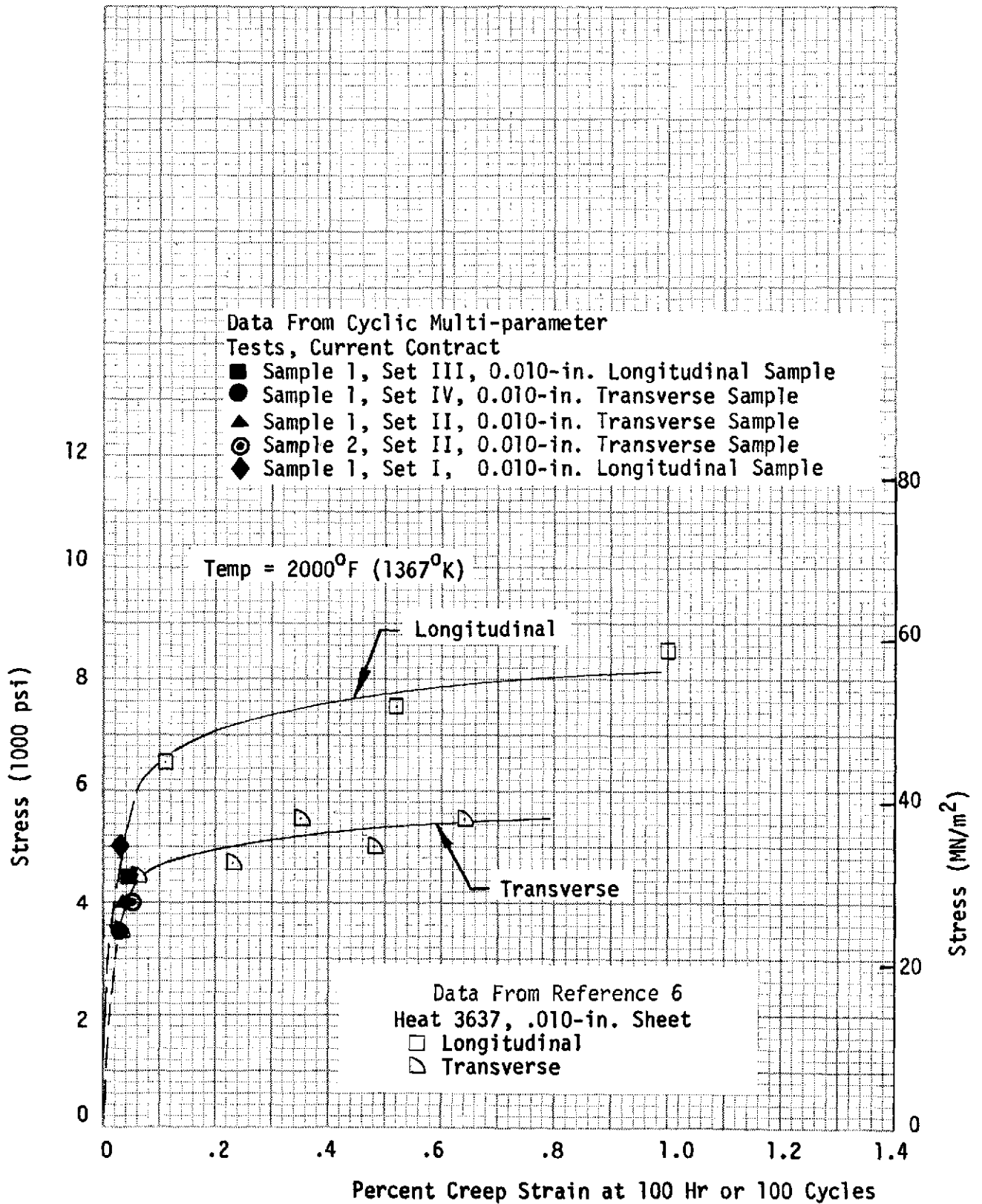
Figure 3-6. Strain Comparison Between Cyclic Test Results and Constant Load Creep Tests

Table 3-2

RESIDUAL STRENGTH OF CYCLIC CREEP SPECIMENS

Specimen Number	Specimen Orientation	Stress Profile	Max. Stress at 1,368°K; MN/m² (psi)	Residual Strength					
				Room Temperature			1368°K (2,000°F)		
				F_{tu}; MN/m² (psi)	F_{ty}; MN/m² (psi)	ε(4)	F_{tu}; MN/m² (psi)	F_{ty}; MN/m² (psi)	ε(4)
1	L(1)	Basic(3)	34.4 (5,000)	600 (87,000)	490 (71,100)	2.0			
2	L	Basic	34.4 (5,000)				99.9(14,500)	—	1.0
3	T(2)	0.8 x Basic	27.6 (4,000))	308 (44,700)	—	—			
4	T	0.8 x Basic	27.6 (4,000)				48.8 (7,100)	—	1.0
5	L	0.9 x Basic	31.0 (4,500)	497 (72,100)	472 (68,500)	1.0			
6	L	0.9 x Basic	31.0 (4,500)				91.8(13,300)	—	—
7	T	0.7 x Basic	24.1 (3,500)	237 (34,400)	—	—			
8	T	0.7 x Basic	24.1 (3,500)				54.4 (7,900)	—	1.0
9	L	0.8 x Basic	27.6 (4,000)	730(106,000)	492 (71,400)	7.0			
10	L	0.8 x Basic	27.6 (4,000)				93.7(13,600)	—	1.0
11	T	0.7 x Basic	24.1 (3,500)	488 (71,000)	—	1.0			
12	T	0.7 x Basic	24.1 (3,500)				88.9(12,900)	—	—

(1)Longitudinal

(2)Transverse

(3)See Figure 3-1

(4)Percent elongation in 5.08 cm (2-in.) gage length

levels obtained from TD Ni-20Cr sheet material in these conditions. Such comparisons of average ultimate strengths are shown in Figure 3-7 for (1) as-received TD Ni-20Cr sheet, (2) samples tested after exposure to temperature and reduced pressure environments, and (3) the multiple-parameter creep strain samples that were subjected to programmed stress, temperature, and reduced pressure cycles. The results of the three types of tests showed that

    A.   Exposure without stress has slightly greater degradation effects on thinner gage material.

    B.   For 0.0254 cm (0.010 in.) thick material tested as longitudinal specimens, exposure without stress produced nearly the same degradation as exposure with stress.

    C.   Transverse specimens were more severly affected than longitudinal specimens in residual room temperature testing.

    D.   The same trend in directionality (i.e., transverse specimens showed more degradation) was noted in tests at $1,368^{\circ}K$ $(2,000^{\circ}F)$, but not to the extent observed at room temperature.

From data obtained in the cyclic multiple-parameter tests, it was concluded that stress levels of 24.1 to 27.6 MN/m^2 (3,500 to 4,000 psi) in the transverse direction can produce a strength degradation of approximately 50 percent at room temperature for 0.0254-cm (0.010-in.) thick TD Ni-20Cr sheet. Ductility at room temperature was also shown to be severely reduced.

Despite the strength degradations noted in the multiple-parameter tests, subsequent design and testing of candidate heat shield configurations showed the noted strength reductions to have a minimum impact on panel weights and on overall TPS weights. The lessening of strength degradation effects on weight resulted from: (1) the relatively low tensile stresses that accompany critical compressive buckling loads at low temperature conditions where degradation was most severe, (2) the isotropic panel designs utilized the greater strength and lower degradations of the sheet material's longitudinal direction, and (3) the Phase I panel tests showed critical areas on the heat shields to be attach

31
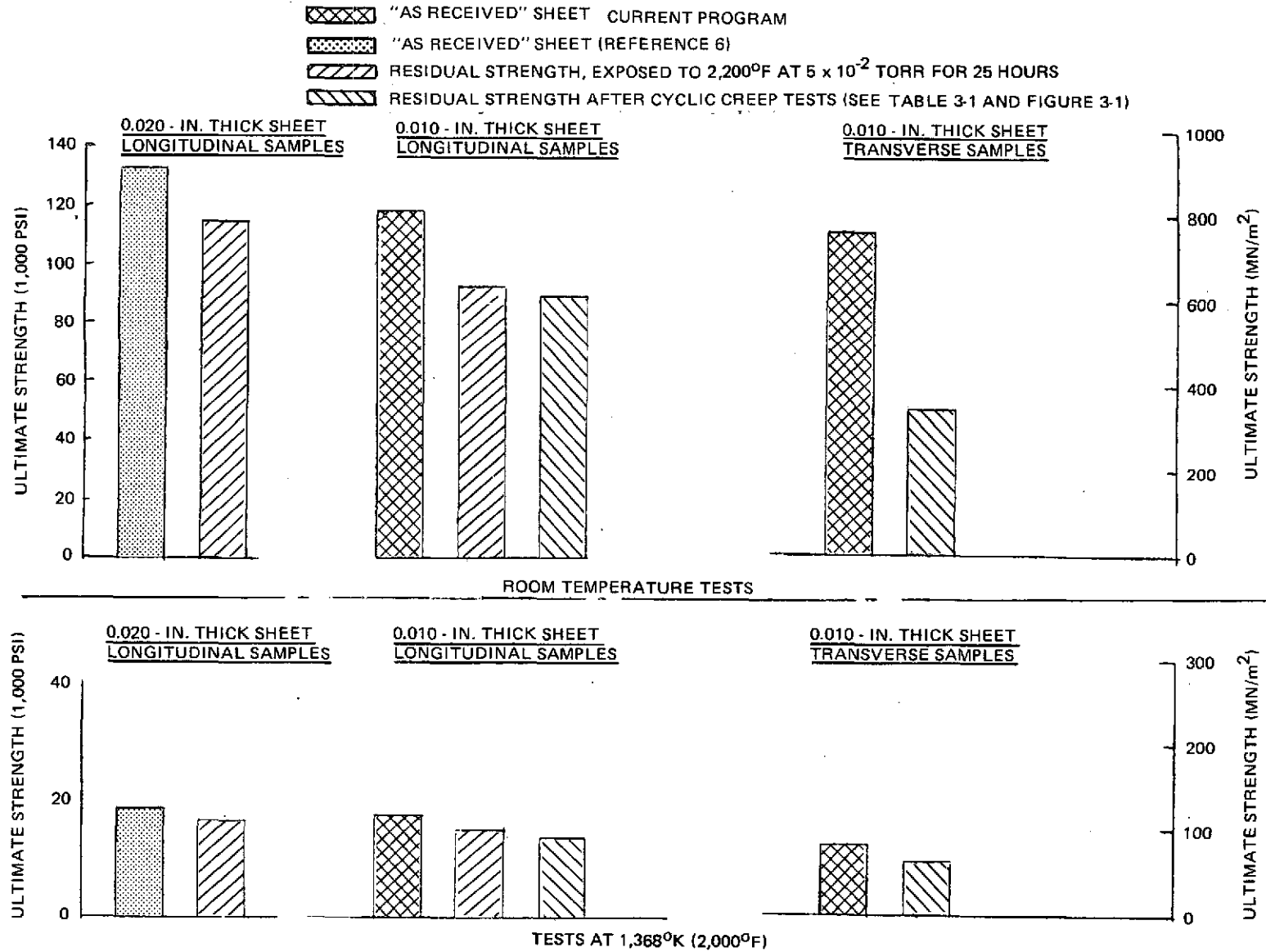
Figure 3-7. Average Ultimate Strength Comparisons of Basic TD Ni — 20 Cr Sheet and Residual Strength Samples

points and edge stiffeners rather than panel midspan areas where maximum stresses from static design loads were computed. The impact on overall TPS weights was also minimal because panel weights were computed to be less than 35 percent of the overall TPS weight (See Table 4-2, Section 4).

3.1.3 Metallurgical Evaluations

Metallurgical evaluations were also conducted on sections removed from the cyclic creep samples. Several samples showed visual evidence of surface oxidation on the fracture edge where final failure and sample separation occurred during residual strength tests. The oxidized appearance was evident on only a portion of the fracture edge, an appearance that suggested initial cracking may have occurred during elevated-temperature creep strain cycles applied in the Astrofurnace test chamber. Microstructure studies were conducted on two of the failed samples to determine whether internal oxidation could be detected in the samples.

Photomicrographs were first taken with a scanning electron microscope (SEM) at two positions along the fracture edge of specimen No. 7, a cyclic creep sample with a transverse orientation. The two areas photographed are shown in Figure 3-8, where the difference in appearance is evident. Cyclic creep specimen No. 7 was tested for residual strength at room temperature (Table 3-2) and showed severe loss in ultimate tensile strength. Since the residual strength test of specimen No. 7 was conducted at room temperature, any oxidation of the fracture edge could have occurred only during elevated-temperature portions of the creep strain test cycles. The latter fact, combined with the low ultimate stress of 237.5 MN/m^2 (34,400 psi) recorded in residual strength tests, indicates that initial intergranular cracks may have occurred during the cyclic creep strain tests.

A set of photomicrographs was obtained with a light microscope on sections taken from specimens No. 5 and 7. The former sample had a longitudinal orientation. The two photomicrographs are shown in Figure 3-9 and 3-10, which also indicate the orientation of sections taken from the failed samples. The photomicrographs of Figures 3-9 and 3-10

33
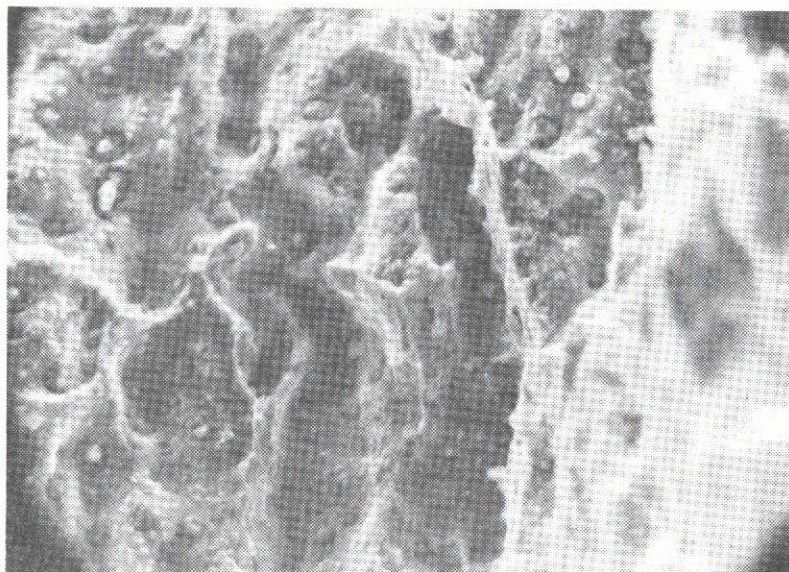
1600X

A. FRACTURE SURFACE WITHOUT OXIDATION.

1820X

B. FRACTURE SURFACE WITH APPARENT SURFACE OXIDATION.

Figure 3-8. Photomicrographs of Fracture Edge Taken with Scanning Electron Microscope, Cyclic Creep Specimen No. 7
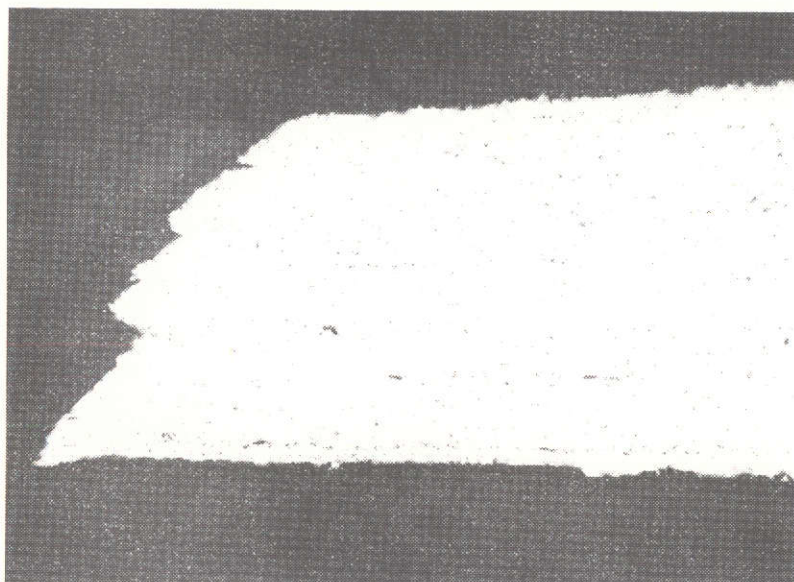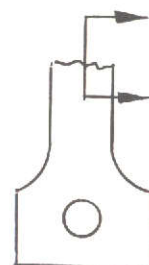
UNETCHED   250X

Figure 3-9. Photomicrograph of Section at Fracture Edge, Cyclic Creep
           Specimen No. 5   (Longitudinal Sample)
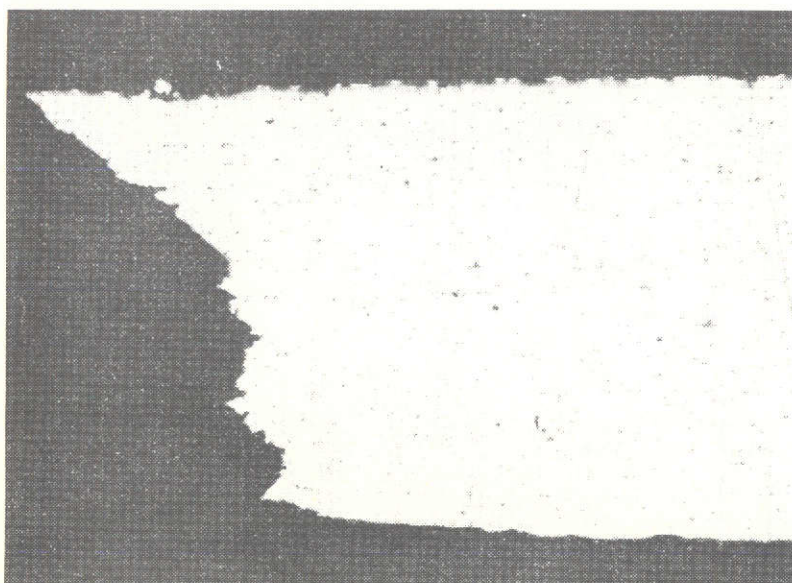
UNETCHED   250X
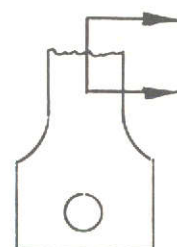
Figure 3-10. Photomicrograph of Section at Fracture Edge, Cyclic Creep
           Specimen No. 7   (Transverse Sample)

showed no evidence of internal oxidation in either sample, and it was thus concluded that internal oxidation was not a significant factor in causing the strength degradation experienced by the cyclic creep samples.

3.2 BRAZE-REINFORCED JOINT TESTS

The use of thin-gage sheet material combined with the severe Shuttle acoustic environment provided a requirement to evaluate an improved joining technique in which conventional spot-welds, spot diffusion-bonds, and resistance seam-welds were reinforced by a brazed area surrounding the nuggets or bond areas. Previous tests with braze-reinforced spot-welded joints had shown a potential for doubling the fatigue strength of 0.0254 cm (0.010 in.) simple lap-shear joints when compared to the fatigue strength levels of conventional unreinforced spot-welded joints. Thus, three types of standard joints used in thin-gage parts (spot-welds, diffusion-bonds, and seam-welds) were selected for evaluating the improved strength characteristics provided by braze reinforcement. Two gage combinations were evaluated, the combinations being 0.0254 cm (0.010 in.) joined to 0.0254 cm (0.010 in.) sheet and 0.0508 cm (0.020 in.) joined to 0.0508 cm (0.020 in.) sheet.

Four types of tests were conducted with braze-reinforced joints, (1) tensile-shear strength, (2) fatigue tests at room temperature and at 1,368°K (2,000°F), (3) stress-rupture tests at 1,368°K (2,000°F) and 1,477°K (2,200°F) and (4) residual strength at room temperature, 1,368°K (2,000°F), and 1,477°K (2,200°F). The test matrix and sample configuration are shown in Table 3-3.

The results of all braze-reinforced joint tests showed significant improvement when compared to results from similar tests with unreinforced joints. The tests conducted in this program indicated that full joint efficiency could be obtained in designs typically found in full-scale TD Ni-20Cr heat shield panels.

3.2.1 Fabrication Trials

A two-step fabrication procedure was developed for the braze-reinforced joint samples in which the samples were first spot-welded, diffusion-bonded, or seam-welded. This step was then followed by brazing.

Table 3-3

BRAZE REINFORCED (BR) TD Ni-20Cr JOINT TESTS

Type of Joint		Tensile-Shear	Type of Test and Number of Samples				
			Fatigue		Stress Rupture		Residual Strength [1]
			RT	1,368°K	1,368°K	1,477°K	
BR Spotweld	0.0254-0.254 [2]	10	5	5	5	5	6
	0.0508-0.0508	10	5	5	5	5	6
BR Spot-Diffusion Bond	0.0254-0.0254	10	5	5	5	5	6
	0.0508-0.0508	10	5	5	5	5	6
BR Roll Seam Weld	0.0254-0.0254	10	5	5	5	5	6
	0.0508-0.0508	10	5	5	5	5	6

[1] Tests at room temperature, 1,368°K, and 1,477°K

[2] Sheet thicknesses in cm.

ALL DIMENSIONS IN cm (in.)

1.91 (0.75)

1.91 (0.75)

SPOT DIFFUSION BOND PLUS BRAZE

RESISTANCE SEAMWELD PLUS BRAZE

SPOTWELD PLUS BRAZE
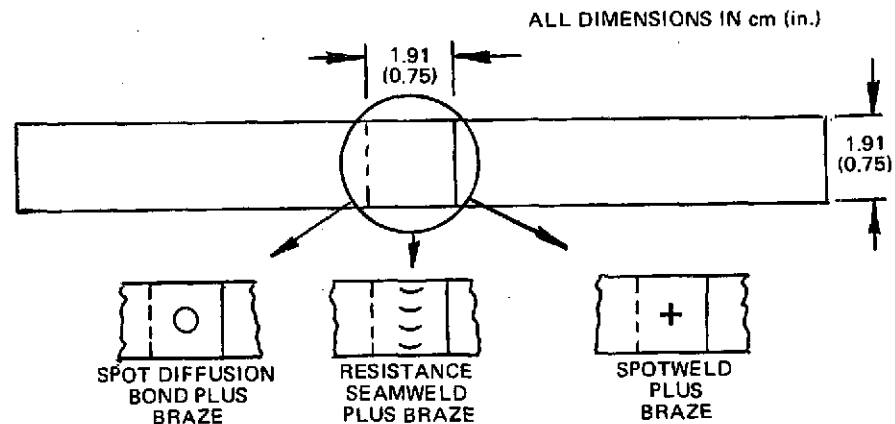
TD-6 braze alloy was selected for the tests, since it was the best of the available alloys for brazing TD Ni-20Cr during Phase I. TD-6 alloy has approximately the same alloy composition as Hastelloy C, with the exception of the addition of silicon, which has the effect of lowering the melting point to the range of 1,559 to 1,588°K (2,350 to 2,400°K). The nominal composition of TD-6 is

(Reference 7):

Element	Percent Weight
Cr	16
Mo	17
W	5
Fe	4 to 7
Si	4
Ni	Balance

The braze alloy was obtained in tape form from Alloy Metals, Inc., which produces the tape with an adhesive back permitting application to sheet faying surface areas. Braze tape width was 1.27 cm (0.50 in.) and thickness was 0.0101 cm (0.004 in.). A tape form of the braze was selected rather than a powder form for the joining trials, since the tape is considerably easier to handle during shop operations and offers a simpler fabrication approach. Of equal or greater importance is the fact that a more uniform application of the braze alloy is obtained through use of a prepared tape as opposed to hand-applied braze powder and binder.

Brief tests were conducted to confirm the brazing temperature developed in previous work with TD-6 (Reference 8). Tests were conducted in a Marshall furnace using a dry hydrogen environment. The selected temperature for good braze flow was 1,579°K (2,380°F).

Concurrent tests were also conducted to determine the best process for tape emplacement and subsequent joining by spot-welding or spot diffusion-bonding. Spot diffusion-bonding requires intimate contact of the faying surfaces and therefore a hole was placed in the tape at points where bonding was to be accomplished. However, investigations were made to assess the possibility of spot-welding through the tape without placing a hole in the braze tape. Results of these tests are shown as typical macrographs in Figures 3-11
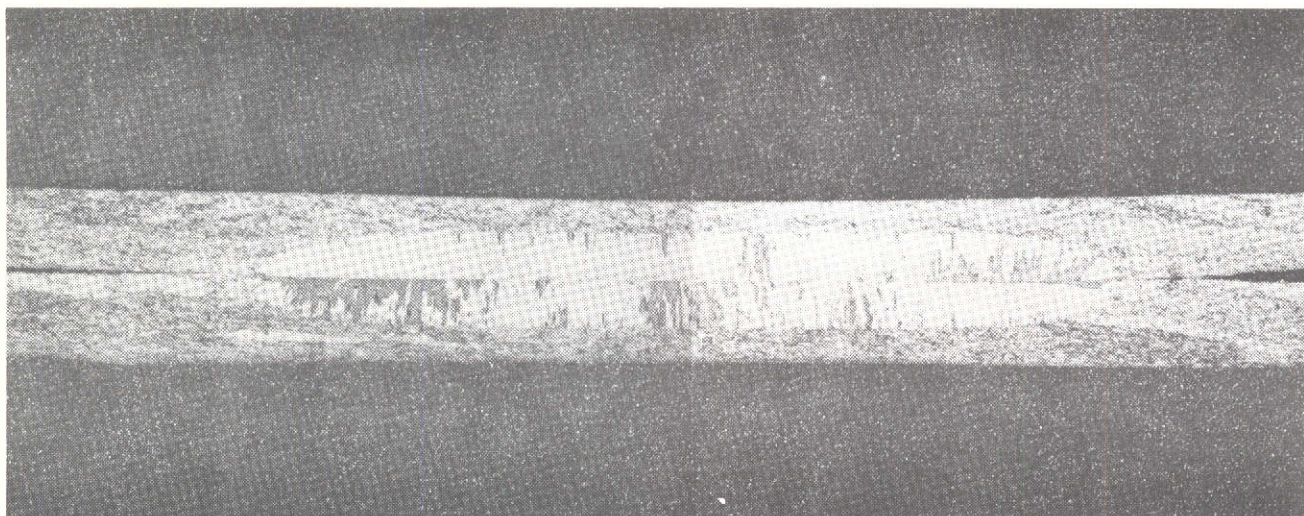
ETCHED   40X

Figure 3-11. Typical Macrograph of Standard Spotweld; 0.010-to 010 TD Ni-20Cr

through 3-13. Figure 3-11 shows a typical spot-weld nugget joining two sheets of 0.025-cm (0.010-in.) thick TD Ni-20Cr without braze tape emplacement in the faying surface. This macrograph was used as a baseline spotweld for comparisons to assess the nugget quality attained in spot-welding through a hole in the braze tape and in spot-welding attempts through the tape itself. Figure 3-12 shows a typical nugget obtained in spot-welding through a hole, while Figure 3-13 shows the results of attempting to spot-weld through the tape. As seen in Figure 3-13, a nugget was not obtained in the latter trials. The large elongated white area in Figure 3-13 is a grain in the 0.0254 cm (0.010-in.) sheet brought out by the electrolytic etching technique. This same type of grain structure is also seen in Figure 3-12, but the spot weld nugget is also obvious at the sheet faying surface area. Higher current settings were tried, but with such settings, excessive interface expulsion occurred without producing a fusion nugget. It was concluded from the tests that good quality spot welds could best be obtained by placing holes in the braze tape, and the spot-welded and brazed-joint test specimens were fabricated in the following steps:

A. Cut specimen blanks, inspect, and clean.

B. Place braze tape with 0.635-cm (0.25-in.) diameter hole in position at joint faying surface.

C. Fixture specimen, spotweld, inspect, and clean.

D. Fixture specimen, braze, and inspect.

A macrograph of a trial sample joint fabricated in the above sequence of steps is shown in Figure 3-14. Good braze flow was obtained well up into the faying surface area near the edge of the spot-weld nugget. Results of the sample specimen shown in Figure 3-14 was considered good, and fabrication of all braze-reinforced spot-welded and diffusion-bonded joints was accomplished with pre-holed tape using the four-step sequence given above. Seam-welded sample fabrication was conducted similarly, the difference being in use of braze tape strips layed parallel to and on both sides of the seam weld line.

3.2.2 Tensile-Shear Tests

The average ultimate strengths of the three types of braze-reinforced joints are compared in Figure 3-15 with the average strength of as-received

ETCHED   40X
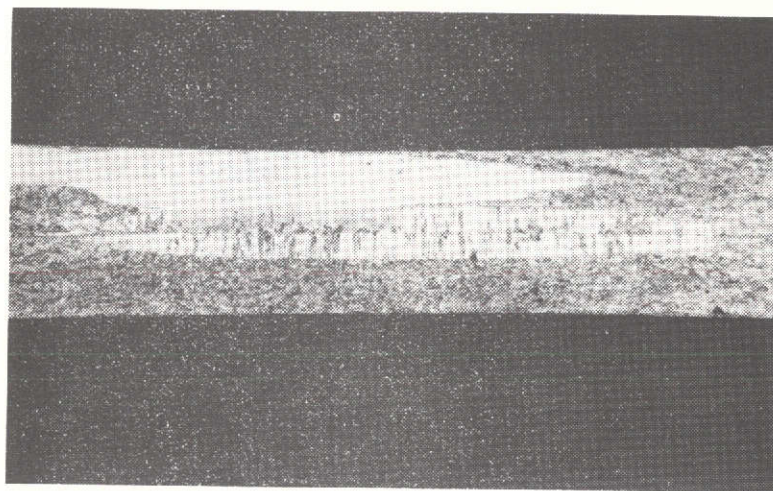
Figure 3-12. Spotweld Through 0.25-in. Diameter Hole in Braze Tape

ETCHED   40X
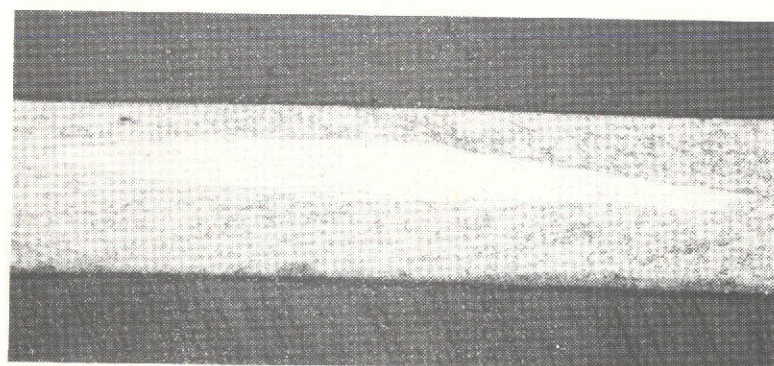
Figure 3-13. Attempted Spotweld Without Hole in Braze Tape
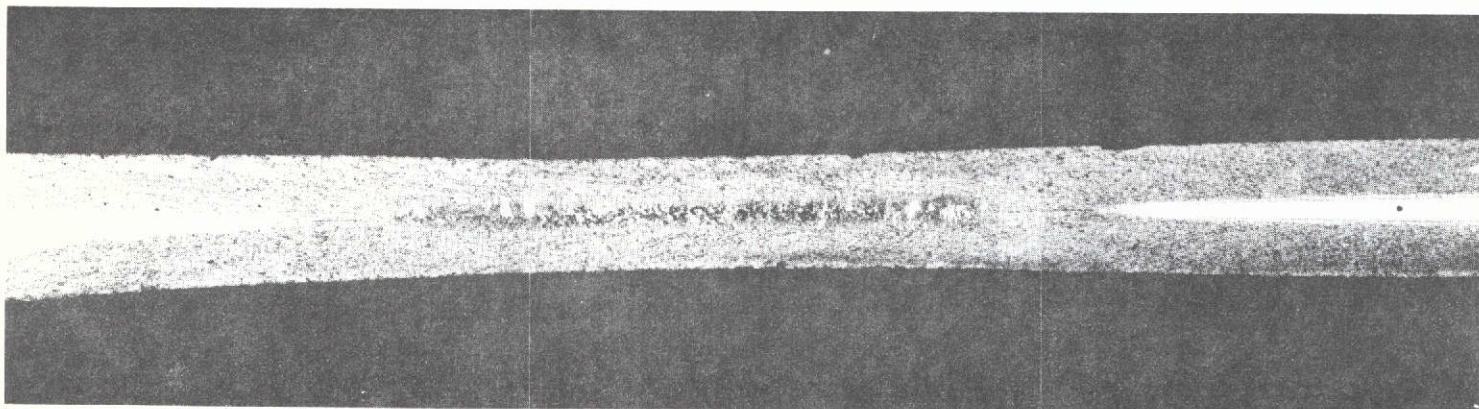
ETCHED   30X

Figure 3-14. Spotwelded and Braze-Reinforced Sample
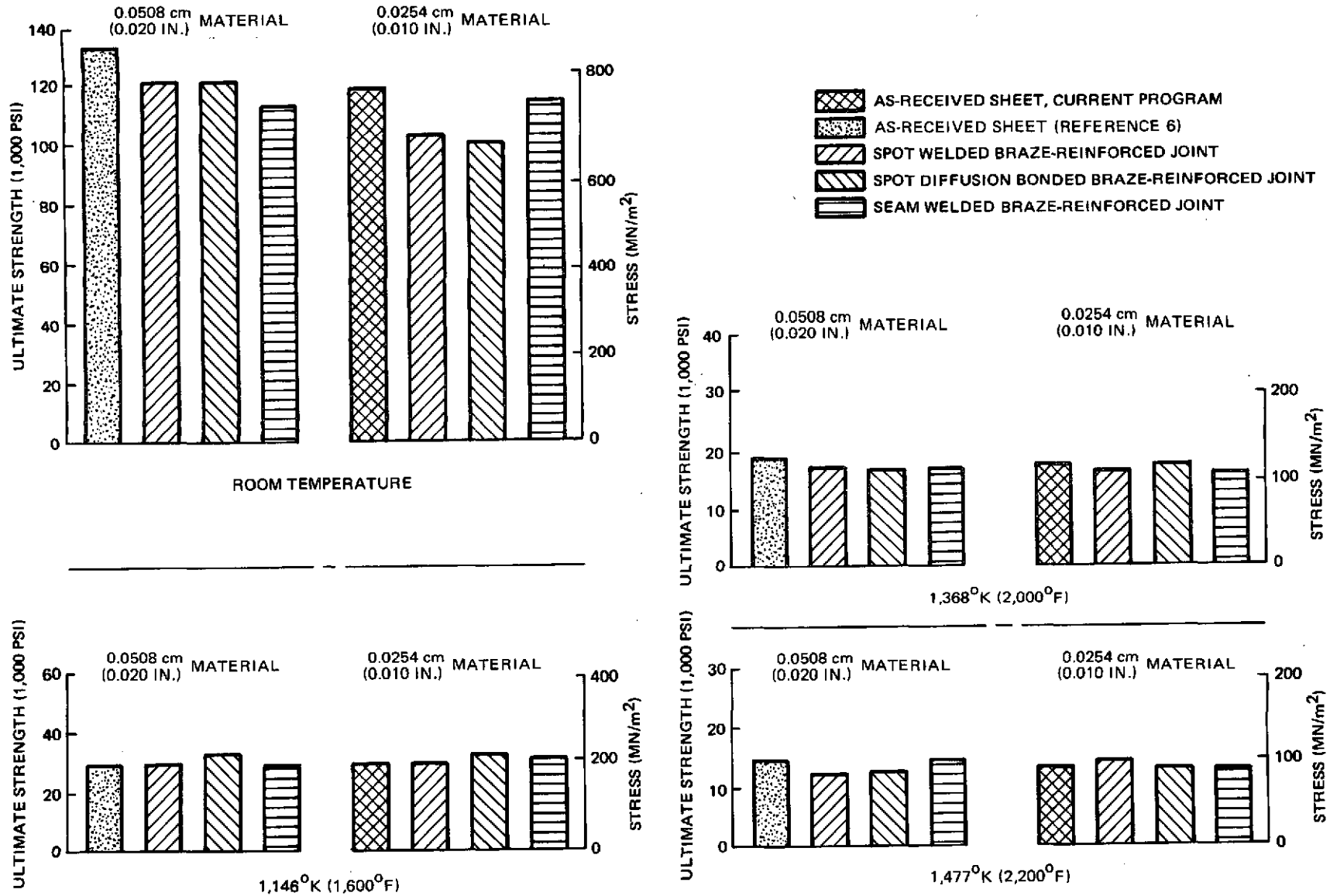
Figure 3-15. Average Ultimate Strength Comparisons of Basic TD Ni-20Cr and Braze-Reinforced Joints

43

TD Ni-20Cr sheet material at room temperature, 1,146°K, 1,368°K, and 1,477°K (1,600°F, 2,000°F, and 2,200°F). The joint stresses shown in Figure 3-15 were based on the cross-sectional area of the sheet strip outside of the joint and are therefore typical of the sheet tensile stresses outside of the joint area. The joint configuration, shown in Table 3-3, contained a 1.91-cm (0.75-in.) sheet width, and the test results are typical of the expected performance for thin-gage sheets spot-welded or diffusion-bonded with similar spacings between points of attachment. The average strengths of 0.0508-cm (0.020-in.) TD Ni-20Cr shown in Figure 3-15 were taken from Reference 6 and the joint strengths were obtained from tests conducted as part of this program. The differences in strength levels shown in Figure 3-15 for 0.0508-cm (0.020-in.) samples were partially attributed to the use of different material heats in the two sets of tests. The 0.0254-cm (0.010-in.) sheet test samples were cut from the same material heat (Heat 3711) used for the 0.0254-cm (0.010-in.) joints. Strength differences in test data from both 0.0254-cm (0.010-in.) and 0.0508-cm (0.020-in.) joint samples are within the expected scatter for TD Ni-20Cr ultimate strength values, and the comparisons of Figure 3-15 indicate that high joint efficiencies can be obtained at elevated temperatures in braze-reinforced joints of all three types tested. Inspection of the failed specimens showed failure to occur in the parent metal of all of the tested joints. At room temperature, the data of Figure 3-15 indicate a decrease in joint efficiency of approximately 10 to 15 percent. The cause of the decrease, while not firmly established, was judged to be either the result of local stress increases near the joint caused by the eccentricity in the test samples (Table 3-3) or the result of degradation of the parent material caused by the braze cycle.

3.2.3 Fatigue Tests
Results of room-temperature fatigue tests conducted with 0.0254-cm (0.010-in.) and 0.0508-cm (0.020-in.) samples are compared in Figure 3-16 with parent metal fatigue strengths obtained from tests in this program and from Reference 6. Fatigue strengths exhibited by the joints are also compared with strength levels of unreinforced spot-welded samples (Reference 8). The higher fatigue strength shown by the 0.0254-cm (0.010-in.) braze-reinforced joints in Figure 3-16 is attributed to the lower bending stresses induced in the
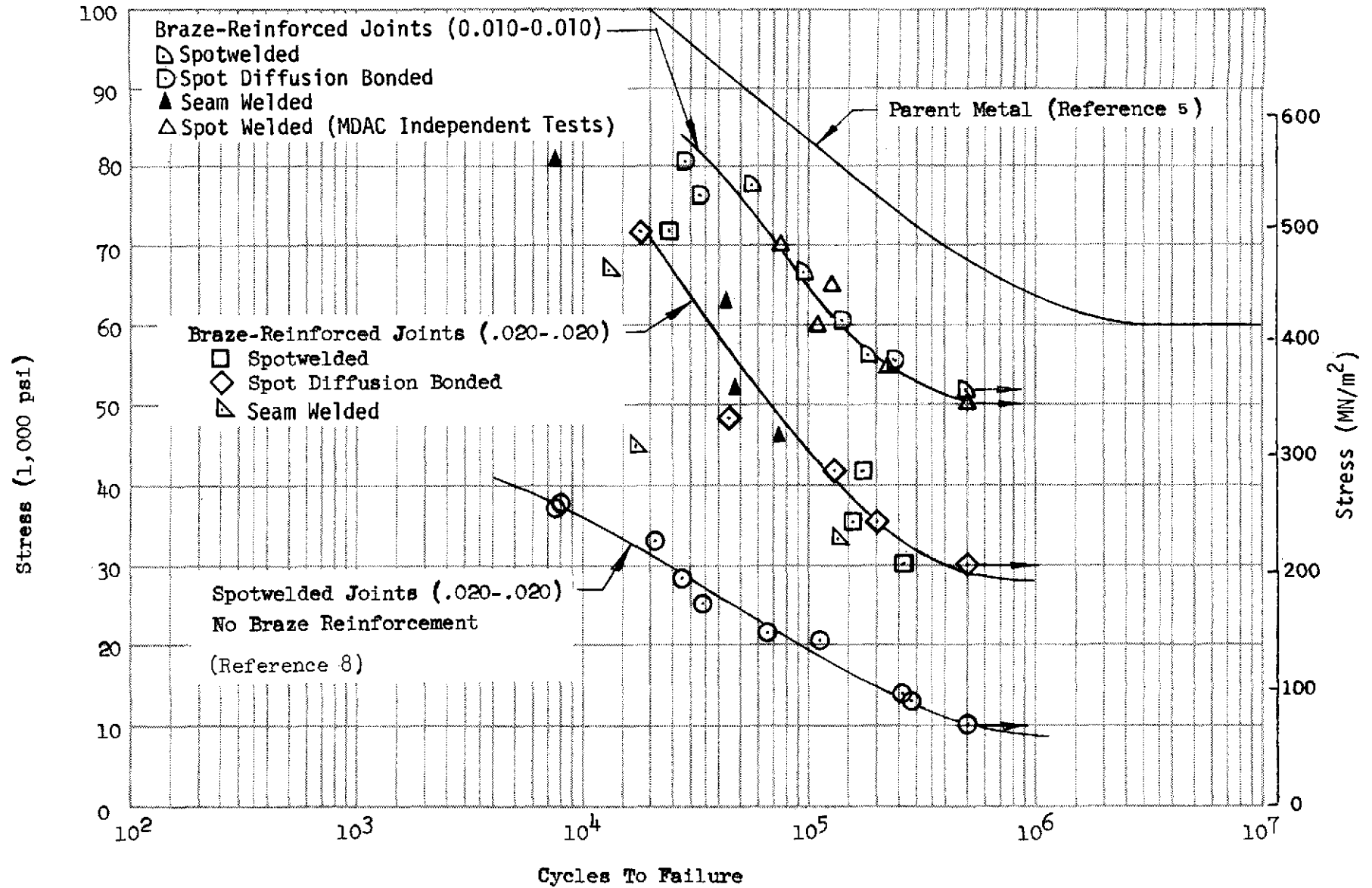
Figure 3-16. Room Temperature Fatigue Test Results for Braze-Reinforced Joints

thinner lap-joint specimens. Results from previous tests conducted by MDAC with 0.0254 cm (0.010-in.) braze-reinforced joints, also shown in Figure 3-16, agree very closely with the data from tests conducted as part of this program. No significant difference was noted between the performance of the spot-welded and spot diffusion-bonded samples, but the seam-welded joints showed somewhat lower fatigue strength in test samples made from either 0.0254-cm (0.010-in.) or 0.0508-cm (0.020-in.) sheet material. Despite the lower fatigue strength of the seam-welded samples, all of the braze-reinforced joints showed markedly improved room-temperature fatigue strength when compared to unreinforced spot-welded joints. For the acoustic fatigue conditions of the Shuttle ascent flight, an improvement in joint fatigue strength of from 138 to 276 MN/m^2 (20,000 to 40,000 psi) could possibly be realized through use of braze-reinforced joining techniques. In terms of fatigue life for equally stressed joints, a fatigue life improvement by a factor of 10 could possibly be realized through use of braze-reinforced joints.

Results from fatigue tests of braze-reinforced joints conducted at 1,368°K (2,000°F) are shown in Figure 3-17. All of the braze-reinforced joints tested at 1,368°K (2,000°F) showed reasonably close agreement whether made from 0.0254-cm (0.010-in.)-thick or 0.0508-cm (0.020-in.)-thick TD Ni-20Cr sheet. This behavior was in contrast to the distinctly higher fatigue stress levels achieved by the 0.0254-cm (0.010-in.)-thick samples in fatigue tests at room temperature (Figure 3-16). Also, the braze-reinforced joints tested at 1,368°K (2,000°F) exhibited high joint efficiencies that were comparable to parent metal values (Figure 3-17). Again, this behavior contrasted with the room temperature fatigue tests where none of the samples attained joint efficiencies near the parent metal strength levels. As in the tensile-shear tests of braze-reinforced joints (Section 3.2.2), the cause of lowered fatigue strengths could be either stress increases from the eccentric single-lap configuration or degradation from the braze cycle.

3.2.4 Stress Rupture Tests

Typical stress-rupture test results are presented in Figure 3-18 for braze-reinforced joints tested at 1,368°F (2,000°F). The stress-rupture strengths exhibited by the joint samples were lower than parent metal strength (see
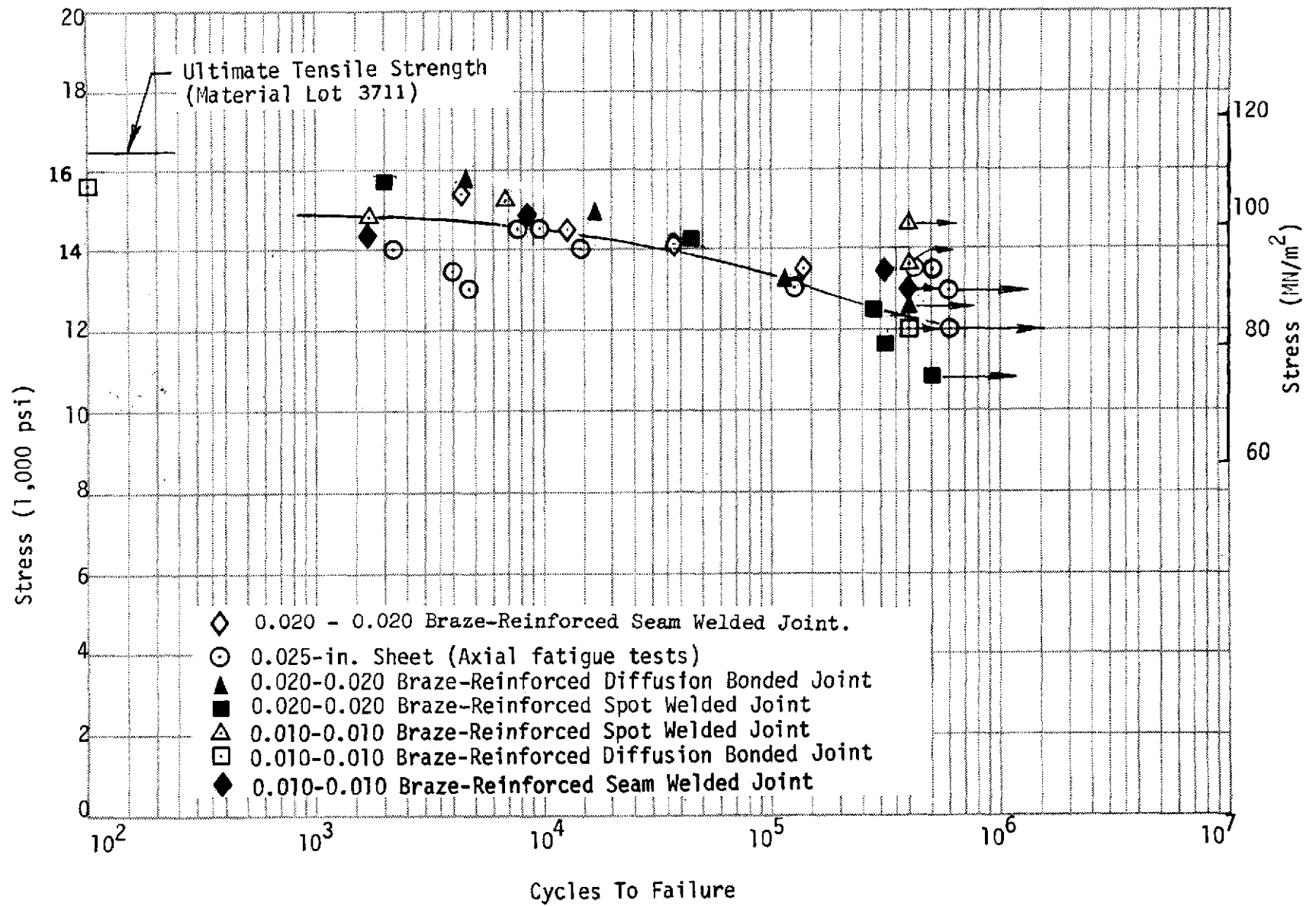
Figure 3-17. Fatigue Tests of Braze-Reinforced Joints at 2,000°F (1,368°K)
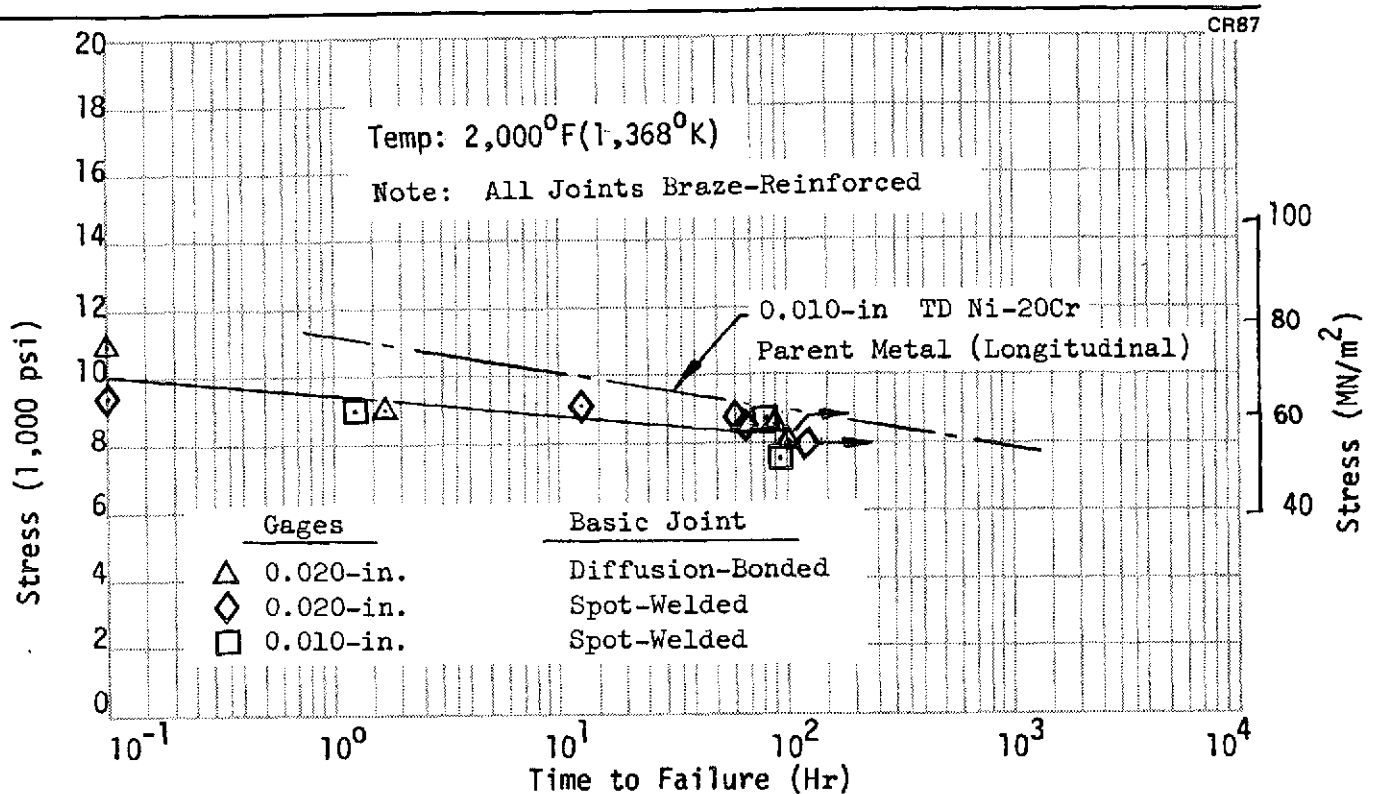
Figure 3-18. Stress Rupture Tests of Braze-Reinforced Joints at 2,000°F

Appendix B) of either 0.0254-cm (0.010-in.) or 0.0508-cm (0.020-in.) sheet thicknesses. Stress-rupture strength levels from tests of parent metal samples are shown in Figure 3-18 for comparison. All joint samples used material with a longitudinal orientation, and thus the parent metal values are also shown for longitudinal samples.

Similar stress-rupture test results are shown in Figure 3-19 for braze-reinforced joints tested at 1,477°K (2,200°F). In contrast to samples tested at 1,368°K (2,000°F), the joints tested at 1,477°K (2,200°F) exhibited a difference in stress-rupture strengths recorded for the two different sheet gages used in the samples. Joint samples made from 0.0254-cm (0.010-in.) sheet had higher stress-rupture strengths by approximately 13.8 MN/m^2 (2,000 psi) when compared to 0.0508-cm (0.020-in.) samples. Again, the parent metal stress-rupture strength levels at 1,477°K (2,200°F) were higher than joint strengths throughout the range of the tests.

All of the stress-rupture samples failed in the parent metal, a majority of the failures occurring immediately adjacent to the joint area. Thus, for the con-
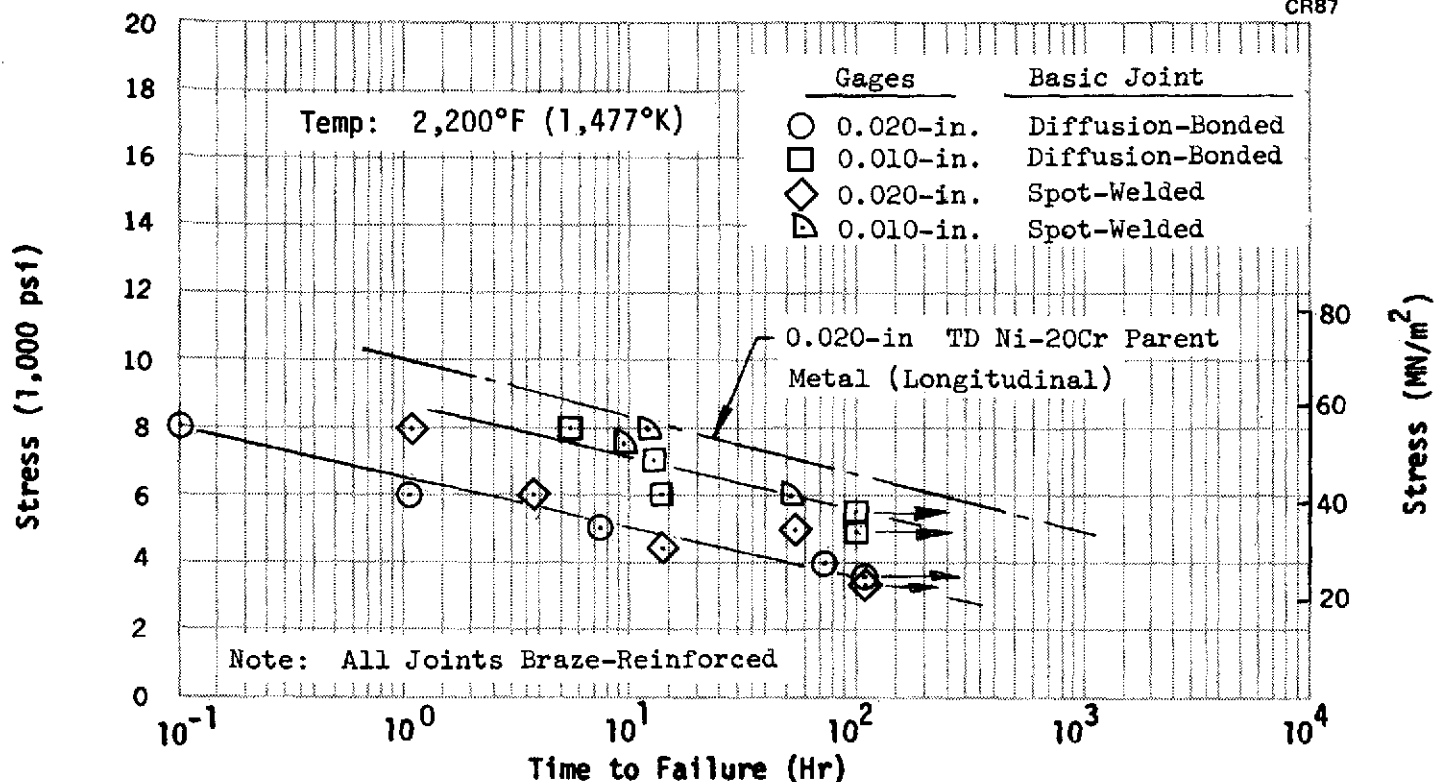
Figure 3-19. Stress Rupture Tests: Braze-Reinforced Joints at 2,200°F

figuration used in the braze-reinforced joint tests (Table 3-2), the joint
efficiencies were high when compared to the parent metal.

3.2.5 Residual Strength Tests

Residual strength tests were conducted to determine degradation effects on
braze-reinforced joints caused by exposure to elevated-temperature, low-
pressure environments. Residual strengths were determined at room tem-
perature, at 1,368°K (2,000°F), and at 1,477°K (2,200°F). The joint samples
were exposed in a vacuum furnace to a temperature environment of 1,477°K
(2,200°F) for 25 hours at a partial pressure of 5 x 10^{-2} torr prior to testing.
This environment approximates the cumulative temperature and pressure
combination experienced by a metallic heat shield in 100 Shuttle entry flights.

As in the case of the stress rupture samples, the residual strength specimens
failed in the parent metal area instead of the joint overlap region. Failure in
the parent metal occurred in the same manner as previously noted in the
tensile specimens, and thus data obtained from the braze-reinforced joints

were compared with the residual strength results obtained from cyclic creep specimens tested in the Astrofurnace chamber. Data from the residual strength tests of braze-reinforced joints are included in Figure 3-15. The comparisons of Figure 3-15 show joint efficiencies to be 10 to 15 percent below the strength levels of the basic TD Ni-20Cr sheet material. This decrease was judged to be caused from either eccentricity in the joint configuration or degradation from the braze cycle.

3.2.6 Summary of Braze-Reinforced Joint Tests

Results from braze-reinforced joint tests are summarized as follows:

- Fatigue life at room temperature is improved considerably when compared to unreinforced spot-welded joints. Life improvement by a factor of 10 is indicated from room temperature fatigue tests. Fatigue strength was approximately doubled for a given life.

- Efficiency in fatigue for braze-reinforced joints approaches that of TD Ni-20Cr parent metal at 1,368°K (2,200°F).

- Stress-rupture strengths at 1,368°K and 1,477°K (2,000°F and 2,200°F) were reduced from parent metal values. Reductions in joint efficiencies generally ranged from 6.89 MN/m^2 to 20.6 MN/m^2 (1,000 psi to 3,000 psi), with the reduction being dependent on gages used in the samples. Such reductions in joint efficiencies were judged to result from eccentricity of the joint configuration or from braze cycle effects.

- The braze-reinforced joints showed no significant degradation from exposure to 1,477°K (2,200°F) for 25 hours in a partial pressure of 5 x 20^{-2} torr.

- Joint efficiences approaching 100 percent can be achieved with overlap configurations similar to that found in actual structure.

Section 4
DESIGN CONCEPT SELECTION

Parametric studies of candidate TPS designs were conducted to serve as
a basis for selecting two promising panel designs for Phase I tests. Initial
efforts were devoted to layout drawings of candidate panel designs, attachment
systems, support structure, and insulation systems. TPS studies included
panel designs of the types shown in Figure 4-1, with a basic panel size having
a 50.8-cm (20-in.) length and 91.2-cm (36-in.) width. The panel cross
sections were sized initially using material properties reduced to account for
degradation effects of 100 missions as outlined in Appendix C. Subsequently,
cumulative creep data from cyclic multiple-parameter tests were used in
creep analyses to check the selected designs for expected maximum permanent
deflections. A maximum creep deflection criteria of $\delta \leq 0.025L + 0.25$ (cm)
($\delta \leq 0.01L + 0.10$ (in.)) was used in the studies (see Section 2). Panel designs
were also checked for resistance to flutter and fatigue, and evaluations of the
designs were made with regard to thermal performance, fabricability, cost,
reliability, and ease of installation or refurbishment.

The TPS parametric study utilized a summation of weighted values for each
design concept, each concept being evaluated in the areas of weight, cost,
fabricability, refurbishability, reliability, and efficiency. In cases where
two support systems for the heat shield panels appeared feasible, both systems
were evaluated. Also, variations in joining methods were studied; the three
joining approaches evaluated were spot-welding, braze-reinforced spot-welds,
and brazing (honeycomb concept).

While detailed discussions of the parametric studies are contained in
Appendix D, a summary of the TPS evaluation parameters is presented at
this point.
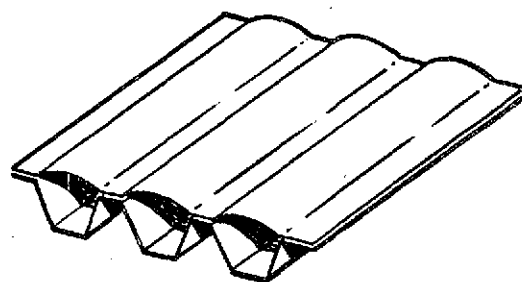
1. SINGLE FACE
CORRUGATION-STIFFENED
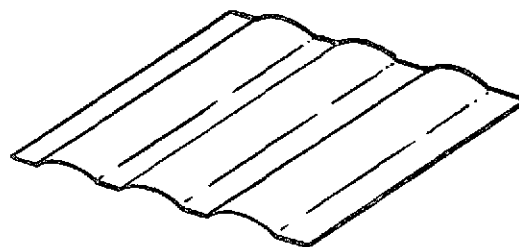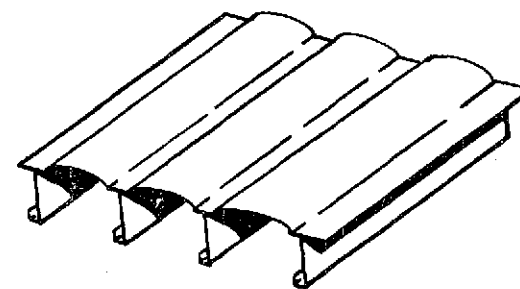
2. CORRUGATED SINGLE SHEET

3. ZEE-STIFFENED SHEET
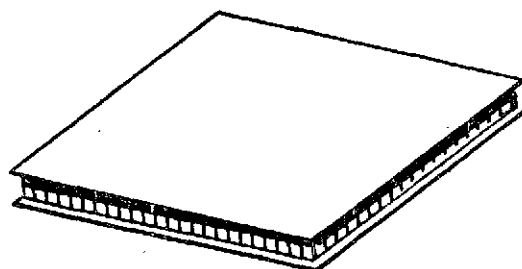
4. HONEYCOMB
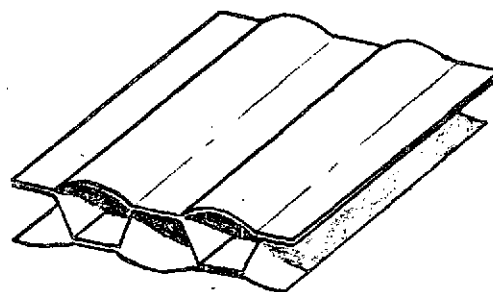
5. DOUBLE FACE
CORRUGATION-STIFFENED
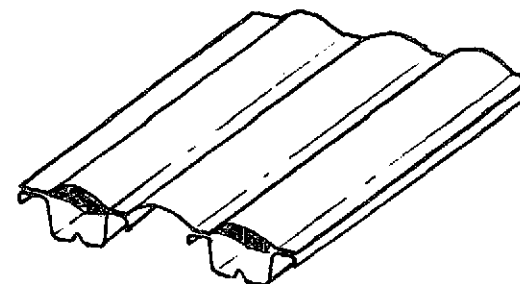
6. SINGLE FACE CHANNEL-STIFFENED

Figure 4-1. TPS Heat Shield Panel Configurations for Parametric Studies

Weight. Weight evaluations were based on layout drawings for the various panel and support concepts, the required insulation and insulation retaining material, fasteners, closeouts, panel edge members, and doublers. Packaged insulation weights were based on thermal studies that defined insulation thickness required to maintain a substructure temperature of 364 K (200 °F) throughout the entry flight until landing. Panel weights were based on differential pressure loads, acoustic sound pressure levels, and stiffness requirements to prevent panel flutter.

Cost. Production costs were evaluated by outlining detailed fabrication requirements based on heat shield configuration and scrappage rates; assessing tooling requirements; determining material costs; and estimating manhours associated with all tooling, planning, manufacturing, and quality assurance operations.

Fabricability. The detailed fabrication procedures used in cost evaluations also formed the basis for evaluating the fabricability of each concept. Industrial engineering and manufacturing engineering personnel used past fabrication experience to evaluate development time, tooling complexity, and projected rejection rates associated with the various concepts.

Refurbishability. Refurbishability studies utilized data from Reference 9 and combined such data with evaluations of the attachment systems developed in layout drawings of the various designs to assess ease of replacement for each concept. Frequency of replacement for each concept was also estimated and combined with ease of replacement to evaluate the refurbishability of each design approach.

Reliability. Evaluations of reliability were based upon the experience and judgment of key personnel in areas of design, manufacturing engineering, and quality assurance.

Efficiency. Overall efficiency of each TPS concept was evaluated as to (1) flexibility in mating with various substructure geometries and arrangements, (2) potential service life, (3) minimal heat paths to substructure, and (4) potential for design modifications with minimum cost.

The TPS parametric studies are summarized in Table 4-1. As a result of the parametric studies, the two panel configurations selected for tests in Phase I were the single-faced corrugation-stiffened panel and the zee-stiffened panel. Spot-welding was selected for the joining technique to be used in fabrication of both panel designs.

The weight and cost penalties associated with braze reinforcement may be noted in the rankings of Table 4-1, where the zee-stiffened panel dropped from first to fifth ranking when braze reinforcement of the spot-welded panels was added to the fabrication cycle. Similarly, the corrugation-stiffened heat shield dropped from second to sixth in overall ranking when braze reinforcement was considered.

The single-corrugated-sheet configuration supported by transverse beams at its ends was rated high for its low weight. However, it was reduced in the overall rankings because of sensitivity to flutter (Appendix D). This sensitivity was reflected in lowered ratings in reliability and efficiency.

The two approaches with the highest rankings, the single-face zee-stiffened panel and the single-face corrugation-stiffened configuration, were selected for Phase I full-scale, subsize panel tests. The support system selected used transverse beams at the panel ends, the support beam spacing being approximately 50.8 cm (20 in.). Metallic-foil-packaged, low-density insulation was placed on the interior side of the heat shields.
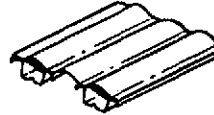
Detailed weight breakdowns for each configuration evaluated are shown in Table 4-2. These weights reflect the increases associated with braze-reinforcement.

Table 4-1
SUMMARY OF HEAT SHIELD PARAMETRIC STUDY

Heat Shield Configuration	Support System	Panel Joining Method	TPS Weight (0.20)		Cost (0.20)		Fabricability (0.15)		Refurbishability (0.15)		Reliability (0.15)		Efficiency (0.15)		Sum of Weighted Rating	Order of Rating
	Transverse Beams at Panel Ends	Spotwelded	6	1.20	8	1.60	7	1.05	8	1.20	7	1.05	7	1.05	7.15	2
		Spotwelded and Braze Reinforced	4	0.80	5	1.00	5	0.75	8	1.20	8	1.20	8	1.20	6.15	6
	Multiple Post	Spotwelded[1]	3	0.60	10	2.00	7	1.05	7	1.05	4	0.60	2	0.30	5.60	7
	Transverse Beams at Panel Ends	Spotwelded[1]	9	1.80	9	1.80	6	0.90	9	1.35	3	0.45	1	0.15	6.45	4
	Transverse Beams at Panel Ends	Spotwelded	8	1.60	9	1.80	7	1.05	7	1.05	7	1.05	7	1.05	7.60	1
		Spotwelded and Braze Reinforced	5	1.00	6	1.20	5	0.75	7	1.05	8	1.20	8	1.20	6.40	5
	Multiple Post	Brazed	3	0.60	2	0.40	2	0.30	6	0.90	6	0.90	9	1.35	4.45	8
	Transverse Beams at Panel Ends	Spotwelded	2	0.40	6	1.20	4	0.60	5	0.75	5	0.75	3	0.45	4.15	9
	Transverse Beams at Panel Ends	Spotwelded	8	1.60	7	1.40	6	0.90	7	1.05	7	1.05	5	0.75	6.75	3

[1]Edge members and clips spotwelded to panel.

Table 4-2

WEIGHT BREAKDOWN FOR CANDIDATE CONCEPTS

TPS Configuration Summary			Unit Weights, kg/m^2 (lb/ft^2)						
Heat Shield Configuration	Support System	Panel Joining Method	Basic Panel	Edge Reinforcements, Doublers	Support Beams	Support Posts	Bolts, Attach Fittings	Insulation and Packaging	Total Weight
	Transverse Beams at Panel Ends	Spotwelded	5.95 (1.22)	1.76 (0.36)	0.63 (0.13)	0.58 (0.12)	0.44 (0.09)	10.64 (2.18)	20.00 (4.10)
		Spotwelded and Braze Reinforced	6.20 (1.27)	1.95 (0.40)	0.63 (0.13)	0.58 (0.12)	0.39 (0.08)	10.64 (2.18)	20.39 (4.18)
	Multiple Post	Spotwelded[1]	5.27 (1.08)	2.00 (0.41)	---	1.85 (0.38)	0.63 (0.13)	11.37 (2.33)	21.12 (4.33)
	Transverse Beams at Panel Ends	Spotwelded[1]	5.27 (1.08)	1.80 (0.37)	0.63 (0.13)	0.58 (0.12)	0.29 (0.06)	10.64 (2.18)	19.21 (3.94)
	Transverse Beams at Panel Ends	Spotwelded	5.71 (1.17)	2.00 (0.41)	0.63 (0.13)	0.58 (0.12)	0.39 (0.08)	10.64 (2.18)	19.95 (4.09)
		Spotwelded and Braze Reinforced	5.95 (1.22)	2.14 (0.44)	0.63 (0.13)	0.58 (0.12)	0.39 (0.08)	10.64 (2.18)	20.33 (4.17)
	Multiple Post	Brazed	6.15 (1.26)	2.00 (0.41)	---	0.68 (0.14)	0.63 (0.13)	11.08 (2.26)	20.54 (4.20)
	Transverse Beams at Panel Ends	Spotwelded	7.42 (1.52)	2.24 (0.46)	0.63 (0.13)	0.58 (0.12)	0.54 (0.11)	10.64 (2.18)	22.05 (4.52)
	Transverse Beams at Panel Ends	Spotwelded	5.66 (1.16)	1.76 (0.36)	0.63 (0.13)	0.58 (0.12)	0.39 (0.08)	10.64 (2.18)	19.66 (4.03)

[1] Edge members and clips spotwelded to panel.

Section 5
HEAT SHIELD PANEL DESIGN AND TESTING

Evaluation tests were conducted on the two design approaches selected at the conclusion of the parametric studies. The objective of Phase I testing was to determine the better-performing design for use in Phase II evaluations where full-size TPS designs are to be tested. The evaluation tests conducted in Phase I were of the following three types: (1) cyclic tests of full-scale, sub-size TPS designs with programmed temperature, load, and ambient pressure conditions interspersed with acoustic tests; (2) flowing gas tests of two different panel edge joint designs; and (3) meteoroid impact tests followed by simulated entry in a flowing gas (plasma-arc) environment on sample panels of the two selected heat shield designs. The panel designs, fabrication of the panels, instrumentation and test results are described in this section for each of the three types of test panels.

All panel designs had full-scale cross sections, but were subsize in planform area. Panels to be tested in the Plasma Arc Tunnel (PAT) facility were restricted to a planform size of 10.16 cm by 10.16 cm (4 in. by 4 in.) to fit within the uniform core area of the plasma stream. Thus, the simulated joint components and the meteoroid impact panels were both limited to a 10.16-cm by 10.16-cm (4-in. by 4-in.) planform. The smaller panels also were designed with scarfed corners, again for the purpose of remaining within the uniform stream area. Stiffener depths on both the corrugation-stiffened and zee-stiffened designs were 2.54 cm (1.0 in.) for all test panels, including those tested in the space simulation chamber. The latter panels were 45.7-cm (18-in.) long and approximately 17.3-cm (6.8-in.) wide. The larger panels simulated full-span beam-supported heat shields, but were somewhat smaller in width than projected for full-size Orbiter heat shields. A sheet thickness of 0.0254 cm (0.010 in.) was used for both face sheet and stiffening elements in both panel designs.

The design approach used in Phase I involved sizing the initial panel cross sections based on static loads. The initially sized panels were then evaluated to determine their suitability in areas of fatigue and panel flutter (see Appendix D). Also, meteoroid penetration of the panel designs was considered, as discussed in Section 5.1 and Appendix E. In both zee-stiffened and corrugation-stiffened designs, the panel cross sections developed from static loadings (see Table 5-1) were sufficient to meet fatigue and flutter criteria. The meteoroid penetration criterion (Appendix E) was relaxed to allow a 0.95 probability of one or less penetration in a seven-day mission.

Following panel cross-section sizing, the details of panel edge members, closeouts, and attachment systems were developed for the full-length panels that were to be tested in programmed cycles of load, temperature, and acoustic environments simulating the Orbiter mission. Details were also developed for the meteoroid impact panels and the panel edge joint samples. Constraints of test fixtures and test facilities were also included in defining the details of the test panel designs. Thermal protection system criteria, test panel configurations, and testing of the heat shield designs are discussed in the remainder of this section.

5.1 DESIGN CRITERIA

Basic design criteria for the heat shields are presented in detail in Appendix A and were discussed briefly in Section 2. For reference, the criteria used in design of the full-scale subsize test panels and TPS components are summarized in Table 5-1.

The meteoroid criteria for the Shuttle, outlined as a part of Appendix A, were applied to the TD Ni-20Cr heat shield designs to evaluate their effects on the required thickness of material. Detailed calculations are presented in Appendix E while the results of the evaluations are summarized at this point.

The meteoroid flux-mass model of Figure 2-8 was used in the evaluation, and a criterion specifying a 0.95 probability of no puncture was assessed initially. A mission duration of 7 days was selected (Appendix E) and an exposed surface

Table 5-1

SUMMARY OF HEAT SHIELD DESIGN CRITERIA

Mission Phase	Limit Differential Pressure (psi)	Overall Sound Pressure Level	Panel Flutter	Meteoroid Impact	Cumulative Creep In 100 Missions cm (in.)	Factor of Safety[1]
Boost Flight	+3.30 (Collapse) -1.00 (Burst)	160 db	No flutter at 1.5 times local dynamic pressure.	--	--	1.50
Orbital Mission	--	--	--	Designed for a 0.95 probability of one or less puncture in a 7-day mission.	--	--
Entry Flight	+0.50 (Collapse) -0.50 (Burst)	--	Same as Boost Flight	--	$\delta = 0.254 + 0.0254\,L$ ($\delta = 0.10 + 0.01L$) (See Section 2)	1.50

(1) See Appendix A for detailed factors used in combined loads.

area of approximately 123 m^2 (1,320 ft^2) was estimated for the TD Ni-20Cr heat shield area on the lower surface of the Orbiter. With the above criterion and assumptions, a heat shield thickness of 0.106 cm (0.0417 in.) is required to provide a 0.95 probability of no puncture. A relaxation of puncture criterion to allow one or less puncture [P(0, 1) = 0.95] would reduce the thickness required to 0.0605 cm (0.0238 in.). The latter criterion of P(0, 1) = 0.95 was selected as an initial meteoroid penetration design criterion for the combined sheet thicknesses of test heat shield panels. This criterion was assessed in simulated meteoroid impact tests followed by exposure to simulated entry heating in the Plasma Arc Tunnel facility. Results from the meteoroid impact and PAT tests are reviewed in the following section.

5.2 METEOROID IMPACT PANEL TESTS

The tests conducted in this portion of the program were designed to evaluate the damage incurred by TD Ni-20Cr heat shields when subjected to simulated meteoroid impacts, and to further evaluate the survivability of the selected designs when exposed to simulated entry airflow conditions after impact.

The completed test panels are shown in Figure 5-1 before final cleaning and oxidation. As shown in Figure 5-1, the corners of the panels are scarfed at 45 degrees to fit the Plasma Arc Tunnel holder. Lips are provided on the face sheet at each of the eight edges, and retention in the holder is accomplished by pins that fit into holes at the centers of the lips. The panels were subsequently cleaned and oxidized to provide a uniform high-emittance surface. Insulation packages were also fabricated for placement behind the panels during simulated meteoroid impingement tests. Testing was accomplished in two steps, a first set of tests being conducted at the McDonnell Douglas Aerosphysics Laboratory at El Segundo, California. This facility possesses good simulation capabilities through the use of a light-gas gun. Models of known geometry can be launched at high velocity with a controlled flight path into a known atmosphere where flight parameters can be measured and impact on a selected target can be observed. The light-gas gun is able to launch models at velocities considerably in excess of those obtainable by a conventional explosive-powered gun through use of a pure, light, propelling gas such as hydrogen or helium instead of the heavier heterogeneous gases generated as products of the rapid burning of an

4 IN. (10.16 CM)
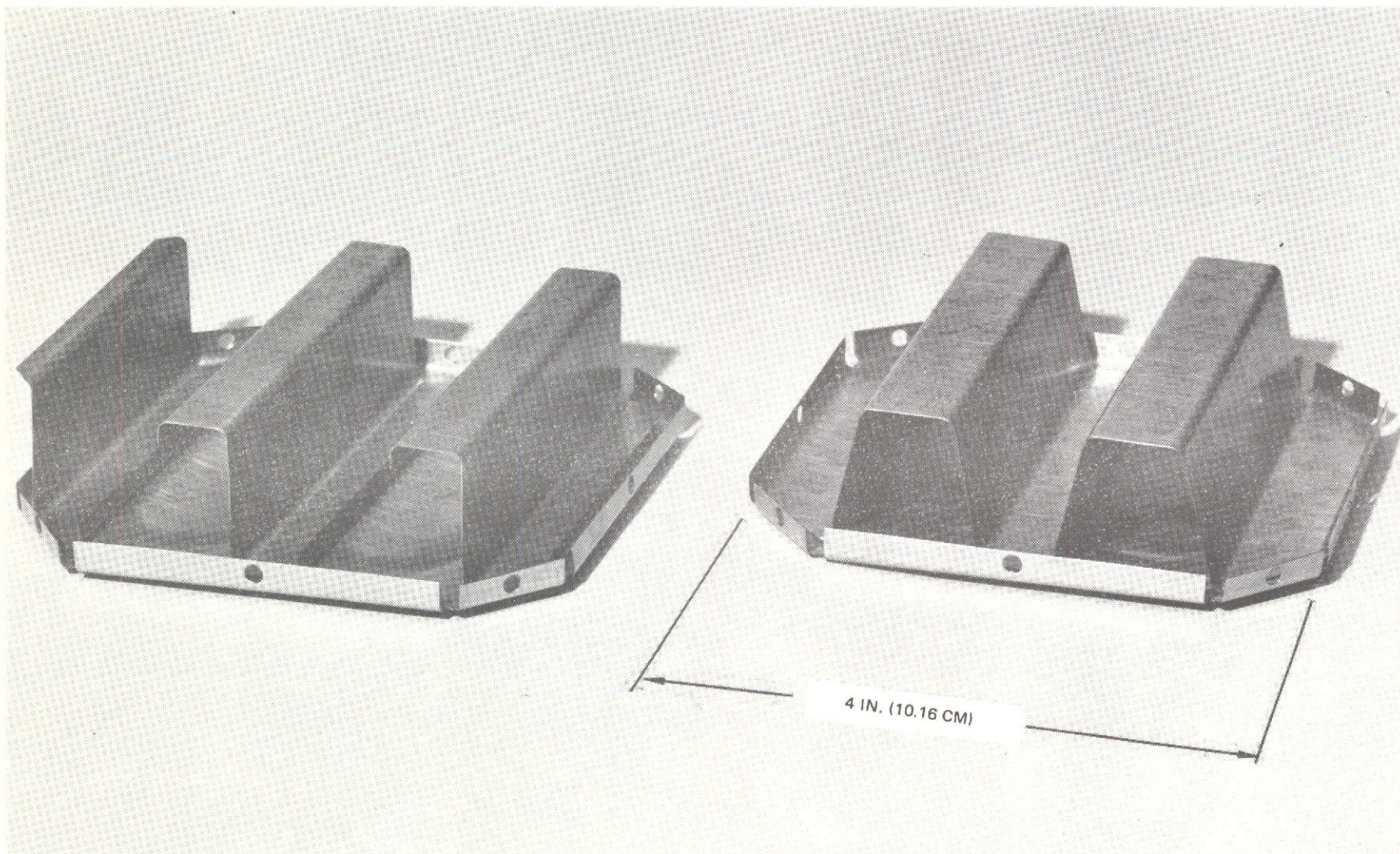
Figure 5-1. Test Panels for Simulated Meteoroid Impact Tests

explosive. Presently, light-gas guns are capable of launching models in excess of 9.1 km/s for studies of meteoroid and projectile impacts on materials. In the current tests, the velocity was reduced to a range of 7.0 to 7.6 km/s (23,000 to 25,000 ft/sec) to obtain better accuracy and to reduce the probability of debris impact on the panels from sabot particles.

The MDAC light-gas gun, shown schematically in Figure 5-2, is a two-stage, heavy-piston type specifically designed for high-speed impact studies with a high firing rate. The nominal diameter of the launch tube is 1.26 cm (0.50-in.). The preflight chamber contains two main sections, the first section being the blast receiver, where baffle plates with holes along the model flight path permit model passage while stopping separated sabot pieces and minimizing the debris that reaches the target. The second section is the instrumentation chamber. Three stations of orthogonal shadowgraphs and flash x-rays are used to detemine integrity and velocity of the model. A specially designed small-model detector is incorporated with each optical system. This detector is sensitive enough to reliably detect models with diameters as small as a 0.0254-cm (0.010-in.), regardless of model luminosity. A quick-operating valve separates the blast receiver and the instrumentation section.

The impact tank has an octagonal cross section with a nominal minimum inside dimension of 43.1 cm (17.0 in.) and a length of 81.3 cm (32.0 in.). Eight windows located around the tank provide ports for optical observation of the target during impact.

Since the light-gas gun cannot match the actual average meteoroid velocity of 20 km/s, the mass of the sphere used in the impact tests was scaled to equal the kinetic energy of an actual meteoroid. The borosilicate glass spheres used in the tests were sized for equal kinetic energy at a velocity of approximately 7.62 km/s (25,000 ft/sec). Using this velocity, the boro-silicate spheres were scaled to a mass of approximately 48.0×10^{-6} grams. This compares to a computed mass for an actual meteoroid of 6.99×10^{-6} grams, this mass being derived in Appendix E using the criterion of a 0.95 probability of one or less penetrations in a seven-day mission. The boro-silicate spheres used in the tests had a diameter of 0.033 cm (0.013 in.).
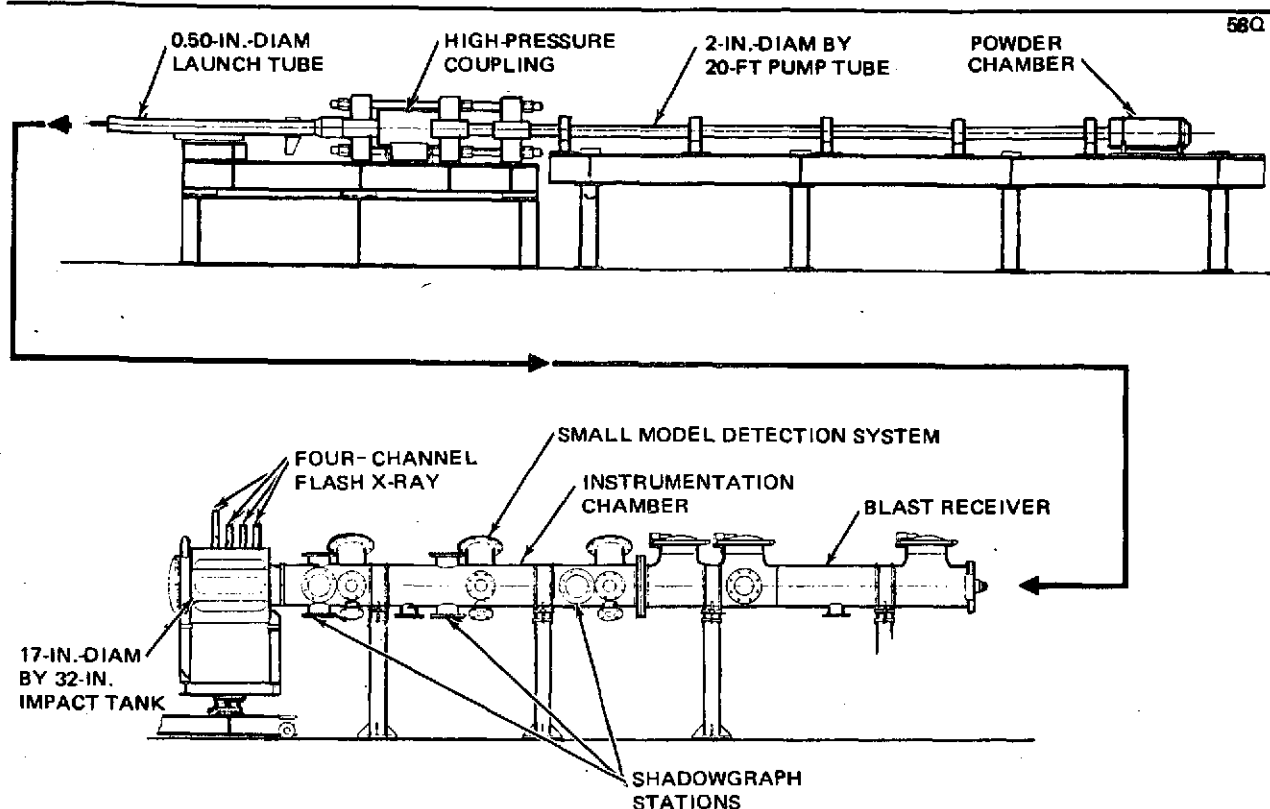
Figure 5-2. Schematic of MDAC Light-Gas Gun

The zee·stiffened panel was tested first with the aiming point on the panel being in an area of single-skin thickness, this thickness being 0.0254 cm (0.010 in.). The glass sphere used in this shot weighed 50.2×10^{-6} grams and the velocity attained by the sphere was 7,170 m/s (23,500 ft/sec). The shot penetrated the front face, and examination under a light microscope showed a hole shape that indicated the penetration was in the ballistic limit range. The stabilizing flange on the outstanding leg of the zee stiffener was located approximately 2.54 cm (1 in.) behind the point of penetration, and an examination of the stiffener showed no damage from the sphere. The point of penetration on the panel face is shown in Figure 5-3a. The hole shown in Figure 5-3a was 0.033 cm (0.013 in.) in diameter.

The second panel was tested using an aiming point where the corrugation stiffener was attached to the face sheet, thus forming a double thickness of TD Ni-20Cr sheet material. Both the face sheet and the corrugation-stiffening member were 0.0254 cm (0.010-in.) thick sheet, providing a total thickness

10X
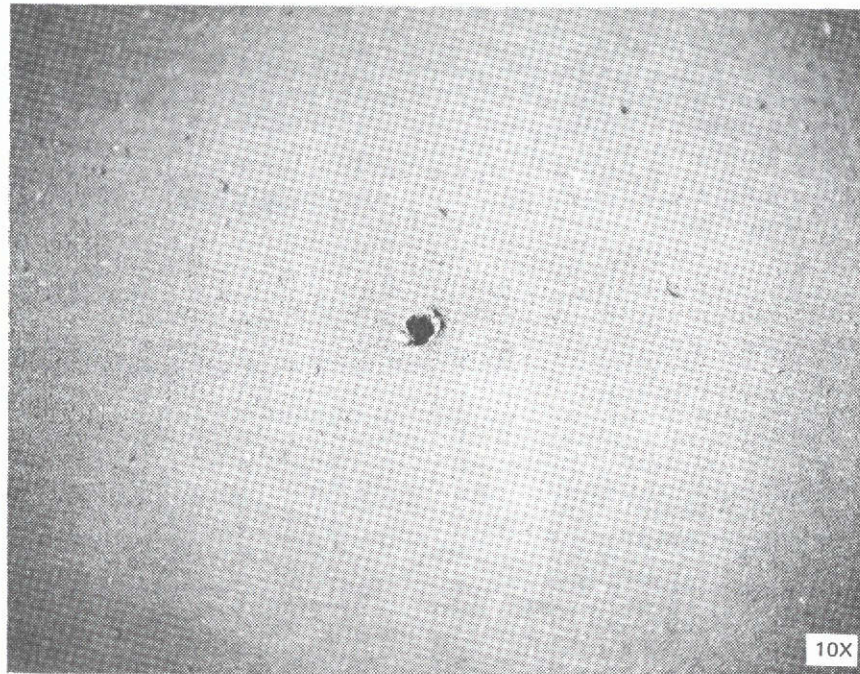
a. PENETRATION POINT IN FACE SHEET OF ZEE-STIFFENED PANEL

BOROSILICATE SPHERE IMPACT

SABOT PARTICLE
IMPACTS

10X
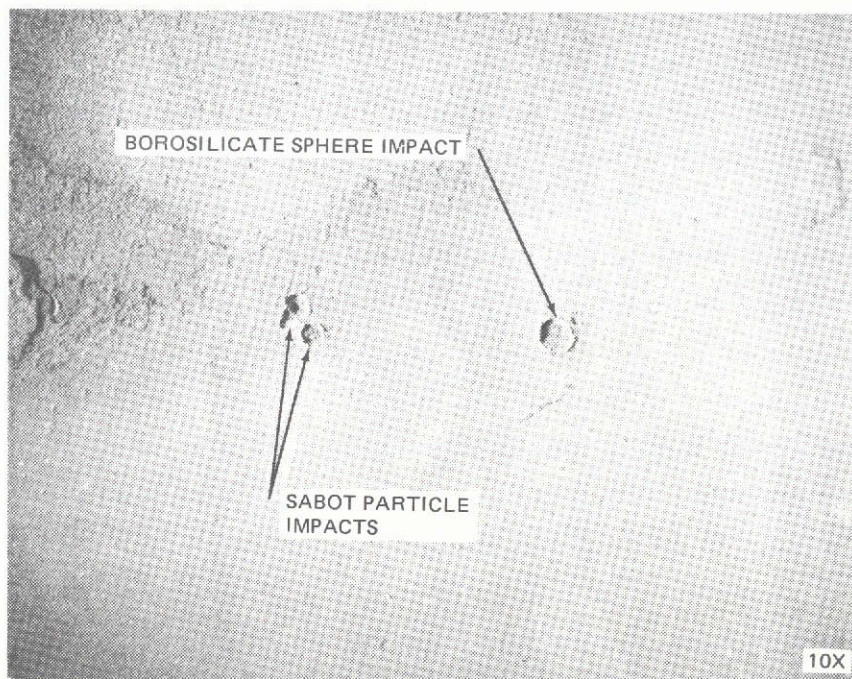
b. IMPACT AREAS ON FACE SHEET OF CORRUGATION-STIFFENED PANEL

Figure 5-3. Magnified Views of Panel Faces After Simulated Meteoroid Impact Tests

of 0.0508 cm (0.020 in.) at the aiming point. The borosilicate sphere used in this test weighed 47.8 x 10⁻⁶ grams and attained a velocity of 7,010 m/s (23,000 ft/sec). No penetration occurred in this test, the double thickness being sufficient to sustain impact without penetration. A magnified view of the impact area is shown in Figure 5-3b. Particles from the disintegrated sabot also impacted the second test panel, and a portion of the plastic carrier was deposited on the panel as a thin layer of char material. This area may be seen in the middle left portion of Figure 5-3b. The two impacted panels were then shipped to St. Louis for the second set of tests in the Plasma Arc Tunnel.

5.3 PLASMA-ARC TESTS OF METEOROID IMPACT PANELS

The impacted panels were each subjected to one simulated entry cycle in the Plasma Arc Tunnel to determine whether entry airflow conditions caused further damage to the impact areas on the panels.

The arc heater currently used in the PAT facility is a Huls type with tandem, water-cooled, cylindrical, hollow electrodes. The electrode materials used are OFHC copper and 20-percent Cu/80-percent Ag alloy. Contamination resulting from electrode erosion is small (less than 0.1 percent by weight), even at high (2,000-A) operating currents. The arc heater employs a central gas-vortex injection chamber and magnetic arc positioning.

Several nozzles are available with exit diameters that range from 3.18 to 20.3 cm (1.25 to 8.00 in.). These nozzles are all of conical design and provide flow expansion up to Mach 5.9.

The arc heater configuration for tests in the current program utilized a nozzle with a 2.54-cm (1.0-in.) throat diameter and a 20.3-cm (8.0-in.) exit diameter. Nominal arc parameters were:

Arc voltage	390 volts
Arc current	530 amps
Arc chamber pressure	310 torr
Primary air flow	5.90 g/sec (0.013 lb/sec)
Secondary air flow	3.16 g/sec (0.007 lb/sec)
Air bulk enthalphy	10,000 J/g (4,300 Btu/lb)

The operating envelope of the Plasma Arc Tunnel is shown in Figure 5-4; the point at which stream conditions were set is noted in the envelope. The noted condition was used in both the meteoroid impact panel tests and the simulated panel joint tests.

The 10.16 by 10.16-cm (4 by 4-in.) panels were mounted on a three-arm rotating water-cooled holder that is shown in Figure 5-5 with a calibration module mounted on the arm. The two meteoroid impact panels were mounted on the second and third arms of the holder. Test stream conditions were checked with the calibration module and, after the stream was stabilized at the desired test conditions, each of the test panels was rotated into the stream and held for the desired time. Each of the meteoroid test panels was tested at a nominal surface temperature of 1,477°K (2,200°F) for 30 minutes (1,800 sec).

In addition to using a calibration module to check stream conditions, sample sheets of TD Ni-20Cr were tested in a preliminary run to verify test sample front-face temperatures. Figure 5-6 shows two single-sheet TD Ni-20Cr samples used in the preliminary runs.
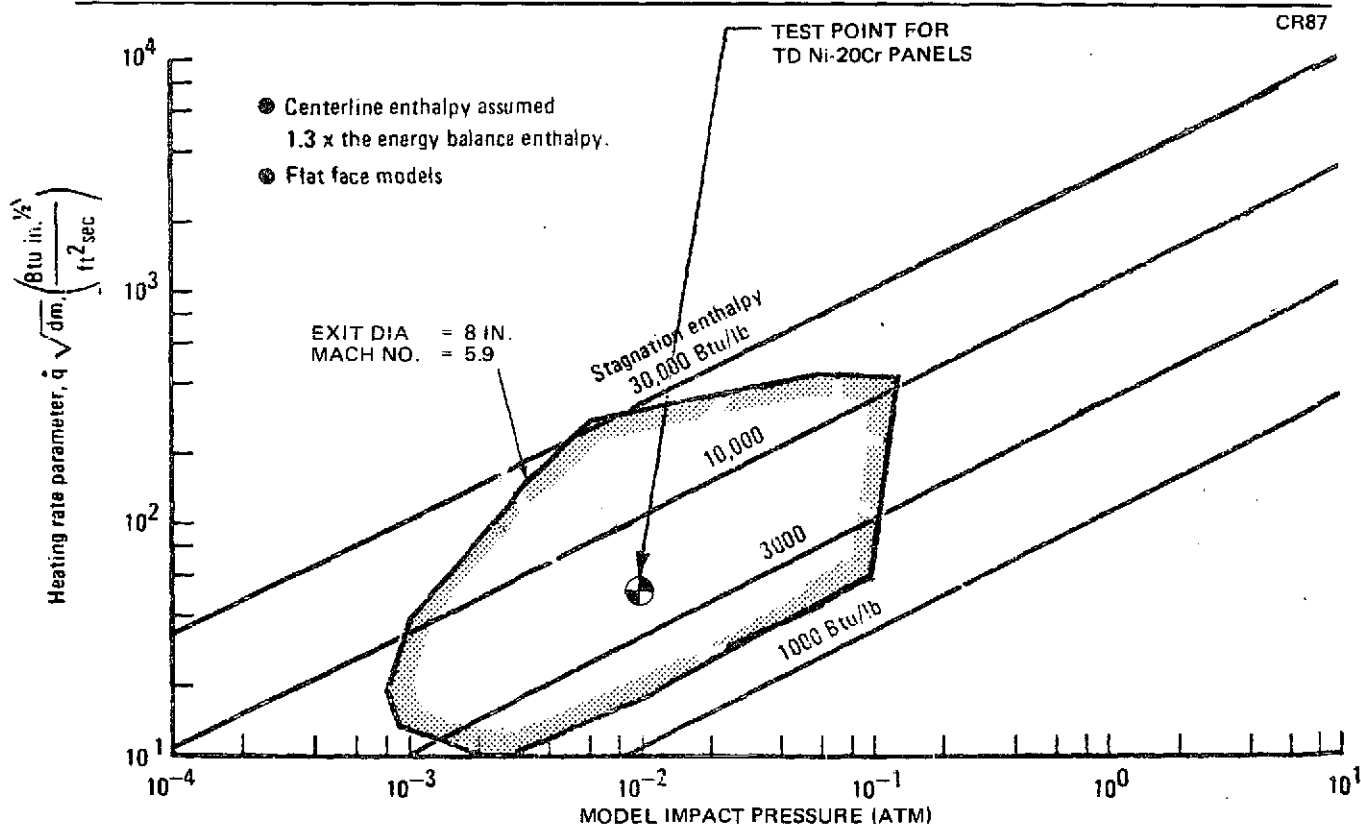
Figure 5-4. PAT Facility Testing Capability (Flat Face Model)

CALIBRATION
MODEL
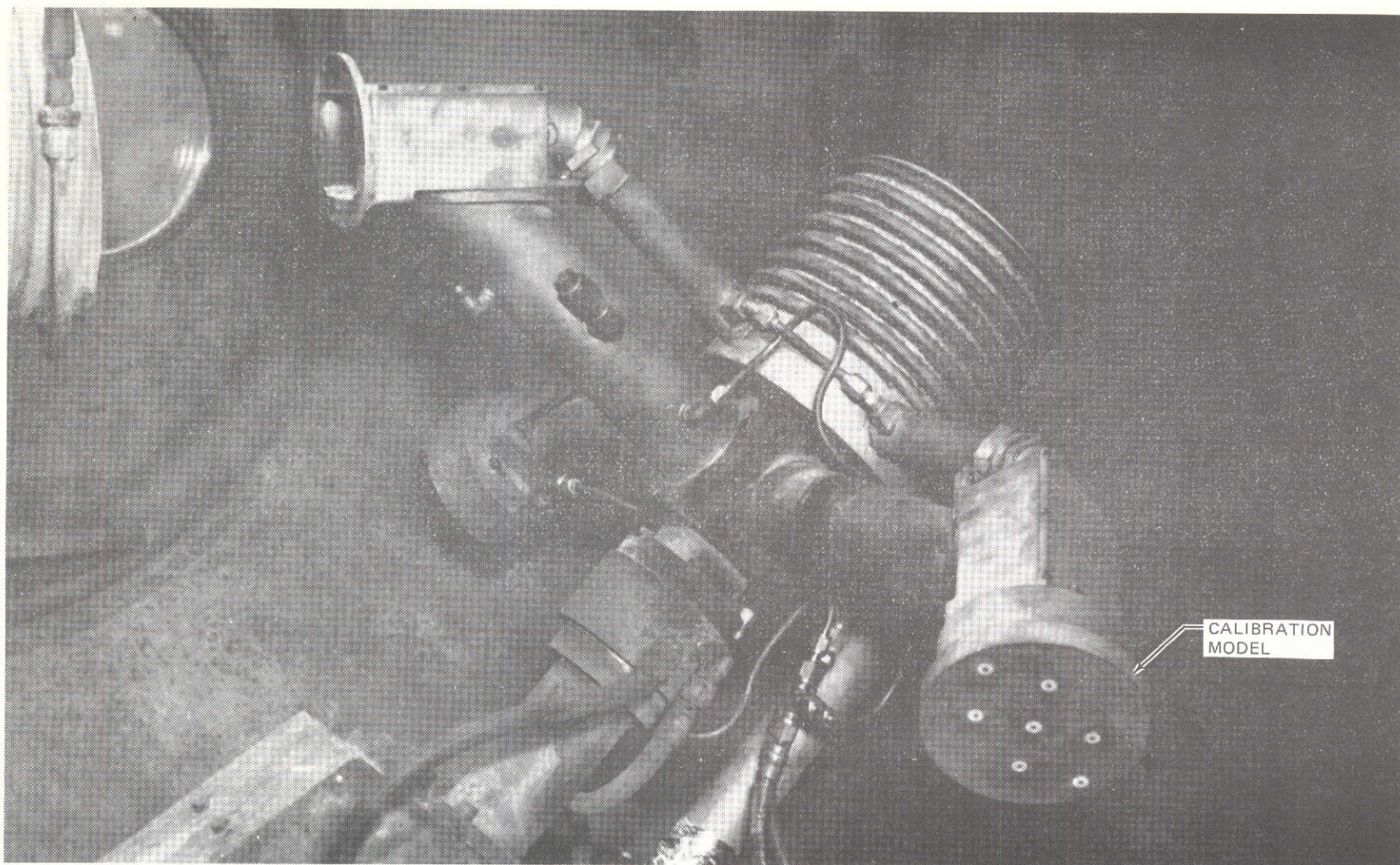
Figure 5-5. Plasma Arc Tunnel Model Holder Inside Test Chamber
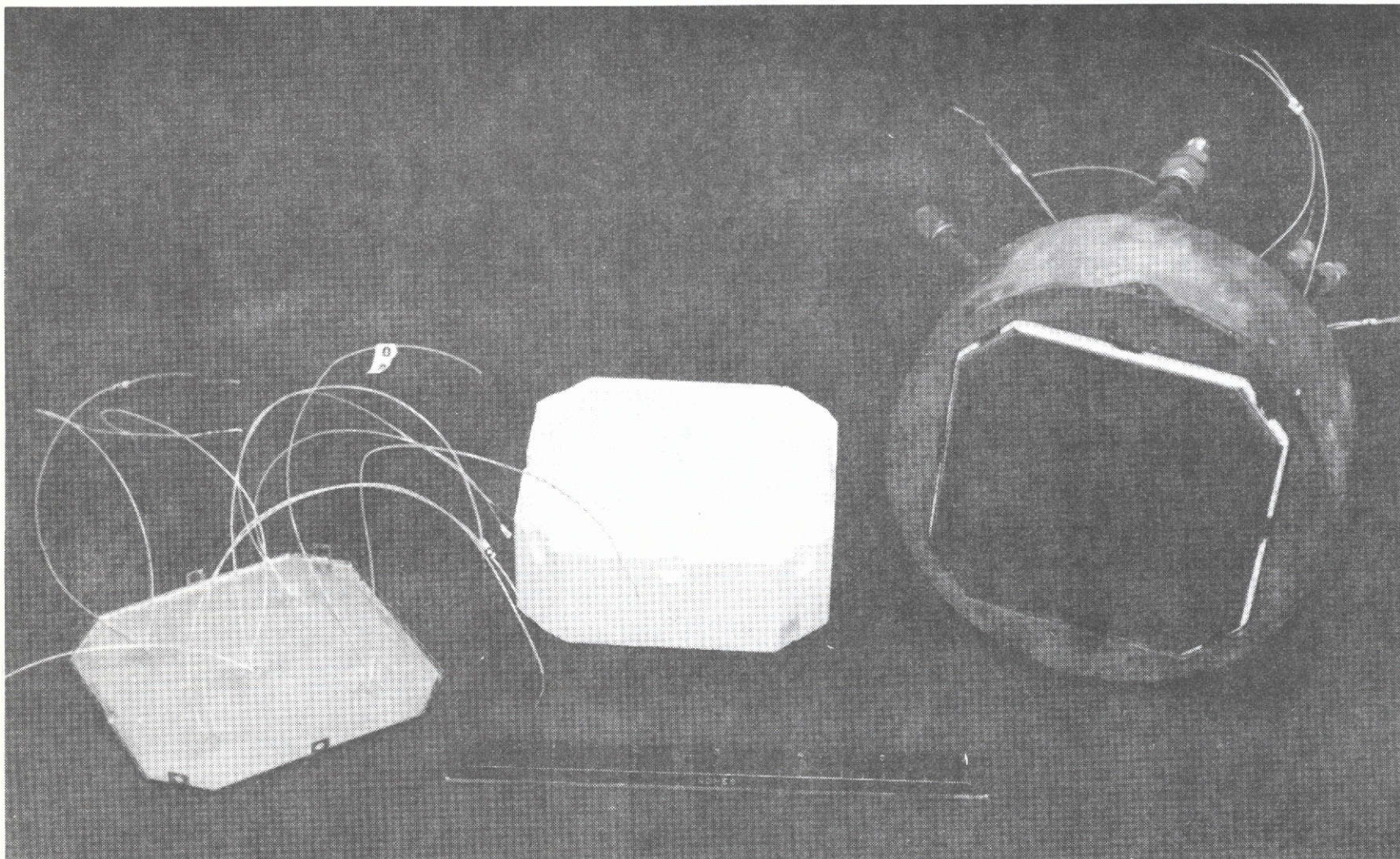
Figure 5-6. Single Sheet TD Ni-20 Cr Samples Used in Preliminary Runs

All of the test panels were instrumented with Pt/Pt-10 percent Rh thermo-couples tack welded to the rear surface of the face sheet and to the stiffening members. Figure 5-7 shows the thermocouples installed on the corrugation-stiffened test panel that had been subjected to simulated meteoroid impingement. Temperature histories measured with the thermocouples provided data defining the temperature gradients from the face sheet to the inner surface of the stiffening elements. Thermocouple and pyrometer sighting locations are shown in Figure 5-8.

Surface temperatures were measured with a TD-9H infrared pyrometer mounted on an automatic model surface scanning system. This system auto-matically sighted the pyrometer at five panel surface locations during a system scan. Scanning time was 5 minutes. The measured temperatures were true surface temperatures since the emittance control on the pyrometer was set to 0.62 to compensate for viewing port transmittance (0.87 at $\lambda = 0.80$ μm) and a TD Ni-20Cr surface emittance of 0.71. The TD Ni-20Cr surface emittance was based on previous measurements obtained from an oxidized TD Ni-20Cr strip at 1,477°K (2,200°F).

CR87
N/A

SCALE - INCHES
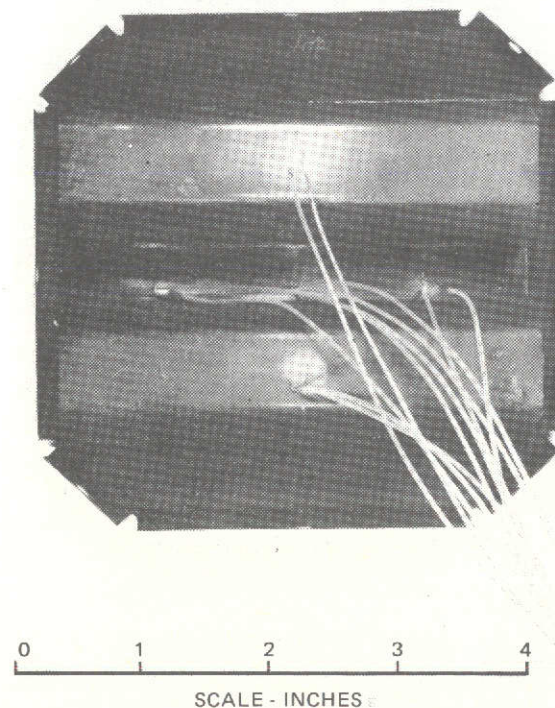
Figure 5-7. Instrumented Corrugation — Stiffened Panel Prior to Plasma Arc Tunnel Tests
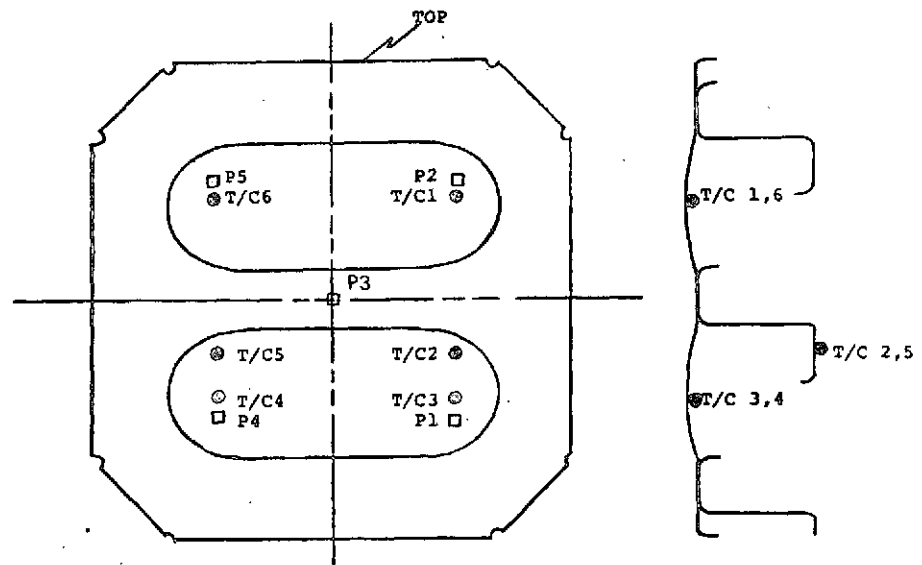
MODEL 1T44104

Notes:

°Pl through P5 - Pyrometer sighting locations.

°T/C 1 through T/C 6 - Tack-welded thermocouple locations.

a. ZEE-STIFFENED PANEL
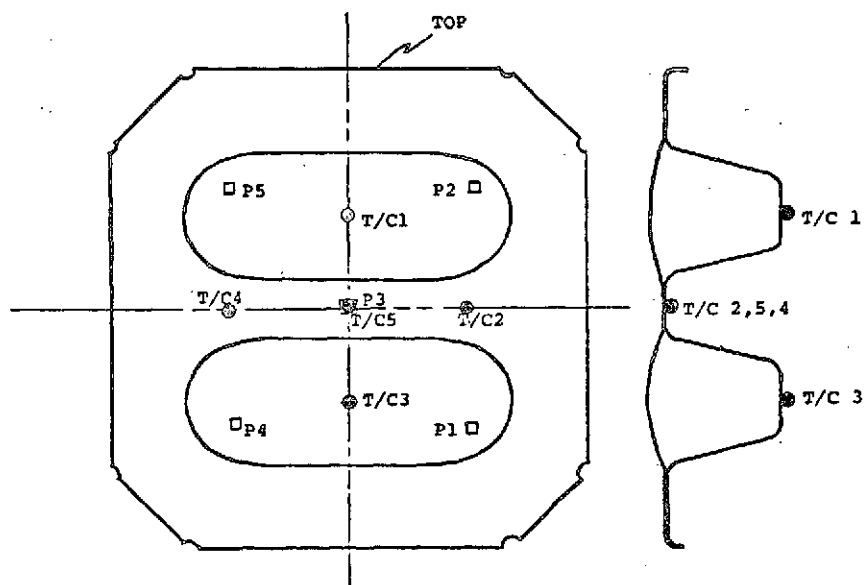
MODEL 1T44102

Notes:

•Pl through P5 - Pyrometer sighting locations.

•T/C 1 through T/C 5 - Tack-welded thermocouple locations.

b. CORRUGATION-STIFFENED PANEL

Figure 5-8. Thermocouple and Pyrometer Sighting Locations on Meteoroid Impact Panels

The optically measured meteoroid panel surface temperatures are presented in Table 5-2 for the pyrometer sighting locations shown in Figure 5-8. Temperature variations across the surface of the corrugation-stiffened panel ranged from 1,378°K (2,020°F) to 1,485°F (2,210°F). Similarly, temperatures on the zee-stiffened panel ranged from 1,361°K (1,990°F) to 1,489°K (2,220°F). Where comparisons between pyrometer readings and thermocouple recordings were possible, good agreement was noted between the two techniques.

Surface temperature distributions were also obtained through thermograms that were taken at the half-way point of each cycle using the scanning infrared camera (AGA Thermovision). They indicated the surface temperature distribution to be symmetrical with respect to the test surface shape.

Several points were visible in the thermograms which indicated localized heating as a result of small surface distortions. Calibration of the AGA thermovision unit was obtained by viewing the McDonnell Aircraft Company Standards Laboratory blackbody source at the AGA instrument settings used during these tests.

Temperature time histories of thermocouple locations on the corrugation-stiffened meteoroid impact panel are shown in Figure 5-9, while similar data for the zee-stiffened panel are presented in Figure 5-10. Maximum temperature difference on the corrugation-stiffened panel during the steady-state

Table 5-2

OPTICALLY MEASURED PANEL SURFACE TEMPERATURES,
METEOROID IMPACT PANELS

Panel Configuration	Run No.	Temperature at Pyrometer Sighting Position					Run Time (sec)
		P1	P2	P3	P4	P5	
Corrugation-Stiffened	3659	1,400 (2,060)	1,400 (2,060)	1,378 (2,020)	1,482 (2,210)	1,378 (2,020)	1,810
Zee-Stiffened	3659	1,432 (2,120)	1,361 (1,990)	1,372 (2,010)	1,489 (2,220)	1,368 (2,000)	1,795

Note: Temperatures shown as °K primary units and (°F) secondary units.
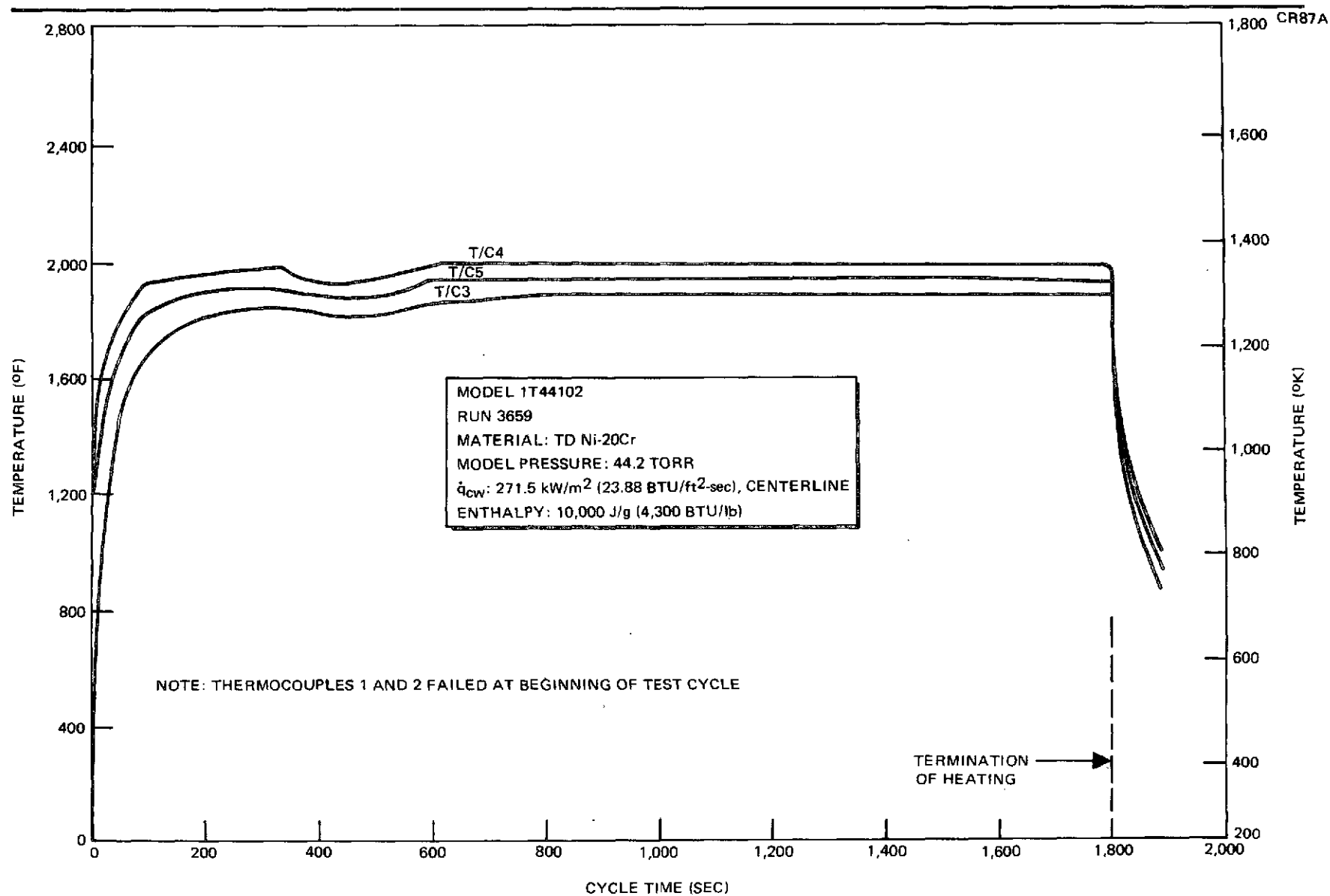
Figure 5-9. Panel Thermocouple Temperature Histories, Corrugation-Stiffened Meteoroid Impact Panel

The figure contains the following labels and annotations:

CR87A

TEMPERATURE (°F) (left vertical axis)
TEMPERATURE (°K) (right vertical axis)
CYCLE TIME (SEC) (horizontal axis)

T/C4
T/C5
T/C3

MODEL 1T44102
RUN 3659
MATERIAL: TD Ni-20Cr
MODEL PRESSURE: 44.2 TORR
$\dot{q}_{cw}$: 271.5 kW/m^2 (23.88 BTU/ft^2-sec), CENTERLINE
ENTHALPY: 10,000 J/g (4,300 BTU/lb)

NOTE: THERMOCOUPLES 1 AND 2 FAILED AT BEGINNING OF TEST CYCLE

TERMINATION OF HEATING

72

Figure 5-10. Panel Thermocouple Temperature Histories, Zee-Stiffened Meteoroid Impact Panel

MODEL 1T44104
RUN 3659
MATERIAL: TD Ni-20Cr
MODEL PRESSURE: 44.2 TORR
$\dot{q}_{cw}$: 271.5 kW/m^2 (23.88 BTU/ft^2-sec), CENTERLINE
ENTHALPY: 10,000 J/g (4,300 BTU/lb)

portion of the test was approximately 67°K (120°F). This difference occurred between Thermocouple 4, located on the face sheet, and Thermocouple 3, located on the corrugation at its maximum-depth position (Figure 5-8). This difference was less between Thermocouples 5 and 3, Thermocouple 5 being located at the center of the panel in a position closer to Thermocouple 3.

Temperature differences between face-sheet positions and stiffener flanges on the zee-stiffened panel were greater than similar readings on the corrugation-stiffened panel. During steady-state portions of the test, a temperature difference of approximately 200°K (360°F) existed between Thermocouples 2 and 3 (Figures 5-8 and 5-10). Also, a difference of approximately 189°K (340°F) was noted between Thermocouples 4 and 5 on the zee-stiffened panel. Relatively close agreement was obtained between Thermocouple 3 and pyrometer sighting position P1, the thermocouple reading (Figure 5-10) being approximately 1,400°K (2,060°F), compared to a pyrometer reading (Table 5-2) of 1,432°K (2,120°F) during the steady-state portion of the run. Good agreement was also obtained between thermocouple and pyrometer readings on the face sheet of the zee-stiffened panel at the common positions of T/C 1 and P2, T/C 4 and P4, and T/C 6 and P5.

Pretest and post-test photographs were also made of the penetration point on the zee-stiffened panel to determine if any enlargement or change occurred as a result of exposure to the 1,477°K (2,200°F), simulated entry airflow conditions in the PAT tests. Comparison of the pretest and post-test photographs (Figure 5-11) showed no change in the hole size or appearance. In a similar manner no change of the cratered area on the corrugation-stiffened panel was apparent after the PAT tests. Results from these tests on the meteoroid impingement panels indicated a high survivability capability for TD Ni-20Cr heat shields during entry following meteoroid impact. Based on temperature readings from thermocouples located on the interior side of the panel, no apparent localized temperature excursions which might be ex expected from hot gas ingestion were observed.

Post-test examination of the meteoroid impact test panels showed that several spot welds failed during Plasma Arc Tunnel tests. Since the failures were local and did not precipitate additional spot weld failures, the panels continued to sustain the test conditions until completion of the runs.
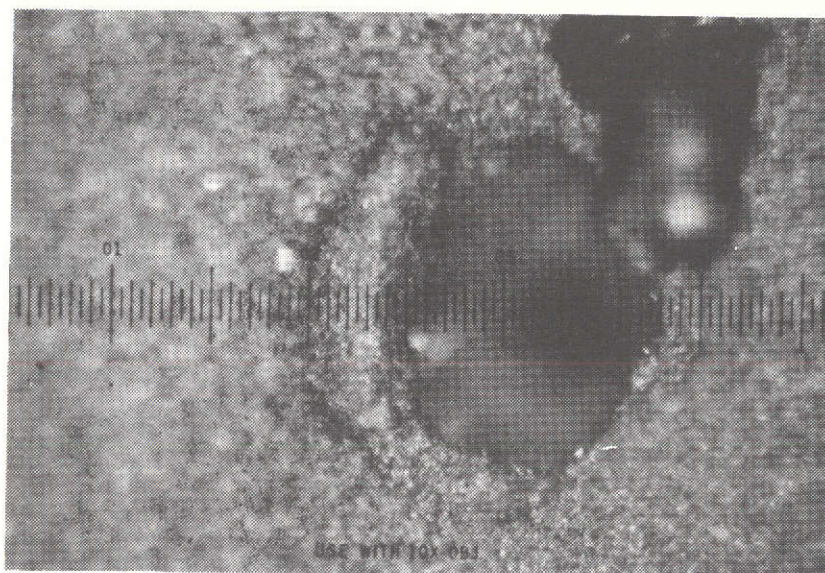
100X

a. PRIOR TO PLASMA ARC TUNNEL TESTS
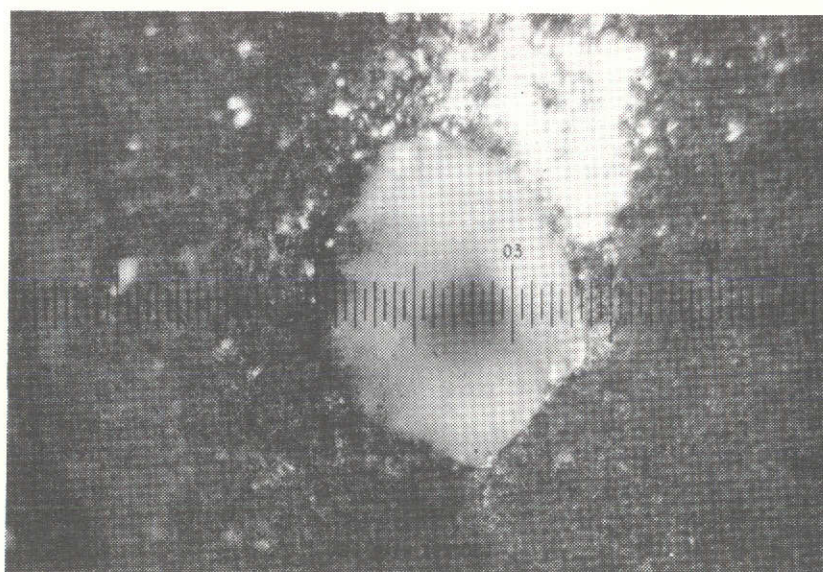
100X

b. AFTER PLASMA ARC TUNNEL EXPOSURE

Figure 5-11. Magnified Views of the Zee-Stiffened Panel Face Sheet Penetration Point

5.4 SIMULATED JOINT TESTS

Tests were also conducted in the Plasma Arc Tunnel to evaluate the effectiveness of two panel joint design concepts. The two joint designs are shown in Figure 5-12 before assembly of the components. One design (Figure 5-12a) simulated a panel closeout design employing a closure strip to cover the gap between panel edges. The second design (Figure 5-12b) simulated an overlapping edge joint concept in which one panel edge overlaps the adjacent panel edge. The assembled joint specimens are shown in Figure 5-13. Size was again restricted to a 10.16 by 10.16-cm (4 by 4-in.) planform to fit within the plasma stream core. All sheet metal parts and the threaded fasteners were made from TD Ni-20Cr.

Tests of the joint panels were conducted with the objective of providing comparative evaluations of the two designs under high-velocity, elevated-temperature flow conditions simulating entry airflow over heat shield panel edges. Thermocouples were installed on the joint designs as shown in Figure 5-14 to determine if local heating inside the joint occurred from flow penetration. Qualitative evaluations were also made by observing post-test flatness of the edges and the general condition of the panels and fasteners.

Each of the joint designs was subjected to 10 plasma stream exposures with the front face of the sample being held at 1,477°K (2,200°F) for 20 minutes in each exposure. The samples were tested alternately so that each design experienced a 20-minute cooling cycle between immersions in the plasma stream.

The overlapping edge test sample is shown in Figure 5-15 after completion of cyclic exposure in the Plasma Arc Tunnel. This joint design developed a crack at one corner, which is shown in Figure 5-16. Figure 5-16 shows a closeup view of the crack as it extends from a relief radius along the bend line where the diagonal corner flange intersects a side flange on the panel face sheet.

Temperatures obtained by pyrometer measurements during each test cycle are listed in Table 5-3 for both types of panel edge closeout designs. The temperatures in Table 5-3 were measured at the approximate half-way point
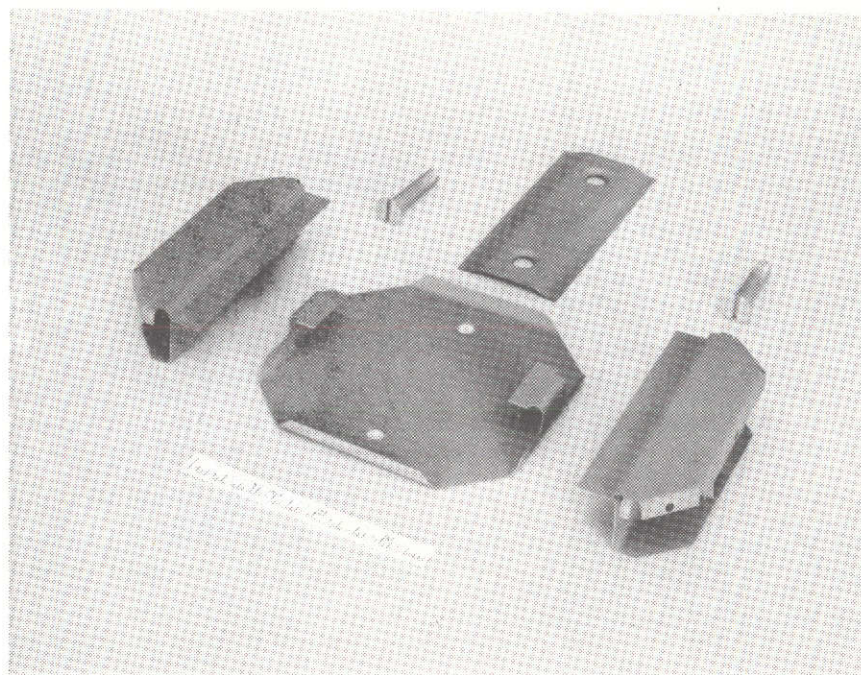
a. CLOSURE STRIP JOINT DESIGN
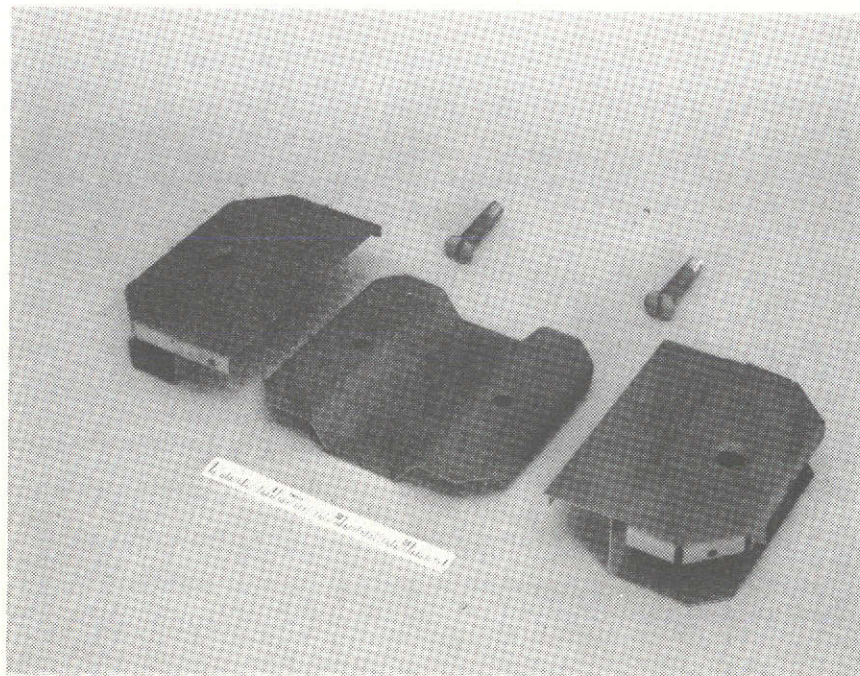
b. OVERLAPPING EDGE JOINT DESIGN

Figure 5-12. Detail Parts of Panel Joint Test Components
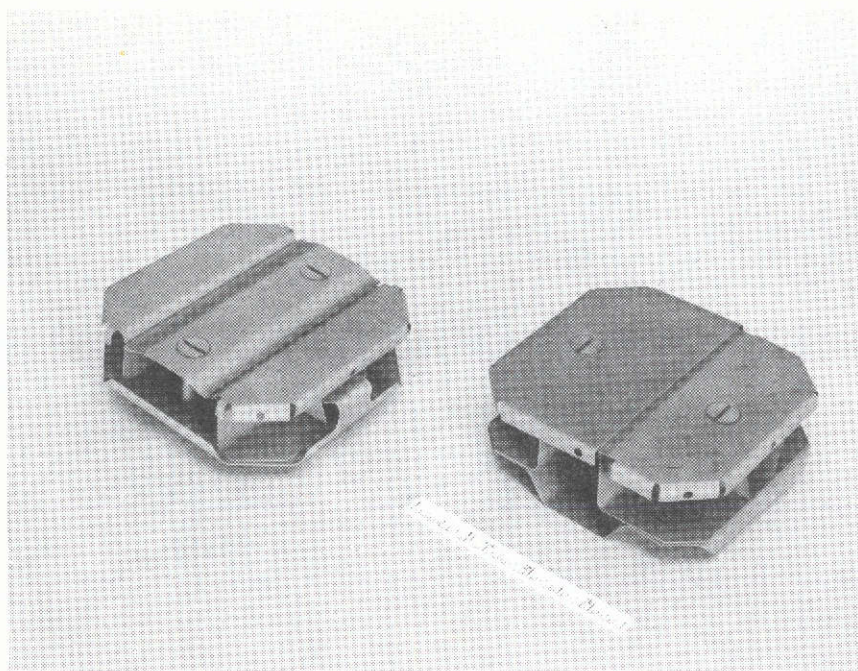
Figure 5-13. Panel Edge Joint Test Parts

in each run. Maximum surface temperature measured by pyrometer readings ranged from 1,397°K (2,050°F) to 1,545°K (2,300°F). The differences between maximum and minimum temperatures that were measured on the surface of the test samples during any given run ranged from 44.4°K (80°F) to 144.5°K (260°F).

Temperature time histories taken from thermocouple recordings during the tenth test cycle are shown in Figures 5-17 and 5-18. Such data show the temperature histories of interior portions of each joint design as well as the surface temperature histories. In both designs, the interior temperatures remained nearly constant after achieving equilibrium heating, a condition that indicates no significant ingestion of hot gases into the interior portions of the joints. Since the data of Figure 5-17 and 5-18 were obtained on the tenth test cycle, it was concluded that repeated cycles would not degrade the joint designs significantly, even though slight waviness from thermal stresses occurred on the outer surface of the overlapping edge design. The data of Figure 5-17 show a steady-state temperature difference of approximately
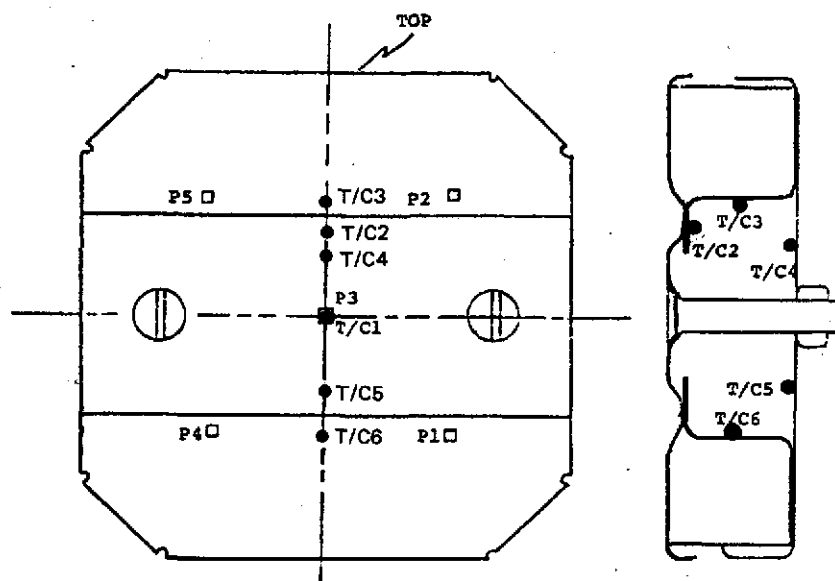
Notes:

*P1 through P5 - Pyrometer sighting locations.

*T/C 1 through T/C 6 - Tack-welded thermocouple locations.

a. CLOSURE STRIP JOINT DESIGN
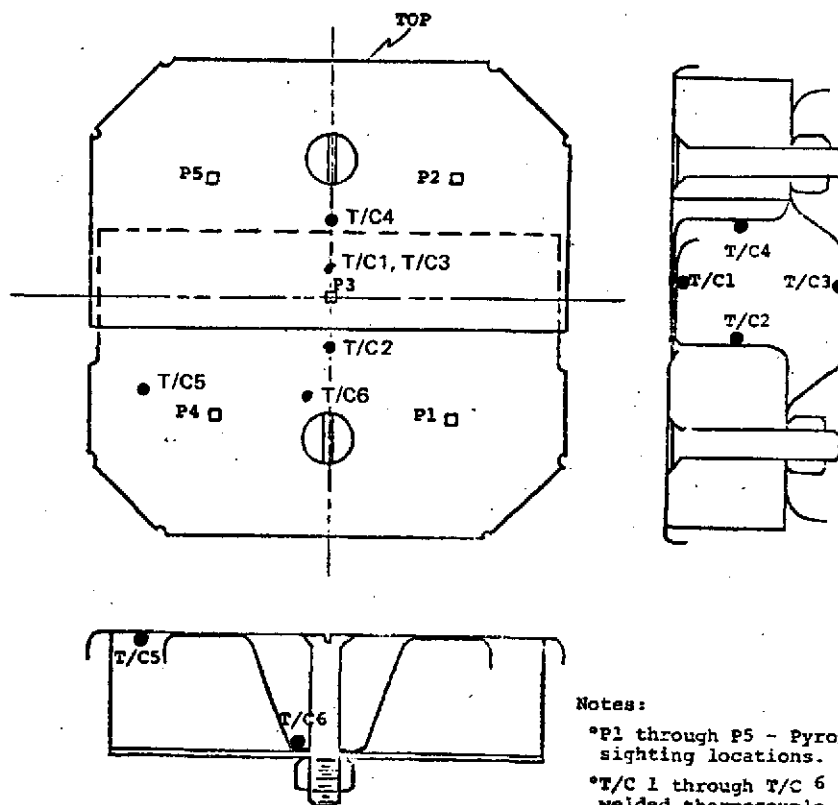
Notes:

*P1 through P5 - Pyrometer sighting locations.

*T/C 1 through T/C 6 - Tack-welded thermocouple locations.

b. OVERLAPPING EDGE DESIGN

Figure 5-14. Thermocouple and Pyrometer Sighting Locations for Panel Joint Samples

Figure 5-15. Overlapping Panel Edge Joint After Cyclic Exposures in the Plasma Arc Tunnel
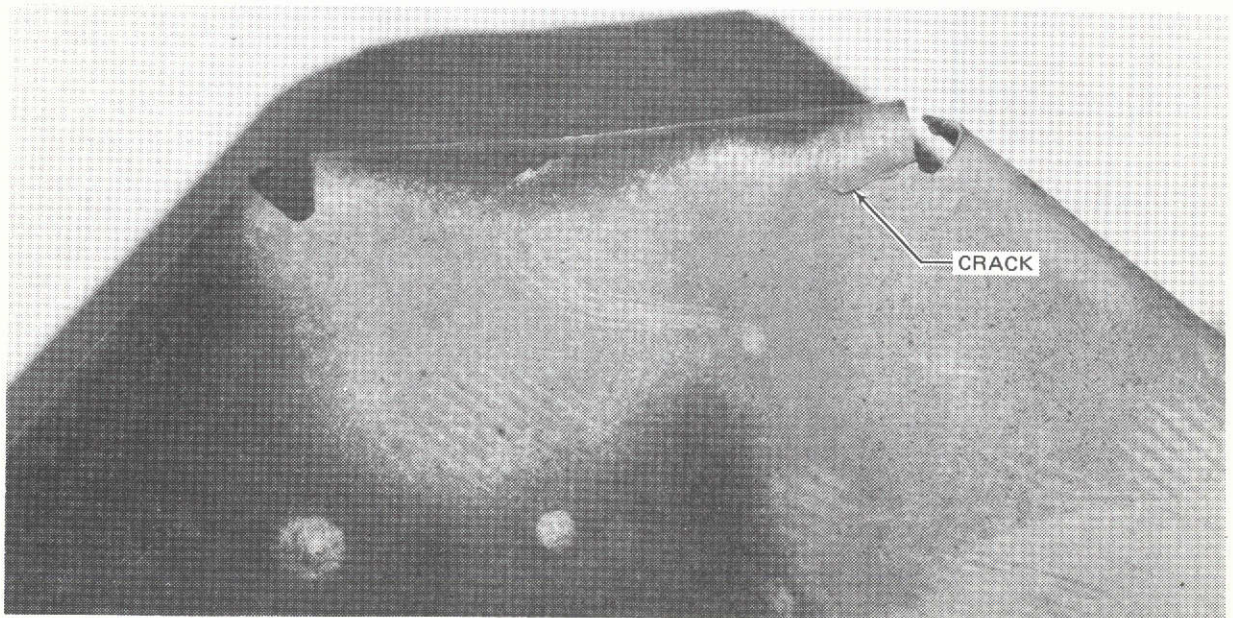
Figure 5-16. Corner of Overlapping Panel Joint Showing Crack at Relief Radius

Table 5-3

OPTICALLY MEASURED PANEL SURFACE TEMPERATURES,
PANEL EDGE CLOSURE DESIGNS

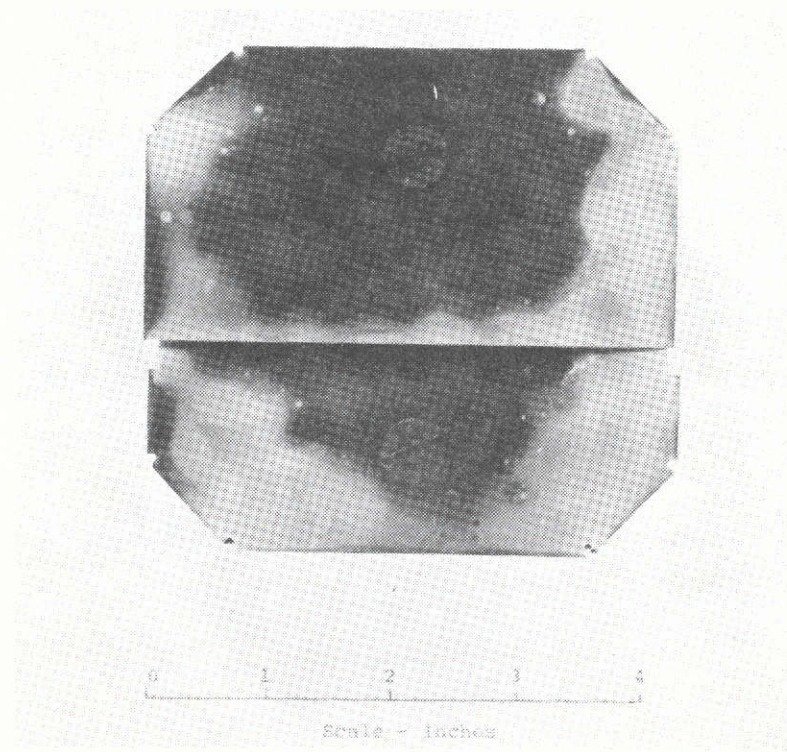| Panel Configuration	Run No.	Temperature [1] at Pyrometer Sighting Position					Run Time (sec)	Cycle No.
		P1	P2	P3	P4	P5		
Overlapping Edge Design	3660	1,432 (2,120)	1,378 (2,020)	1,372 (2,010)	1,384 (2,030)	1,328 (1,925)	1,199	1
	3661	1,453 (2,150)	1,392 (2,040)	1,420 (2,090)	1,430 (2,110)	1,354 (1,970)	1,202	2
	3661	1,495 (2,230)	1,430 (2,110)	1,443 (2,140)	1,464 (2,170)	1,392 (2,040)	1,201	3
	3661	1,477 (2,200)	1,407 (2,070)	1,392 (2,040)	1,458 (2,160)	1,372 (2,010)	1,201	4
	3661	1,477 (2,200)	1,392 (2,040)	1,427 (2,100)	1,458 (2,160)	1,360 (1,985)	1,201	5
	3661	1,545 (2,300)	1,453 (2,150)	1,467 (2,180)	1,477 (2,200)	1,397 (2,050)	1,199	6
	3661	1,477 (2,200)	1,472 (2,190)	1,517 (2,270)	1,472 (2,190)	1,384 (2,030)	1,204	7
	3661	1,545 (2,300)	1,472 (2,190)	1,522 (2,280)	1,458 (2,160)	1,378 (2,020)	1,208	8
	3661	1,545 (2,300)	1,477 (2,200)	1,467 (2,180)	1,458 (2,160)	1,392 (2,040)	1,204	9
	3662	1,407 (2,070)	1,420 (2,090)	1,372 (2,010)	1,409 (2,075)	1,406 (2,070)	1,200	10
Closure Strip Design	3660	1,372 (2,010)	1,397 (2,050)	1,368 (2,000)	1,344 (1,955)	1,359 (1,980)	1,190	1
	3661	1,370 (2,105)	1,430 (2,110)	1,400 (2,060)	1,395 (2,050)	1,453 (2,150)	1,203	2
	3661	1,420 (2,090)	1,467 (2,180)	1,407 (2,070)	1,420 (2,090)	1,432 (2,120)	1,199	3
	3661	1,390 (2,140)	1,480 (2,210)	1,400 (2,060)	1,384 (2,030)	1,397 (2,050)	1,201	4
	3661	1,392 (2,040)	1,378 (2,020)	1,378 (2,020)	1,430 (2,110)	1,444 (2,140)	1,199	5
	3661	(2,250)	1,467 (2,180)	1,392 (2,040)	1,368 (2,000)	1,411 (2,080)	1,198	6
	3661	1,477 (2,200)	1,427 (2,100)	1,384 (2,030)	1,477 (2,200)	1,340 (1,950)	1,200	7

Table 5-3

OPTICALLY MEASURED PANEL SURFACE TEMPERATURES,
PANEL EDGE CLOSURE DESIGNS (Continued)

Panel Configuration	Run No.	Temperature[1] at Pyrometer Sighting Position					Run Time (sec)	Cycle No.
		P1	P2	P3	P4	P5		
Closure Strip Design (Cont)	3661	1,420 (2,090)	1,472 (2,190)	1,378 (2,020)	1,378 (2,020)	1,400 (2,060)	1,198	8
	3661	1,545 (2,300)	1,480 (2,210)	1,392 (2,040)	1,368 (2,000)	1,427 (2,100)	924[2]	9
	3662	1,397 (2,050)	1,411 (2,080)	1,372 (2,010)	1,477 (2,200)	1,347 (1,960)	1,206	10

Note: Temperatures shown as °K primary units and (°F) secondary
units.

(1) Temperatures listed were obtained at the approximate half-way point
of each test cycle and were corrected for surface and window effects.
See Figure 5-14 for pyrometer sighting positions.

(2) Cycle terminated early to change the arc heater electrodes.

111°K (200°F) from the outer surface at Thermocouple 1 to the interior
support rail, where Thermocouple 3 was located.

In the closure strip design (Figure 5-18), the difference between the outer
surface at Thermocouple 1 and the internal support position (Thermocouples 4
and 5) was approximately 122°K (220°F). Thus, both joint designs showed
similar temperature decreases at the centerline of the joint between the outer
surface and the simulated structure to which the panels were attached. The
closure strip design was judged to have the better performance, based on the
fact that it exhibited no distortion, whereas the overlapping edge design
suffered permanent set in the form of sine-wave-shaped distortions along the
lip of the outer panel edge. Temperature recordings showed no increased
transient heating due to hot gas ingestion in either joint design.

Motion pictures were taken in color at three points during each test cycle: at
the start of the cycle, approximately half-way through the cycle, and at the
end of the cycle. The films were studied to determine if any excessive local
heating could be detected or if any tripping of the flow could be observed at
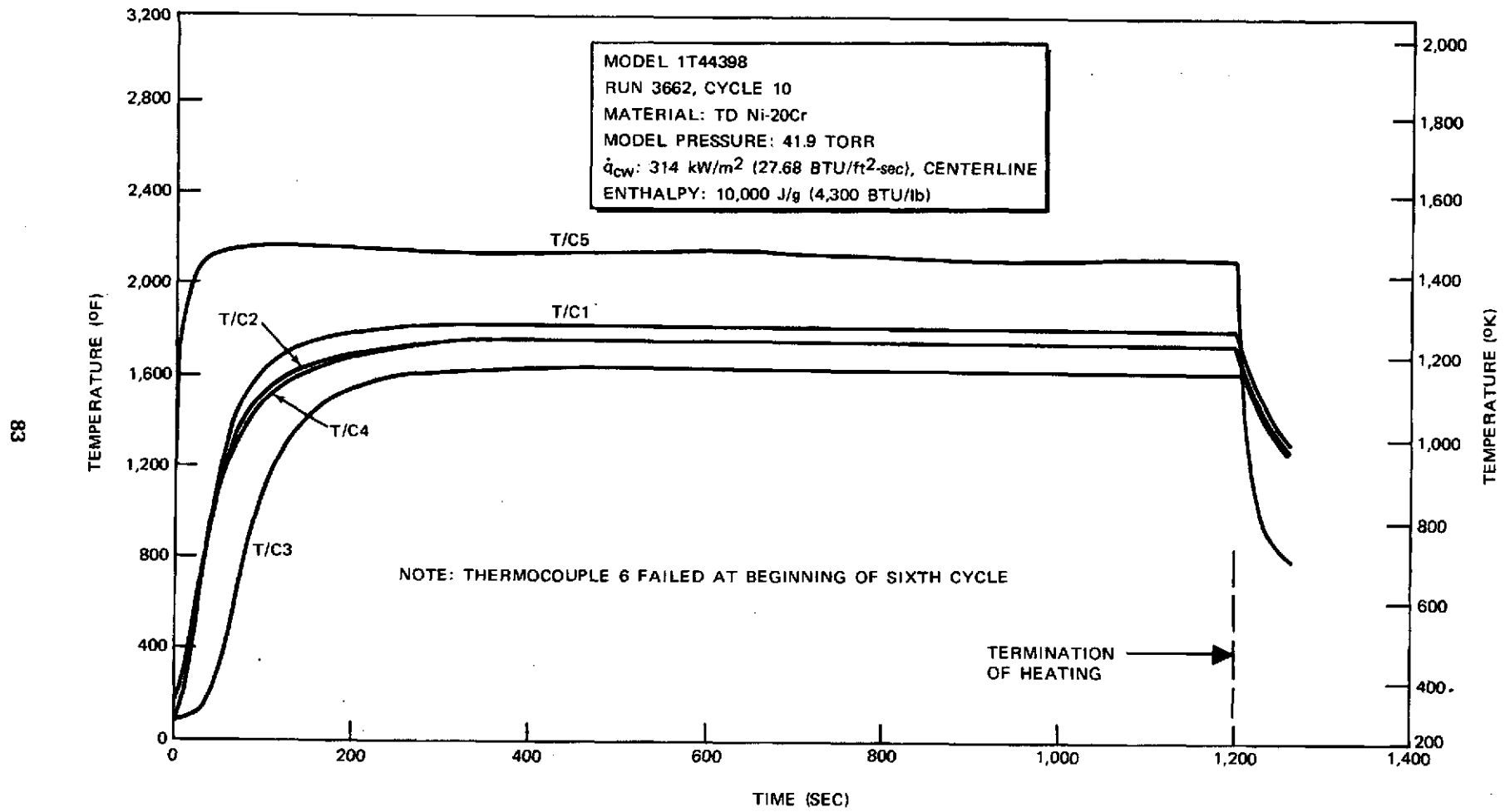
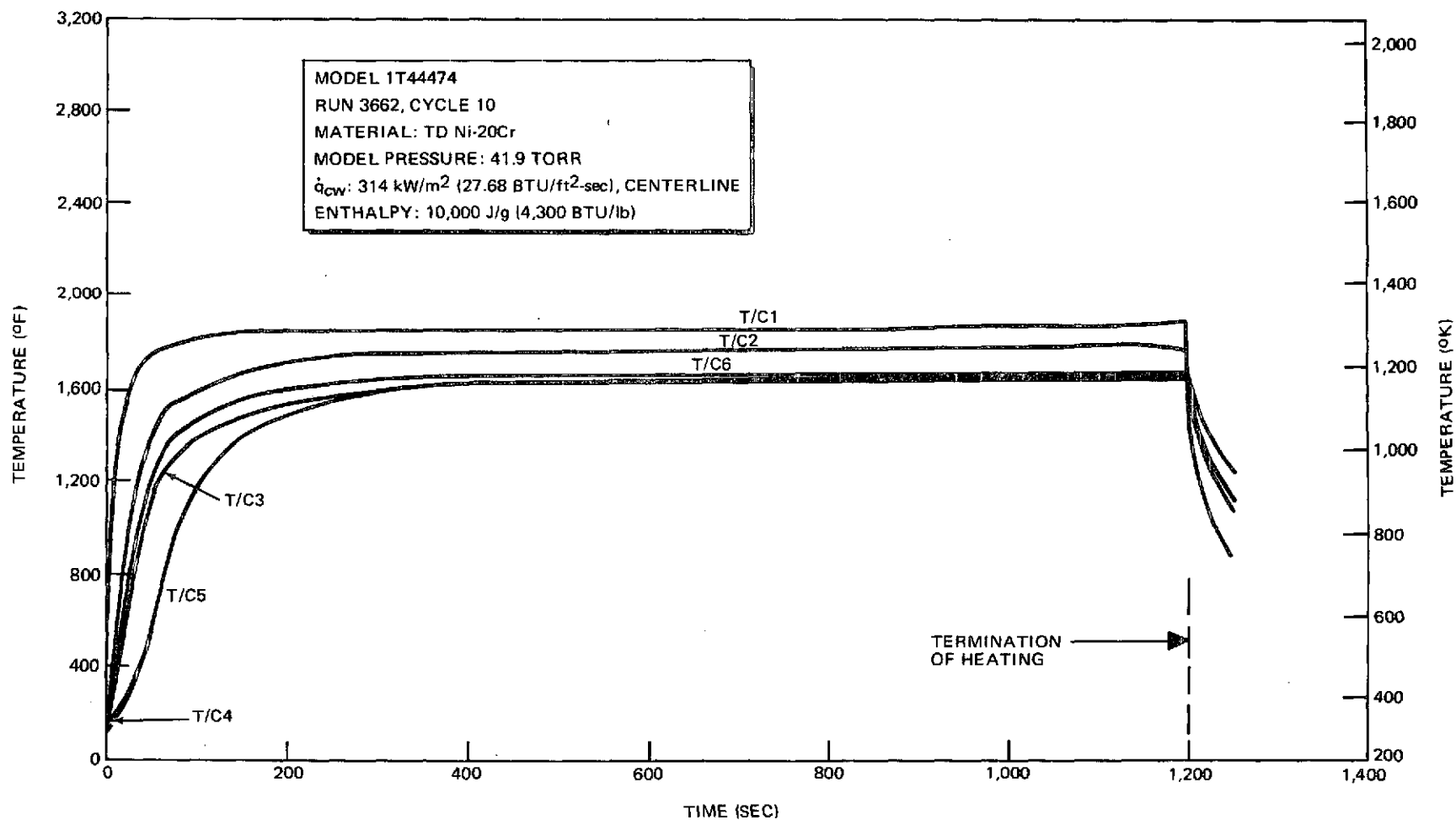Figure 5-17. Panel Edge Joint Temperature Histories, Overlapping Edge Design

Figure 5-18. Panel Edge Joint Temperature Histories, Closure Strip Design

the fasteners. No unusual flow patterns or local heating were detected during the film review.

5.5 FULL-SCALE SUBSIZE PANEL TESTS

The full-scale subsize panels were designed to simulate full-length beam-supported panels with simulated attachments and packaged low-density insulation underneath the TD Ni-20Cr heat shields. Programmed cycles of differential pressure, temperature, and environmental pressure were applied to simulate boost, entry, and cruise flight conditions experienced by a typical TPS area on the lower surface of the Orbiter (Figure 2-5). Simulated boost flight acoustic loads were interspersed with the cyclic pressure and temperature conditions.

The test system used for the Phase I subsize specimens is shown schematically in Figure 5-19, which also shows the sequence of testing. So that both competing panel designs would experience identical histories of loads, temperatures, pressures, and acoustic levels, they were mounted for testing in the same basic test fixture, a stainless steel pressure box with TD Ni-20Cr end supports that held the test panels. The test fixture was designed to permit its use in both the Space Simulation Chamber and the Acoustic Facility so that the test panels could remain in place except for necessary inspections.

The programmed cycles of differential pressure, chamber pressure, and temperature are shown in Figure 5-20, and Figure 5-21 presents the spectrum selected for acoustic tests. The chamber pressure desired for the test profile was lower than that shown in Figure 5-20. However, to maintain the desired panel differential pressure profile, it was necessary to use a higher chamber pressure during portions of the test cycle. During the simulated entry portion of the test cycle, the chamber pressure ranged between approximately 1 and 15 torr. This pressure range, while higher than the computed ambient pressure during the Orbiter entry flight, was sufficiently low to simulate the low-pressure effects that could cause degradation from chromium depletion under elevated-temperature, low-pressure environments (see Appendix C).

SIMULATED BOOST, ENTRY, AND
CRUISE FLIGHT

(TEN CYCLES BEFORE
MOVING TO ACOUSTIC TESTS)

NDT AND INSPECTION

PROGRAMMED HEATING,
PRESSURE, AND PANEL
LOAD PROFILES

EXAMINATION
STATION

5.5 FT DIAMETER
SPACE SIMULATION
CHAMBER

TEMPERATURE
RECORDER

NDT AND INSPECTION

INSPECTION

PRELIMINARY ACOUSTIC TEST
(FIRST TEST SEQUENCE)

EXAMINATION
STATION

ACOUSTIC TESTS
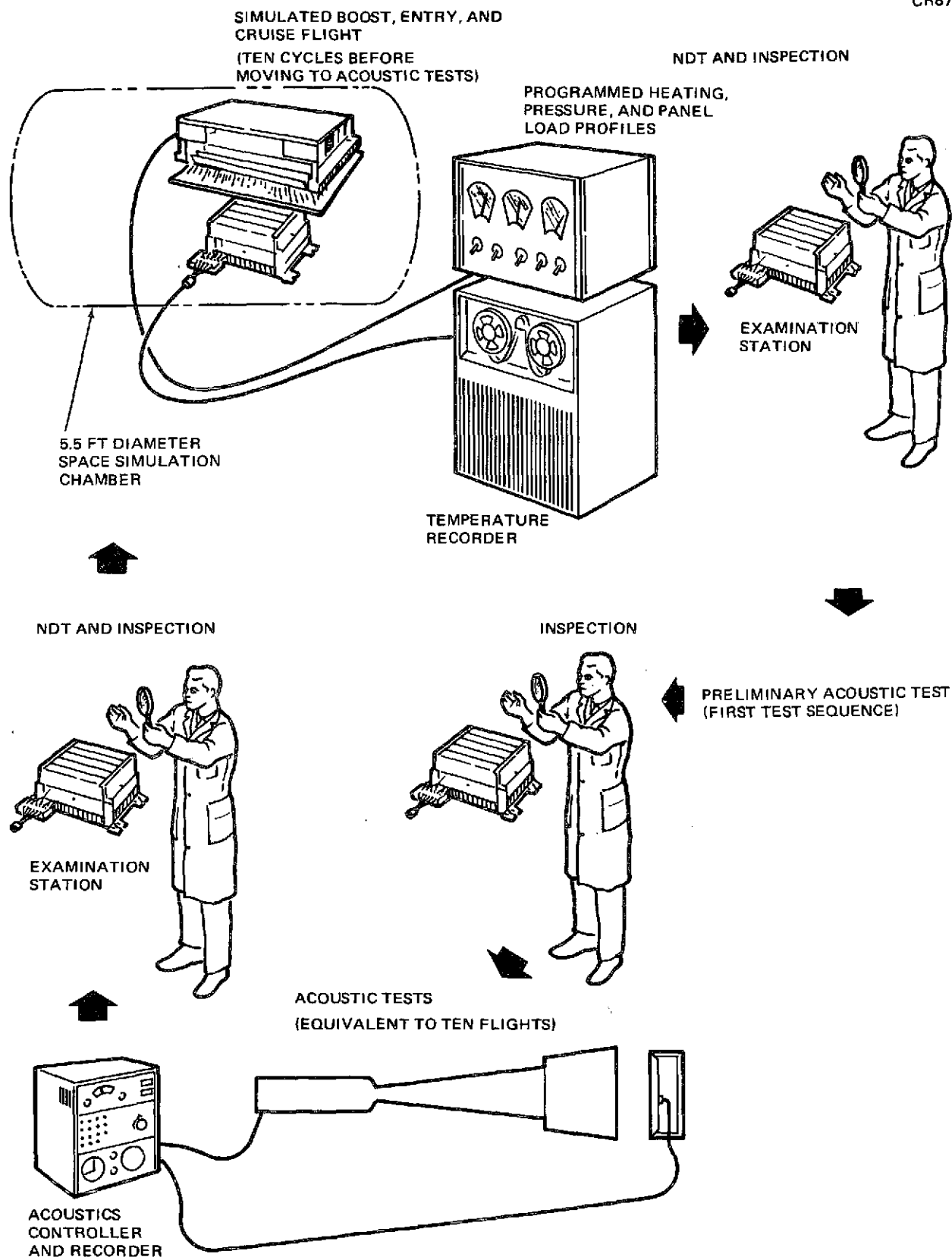(EQUIVALENT TO TEN FLIGHTS)

ACOUSTICS
CONTROLLER
AND RECORDER

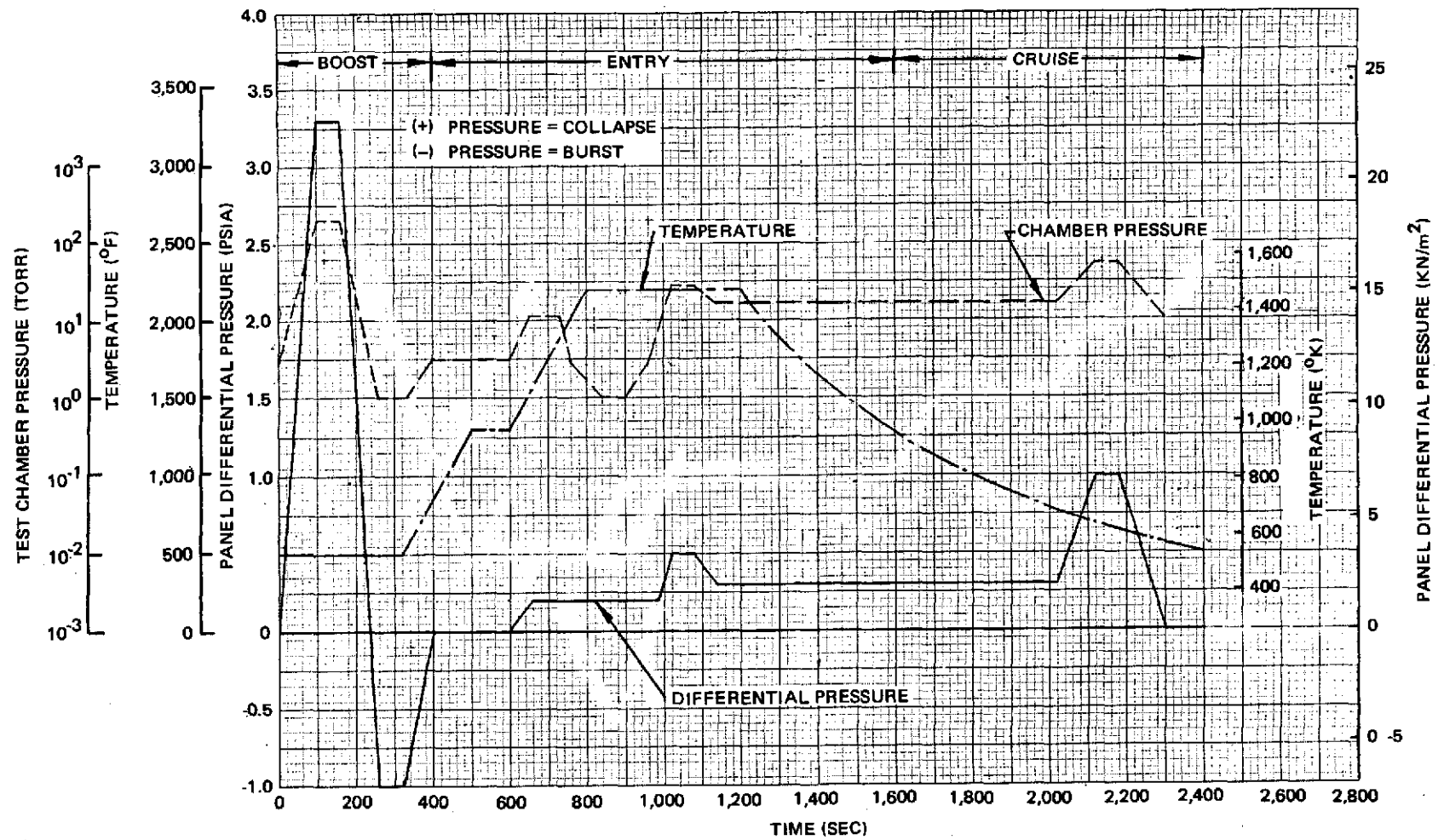Figure 5-19. Full-Scale, Subsize Panel Test Sequence

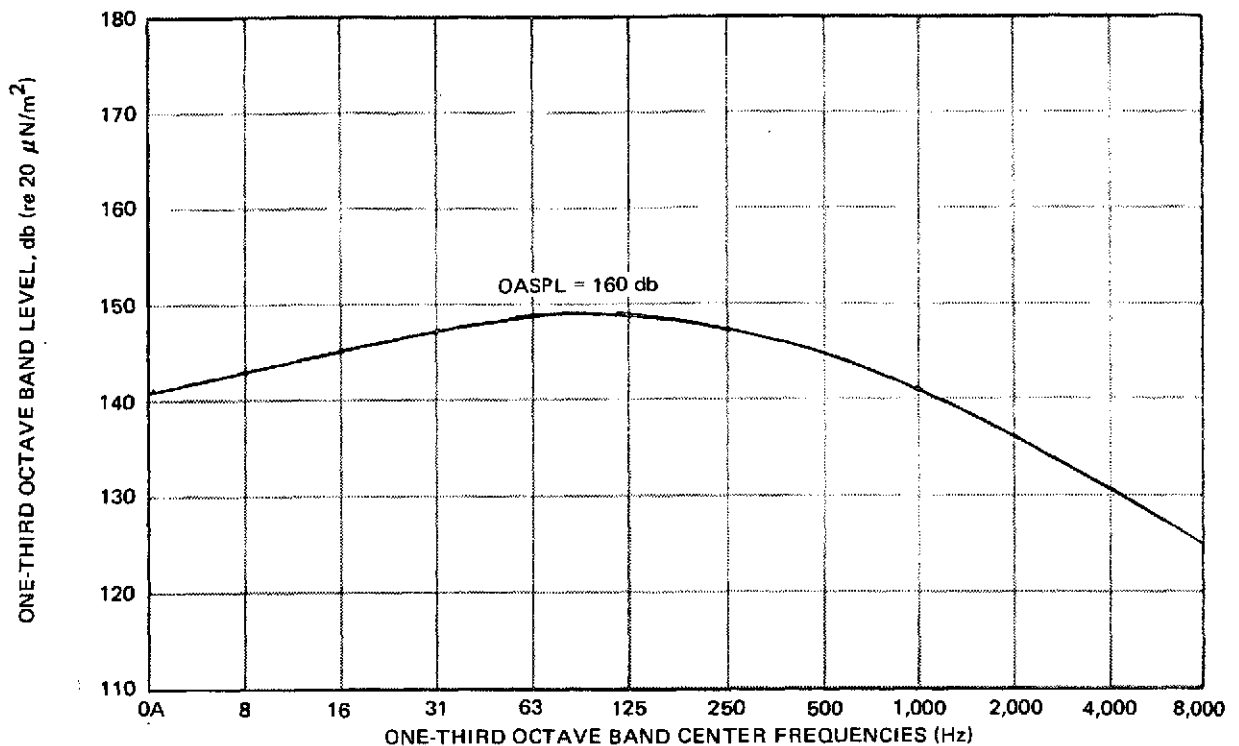Figure 5-20. Full-Scale Subsize Panel Test Profiles

Figure 5-21. Liftoff Acoustic Spectra for TD Ni-20Cr Heat Shield Test Panels

The panel designs and their instrumentation points are shown in Figures 5-22 and 5-23. Detail parts of the corrugation-stiffened panel are shown in Figure 5-24, and Figure 5-25 shows the assembled test panels after being preoxidized to obtain a dark, high-emittance surface. Packaged, low-density insulation was located behind the panels and attached to the inside of the pressure box by fittings that permitted expansion and contraction of the insulation package.

The low-density insulation was 128-kg/m^3 (8-lb/ft^3) Fiberfrax Hi-Fi felt manufactured by the Carborundum Company. This material was contained in a segmented enclosure made of 0.0127-cm (0.005-in.) thick TD Ni-20Cr foil assembled by spot welding. The assembled insulation package is shown in Figure 5-26, and the package is shown installed in the pressure box in Figure 5-27. Beads were formed in the upper and lower surfaces of the insulation enclosure to provide stability and allow a controlled deformation pattern at elevated temperatures. Two passages were provided near the center of the package to allow deflection measuring rods to pass through the

NOTE: DIMENSIONS IN INCHES.

○ THERMOCOUPLE
■ STRAIN GAGE
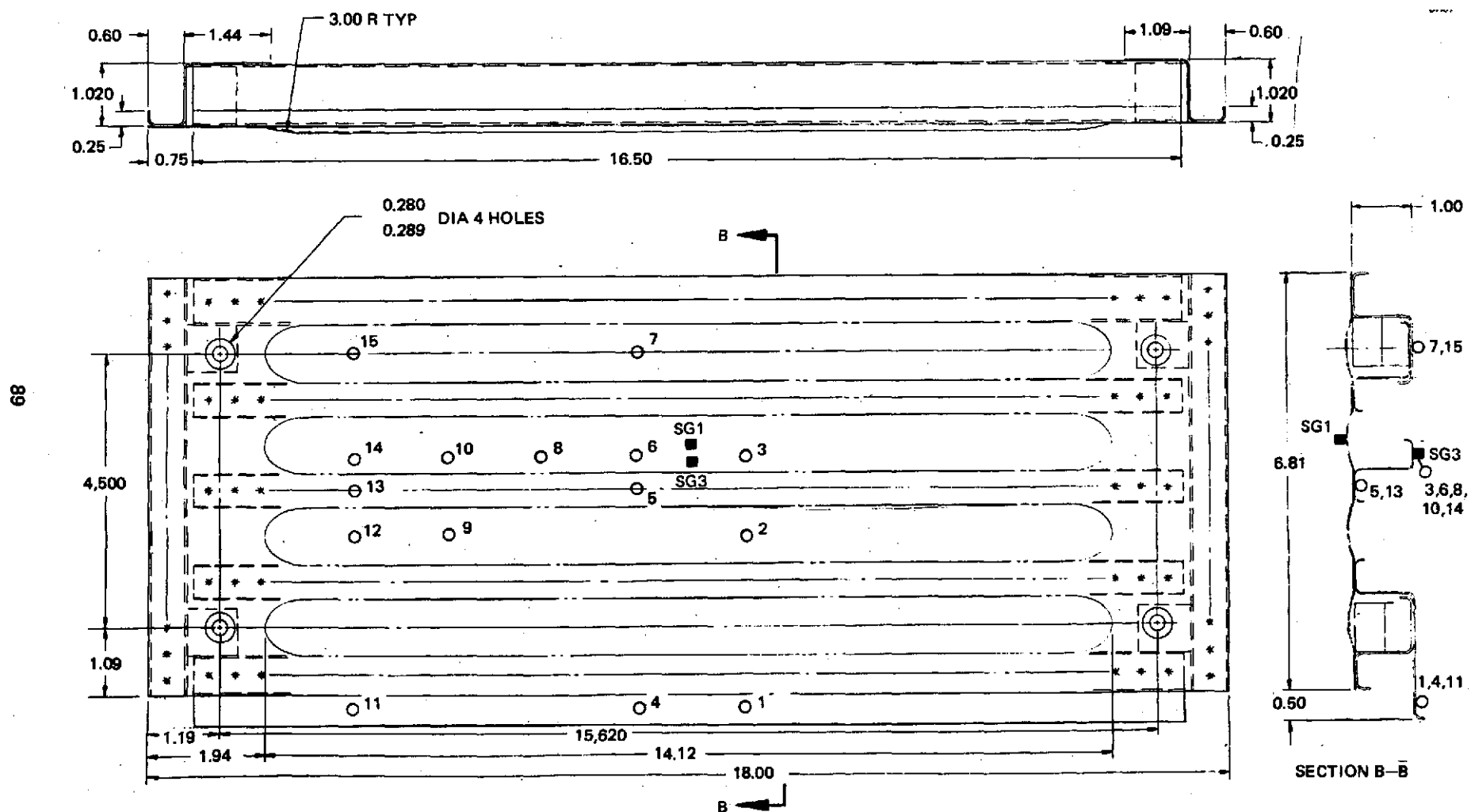
Figure 5-22. Instrumentation Points on Zee-Stiffened Panel
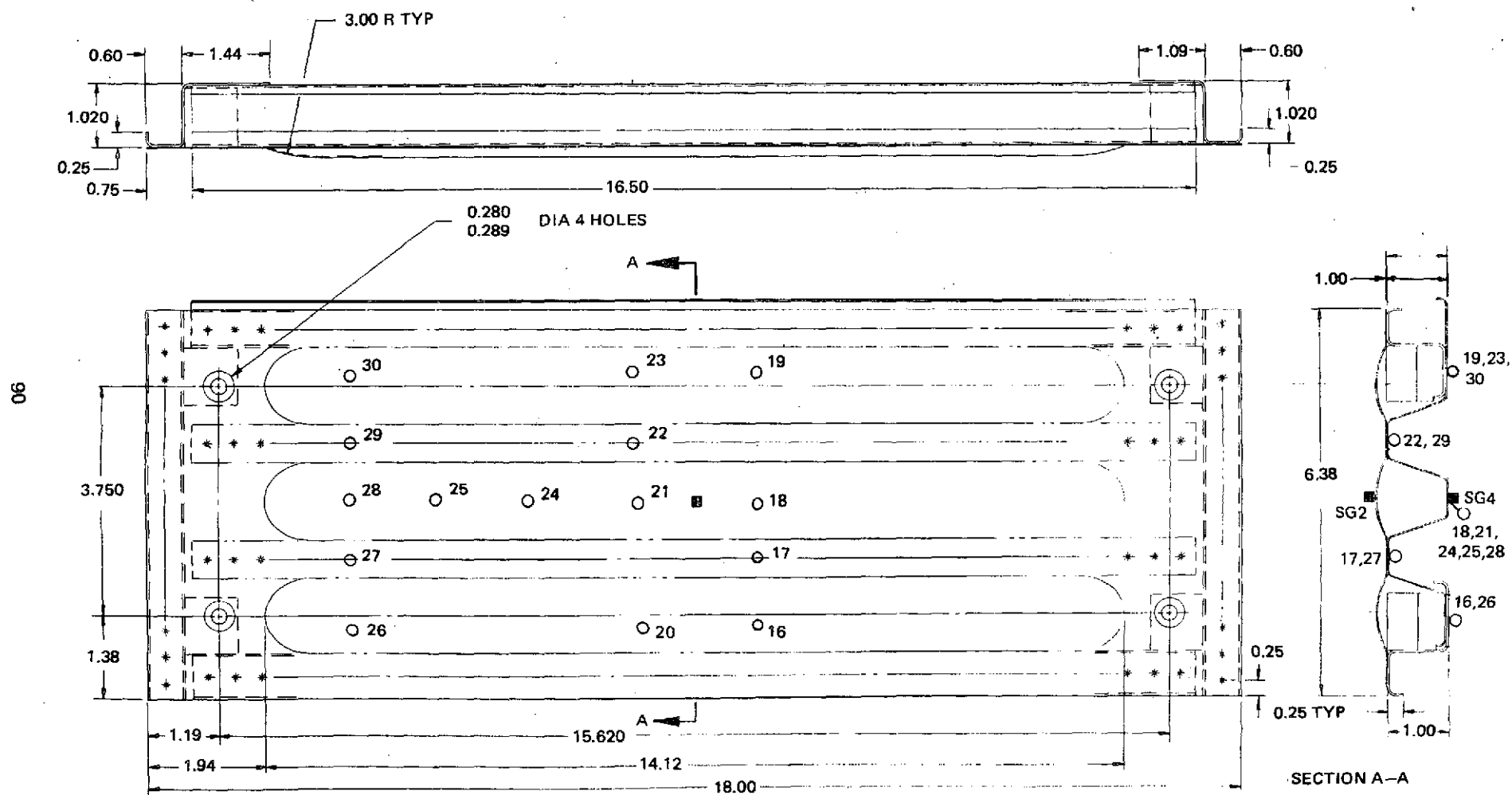
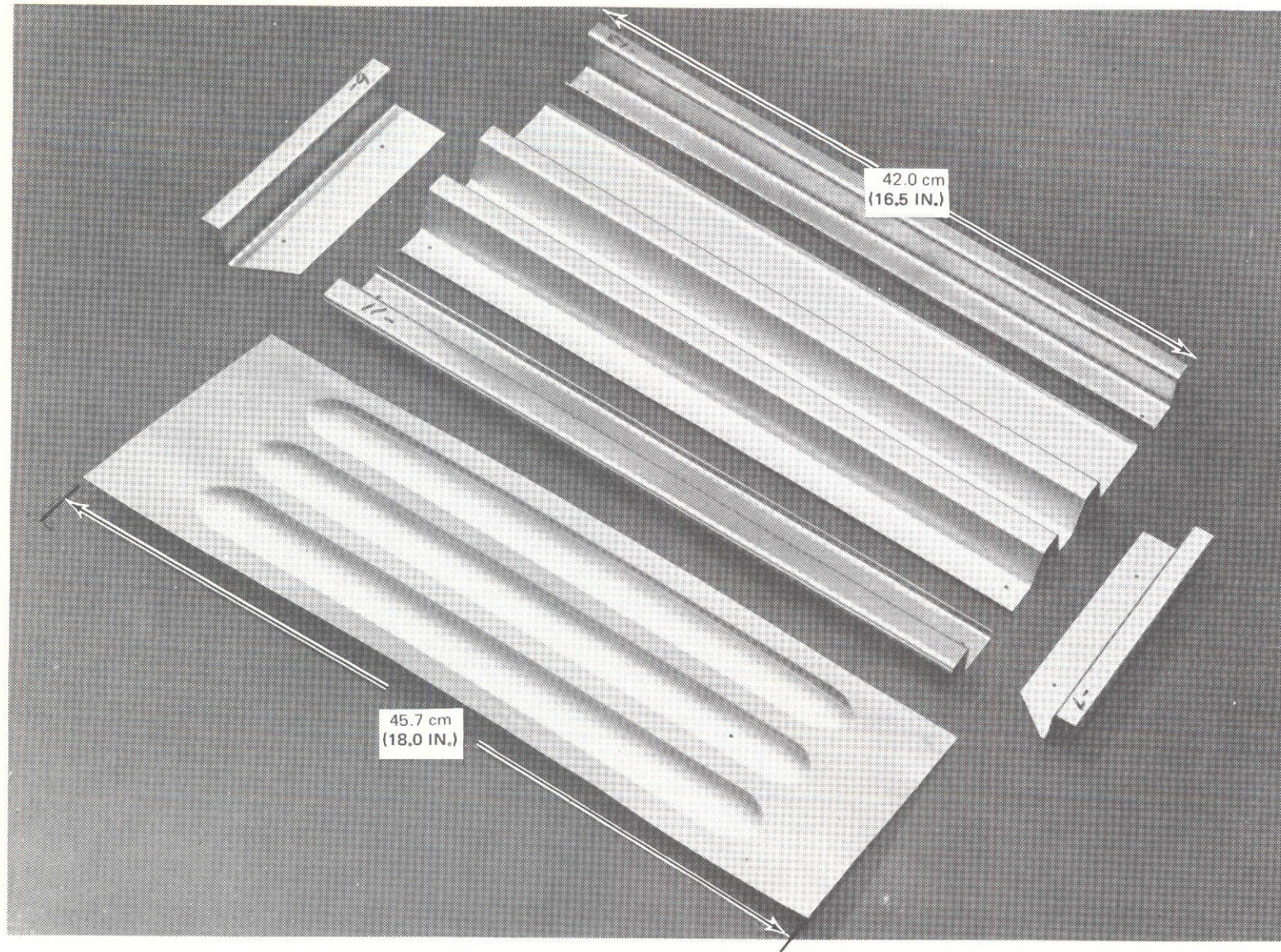Figure 5-23. Instrumentation Points on Corrugation-Stiffened Test Panel

Figure 5-24. Detail Parts for Corrugation-Stiffened Test Panel
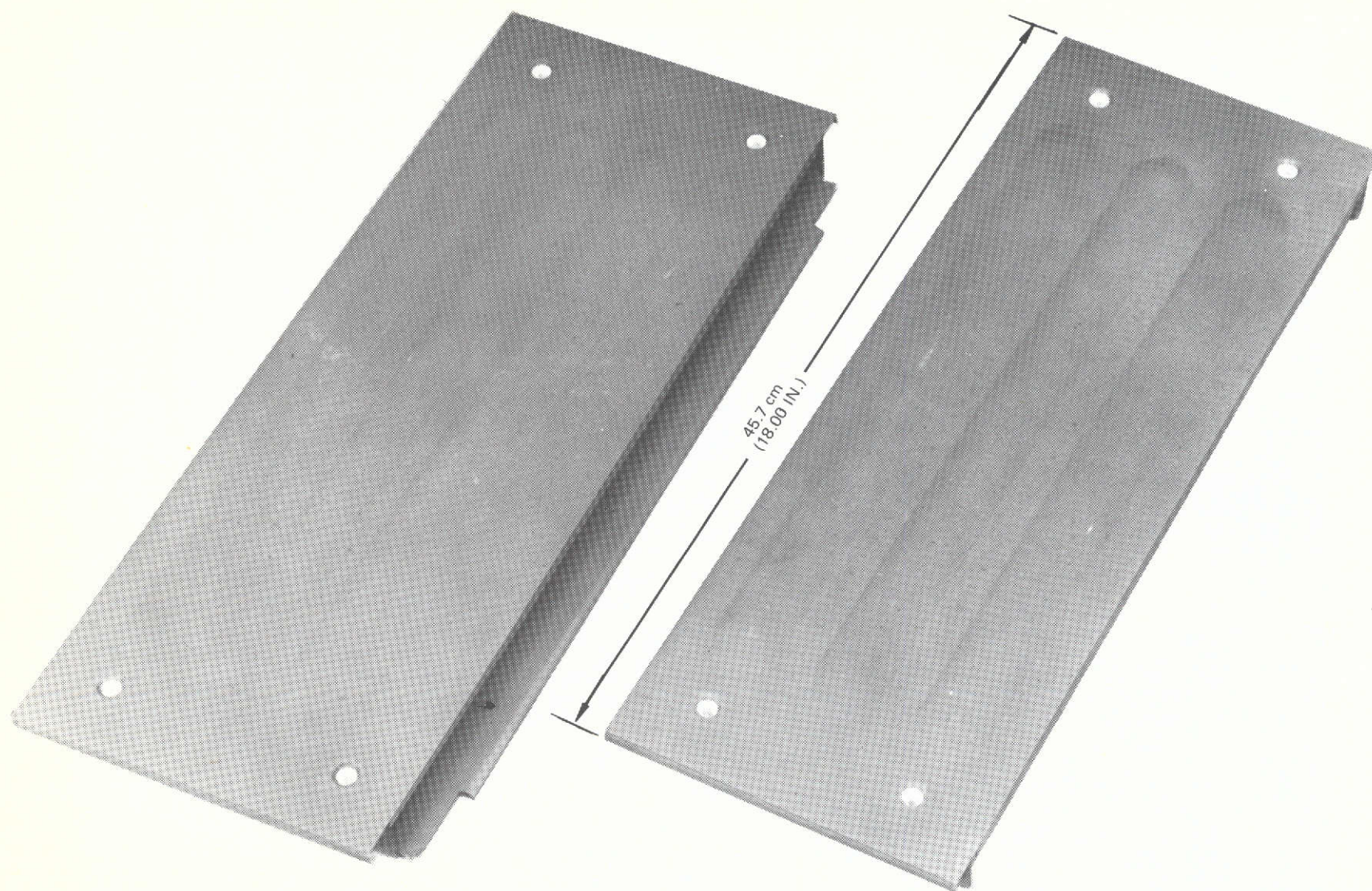
45.7 cm
(18.00 IN.)
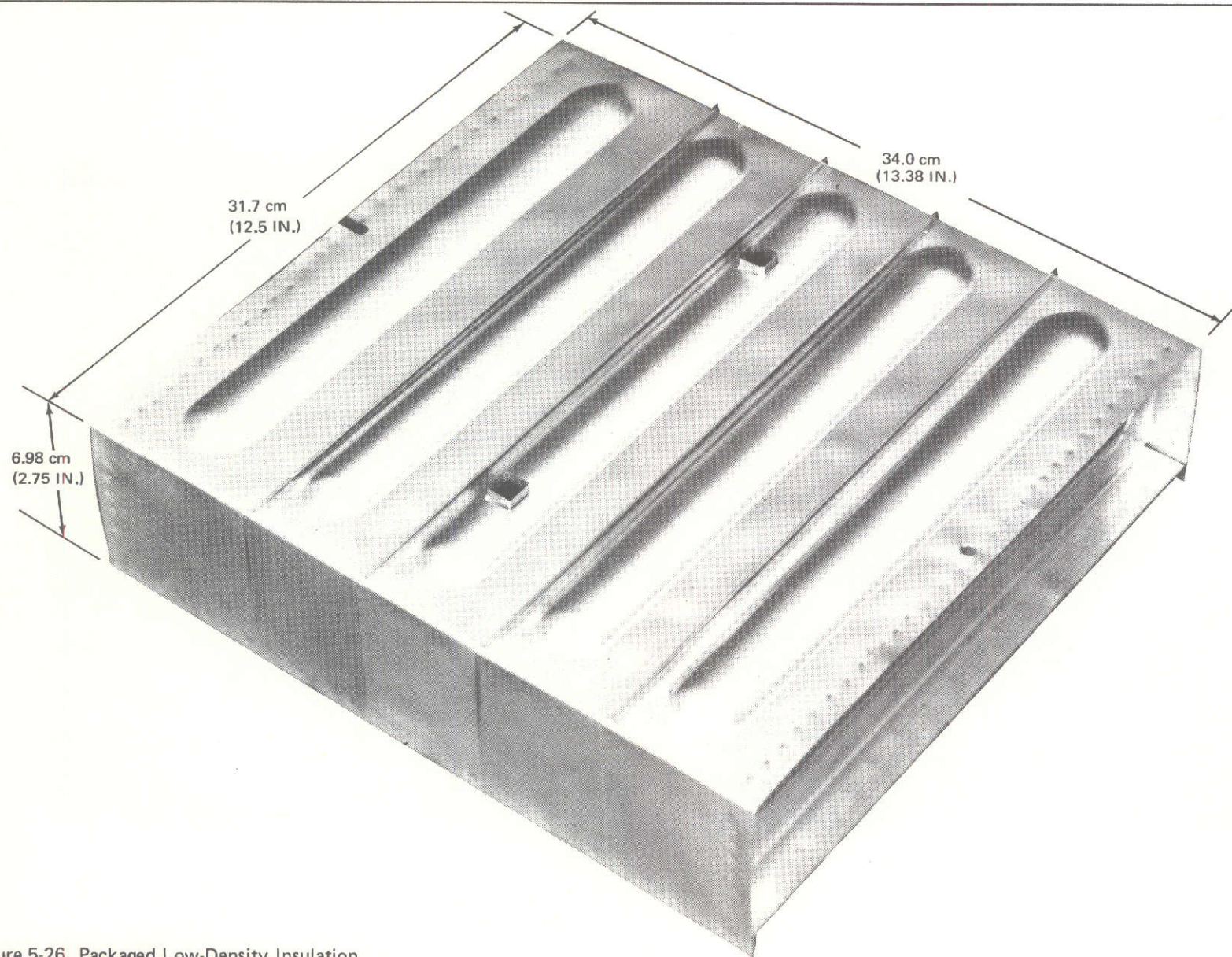
Figure 5-25. Full-Scale Subsize Test Panels

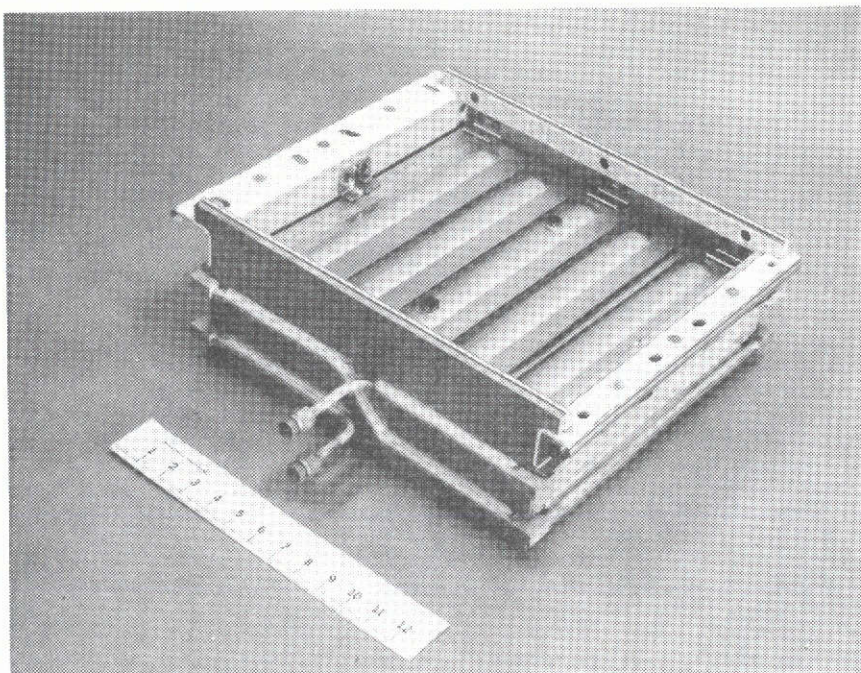Figure 5-26. Packaged Low-Density Insulation

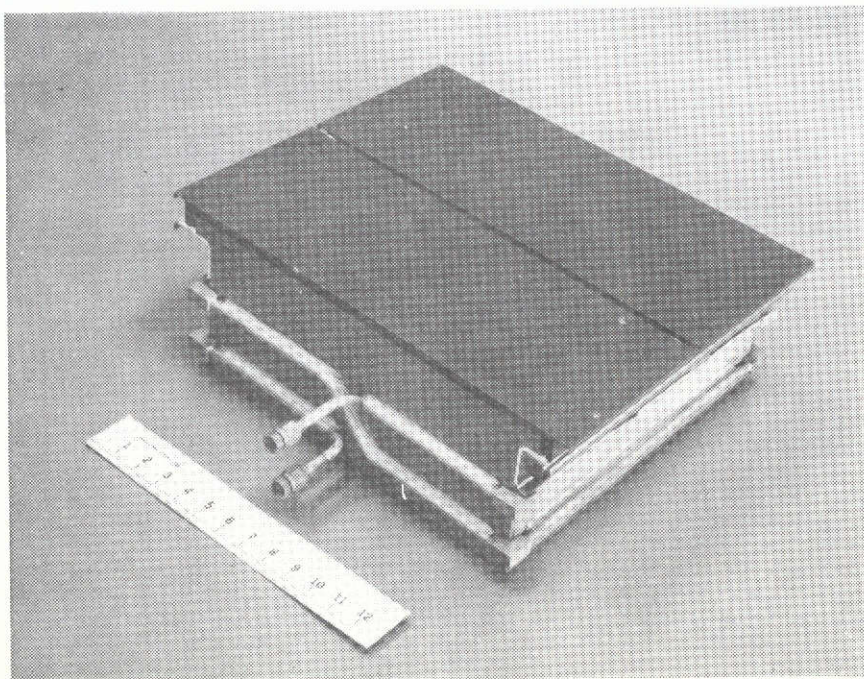Figure 5-27. Pressure Box With Insulation Package Installed

Figure 5-28. Assembled Test Unit

insulation and contact the inner surfaces of the test panels. Figure 5-23 shows the assembled test unit with panels in place. Low-density insulation packaged in quartz cloth was used between the two panels to provide a pressure seal. Temperatures at various points on the insulation package were required to determine the overall effectiveness of the simulated TPS. Thus, three thermocouples were located on the insulation package surface nearest the panels, and three thermocouples were located in similar positions on the cool side of the package away from the test panels. The insulation package thermocouple locations are shown in Figure 5-29.

After delivery of the TD Ni-20Cr test panels and associated components to the Space Simulation Facility, strain gages were installed at the center of each full-scale subsize test panel (Figures 5-22 and 5-23) to monitor stresses in preliminary differential-pressure trials and in preliminary acoustic tests.

Uniaxial gages were mounted on the external surface of the face sheet of each panel and on the stiffening elements on the internal side of the panel. For the zee-stiffened panel, the interior strain gage was mounted on the cap of the stiffener (Figure 5-22); for the corrugation-stiffened panel, a gage was mounted at the center of the panel on the corrugation (Figure 5-23).

Trial runs were conducted at room temperature to determine stress levels realized at various levels of differential pressure. The trial runs were conducted in simple steps up to the maximum collapse and burst differential pressure levels programmed for the boost flight portion of the cyclic tests. As shown in Figure 5-20, a maximum collapse differential pressure of 22.8 kN/m^2 (3.3 psi) and a maximum burst differential pressure of -6.89 kN/m^2 (-1.0 psi) were programmed for the boost portion of the test cycle.

Stress levels recorded in the zee-stiffened panel during preliminary trials at the peak pressure of 22.8 kN/m^2 (3.3 psi) were 47.1 MN/m^2 (6,830 psi) compression in the face sheet and 85.8 MN/m^2 (12,440 psi) tension in the zee stiffener. Similar stresses in the corrugation-stiffened panel were 53.8 MN/m^2 (7,800 psi) compression in the face sheet and 52.3 MN/m^2 (7,560 psi) tension in the corrugation. In the trial burst-pressure tests stresses were lower,

- UNBRACKETED T/C'S LOCATED ON HOT SIDE
- BRACKETED T/C'S LOCATED IN SAME POSITION ON COOL SIDE

INSULATION PACKAGE (HOT SIDE)

T/C33 (36)

T/C31 (34)

T/C32 (35)

ZEE-STIFFENED PANEL POSITION
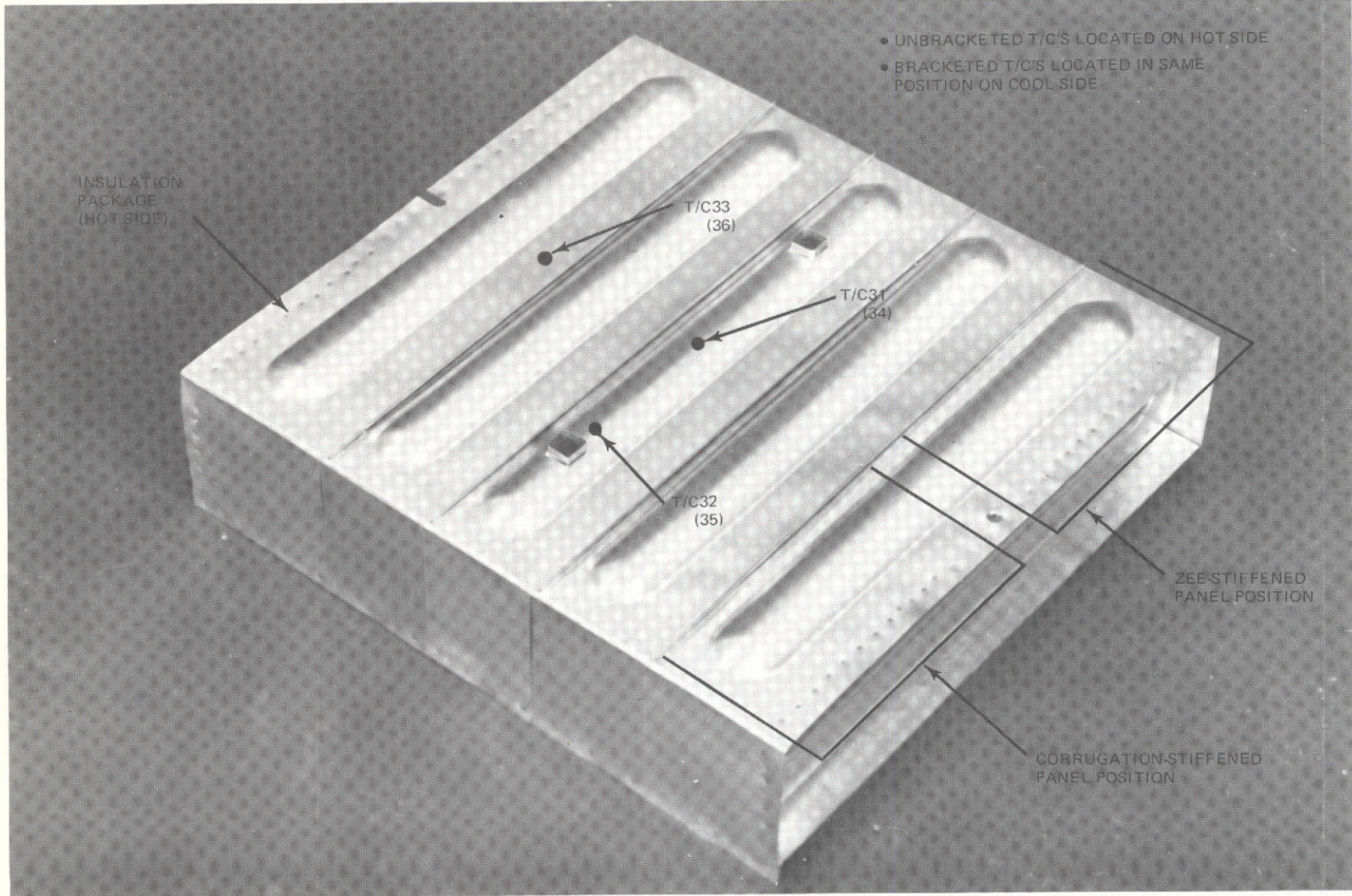
CORRUGATION-STIFFENED PANEL POSITION

Figure 5-29. Insulation Package Thermocouple Locations

ranging from 15.1 MN/m^2 (2,190 psi) tension to 16.8 MN/m^2 (2,440 psi) compression.

Preliminary acoustic tests were also conducted to determine stress responses at the center of each panel. An overall sound pressure level (OASPL) of 150 db was used initially, and progressively higher acoustic levels were applied until an OASPL of 165 db was reached. Maximum stress levels recorded were less than 20.7 MN/m^2 (3,000 psi). The overall rms stress level at each strain gage position varied with OASPL as indicated in Figure 5-30. Actual acoustic spectra achieved in the preliminary tests for each OASPL are presented in Appendix F. Power spectral density analyses of the panel responses at the strain gage positions were also conducted, and the resulting plots of power spectral density versus frequency are presented in Appendix F for each strain gage at each of the four acoustic levels.

Instrumentation of the 45.7-cm (18-in.) long test panels was completed after the preliminary differential pressure and acoustic tests were conducted. The thermocouples installed on the underside of the panels are shown in Figure 5-31. Modifications were also made to the pressure box to permit instrumentation leadouts, to provide mounting positions for the deflection transducers, and to install instrumentation connectors on the box surface opposite the pannels. These modifications are shown in Figure 5-32.

After modifications to the pressure box were completed, the panels were installed and instrumentation checks were made. The box and panel edges were then sealed to prevent leakage and preliminary differential pressure checks were conducted. The initial checks showed the necessity for increasing the pumping capacity, and a larger system having a 0.817-m^3/sec (1,730-ft^3/min) capacity was connected to the pressure box. With this capacity the maximum differential pressure (collapse) of 22.8 kN/m^2 (3.30 psi) was achieved without difficulty.

In addition to the deflection transducers installed to measure normal deflection at the centers of the panels, two transducers were installed at the ends
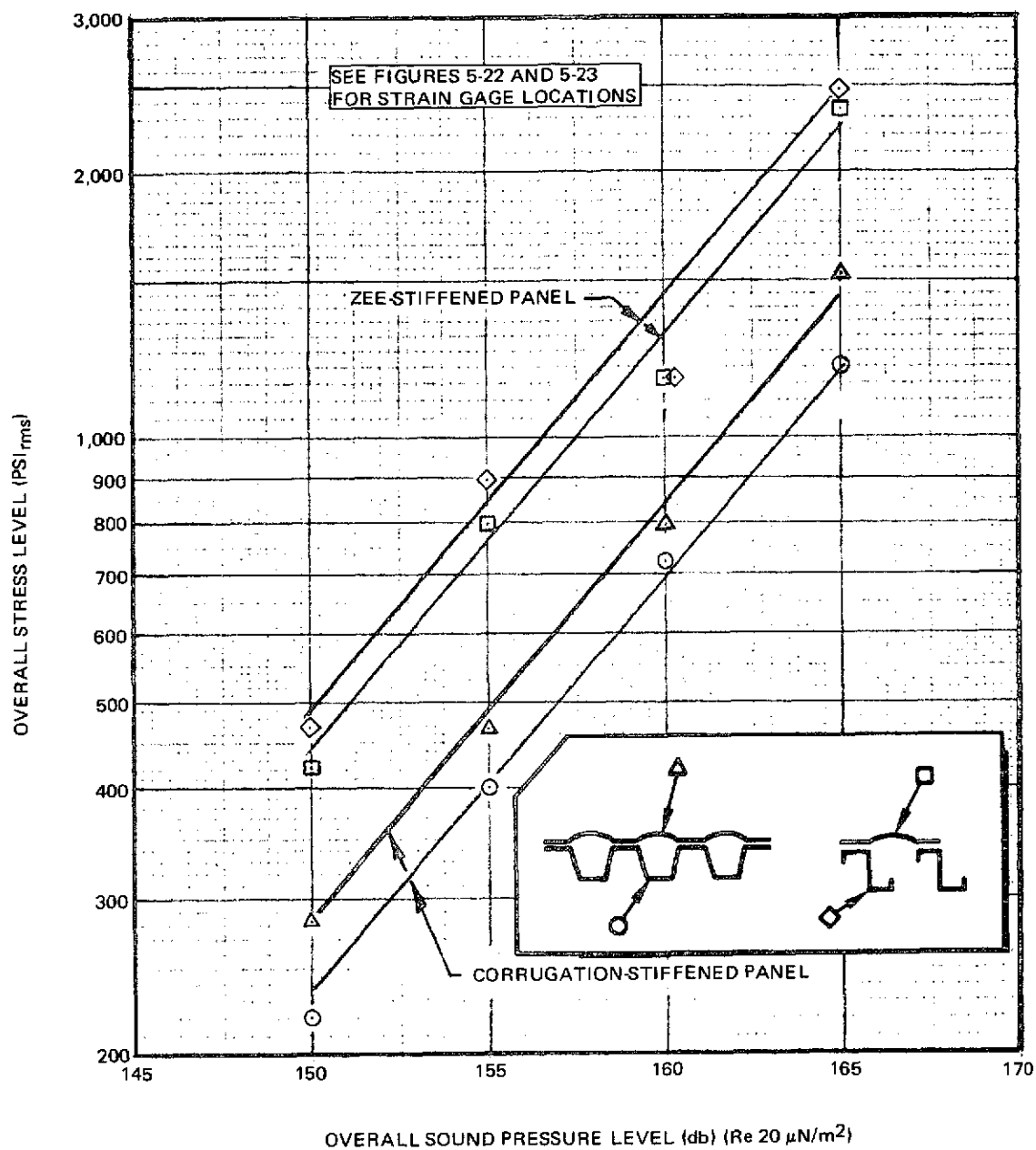
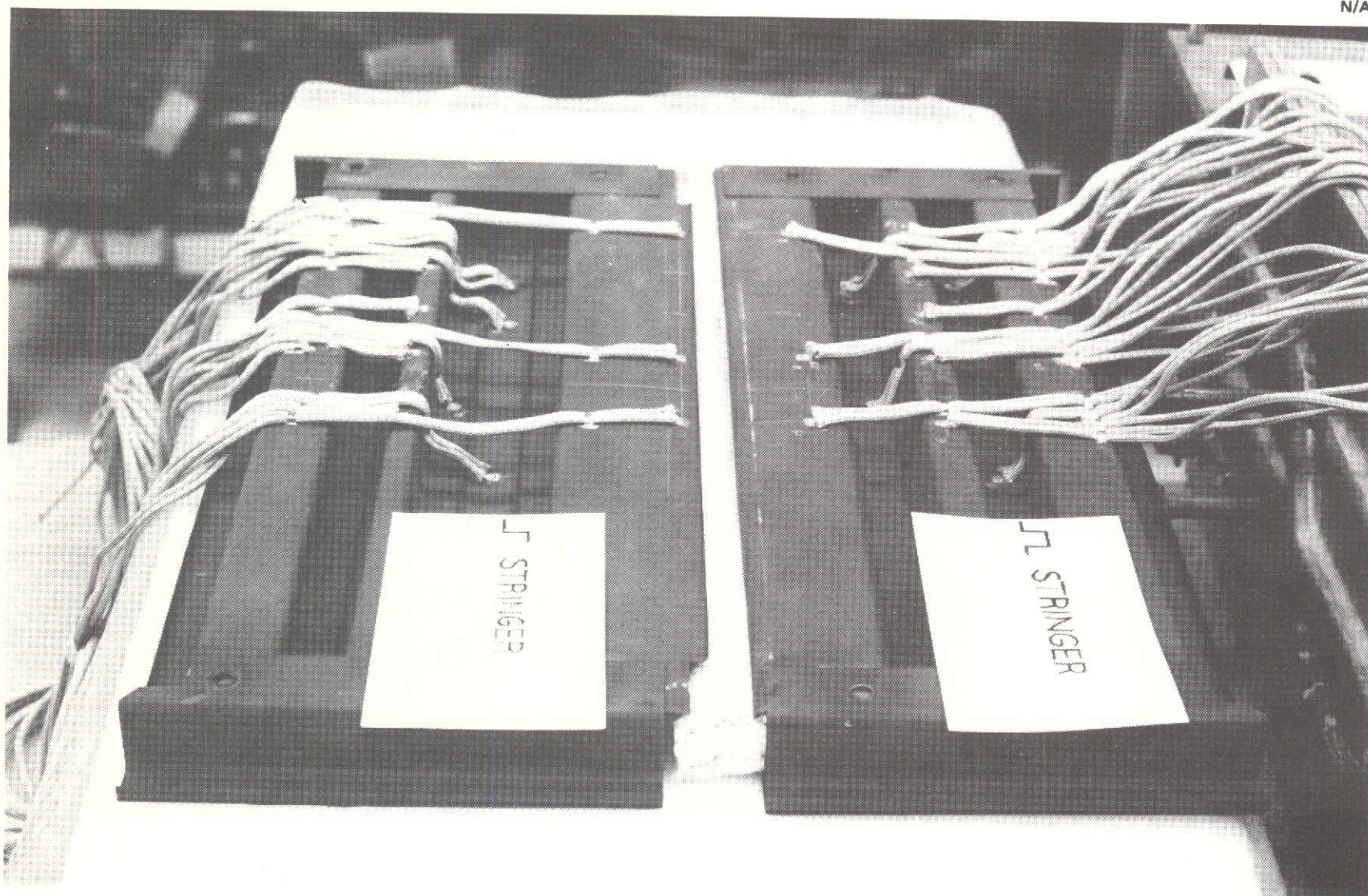Figure 5-30. RMS Stress as a Function of Overall Sound Pressure Level

Figure 5-31. TD Ni-20 Cr Test Panels with Thermocouples Installed
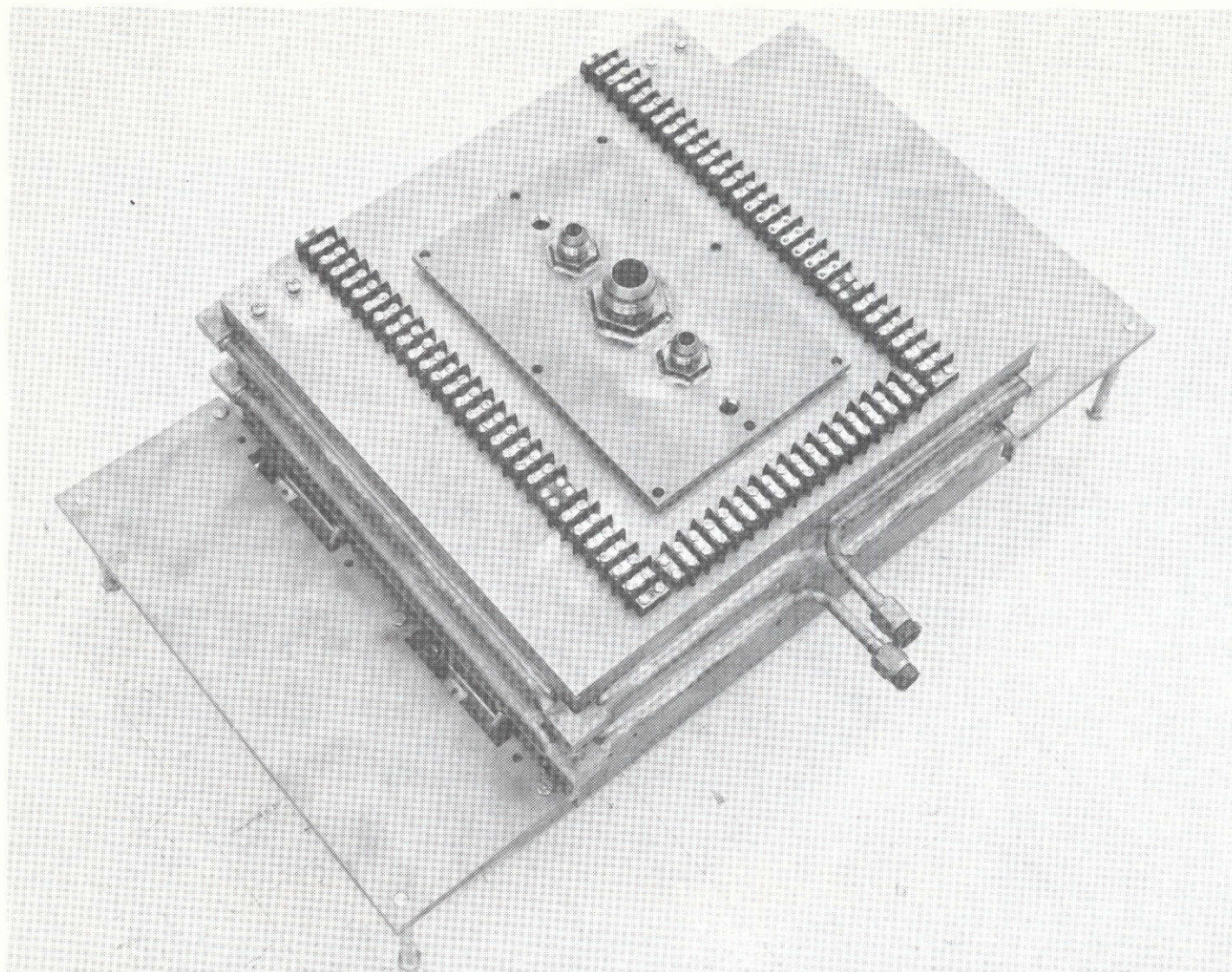
Figure 5-32. Modified Pressure Box

of the panels to measure panel expansion at elevated temperatures. Preliminary thermal cycles were run at several temperature levels up to 1,368°K (2,000°F). Panel expansions appeared normal in the check runs, and testing then proceeded to full load and thermal cycles using the profiles of Figure 5-20.

Twelve cycles were applied to the two panels in the initial set of runs using the Space Simulation Chamber. The panels were then removed and given a detailed visual inspection. As a result of this inspection, a number of hairline cracks were detected. A majority of the cracks were observed around the dimpled holes in the panel face sheets, the cracks progressing radially outward from the edges of the holes. Figure 5-33 shows attach point locations on the outer surfaces of both panels. Typical cracks observed at the end of the first twelve runs are shown in Figure 5-34. Two other hairline cracks were observed along spotweld rows in the zee-stiffened panel as shown in Figure 5-34d. In addition, a slight buckle was observed in one of the face sheet beads on the zee-stiffened panel. An inspection of the internal insulation package showed no deterioration of that portion of the TPS test components.

The cracks appeared to be small enough to permit continuation of programmed test cycles. Consequently, the first acoustic load test was started with a 1-minute exposure of the panels to an overall sound pressure level of 165 db. The programmed level was 160 db, but 165 db was inadvertantly used since the maximum level applied in preliminary tests was 165 db. Examination of the panels after 1 minute at 165 db showed that one of the panel attach screws had pulled through the face sheet hole due to extension of the radial cracks and the severity of the panel vibrations at 165 db. No failure occurred at the edge of the hole where the screw head pulled through, and the edges of the hole were pressed open to permit the screw head to be pulled through to a normal position and then removed. An overall view of the panels is shown in Figure 5-35 and details of several attach points are shown in Figure 5-36. Extension of the cracks is evident when compared to those shown in Figure 5-34. A detailed inspection showed similar extensions of existing cracks at other panel attach positions.

CORRUGATION - STIFFENED PANEL

Z - STIFFENED PANEL
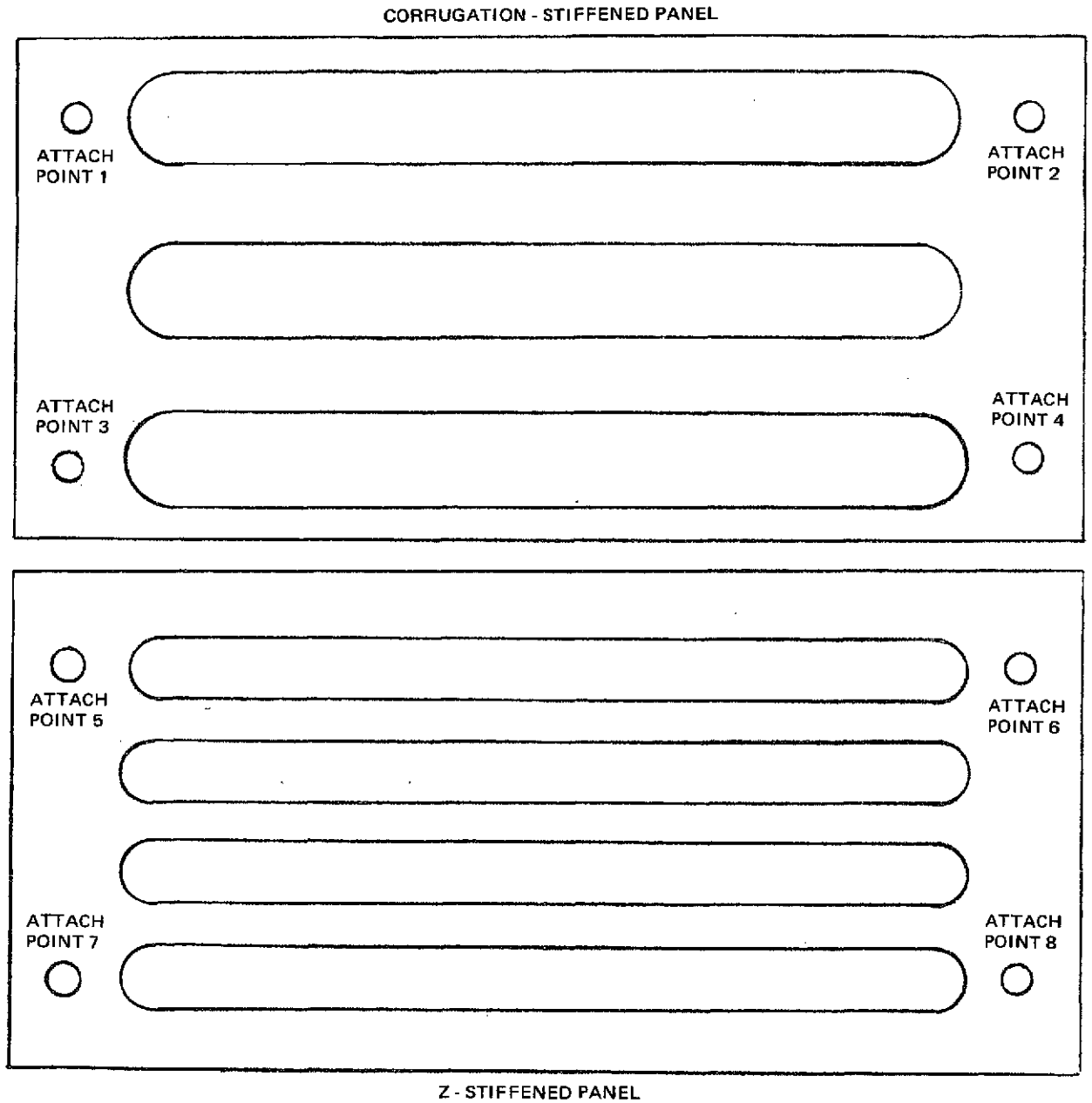
Figure 5-33.   Full-Scale Subsize Panel Attach Locations
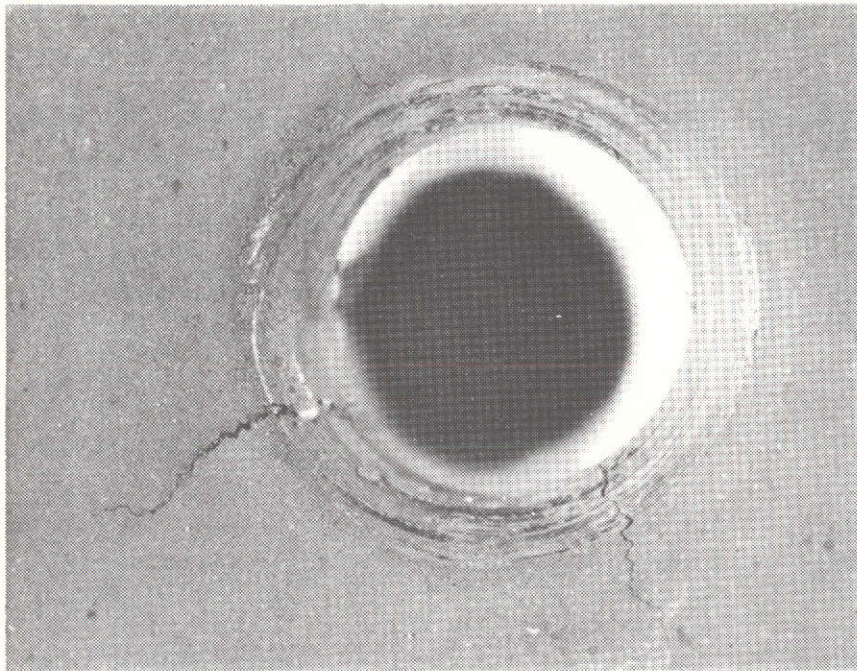
a. ATTACH POINT NO. 1   5X
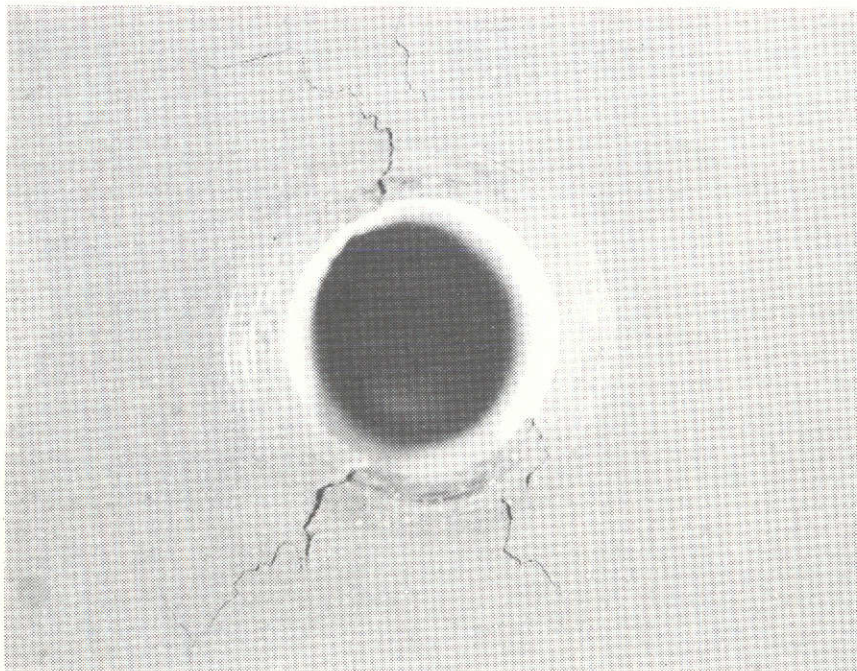
b. ATTACH POINT NO. 3   5X

Figure 5-34. Typical Cracks Observed at End of Twelfth Thermal/Load Cycle (Page 1 of 2)
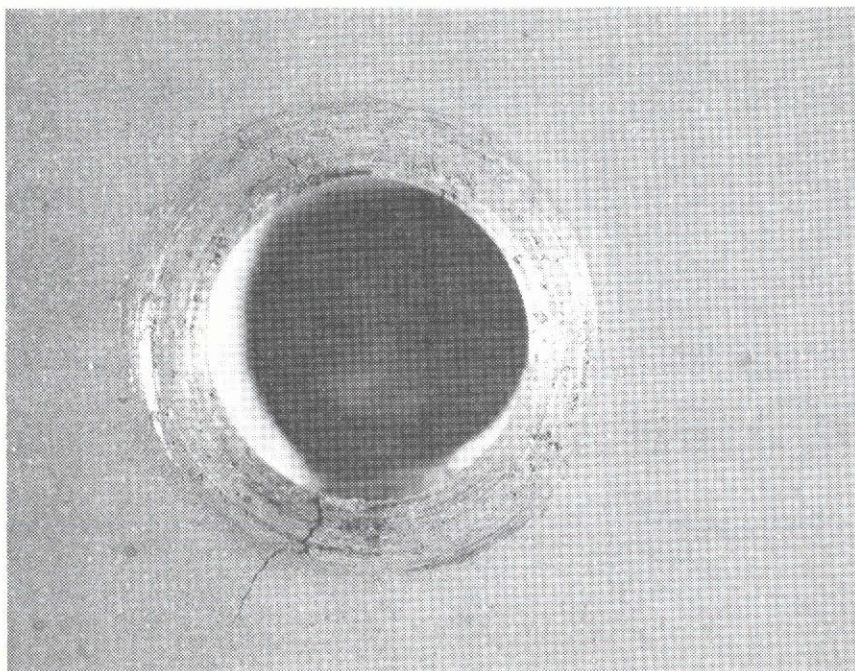
c. ATTACH POINT NO. 5   5X

d. SPOTWELDS NEAR ATTACH POINT 8   3X

Figure 5-34. (Page 2 of 2)
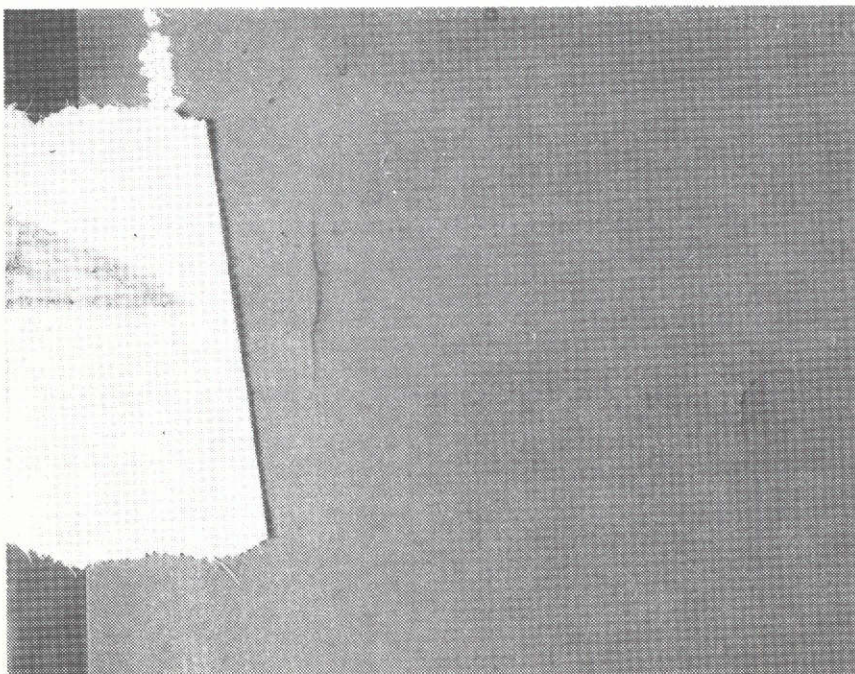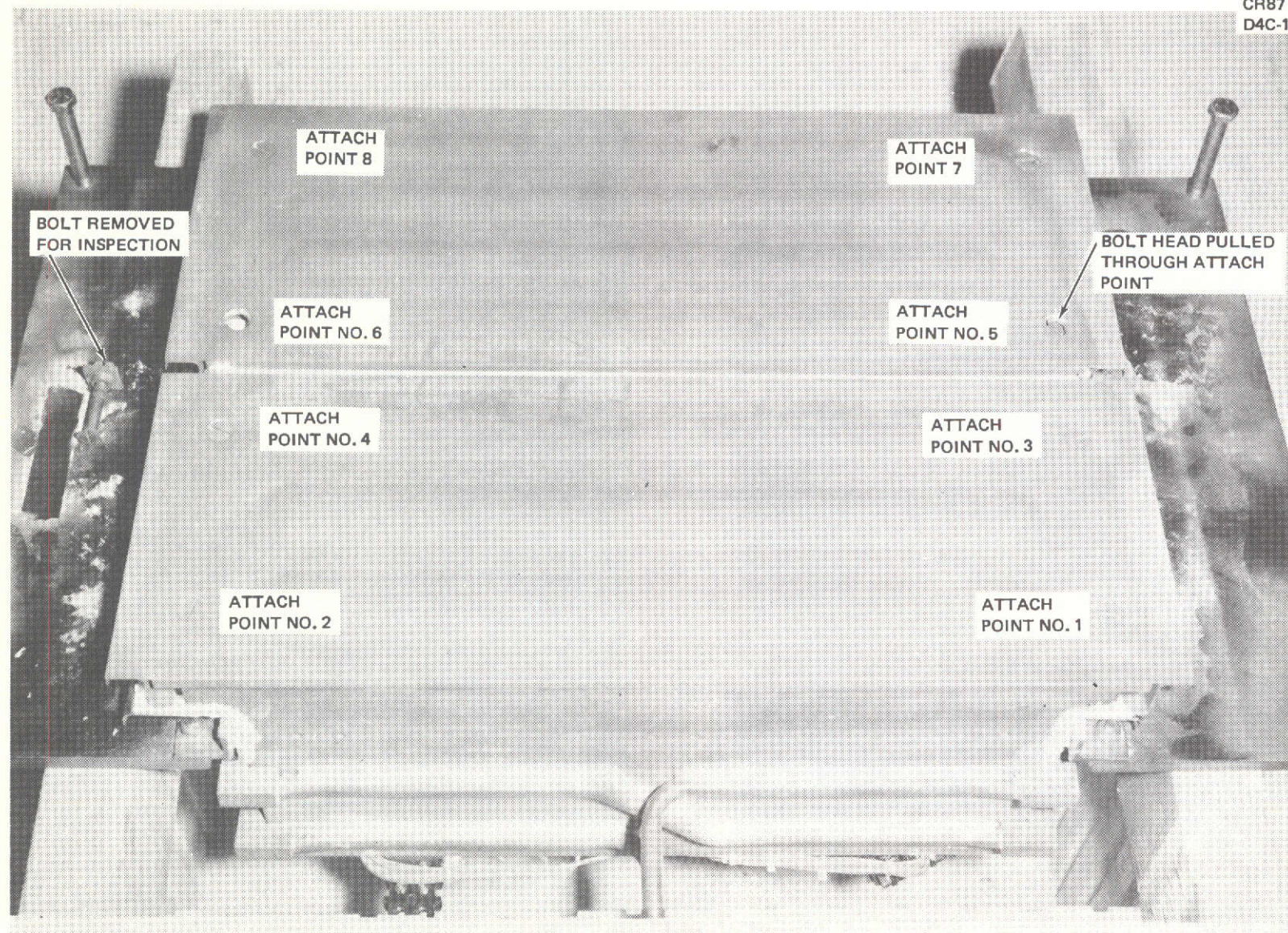
Figure 5-35. Overall View of Test Panels After Acoustic Exposure at 165 db
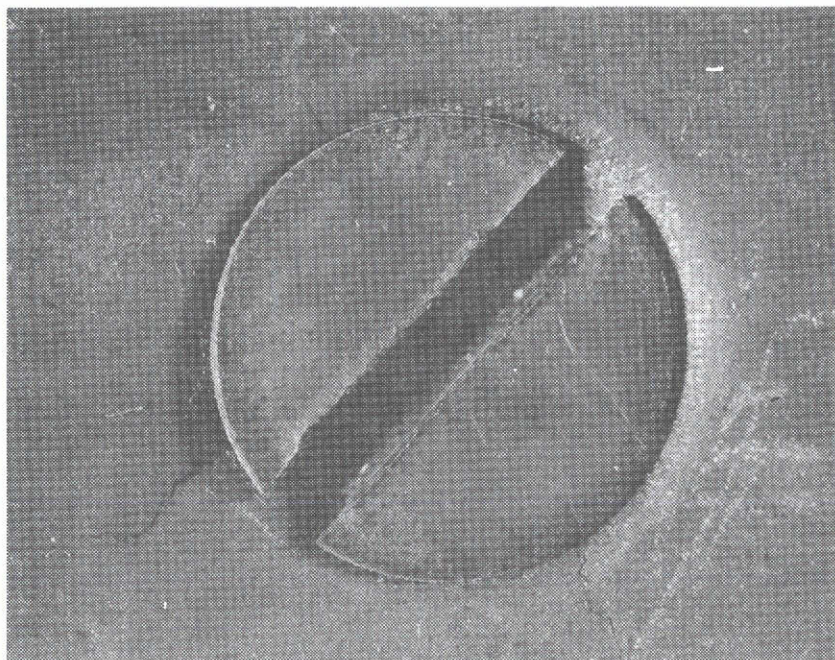
a. ATTACH POINT NO. 1   5X
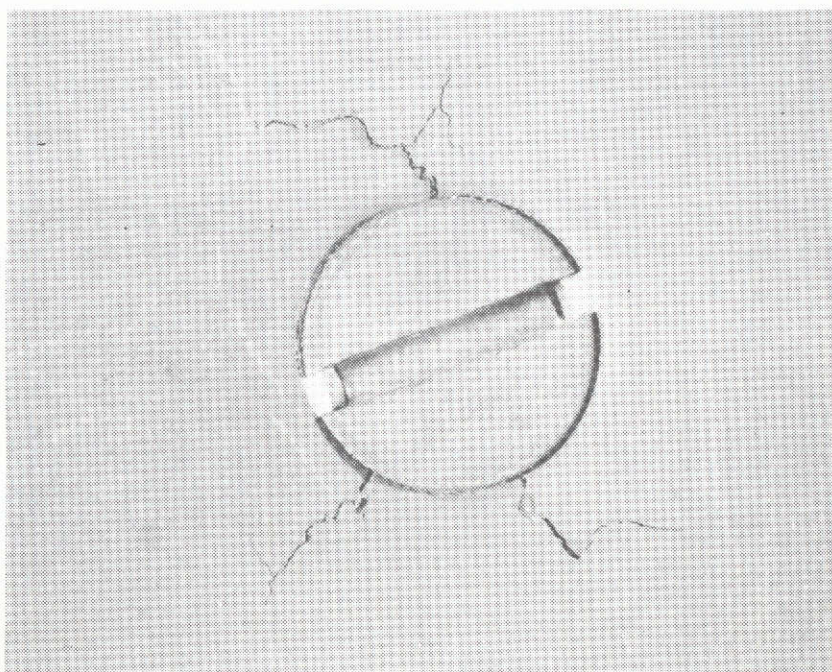
b. ATTACH POINT NO. 3   4X

Figure 5-36. Panel Face Sheet Cracks After Initial Acoustic Exposure at 165 db (Page 1 of 2)

c. ATTACH POINT NO. 5   4X

d. SPOTWELDS NEAR ATTACH POINT 8   3X

Figure 5-36. (Page 2 of 2)

Reinforcement of the holes was necessary to continue through the test series. Despite the cracks in the attach positions, the panels were judged to be capable of sustaining additional testing if the holes in the face sheets were reinforced. Reinforcing washers made from 0.0457-cm (0.018-in.) thick TD Ni-20Cr sheet were added under the head of each screw, the size of each washer being approximately 2.54 by 2.54 cm (1.0 by 1.0 in.). With the reinforcing washers in place, the instrumentation was replaced where necessary and cyclic load and thermal testing was resumed.

During removal of the panels after the twelfth cycle, seizing of two of the fasteners occurred. One fastener was subsequently freed without damage to threads on either the nut or bolt, but the second fastener was damaged beyond use and required replacement before proceeding with additional tests.

Inspection of the screws and nuts showed that fine particles of the fibrous insulation material used for a pressure seal had fallen into the thread engagement area. The insulation particles, combined with some oxide particles from the fasteners, caused the fasteners to seize during the first 12 test cycles. In subsequent tests, care was taken to ensure that all threads were cleaned prior to attaching the panels in place and that the threads were properly coated with antiseize material.

An additional 63 load and thermal cycles were applied before the panels were again removed for inspection. Thus, with a total of 75 cycles, the panels were inspected before applying acoustic load equivalent to 75 simulated boost flights. Crack extensions did not appear beyond the edge of the reinforcing washers except at attach point one. The growth at attach point one, shown in Figure 5-37, extended to the edge of the panel. Despite this extension, the panel was judged to be capable of sustaining additional tests, and acoustic tests at 160 db OASPL were conducted. The acoustic exposure at this point consisted of 36.5 minutes at 160 db, bringing the total acoustic exposure time to 37.5 minutes. With 30 seconds being equivalent to one lift-off exposure, 75 cycles of acoustic exposures had been applied at that point.

a. ATTACH POINT NO. 1   1.5X
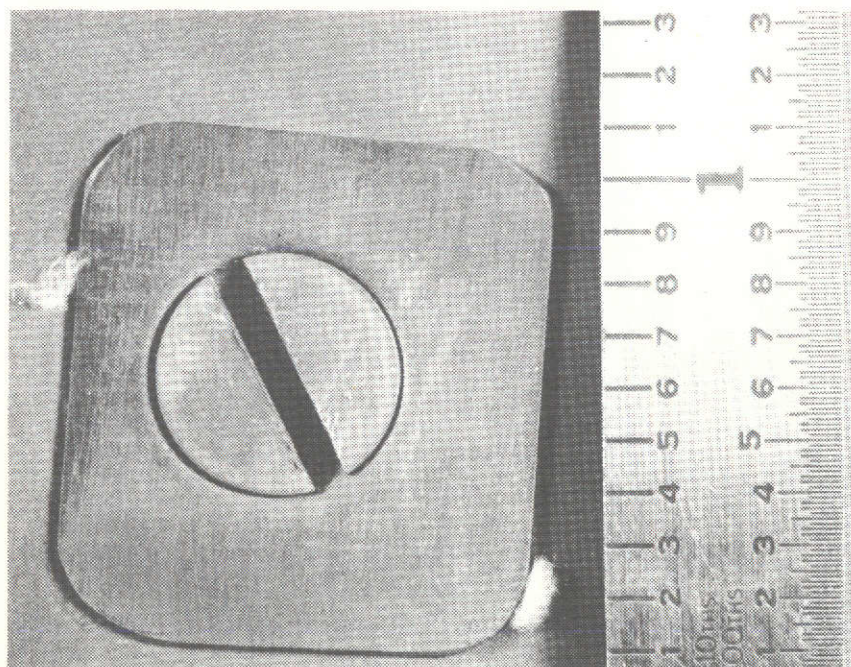
b. ATTACH POINT NO. 3   2.5X

Figure 5-37. Panel Face Sheet Cracks After 75th Thermal/Load Cycle (Page 1 of 2)

c. ATTACH POINT NO.5   2.3X
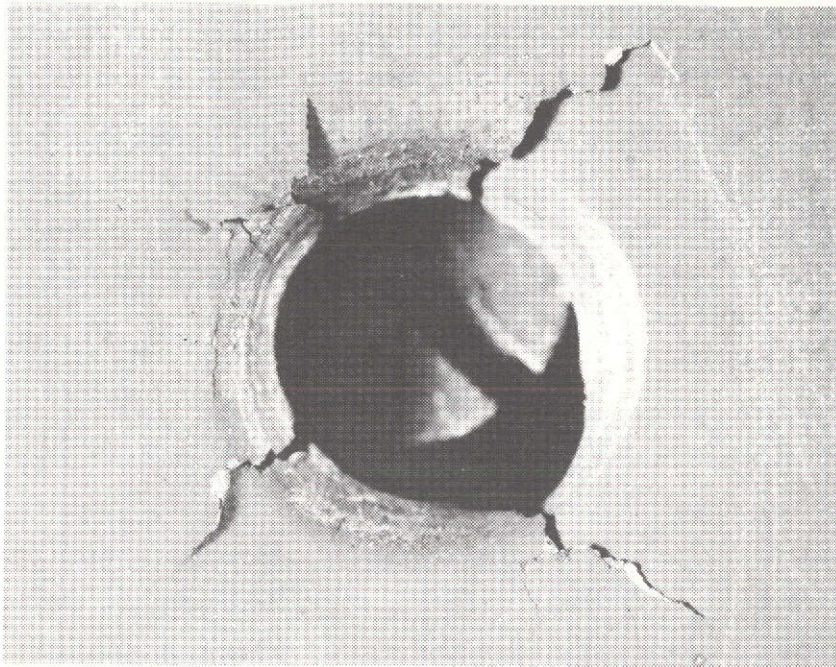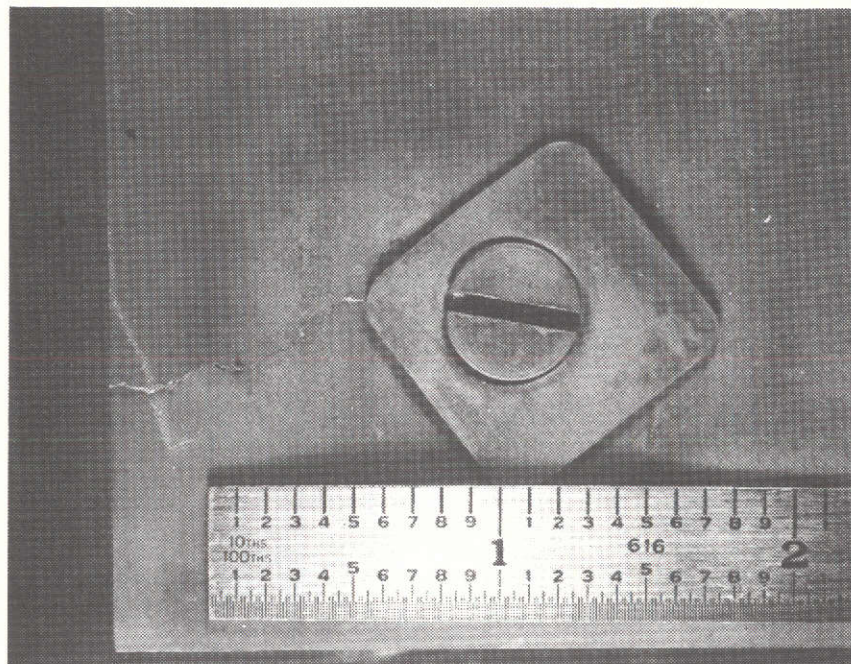

d. SPOTWELD ROW NEAR ATTACH POINT 8   2.5X

Figure 5-37. (Page 2 of 2)

The acoustic exposures were followed by another 14 load and thermal cycles and an additional 7 minutes of acoustic exposure to bring the total simulated cycles to 89. The panels were remov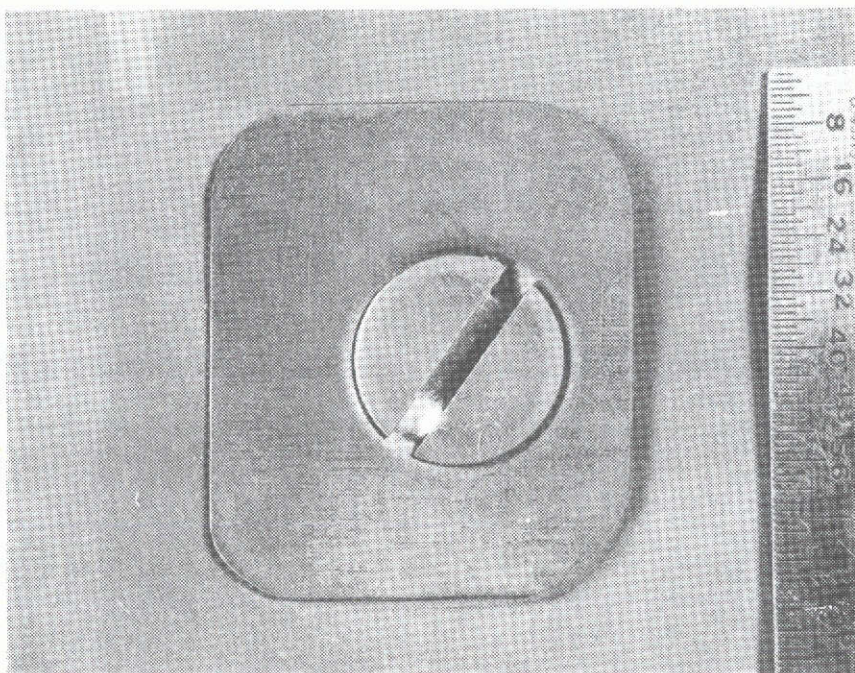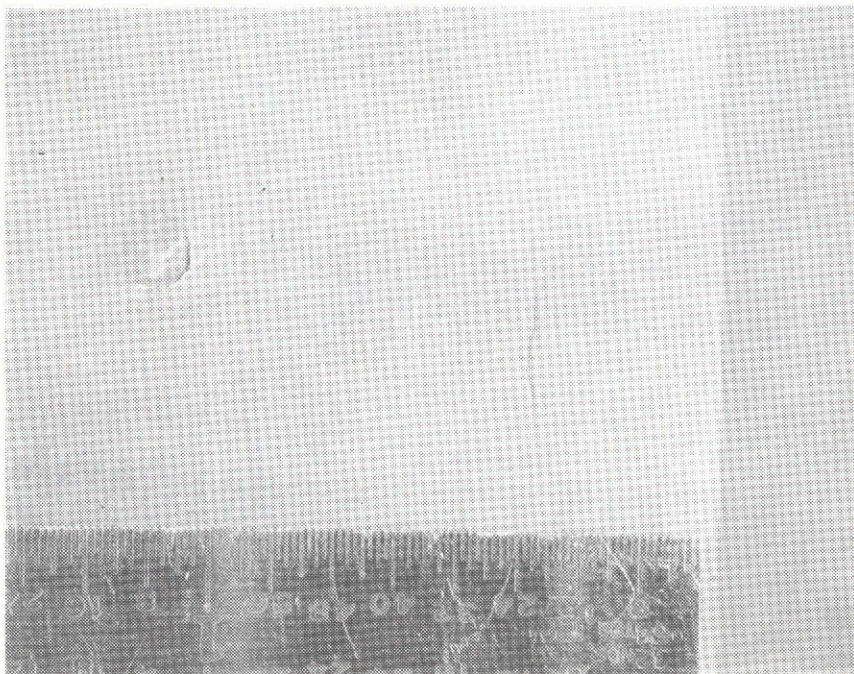ed from the pressure box at that time to permit inspection and to allow replacement and repair of thermocouples where necessary. The appearance of the panels was similar to that seen at the inspection after the 12th cycle. Slight additional growth of the cracks in the panel edge members was noted, but the general condition of the panels was the same as noted after 12 thermal cycles plus the initial 1-minute acoustic exposure at 165 db.

After repair of the instrumentation, the panels were reinstalled on the test fixture and subjected to the final 11 thermal and load cycles plus the additional 5.5 minutes of acoustic loading required to simulate 100 mission cycles.

At the end of the full 100 cycles, a visual inspection was made at the Space Simulation Laboratory before shipment of the components to the Huntington Beach facility. This inspection showed the panels to be in the same condition as noted at the previous inspection after 89 cycles. Post-test photographs of the heat shields and insulation are shown in Figures 5-38 through 5-40 after completion of the full 100 test cycles. Figure 5-38 shows the heat shields after removal of the fasteners and reinforcing washers. The increased cracking and damage at the attach points is evident, particularly at attach point 5 on the zee-stiffened panel (see Figure 5-35). An edge view of the corrugation-stiffened panel is shown in Figure 5-39 while the panels were still attached to the fixture. This view shows the relative overall flatness maintained by the panels even though the 0.0254-cm (0.010-in.) face sheet exhibited a small amount of waviness along its edge. Figure 5-40 shows the insulation package at the termination of 100 test cycles. Permanent set of the outer face of the 0.0127-cm (0.005-in.) foil used for packaging the low-density insulation occurred as shown in Figure 5-40.

Data recorded in each thermal and load cycle included time-histories of the differential pressure applied to the panels; chamber pressure, temperature at each thermocouple location, and deflections at the four deflection trans-ducers. Typical data are shown in Figures 5-41 through 5-44 for test run 41. Panel differential pressure and chamber pressure are shown in
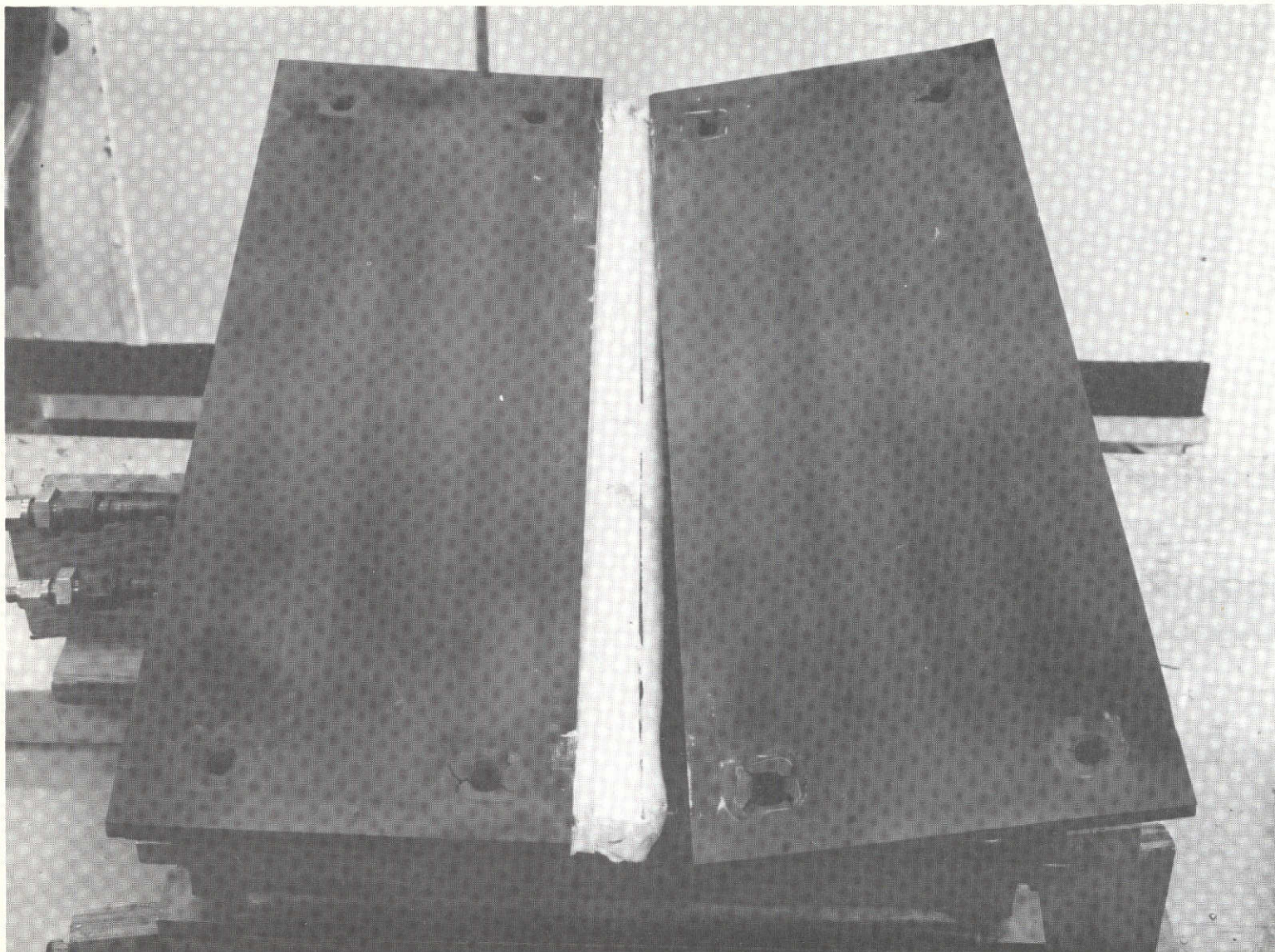
Figure 5-38. Full-Scale Subsize Heat Shields After 100 Test Cycles
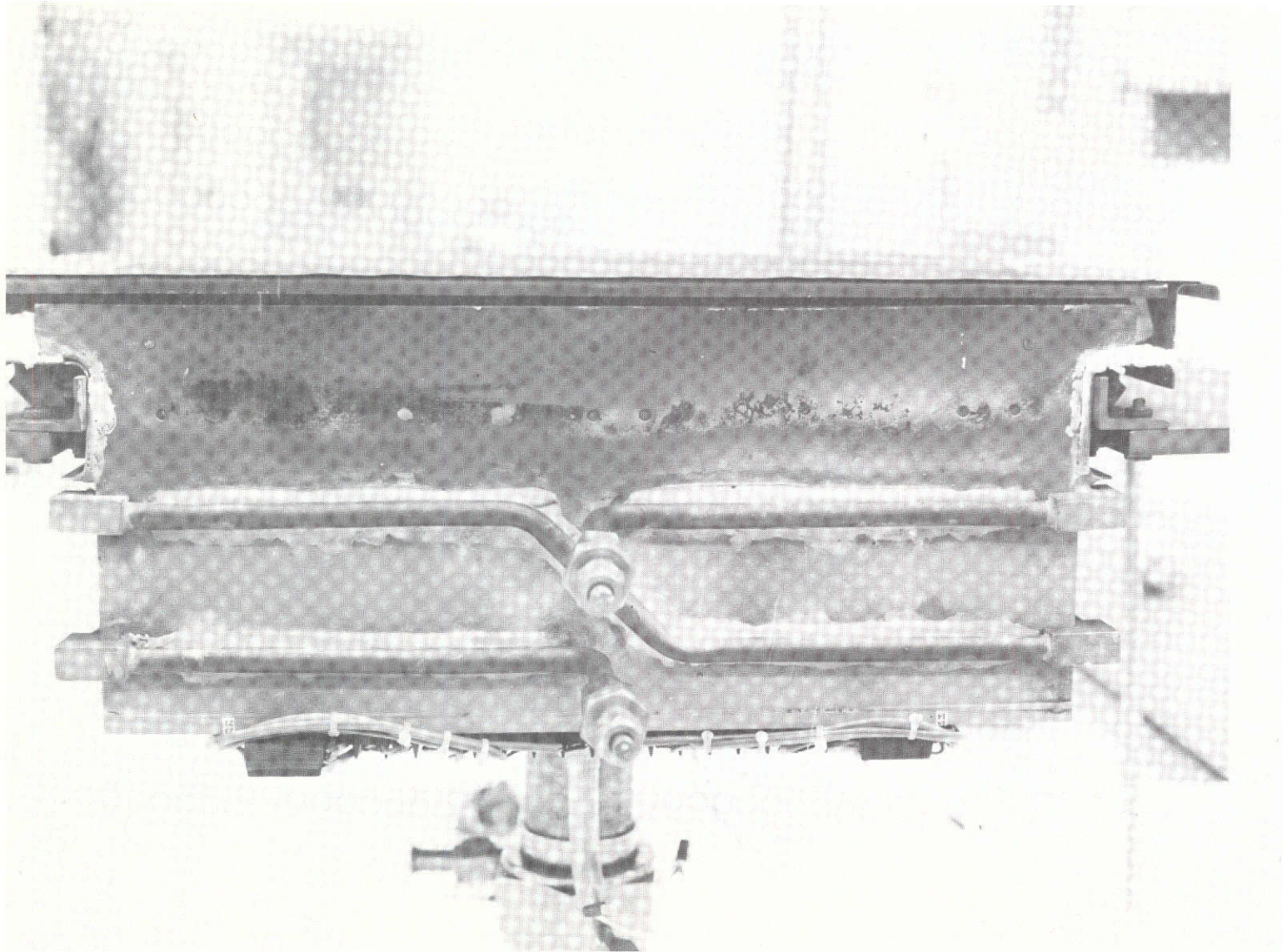
Figure 5-39. Edge View of Panels After 100 Test Cycles
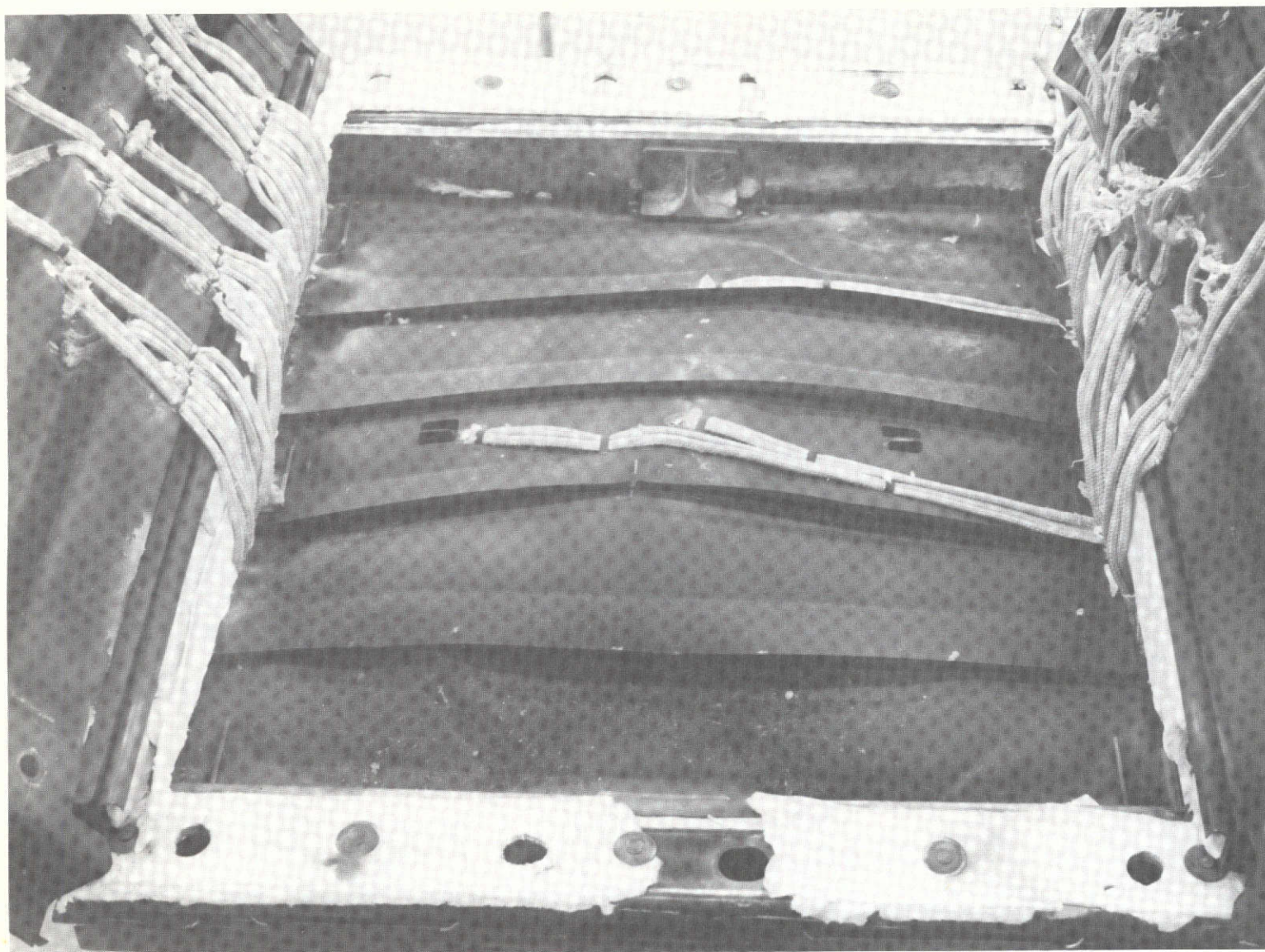
Figure 5-40. Insulation Package at Completion of 100 Test Cycles
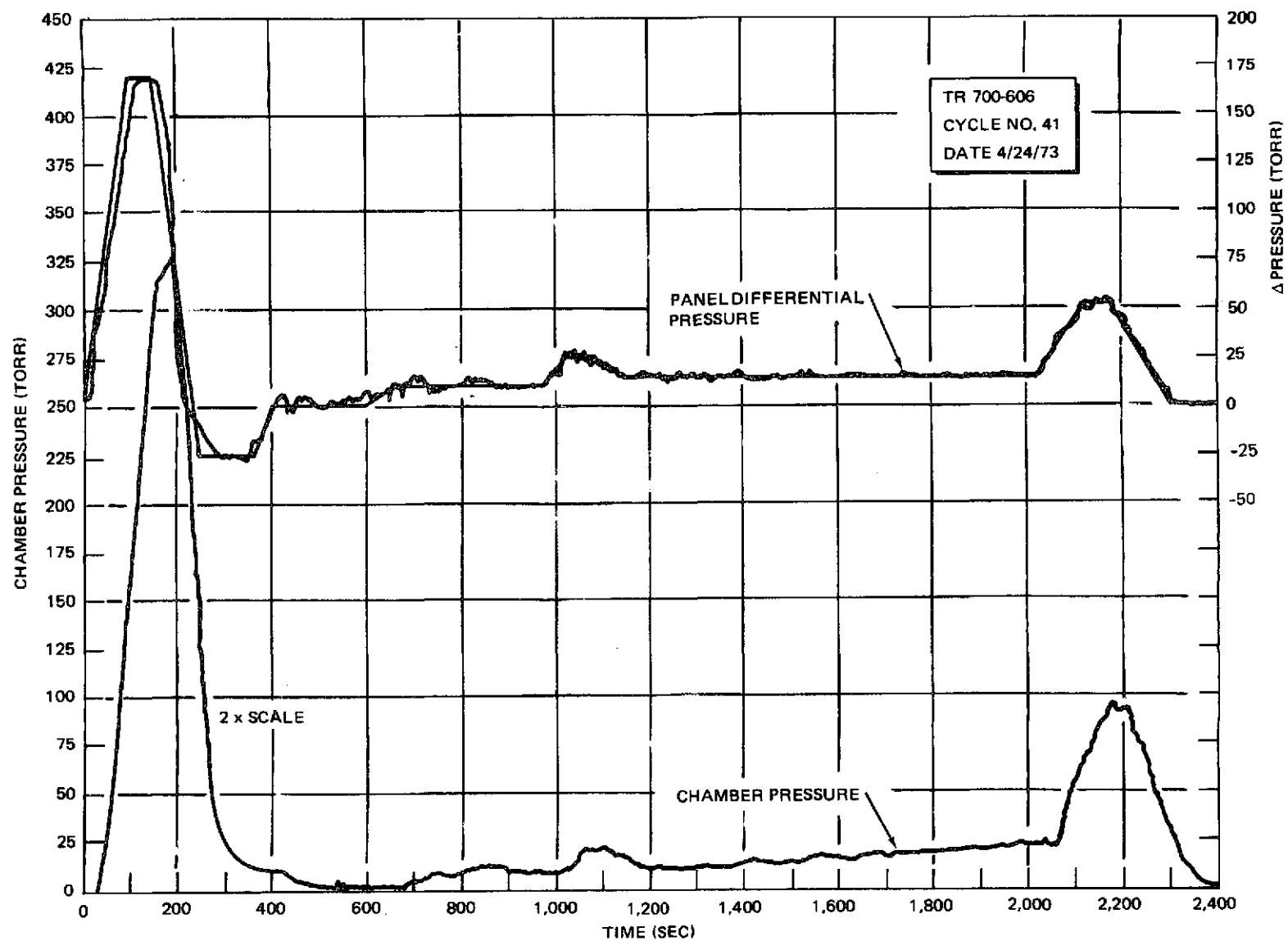
Figure 5-41. Panel Differential Pressure and Chamber Pressure, Run 41
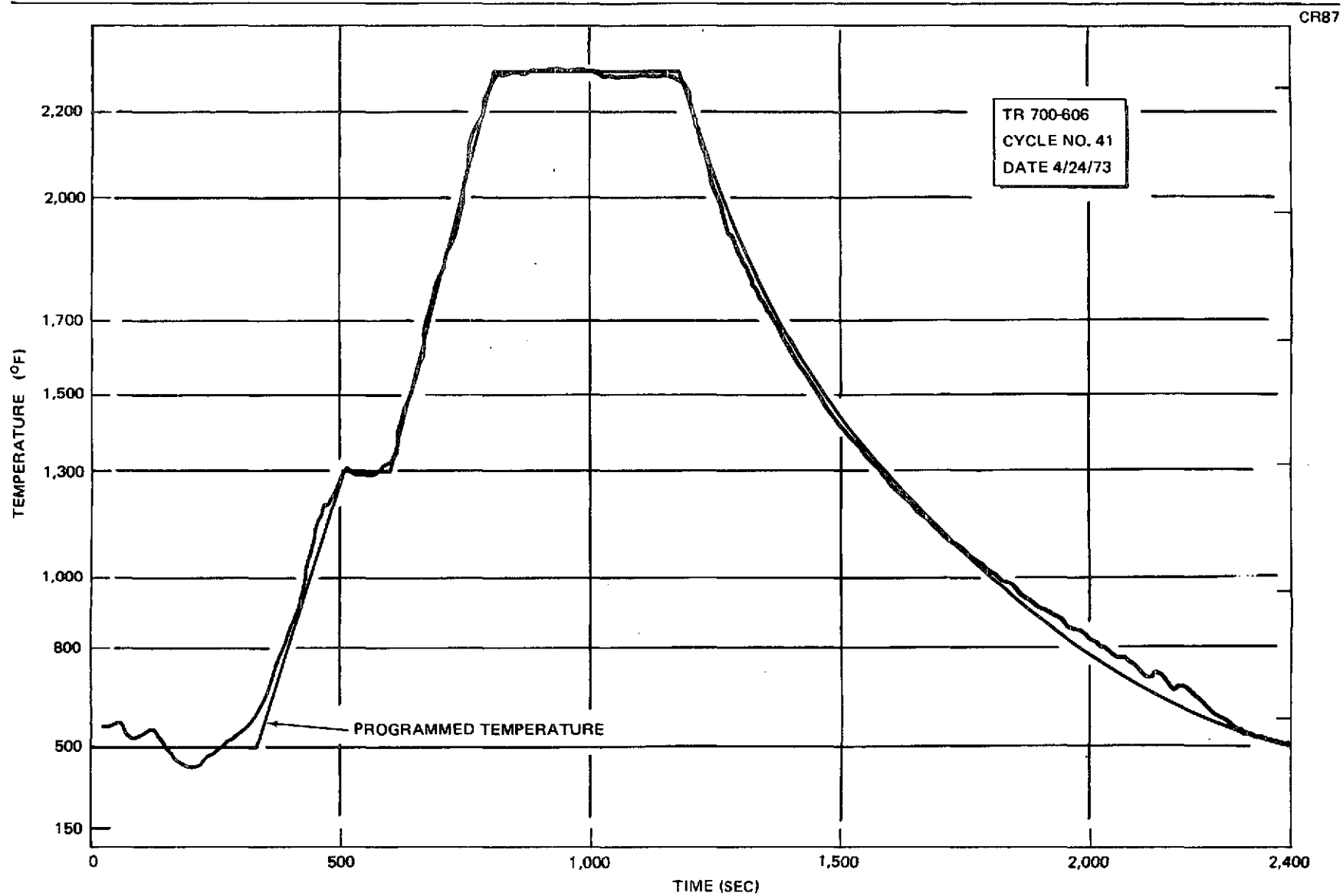
Figure 5-42. Susceptor Plate Temperature, Run 41

CR87
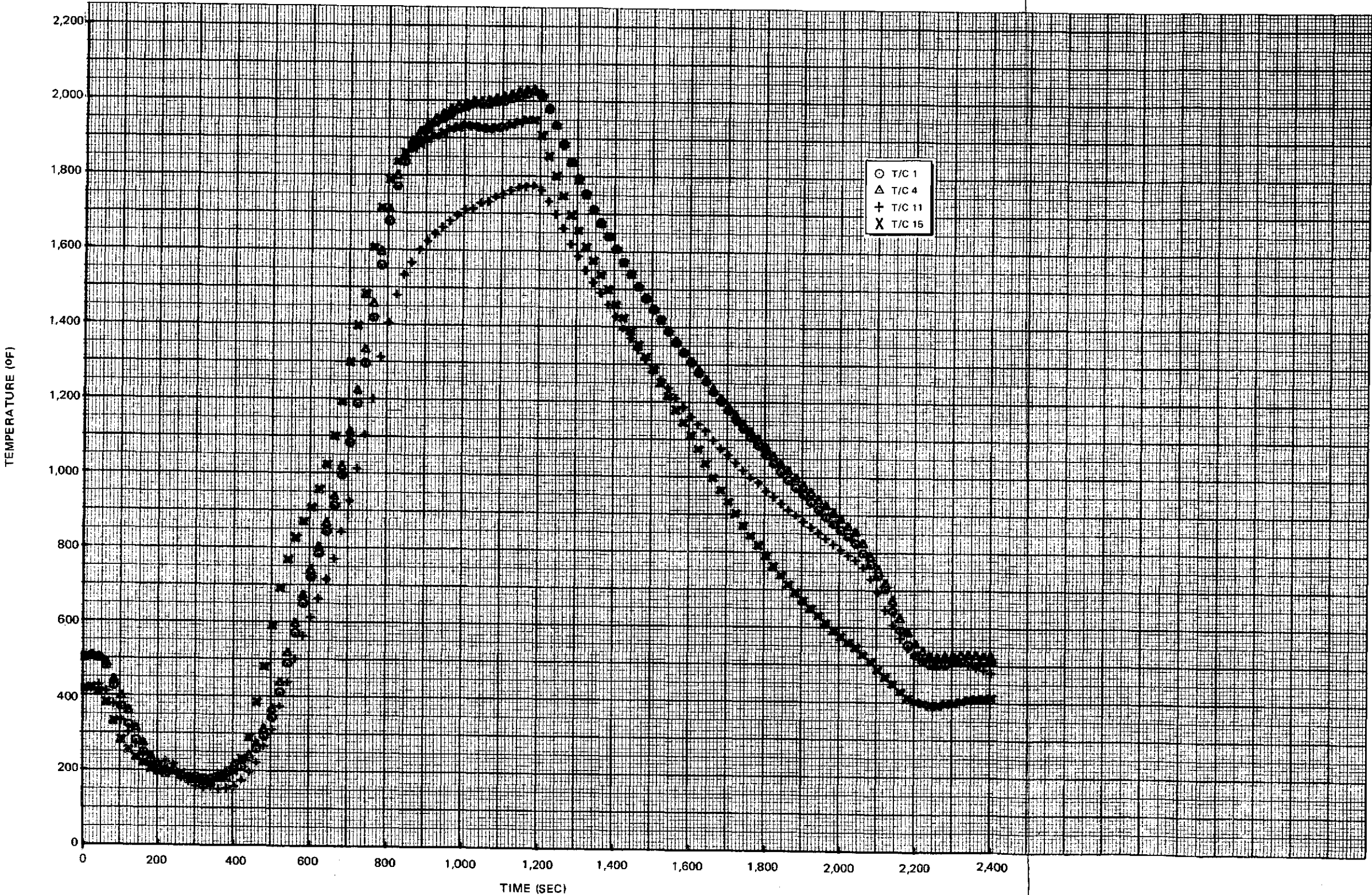
Figure 5-43. Thermocouple Recordings, Run 41 (Page 1 of 7)

CR87
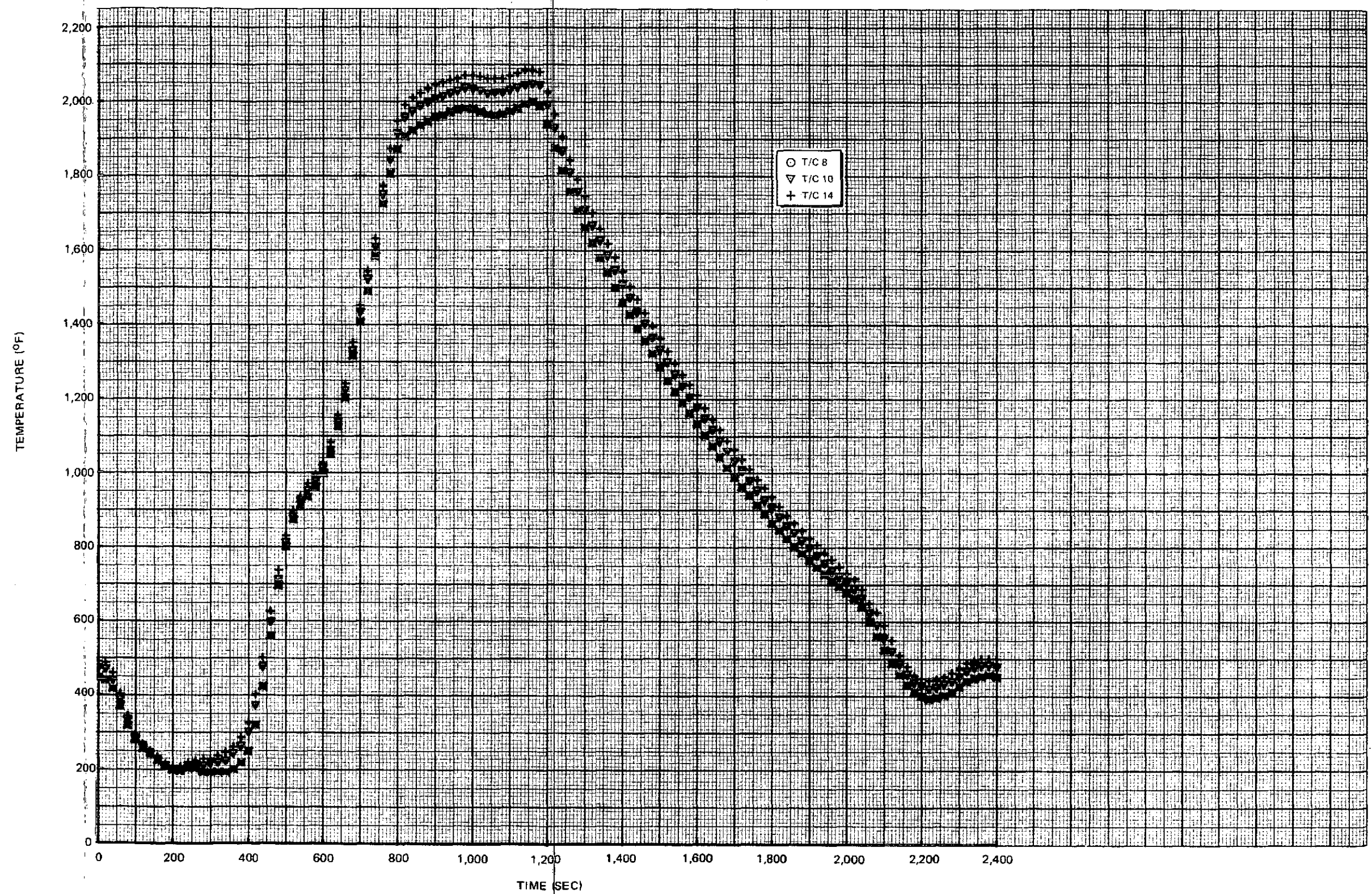
Figure 5-43. Thermocouple Recordings, Run 41 (Page 2 of 7)
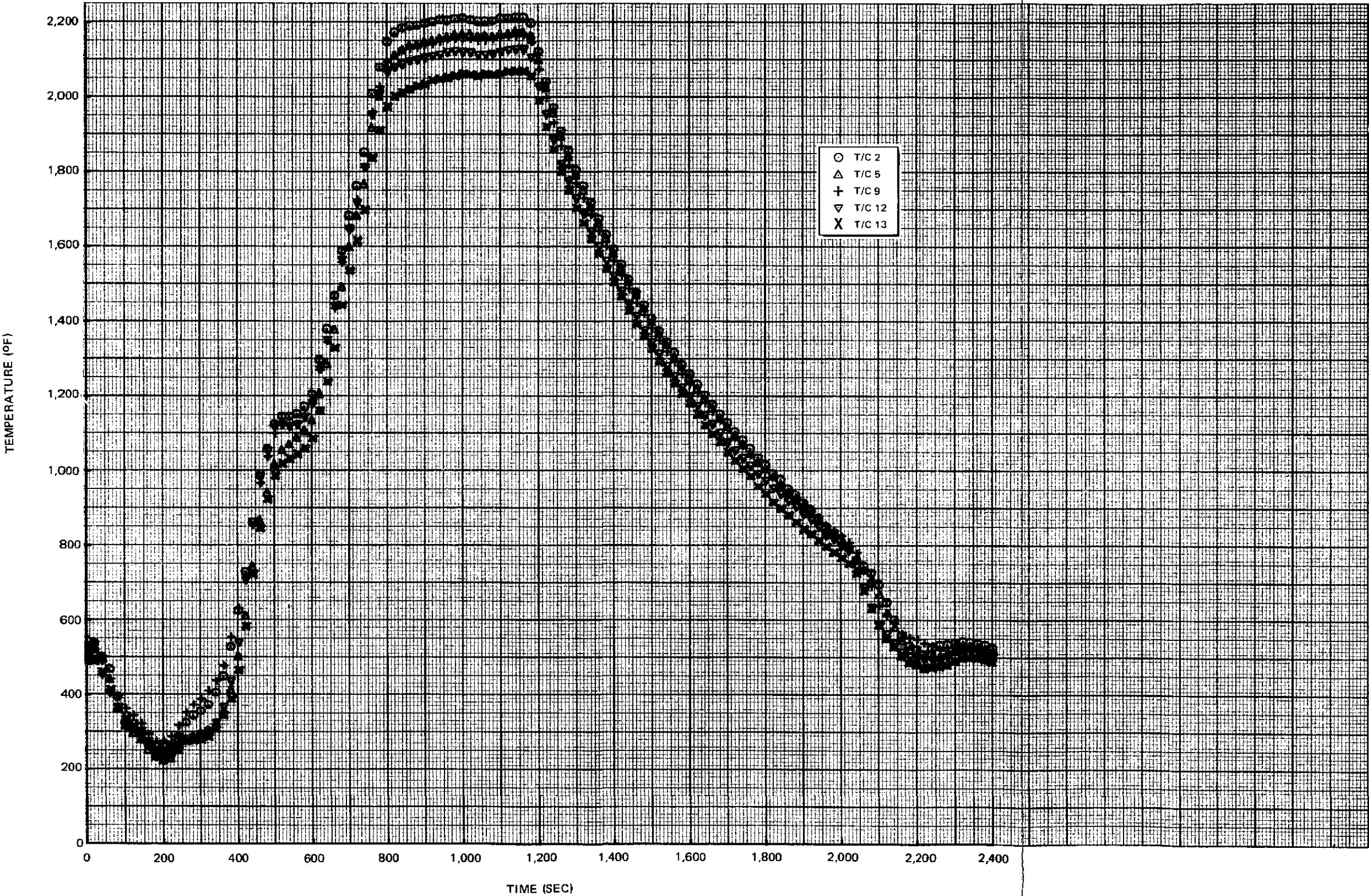
Figure 5-43. Thermocouple Recordings, Run 41 (Page 3 of 7)

119

CR87
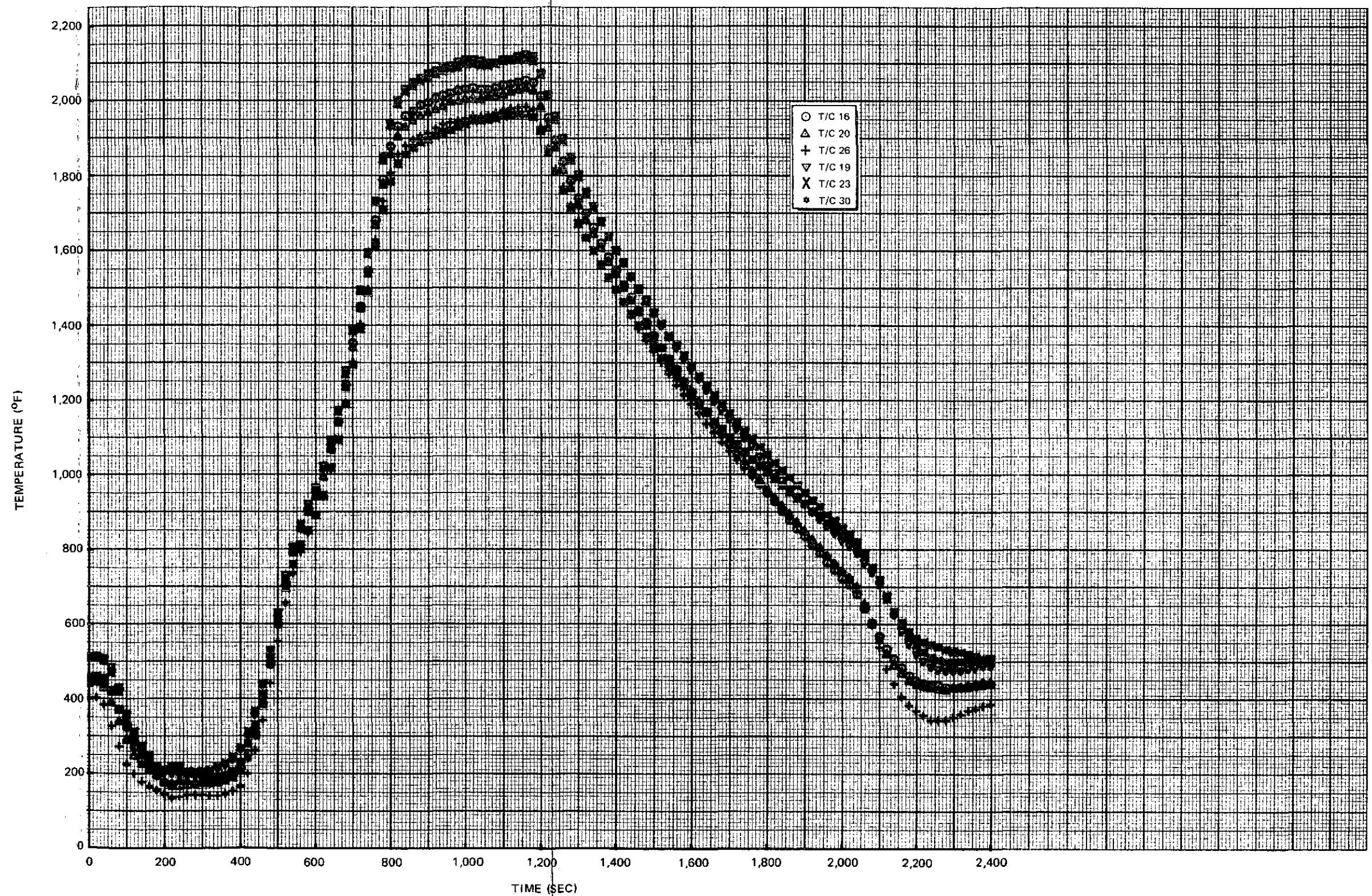
Figure 5-43. Thermocouple Recordings, Run 41 (Page 4 of 7)
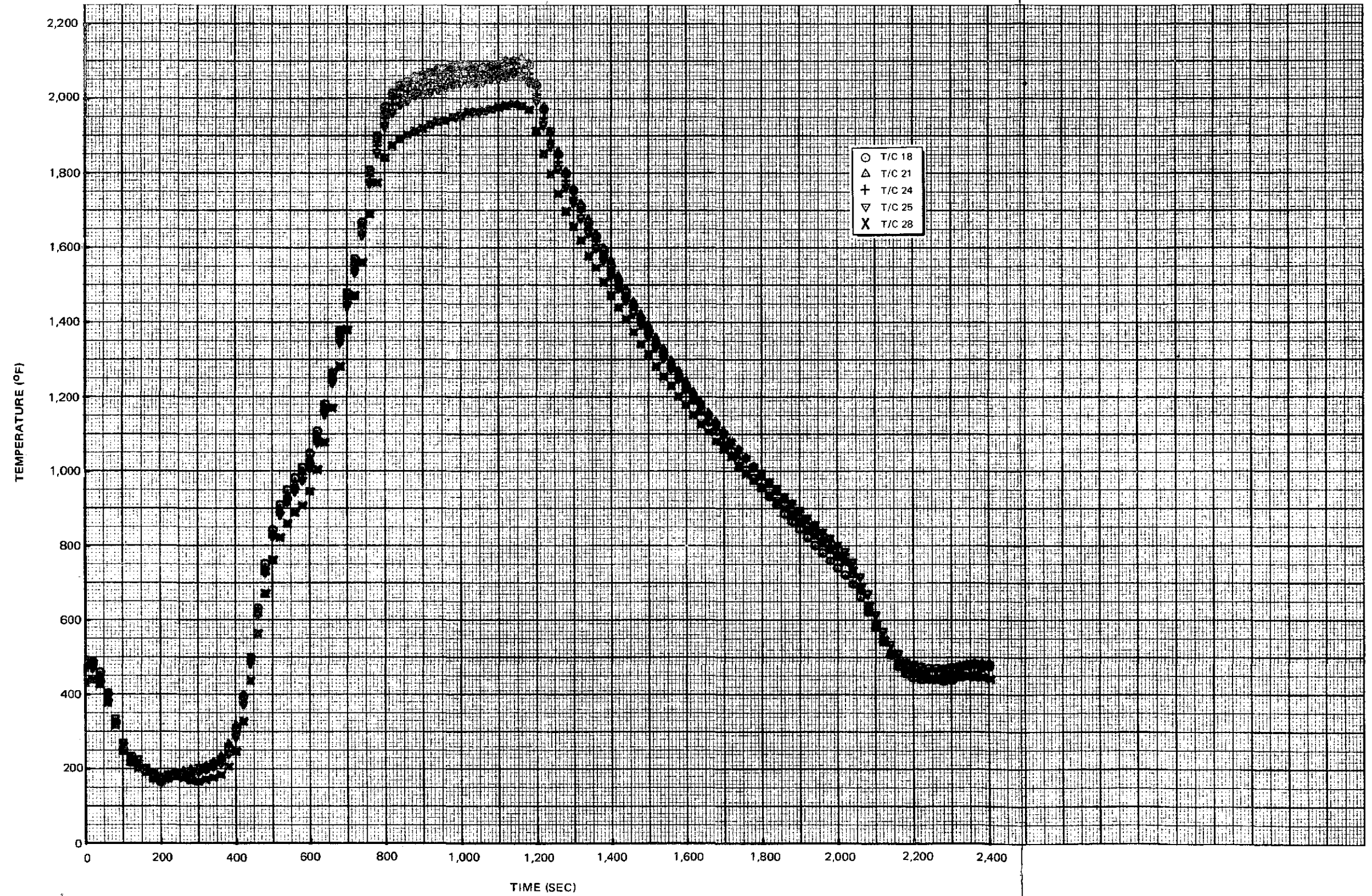
Figure 5-43. Thermocouple Recordings, Run 41 (Page 5 of 7)
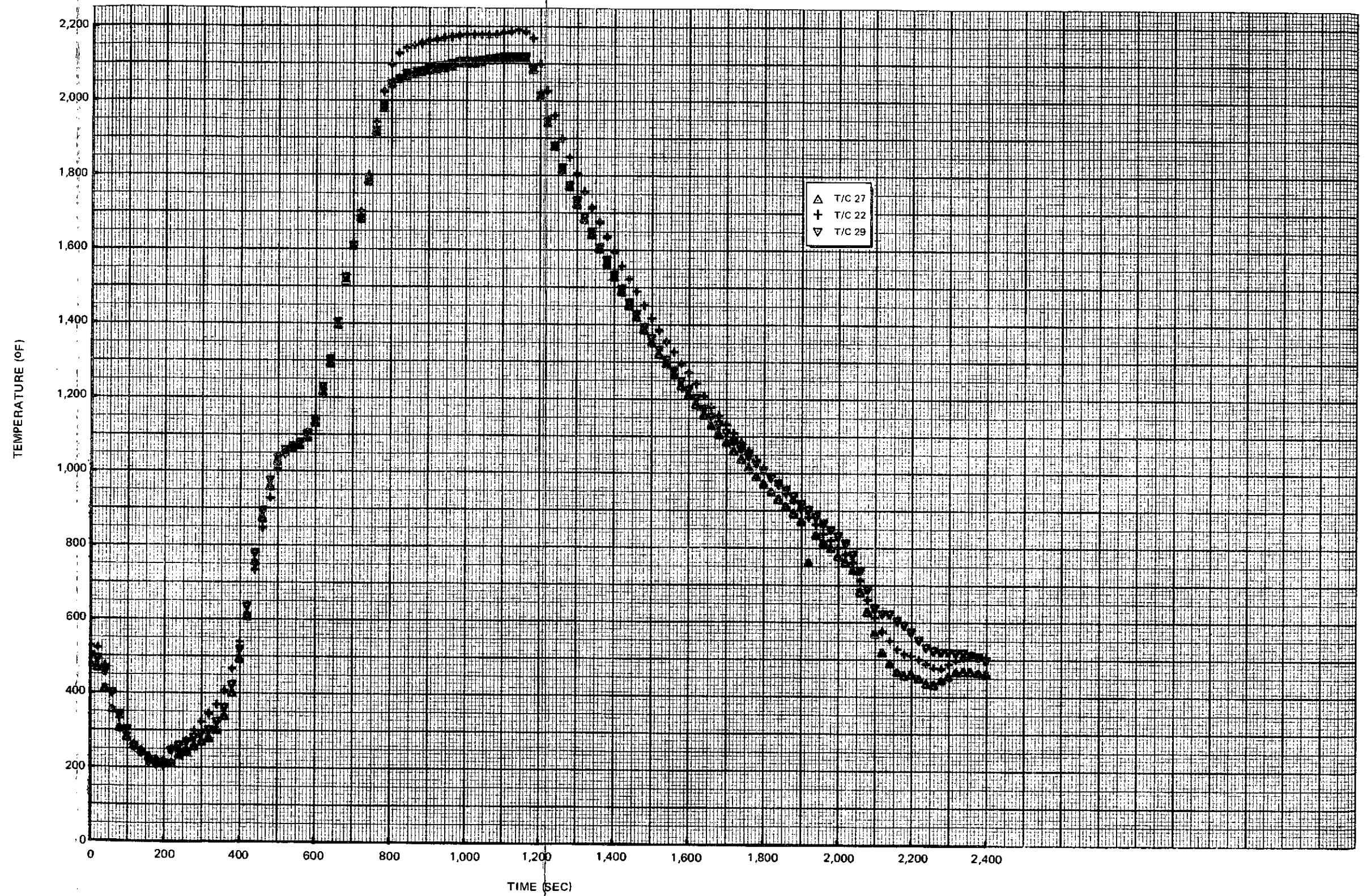
Figure 5-43. Thermocouple Recordings, Run 41 (Page 6 of 7)
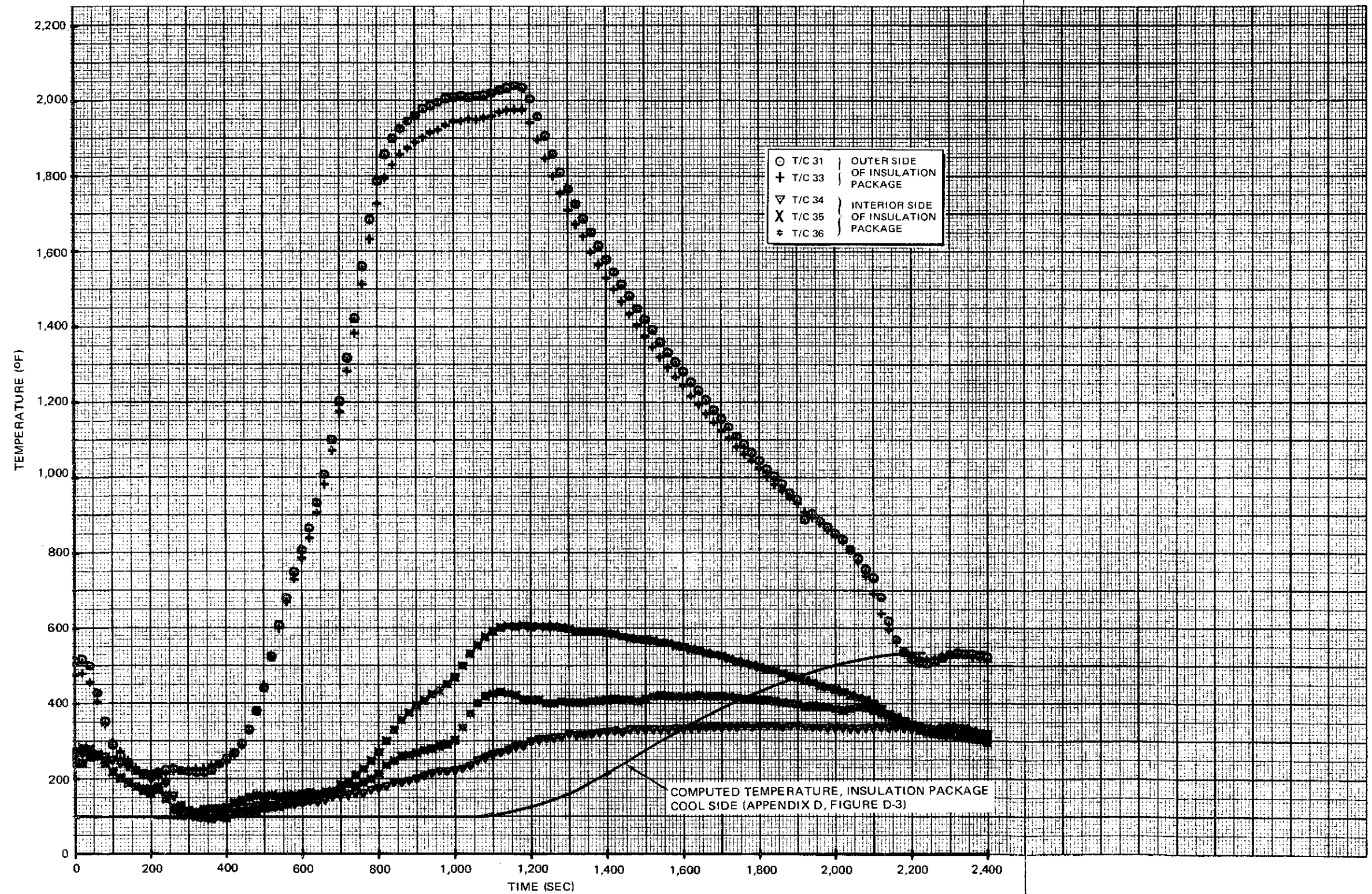
Figure 5-43. Thermocouple Recordings, Run 41 (Page 7 of 7)
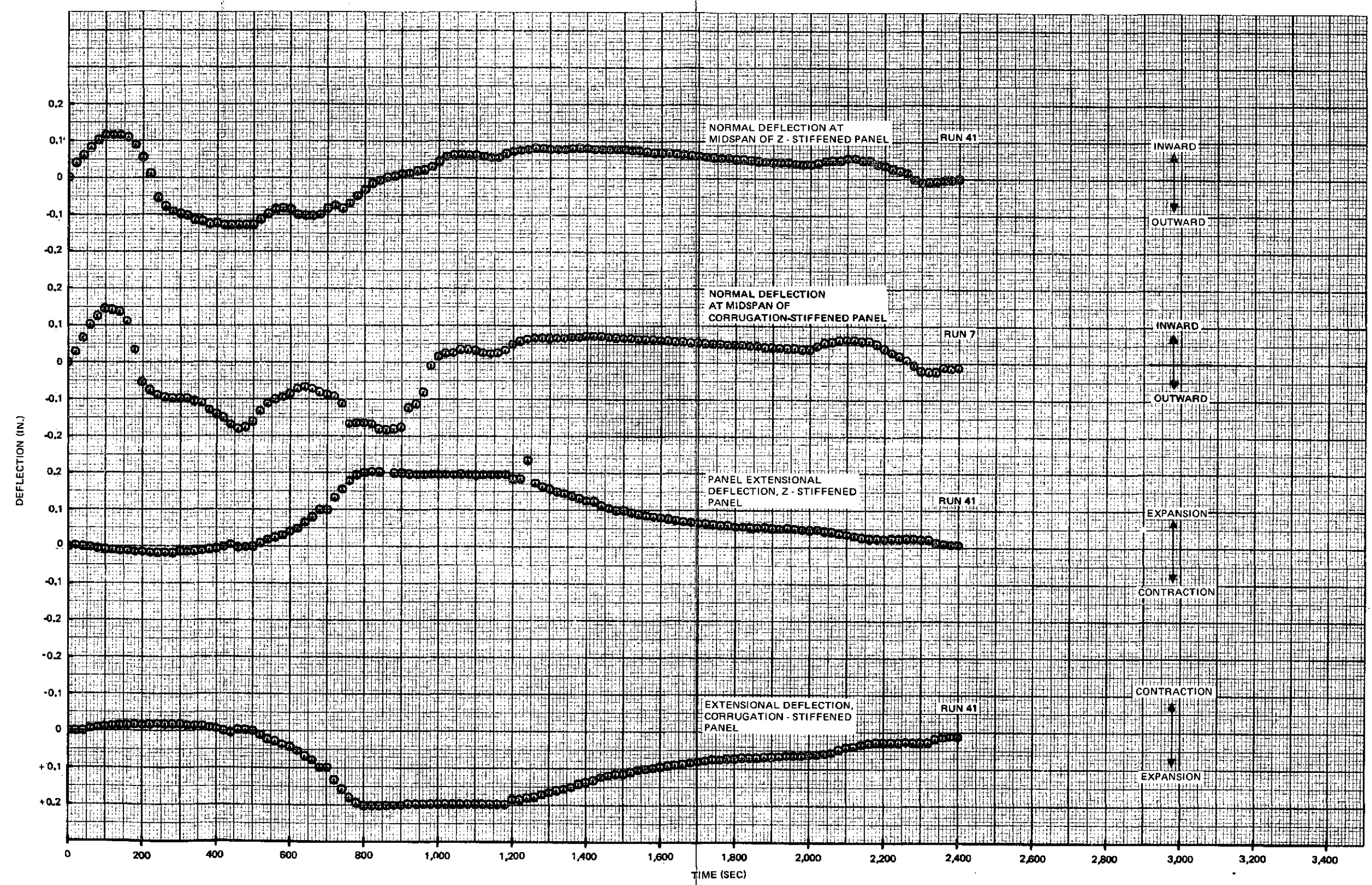
Figure 5-44. Panel Deflections

Figure 5-41, while Figure 5-42 presents the temperature of the susceptor plate in the graphite heater unit. Typical temperatures recorded on the panels are shown in Figure 5-43. Figure 5-44 presents deflection measurements.

The insulation package temperatures presented in Figure 5-43 (Page 123) show the lower temperature registered by Thermocouple 34 on the cool side of the package when compared to the temperatures at Thermocouples 35 and 36. The higher temperatures at the latter two positions was judged to have resulted from convection effects caused by some flow of heated air through the passages used for deflection rods and the gap between the test fixture and the edge of the insulation package. At maximum-temperature conditions (t = 1,100 sec), the temperature differential between Thermocouples 31 and 34 was approximately 973°K (1,750°F). The temperature time history computed in thermal analyses (Appendix D) for the cool side of the insulation package is shown in Figure 5-43 (Page 123) for an assumed ambient pressure of 10 torr. Comparison of Thermocouple 34 and the computed temperature time history indicates the lower efficiency of the actual test package in the initial portion of the test. However, the maximum temperature at Thermocouple 34 did not exceed 445°K (340°F), while the computed temperature near the end of the test was 550°K (530°F). Thus, the test insulation package, in areas not affected by convective heating, maintained cool-side temperatures lower than those predicted by analysis.

The deflections, shown in Figure 5-44, indicate maximum normal deflections at panel midspan positions of approximately ± 0.33 cm (0.13 in.). The normal deflection during the simulated entry portion of the test (t = 800 to 1,600 sec) was 70 percent of the maximum inward deflection during the boost portion of the test cycle, even though the differential pressure (collapse) during entry was only 15 percent of the boost flight pressure loads. The significantly lower modulus of elasticity at elevated temperature conditions accounts for the relatively high deflections during the simulated entry tests. Expansions and contractions caused by heating and cooling portions of the test cycle are also shown in Figure 5-44. Maximum expansion recorded was 0.508 cm (0.20 in.), which occurred during the maximum-temperature portion of the entry (t = 800 to 1,200 sec). The initial contraction between t = 0

and t = 400 sec resulted from a continuation of cooldown from the prior test cycle. Figure 5-43 shows the initial temperature drop in the panel during the early portion of the test cycle. Cooldown of this character occurred in the early portion of each test in a series except the first run, and the temperature drop was primarily due to introduction of air to bring the chamber pressure back to that required for boost flight simulation.

Results of the full-scale, subsize panel tests under programmed load, temperature, and acoustic level profiles showed the TD Ni-20Cr heat shields to be capable of sustaining 100 simulated missions without incurring significant permanent set. With the exception of cracks at attach hole positions in the face sheet and in the 0.0254-cm (0.010-in.) edge members, the overall appearance of the panels was good. The surface condition of both panels appeared to be unchanged, and thus the panel surface emittance was expected to have suffered little or no deterioration. The corrugation-stiffened panel was judged to have performed better during the full-scale subsize panel tests based on (1) lower stress levels in the corrugation-stiffened design in preliminary acoustic tests (Figure 5-30), (2) lower tension stresses in the corrugation-stiffened panel during preliminary static load tests, (3) the more severe cracking at the zee-stiffened panel attach points, (4) the appearance of small cracks along spotweld rows (Figure 5-34d) in the zee-stiffened panel, and (5) the occurrence of a slight buckle in one of the face sheet beads on the zee-stiffened panel. Because of its better performance, the corrugation-stiffened heat shield design was recommended for use in Phase II.

The cracks at the panel attach points were judged to have resulted from an overload in the dimpled area of the 0.0254-cm (0.010-in.) face sheets. Both heat shield designs employed slightly oversize, predimpled holes of approximately 0.710-cm (0.280-in.) diameter. This practice was based upon dimpling tests reported in Reference 8, in which an oversize predimpled hole was required to produce satisfactory crack-free dimples in thin sheets of TD Ni-20Cr. Use of the larger-diameter holes provided a relatively small bearing surface for the flush-head fasteners. The resultant high stresses at the periphery of the hole caused by burst pressure loads and thermal gradients initiated the radial cracks, and subsequent exposure to acoustic loads caused further growth of the cracks. Despite the severity of the cracks, reinforcement of the dimpled holes permitted completion of a full 100 test cycles.

Section 6
CONCLUSIONS

The work performed in Phase I included analytical evaluations of TD Ni-20Cr heat shields; material property tests and a review of current TD Ni-20Cr material properties; panel tests to evaluate simulated meteoroid impact effects; panel and joint tests in a plasma arc stream; and full-scale subsize panel tests simulating boost and entry flight loads, temperatures, pressures, and acoustic levels. Results of Phase I efforts led to the following conclusions:

A. TD Ni-20Cr heat shield panels are capable of sustaining 100 cycles of simulated boost and entry flight conditions without developing significant permanent deformations.

B. Single-face stiffened panels were selected from parametric studies as the most promising heat shield configurations for further study and tests. Two designs were selected for competitive tests in Phase I, one design being a corrugation-stiffened configuration and the second being a zee-stiffened design. Conventional spot welding was selected as the primary joining method because of slightly higher weight of the braze-reinforced panel design. Also, analysis of the Phase I panel designs and comparison with previous use of spot-welded thin-gage TD Ni-20Cr panels showed conventional spotwelding to be adequate.

C. On the basis of full-scale, subsize panel tests, the corrugation-stiffened panel design performed better than the zee-stiffened design in the 100 test cycles simulating boost and entry flight conditions.

D. Multiple-parameter tests of TD Ni-20Cr 0.0254-cm (0.010-in) samples showed low cumulative creep deformation to occur as a result of programmed cycles of stress, temperature, and pressure conditions simulating 100 Shuttle Orbiter missions. However, residual strength at room temperature and at 1,368°K (2,000°F)

decreased from 13 to approximately 55 percent, depending on stress levels to which the sample was subjected and the sample orientation (longitudinal or transverse). Severely reduced elongation at failure accompanied the strength degradation. Strength degradation at room and elevated temperatures did not significantly increase heat shield weights because: (1) relatively low tensile stresses accompany the critical compressive buckling loads which occur at low temperatures where maximum strength degradation occurred, (2) panel tests in Phase I showed critical areas on the heat shields to be attach points and panel edge stiffening members rather than panel midspan areas where maximum design stresses occur, and (3) isotropic panel designs utilized the greater strength and lower degradation of the material's longitudinal properties while avoiding reliance on the lower properties and more severely degraded strength of the sheet material's transverse direction.

E. While adequate joining techniques for thin-gage TD Ni-20Cr were available, it was desirable to conduct supplementary tests for evaluation of strength improvements realized from braze-reinforcement of the joint area. Such tests showed braze-reinforcement to produce significant improvement in spot-welded, diffusion-bonded, or seam-welded joints, particularly in fatigue at room temperature.

F. A double thickness of 0.0254-cm (0.010-in.) sheet TD Ni-20Cr was indicated to resist penetration in simulated meteoroid impact tests; however, a single thickness was penetrated. Subsequent exposure to simulated entry heating in a plasma arc facility showed no deterioration of the impact areas to be caused from high temperature airflow from a single entry cycle.

G. The panel joint design utilizing a closure strip sustained the repeated cycles of plasma stream exposures with less deformation than shown by the overlapping panel edge design.

H. Hot gas ingestion was not a problem in either panel joint test samples or panels subjected to simulated meteoroid impacts and subsequently exposed to plasma arc streams to simulate entry airflow.

I. Based on the Phase I heat shield configurations, the basic TD Ni-20Cr sheet thickness used in all test panel designs (0.0254 cm) proved to

be satisfactory for the basic panel components on face sheet and stiffening elements; however, 0.0254-cm (0.010-in.) thick material was insufficient at attachment points and for use as stiffening members at panel edges. Cracks developed in both of the full-scale, subsize panel designs early in the test series at all unreinforced dimpled holes in 0.0254-cm (0.010-in.) thick face sheets and in several locations along 0.0254-cm (0.010-in.) thick edge stiffening members.

J. Reinforcement of the dimpled holes at attach positions in the panel face sheets distributed the loads sufficiently at those positions to permit completion of the 100 programmed test cycles. Performance of the reinforced attach points indicated that reinforcement at attach points would permit use of 0.0254-cm (0.010-in.) sheet thickness.

K. The panel attachment design used in Phase I test parts was inadequate for use in future heat shield panel designs. Improvements required include (1) better anti-seizing materials, (2) a fastener locking design operable from the exterior side of the panel, and (3) a design permitting panel deformations with a minimum of induced stresses.

REFERENCES

1. Klingler, L. J., Weinberger, W. R., Bailey, P. G., and Baranow, S. Development of Dispersion-Strengthened Nickel-Chromium Alloy (Ni-Cr-ThO2) Sheet for Space Shuttle Vehicles. NASA CR-120796, December 1971.

2. Anon. Meteoroid Environmental Model-1969 (Near Earth to Lunar Surface). NASA SP-8013, March 1969.

3. Anon. Meteoroid Damage Assessment. NASA SP-8042, May 1970.

4. Anon. Space Shuttle Program Request for Proposal No. 9-BC421-67-2-40P Manned Spacecraft Center, Houston, Texas, 17 March 1972.

5. Anon. Space and Planetary Environment Criteria Guidelines for Use in Space Vehicle Development (1971 Revision). NASA TMX-64627, 15 November 1971.

6. Fritz, L. J. Characterization of Mechanical and Physical Properties of TD Ni-Cr (Ni-20Cr-2ThO$_2$) Alloy. Contract NAS 3-15558, Monthly Reports Nos. 1 (7 July 1971) through 15 (1 October 1972).

7. Holko, K. H., Moore, T. J., and Gyorak, C. A. State-of-Technology for Joining TD-NiCr Sheet. NASA TMX-68070, September 1972.

8. Johnson, R., Jr., and Killpatrick, D. H. Dispersion-Strengthened Metal Structural Development. AFFDL-TR-68-130 Part I (1968).

9. Haas, D. W. Refurbishment Cost Study of the Thermal Protection System of a Space Shuttle Vehicle. NASA Report CR-111832, 1 March 1971.

APPENDIX A

CRITICAL ENTRY THERMAL ENVIRONMENTS AND
TPS REQUIREMENTS

Appendix A

CRITICAL ENTRY THERMAL ENVIRONMENTS AND TPS REQUIREMENTS

A. 1 CRITICAL ENTRY THERMAL ENVIRONMENTS

This section of Appendix A contains the entry thermal environments for the MDAC Orbiter Configuration 101/E. Trajectories considered include Missions 1, 2, and 3 as defined in the Space Shuttle Request for Proposal (RFP). The Mission 3 entry (100 nmi, polar orbit) is the most severe with a bottom centerline maximum temperature of 2,300°F and heating time of 1,670 seconds. Time-histories of the reference heating rate, bottom centerline heating rates, and temperatures at several locations on the lower surface centerline are presented in this part of Appendix A.

The Space Shuttle RFP defines three missions which the Shuttle Orbiter must be capable of achieving. The orbits associated with these missions are as follows:

Mission 1 — 100 nmi circular orbit

28. 5° inclination angle

Launch from KSC

Mission 2 — 270 nmi circular orbit

55° inclination angle

Launch from KSC

Mission 3 — 100 nmi circular orbit

90° inclination angle (polar)

Launch from WTR

All entries must have sufficient crossrange to return to the launch site after one revolution; the trajectories shown herein satisfy this requirement. The high orbit inclination and crossrange combine to make the Mission 3 entry the most severe in terms of both heating rate and heating time. Provisions for downrange maneuvering capability and the effects of dispersions are required. Therefore, maximum, minimum, and nominal downrange cases (all of which meet the one revolution and return to launch site requirement) were analyzed for Mission 3.

Altitude, velocity, and angle of attack for the above-described cases are presented in Figures A-1 and A-2. The simulated Mission 3 trajectory is an attempt to match the severity of the Mission 3 trajectory from a 55-deg inclination angle orbit. This requires an orbit altitude of 500 nmi.

Orbiter bottom centerline maximum surface temperatures, total heats, and reference heating rates are compared in Table A-1. The Mission 3, maximum downrange trajectory, has the highest heating time and total heat is therefore the design case for sizing the TPS. Mission 3, minimum downrange, yields the highest surface temperatures and was used in Phase B studies for surface material selection. The simulated Mission 3 is slightly less severe than the design case in both temperature and total heat.

Reference heating rate, bottom centerline heating rates, and bottom center-line temperatures are shown as time-histories in Figures A-3 through A-5 for the critical Mission 3 entry.

A.2 TPS PERFORMANCE REQUIREMENTS FROM SPACE SHUTTLE RFP

This portion of Appendix A summarizes the TPS requirements derived from the Space Shuttle RFP No. 9-BC421-67-2-40P, dated 17 March 1972. The paragraph numbers are those used in the original RFP.

TPS Criteria From Space Shuttle RFP:

Design Missions

a. **Mission 1.** This mission is a payload delivery mission to a 100 n.m. circular orbit. The mission will be launched due east and requires a payload capability of 65,000 pounds with the Orbiter Vehicle airbreathing engines removed. The purpose of this mission will be assumed to be place-ment and/or retrieval of a satellite. The Orbiter Vehicle on-orbit transla-tional ΔV requirement is 950 ft/sec from the Orbital Maneuver Subsystem (OMS) and 120 ft/sec from the RCS.

b. **Mission 2.** This mission is a resupply mission to an orbital element in a 270 n.m. circular orbit at 55 degrees inclination. The rendez-vous is accomplished using a 17 orbit coelliptic rendezvous sequence (sequence is for reference only). The payload requirement is 25,000 lbs. with the air-breathing engine requirement as stated in Paragraph 1.3.2.4.3. The Orbiter Vehicle on-orbit translational ΔV requirement is 1,400 ft/sec from the OMS and 120 ft/sec from the RCS.
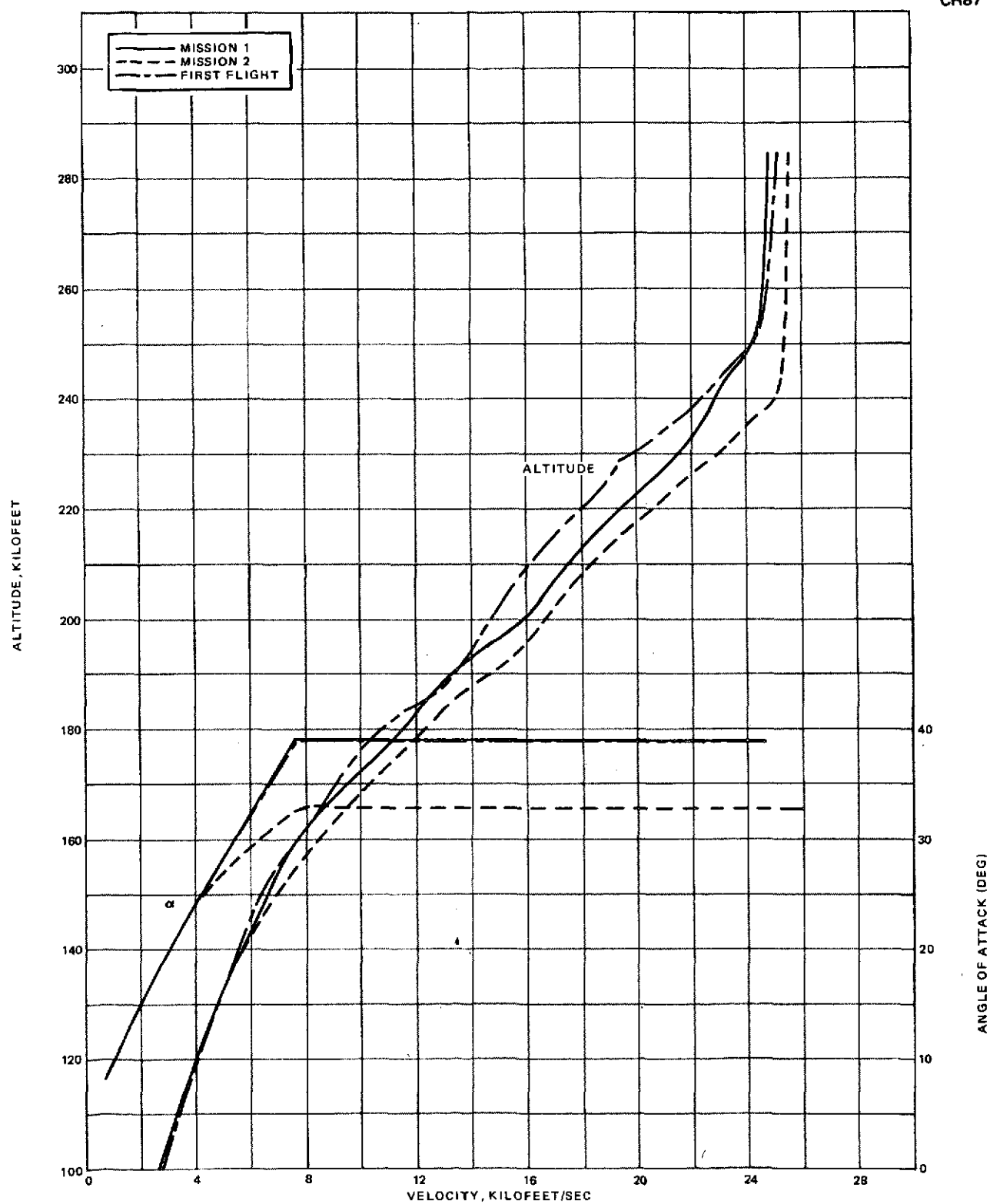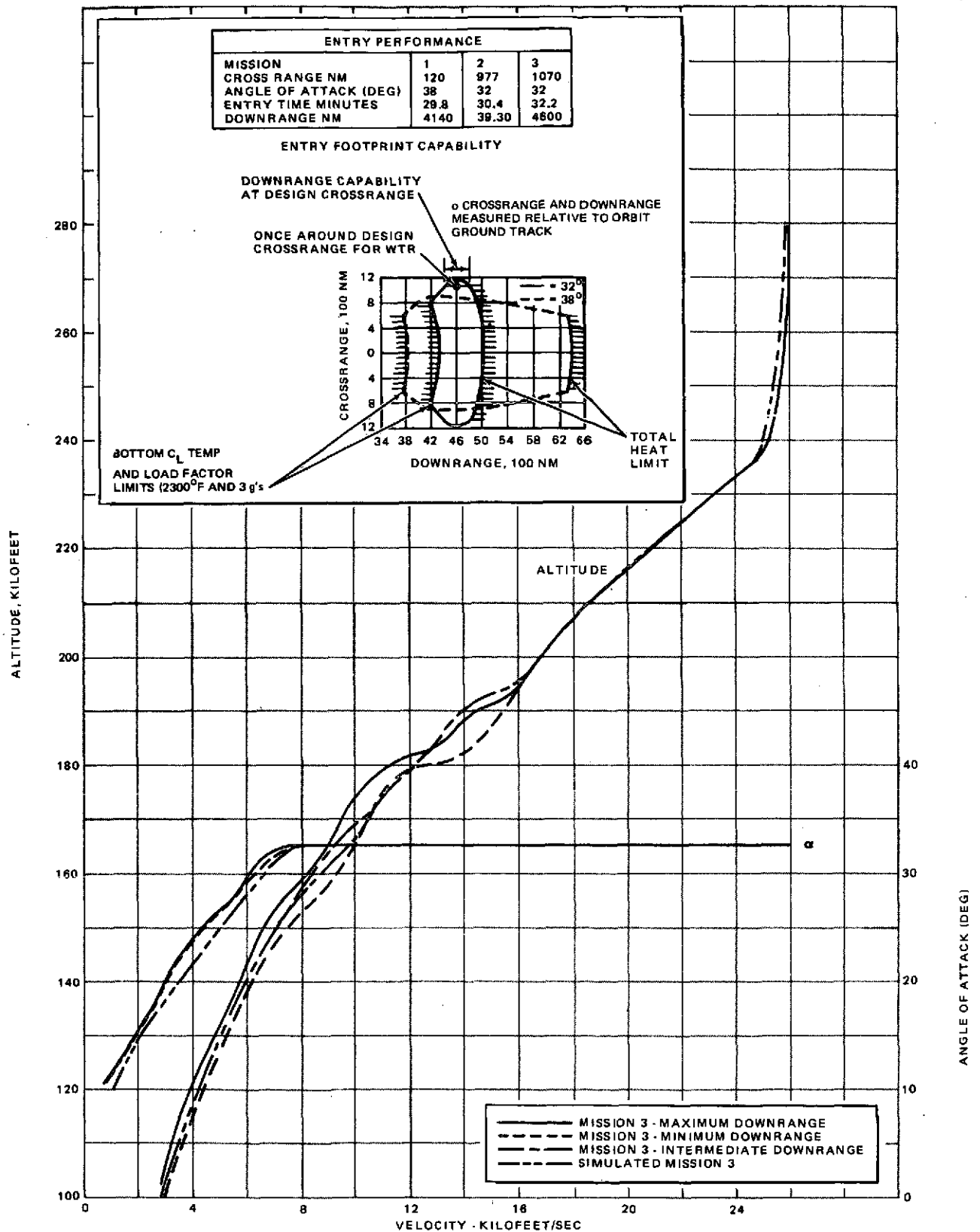
Figure A-1. Missions 1 and 2 Trajectories

Figure A-2. Mission 3 Entry Trajectories

ORBITER CONFIGURATION 101/E BOTTOM CENTERLINE
THERMAL ENVIRONMENT COMPARISON

Correlation Factor = f (α)			$\epsilon = 0.90$			
			Mission 3			
Trajectory	Mission 1	Mission 2	Maximum DR	Intermediate DR	Minimum DR	Simulated (1)
Angle of Attack, deg	38	32	32	32	32	32
Orbital Inclination, deg	28.5	55	90	90	90	55
Downrange, nmi	4139	3932	4798	4511	4387	3871
Design Entry Weight, lb	208,440	210,000	208,440	208,440	208,440	208,440
X/L			Maximum Wall Temperature - Deg F			
0.0865	2,064	2,117	2,142	2,265	2,265	2,145
0.10	2,147	2,214	2,235	2,307	2,307	2,245
0.15	2,193	2,248	2,307	2,307	2,307	2,284
0.25	2,164	2,209	2,268	2,268	2,268	2,239
0.35	2,127	2,174	2,225	2,225	2,225	2,217
0.50	2,085	2,136	2,171	2,171	2,171	2,159
0.75	2,011	2,050	2,085	2,085	2,085	2,077
0.90 (3)	1,995	2,033	2,068	2,068	2,068	2,060
			Total Heat - Btu/ft^2			
0.0865	12,320	15,440	16,560	16,620	16,540	15,904
0.10	12,530	15,910	17,050	16,940	16,870	16,420
0.15	12,670	16,670	17,730	17,590	17,530	17,210
0.25	12,580	16,400	17,300	17,180	17,120	16,860
0.35	12,550	16,230	17,090	16,980	16,930	16,700
0.50	12,740	16,200	17,100	17,000	16,950	16,780
0.75	11,350	14,230	15,050	14,960	14,920	14,730
0.90 (3)	11,070	13,870	14,680	14,600	14,560	14,360
			Reference Heating			
q_{Ref}, Max. $\dfrac{Btu}{ft^2\text{-}sec}$	67.34	87.76	94.12	94.12	94.12	92.49
$Q_{Total, Ref}$ $\dfrac{Btu}{ft^2}$	50,750	65,950	71,380	70,590	70,380	68,020
Reference Heating Time, Sec (2)	1,470	1,490	1,670	1,610	1,564	1,490

(1) 500 nmi orbit
(2) Time from 400,000 ft to time when radiation equilibrium q_{Ref} = 1.0 Btu/ft^2-sec
(3) Assumes zero body flap deflection

c. Mission 3. This mission is a payload delivery or retrieval mission to a 100 n.m. circular polar orbit and return to launch site in a single revolution. The payload requirement is 40,000 lbs. with Orbiter Vehicle airbreathing engines removed. The Orbiter Vehicle on-orbit translation ΔV requirement is 500 ft/sec from the OMS and 150 ft/sec from the RCS.
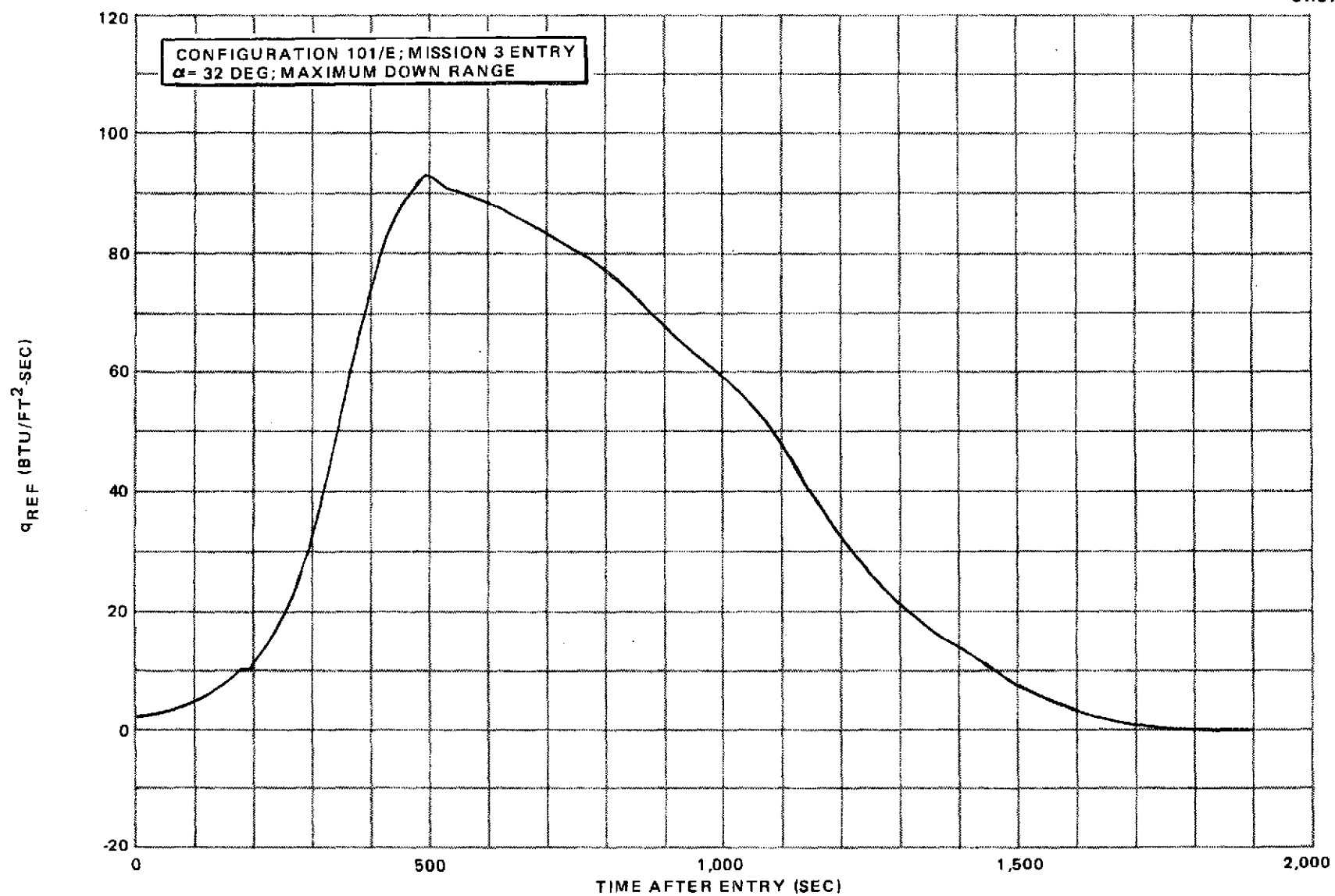
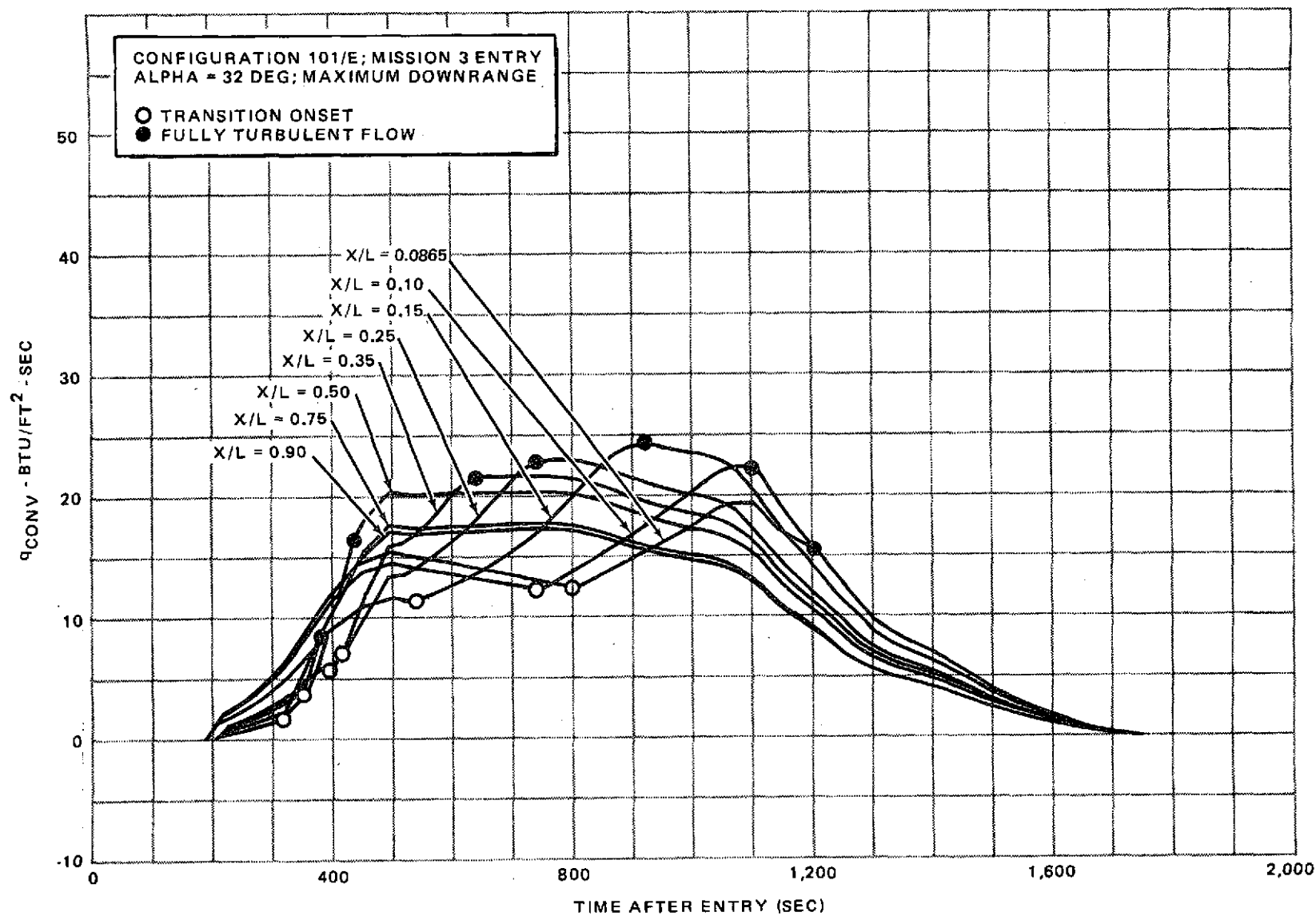Figure A-3. Reference Heating Rate Time-History
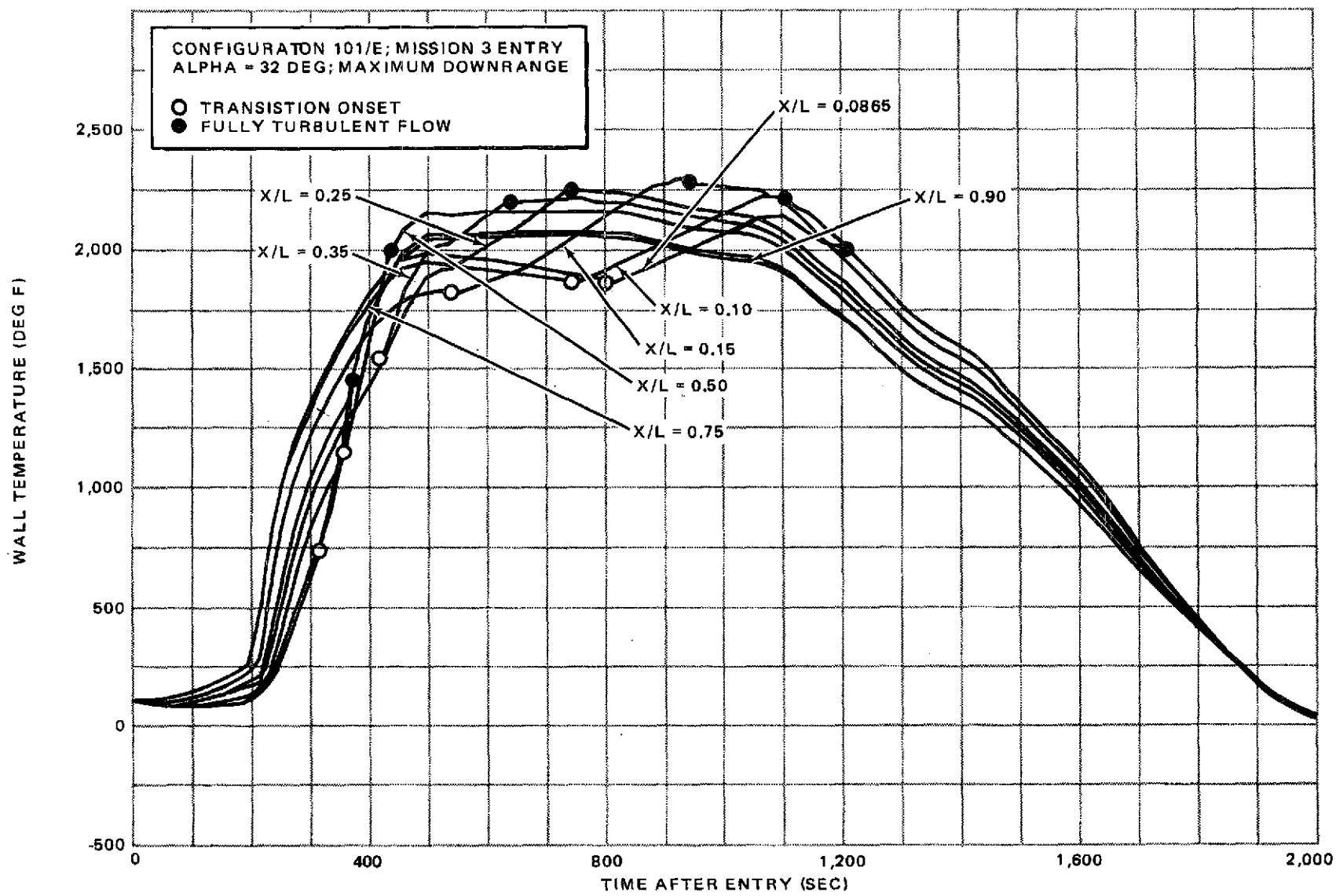
Figure A-4. Lower Centerline Heating Rates

Figure A-5. Lower Centerline Temperatures

Mission Duration

1.3.0.1 The cabin shall accommodate a basic crew of four. The Orbiter shall be provisioned for support of these personnel for a 7-day mission (28 man-days). The 7-day mission duration shall be used to size the vehicle for self-sustaining lifetime (from lift-off to landing).

Orbiter Loads - General

1.3.0.13 Loads and Structural Dynamics. The Orbiter design shall be capable of withstanding all internal and external loads, both steady state and dynamic, imposed during ground and flight operation. The Contractor shall determine all loading conditions necessary for vehicle design considering ground handling, prelaunch, boost, separation, orbital, entry, atmospheric flight, and landing loads.

Panel Flutter

1.3.0.13.6 Dynamic Aeroelasticity. The Orbiter Vehicle shall be free from classical flutter, stall flutter, and control surface buzz at dynamic pressures up to 1.32 times the maximum dynamic pressure expected during flight. External panels shall be free of panel flutter at 1.5 times the local dynamic pressure at the appropriate temperature and Mach number for all flight regimes including aborts.

Orbiter Structure - General

1.3.1.1 Primary Structure. The Orbiter Vehicle structure, including pressure vessels and mechanical systems, shall have adequate strength and stiffness, at the design temperature, to withstand limit loads and pressures without loss of operational capability for the life of the vehicle and to withstand ultimate loads and pressures at design temperature without failure. The structure shall not be designed to withstand loads, pressures, or temperatures arising from malfunctions that prevent a successful abort. It shall be a design goal for the vehicle to be operational after experiencing ultimate loads during an abort.

Structural Load and Strength Definitions

1.3.1.1.1 Definitions. For the purpose of interpretation of this section, the following definitions will apply:

    a.   Limit Load: The maximum load expected on the structure during mission operation. For statistical purposes, limit loads will be based on NASA approved criteria.

    b.   Ultimate Load: The product of the limit load multiplied by the ultimate factor of safety. It is the maximum load which the structure must withstand without rupture or collapse.

c. Ultimate Factor of Safety: The factor by which the limit load is multiplied to obtain the ultimate load. Values for ultimate factors of safety are given in Paragraph 1.3.1.1.2. The wall thickness used in the stress calculations for pressure vessels will be the minimum wall thickness shown on the pressure vessel drawing. The thickness used for other structural members will be the mean thickness or 1.05 times the minimum thickness, whichever is less.

d. Proof Pressure: The pressure to which production pressure vessels are subjected to fulfill the acceptance requirements of the customer, in order to give evidence of satisfactory workmanship and material quality, and to establish the maximum undetected flaw size in the pressure vessel. Proof pressure is the product of limit pressure times the proof factors.

e. Allowable Load: The load that induces the allowable stress in a material.

f. Margin of Safety: The ratio of the excess strength to the required strength.

Factor of Safety

1.3.1.1.2 Design Factors of Safety. Design factors of safety are defined as multiplying factors which are applied to limit loads or pressures in order to obtain the design loads and pressures. The design factors given in the table below shall be used for the Orbiter Vehicle structure and mechanisms. Deviations from these factors will be permitted in those instances where sufficient data on loads and strength variations are available to establish structural integrity on a probability basis. The statistical criteria must be approved by NASA.

Combined Loads

1.3.1.1.3 Ultimate Combined Loads. The structural design shall exclude the use of pressure stabilized structures with the exception of main propulsion tanks. The mechanical external, thermally induced, and internal pressure loads should be combined in a rational manner according to the equation given below to determine the design loads. Any other loads induced in the structure; e.g., during manufacturing, shall be combined in a rational manner. No load conditions outside the crew safety envelope shall be considered. In no case shall the ratio of the allowable load to the combined limit loads be less than 1.40.

$$K_1 L \text{ external} + K_2 L \text{ thermal} + K_3 L \text{ pressure} \geq 1.40 \ \Sigma L$$

$K_1 = 1.4$ for boost conditions when the term is additive to the algebraic sum, ΣL

$K_1 = 1.5$ for entry, atmospheric cruise, and landing when the term is additive to the algebraic sum, ΣL

$K_2 = 1.5$ when the term is additive to the algebraic sum, ΣL

K_3 = 1.4 when the term is additive to the algebraic sum, ΣL

K_1, K_2, K_3 = 1.0 when the term is subtractive to the algebraic sum, ΣL

$L_{external}$ = Mechanical externally applied loads; e.g., inertial loads

$L_{thermal}$ = Thermally induced loads

$L_{pressure}$ = Maximum relief valve setting where additive to algebraic sum, ΣL

= 0 to minimum regulated when subtractive to algebraic sum, ΣL

DESIGN FACTORS OF SAFETY TABLE

Component	Factors of Safety Ultimate
General structure and main propellant tanks	≥ 1.40 (A)
Pressurized windows and hatches	≥ 3.0
Pressurized manned compartments	1.5
Pressure alone	2.0
Main Propellant tanks (pressure alone)	
Pressure vessels (other than main propellant tanks)	≥ 1.5
Less than 1.5" diameter	4.0
1.5" diameter or greater	2.0

(A) See Paragraph 1.3.1.1.3

Fatigue

1.3.1.1.6 Fatigue. Safe life design shall be adopted for all major load carrying structures. These structures shall be capable of surviving without failure a total number of mission cycles that is four times greater than the total number of mission cycles expected in service (shown by analysis or by test through a rationally derived cyclic loading and temperature spectrum).

Creep

1.3.1.1.8 **Creep.** Materials shall not exhibit cumulative creep strain leading to rupture, detrimental deformation, or creep buckling of compression members during their service life. Analysis shall be supplemented by test to verify the creep characteristics for the critical combination of loads and temperatures.

TPS Specific Requirements

1.3.1.3 **Thermal Protection and Control** The TPS shall protect the primary airframe, the crew and passengers, the payload, and the vehicle subsystems from aerodynamic heating during ascent and entry and from convective and radiative heating from the engine exhaust. The thermal control design shall maintain system, subsystem, and component temperature limits for all mission phases including ground conditions, launch, earth orbit, entry, suborbital flight, and postlanding phase.

1.3.1.3.1 Selection of design trajectory or trajectories shall result in a TPS capable of safe vehicle flights within an operational envelope that includes all mission and abort requirements, trajectory excursions, and atmospheric deviations.

1.3.1.3.3 TPS material properties shall be based on nominal values with statistical uncertainty and reuse degradation effects.

1.3.1.3.4 TPS weight effect of each input variable uncertainty will not be considered sequentially, which would result in a cumulative weight increase from nominal value, but will be considered in a simultaneous manner, allowing adequate mission flexibility at minimum weight and cost.

1.3.1.3.5 The TPS shall be designed to the same criteria as the general unpressurized structure of the airframe.

1.3.1.3.6 The Orbiter Vehicle shall incorporate integrated thermal control management by efficient utilization and integration of systems and subsystem available heat sources and sinks.

1.3.1.3.7 The internal wall temperature limits for the payload bay, not considering payload temperature effects, shall be as specified in Paragraph 1.3.8.9.4. (See Table A-2 below).

1.3.8.3.8 Cabin wall inside temperature shall be higher than the maximum dew point temperature for all pressurized compartments during all operational phases.

Meteoroid Impact Criteria

8.0 **METEOROID.** The Space Shuttle shall be designed for at least a 0.95 probability of no puncture during the maximum total time (for 100-500 missions) in orbit using the meteoroid model defined in Section 2.5.1 of NASA TMX-64627.

Table A-2

PAYLOAD BAY WALL THERMAL ENVIRONMENT
(ADIABATIC PAYLOAD BAY WALL)

CONDITION	MINIMUM	MAXIMUM
Prelaunch	+ 40°F	+120° F
Launch	+ 40°F	+150°F
On-orbit (door closed)	-100°F	+150°F
On-orbit (door open)	-	-
Entry and postlanding	-100°F	+200°F

8.1 <u>METEOROID IMPACT</u>. Space Shuttle meteoroid impact requirements shall be as specified below:

a. <u>Pressure Loss</u>. The Space Shuttle manned volume shall be protected from meteoroid impact damage which would result in pressure loss when subjected to the meteoroid flux model as defined in NASA TMX-64627.

b. <u>Functional Capability</u>. The Space Shuttle shall provide protection against loss of functional capability of selected critical items when subjected to the meteoroid flux model as defined in NASA TMX-64627. The probability of no penetration shall be assessed on each item dependent upon function criticality.

APPENDIX B

EVALUATION OF CURRENT TD Ni-20Cr MECHANICAL
AND PHYSICAL PROPERTIES

Appendix B
EVALUATION OF CURRENT TD Ni-20Cr MECHANICAL
AND PHYSICAL PROPERTIES

This appendix presents a review of TD Ni-20Cr material property data from the most recently available tests conducted under NASA contracts as well as data from previous material characterization tests conducted under Air Force contracts and MDAC company-funded efforts. A comparison of recent test data with those generated in the 1966-1970 time period shows very similar properties in terms of tensile strength, creep rupture strength, modulus of elasticity, fatigue strength, shear strength, and linear thermal expansion. Other characteristics being evaluated under Contract NAS 3-15588[1] include compressive yield stress, bearing strength, sharp notch strength, thermal conductivity, and specific heat.

The primary sources of recent test data were:.
  A. Contract NAS 3-15558, Characterization of the Mechanical and Physical Properties of TD Ni-Cr (Ni-20Cr-2ThO$_2$) Alloy.
  B. Contract NAS 3-15567, Development of Forming and Joining Technology for TD Ni-Cr Sheet.
  C. Contract NAS 8-21781, Crack-Propagation and Tensile Tests of TD Ni-Cr Sheet.
  D. Contract NAS 8-27189, Creep and Creep Rupture Tests of TD NiCr and HS - 188.

Discussions of the test data reviewed are presented below.

Tensile Ultimate Strength.   The tensile strength results from tests reported in Reference B-1 are shown in Figures B-1 through B-4. The data are plotted separately for longitudinal and transverse properties as well as being

_____

(1) Characterization of the Mechanical and Physical Properties of TD NiCr (Ni-20Cr-2ThO$_2$) Alloy.
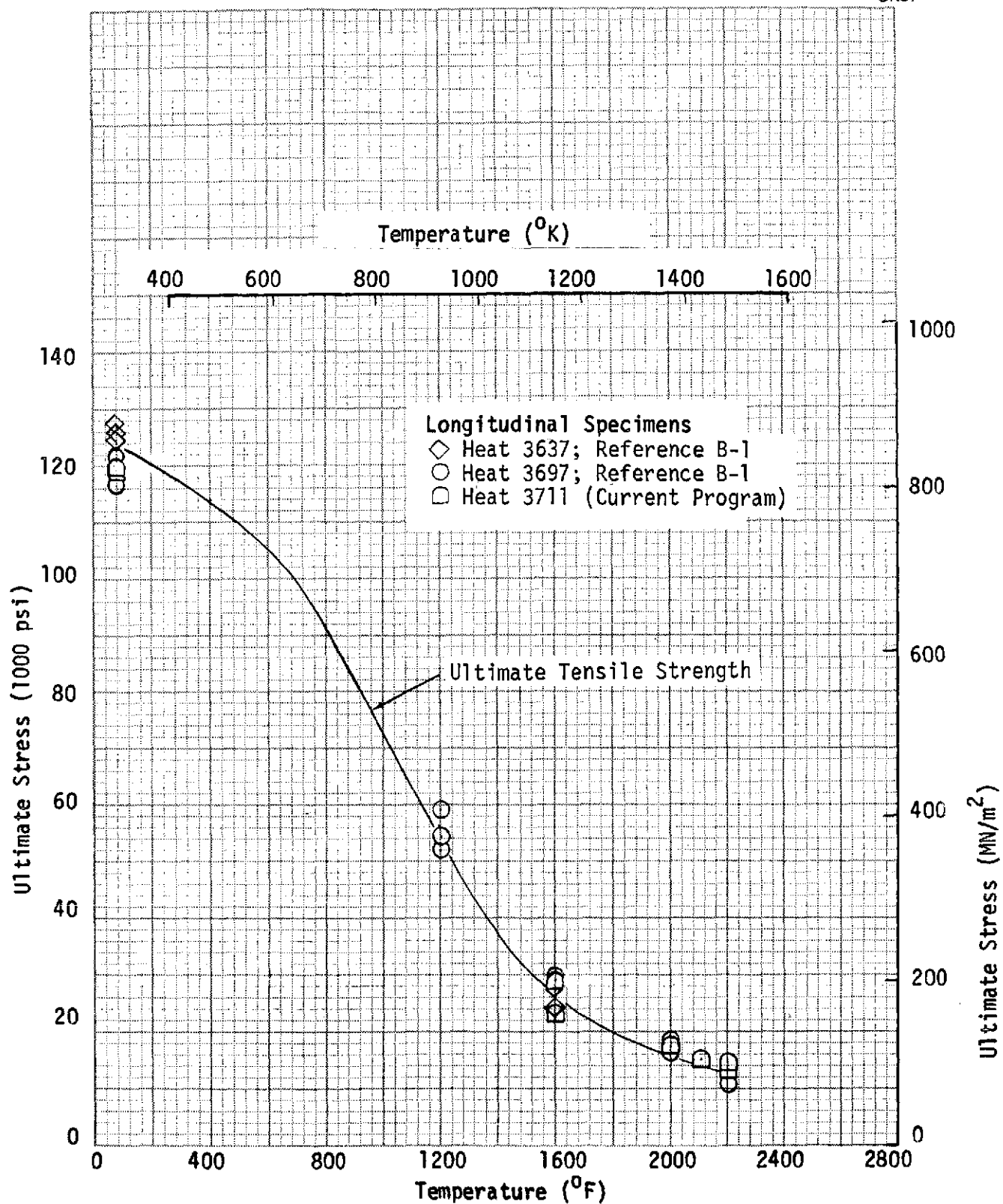
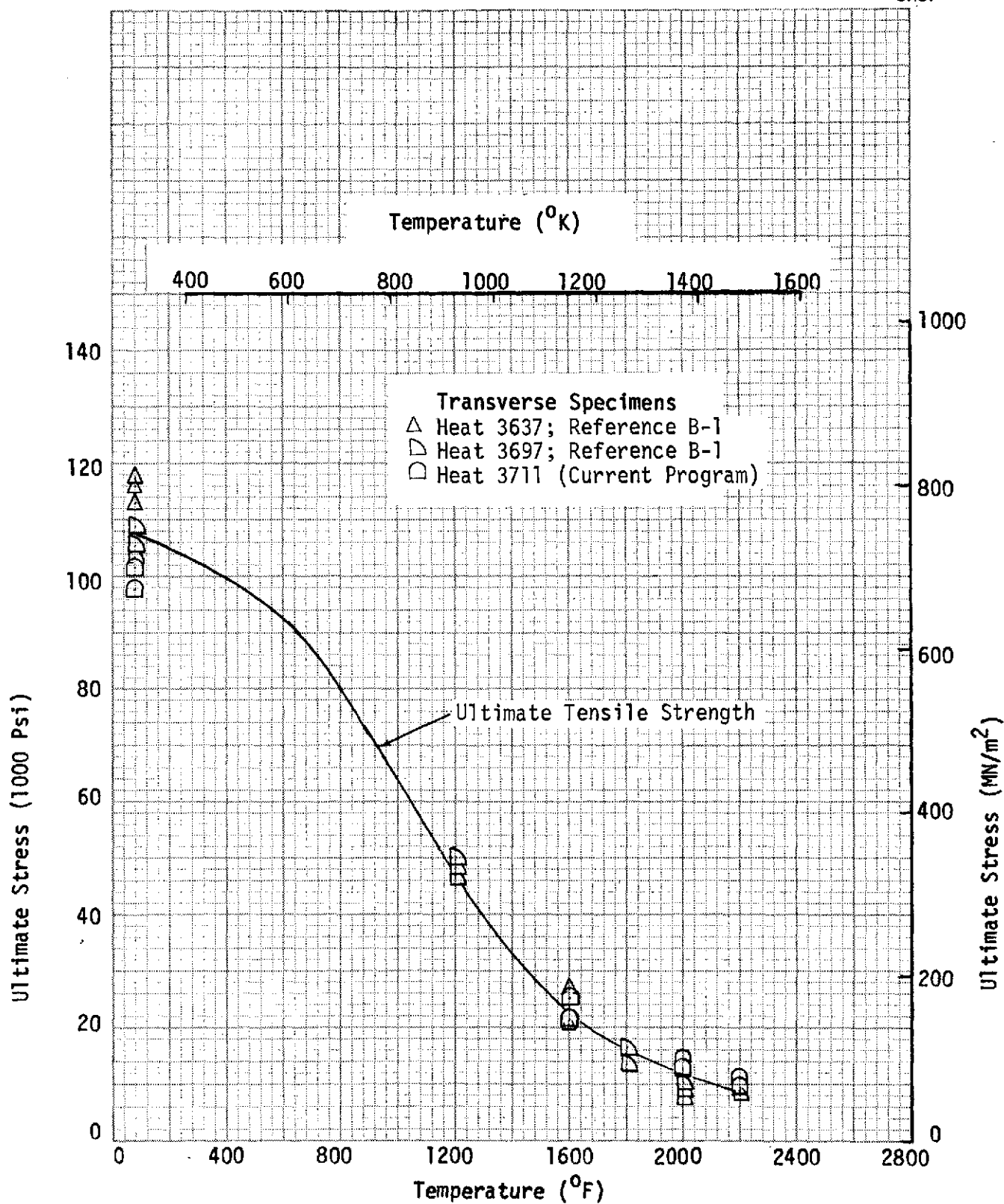Figure B-1. TD Ni-20Cr 0.010-in. Ultimate Tensile Strength (Longitudinal)

Figure B-2. TD Ni-20Cr 0.010-in. Ultimate Tensile Strength (Transverse)
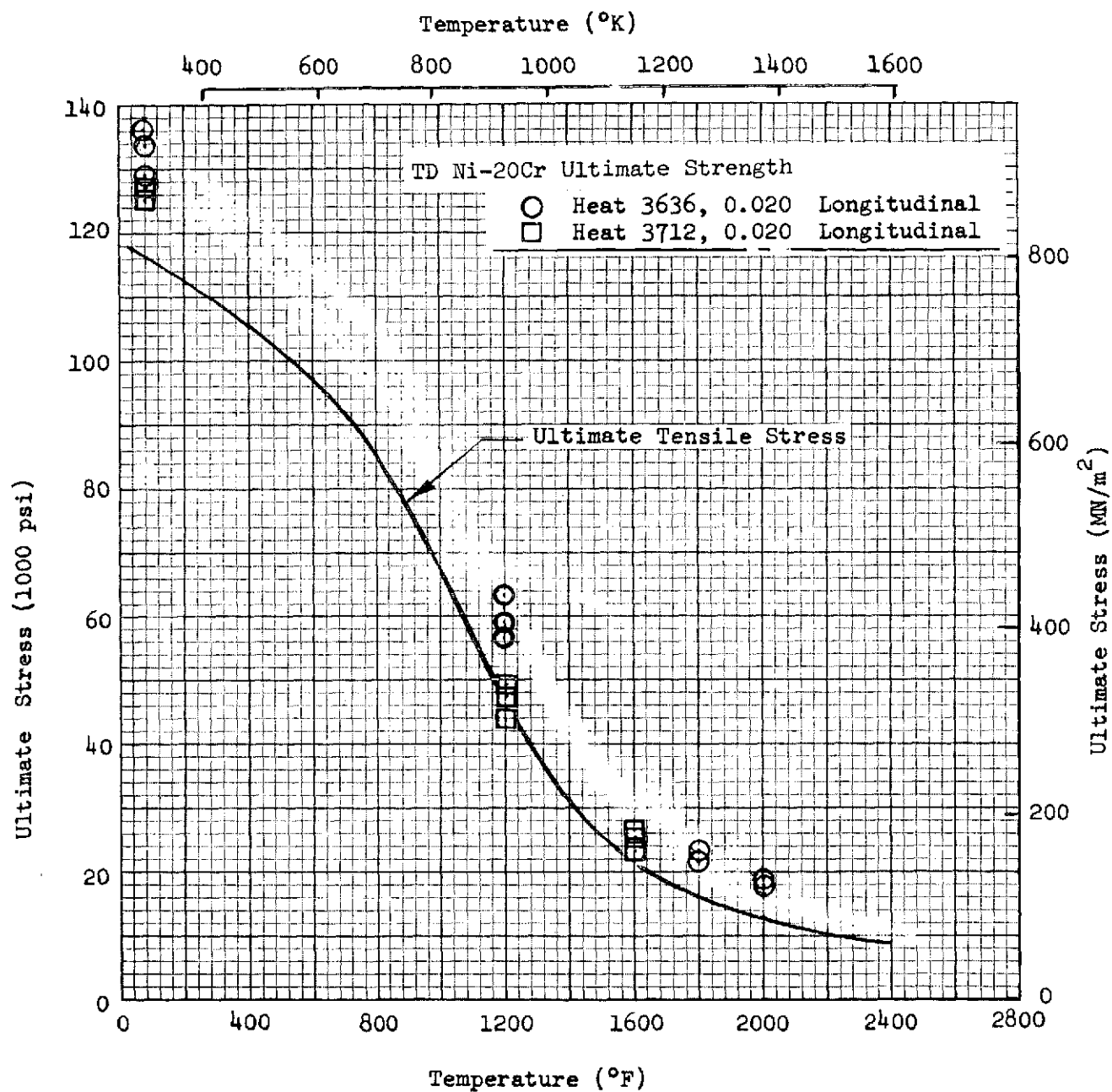
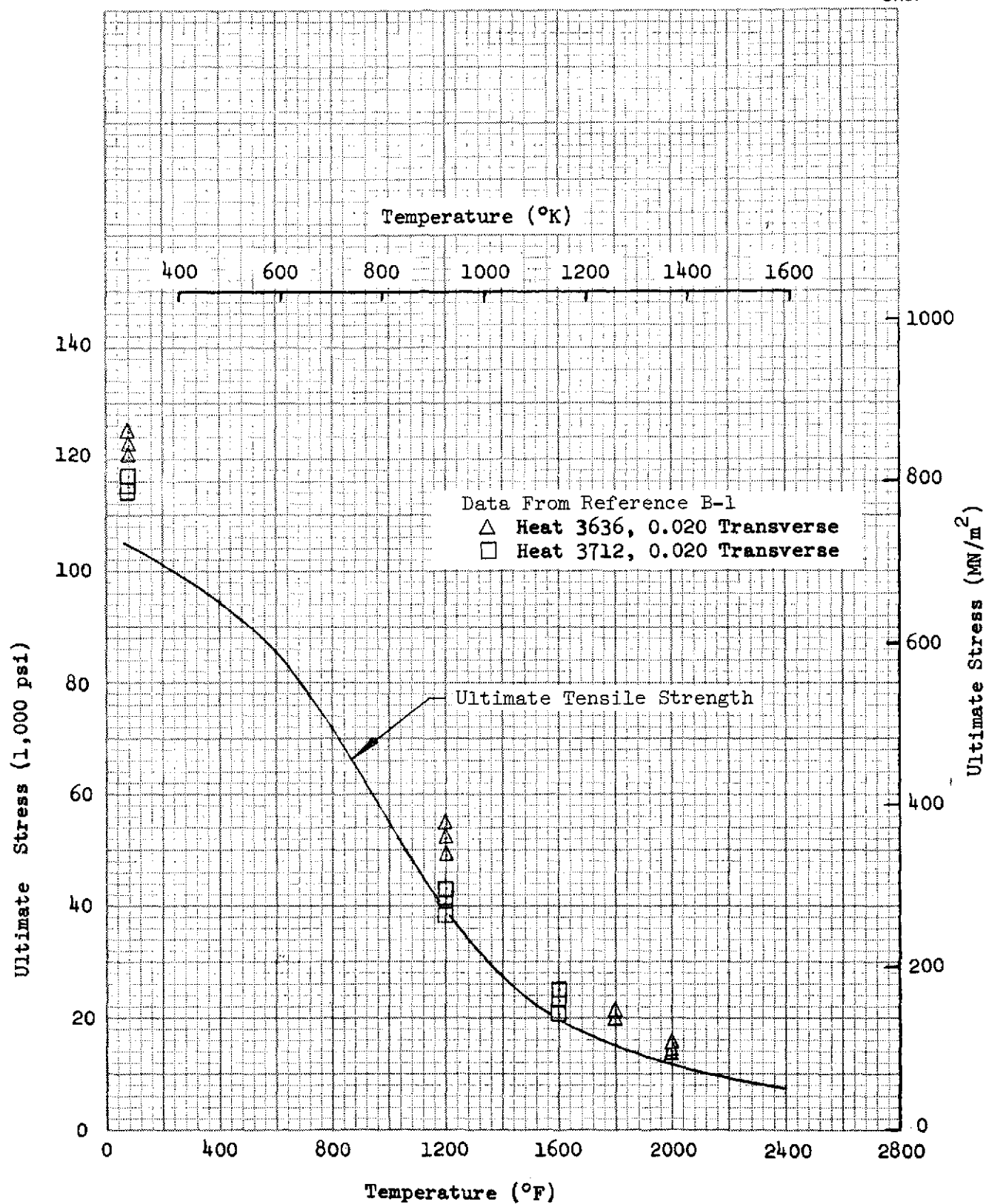Figure B-3. Ultimate Tensile Strength; TD Ni-20Cr 0.020-in. to 0.060-in. Sheet

Figure B-4. TD Ni-20 Cr Ultimate Tensile Strength; 0.020-in. to 0.060-in. Sheet Transverse Properties

presented separately for 0.0254-cm (0.010-in.) thick sheet and for the 0.0508-cm to 0.152-cm (0.020 to 0.060-in.) thickness range. Differences in transverse and longitudinal properties have been well established for TD Ni-20Cr sheet in previous work, and the drop in transverse properties shown here from recent tests is consistent with values noted in previous work (Reference B-2). Lower tensile properties have also been noted for 0.0254-cm (0.010-in.) gage material in past studies, a characteristic that is primarily the result of different thermomechanical processing during production of the 0.0254-cm (0.010-in.) sheet compared to that employed for thicknesses of 0.0508 cm (0.020 in.) or greater.

Data shown in Figures B-1 through B-4 were compared with similar properties exhibited by TD Ni-20Cr material in previous work (References B-3 through B-5) and the present data show good correlation with that recorded in previous efforts.

Average tensile ultimate strength values obtained from tests reported in Reference B-1 were reduced to account for strength degradation from repeated exposure to elevated-temperature, low-pressure entry environments. This reduction was based on residual strength data obtained in previous tests in which TD Ni-20Cr sheet samples had been exposed to temperature, pressure, and stress levels representative of Orbiter entry conditions. Initial calculations of oxidation effects (Appendix C) were subsequently compared to test data and showed reasonable agreement between the theoretical approach and test results. The selected design tensile allowable stresses arc shown in Figures B-1 through B-4 as solid lines.

Tensile Yield Strength

Yield strength (0.2-percent yield) data from Reference B-1 are shown in Figures B-5 through B-7. A comparison of these data with earlier test results on similar gages of TD Ni-20Cr sheet material indicate that similar properties where exhibited by both groups of material.

The design yield strengths, shown in Figures B-5 through B-7 as solid lines, were derived by reducing the short-time test results by the analytical methods described in Appendix C. These computed allowables, reduced analytically to

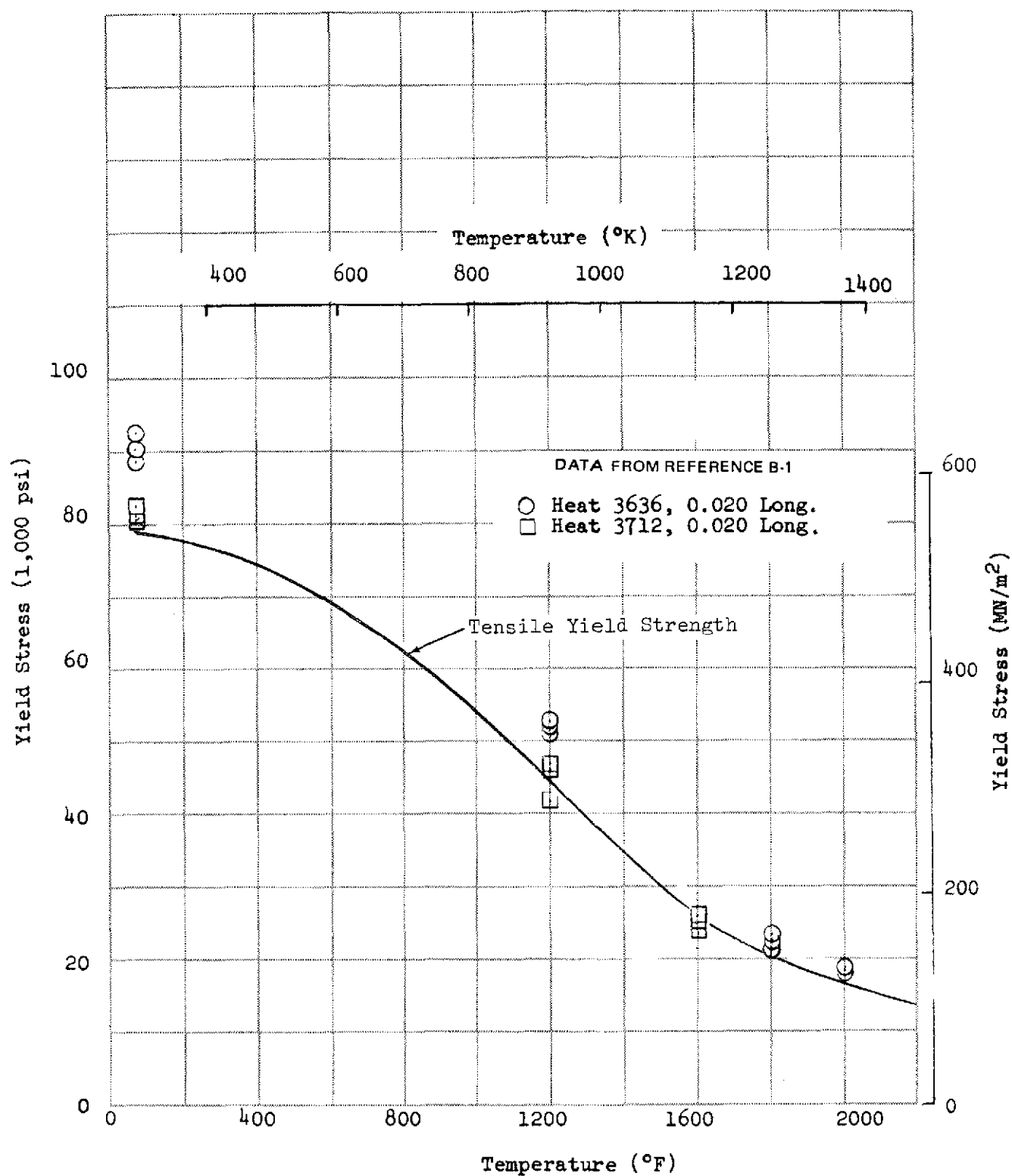Figure B-5. TD Ni-20Cr 0.010 Tensile Yield Strength (Longitudinal)

Figure B-6. TD Ni-20 Cr Tensile Yield Strength; 0.020-in. to 0.060-in. Sheet Longitudinal Properties
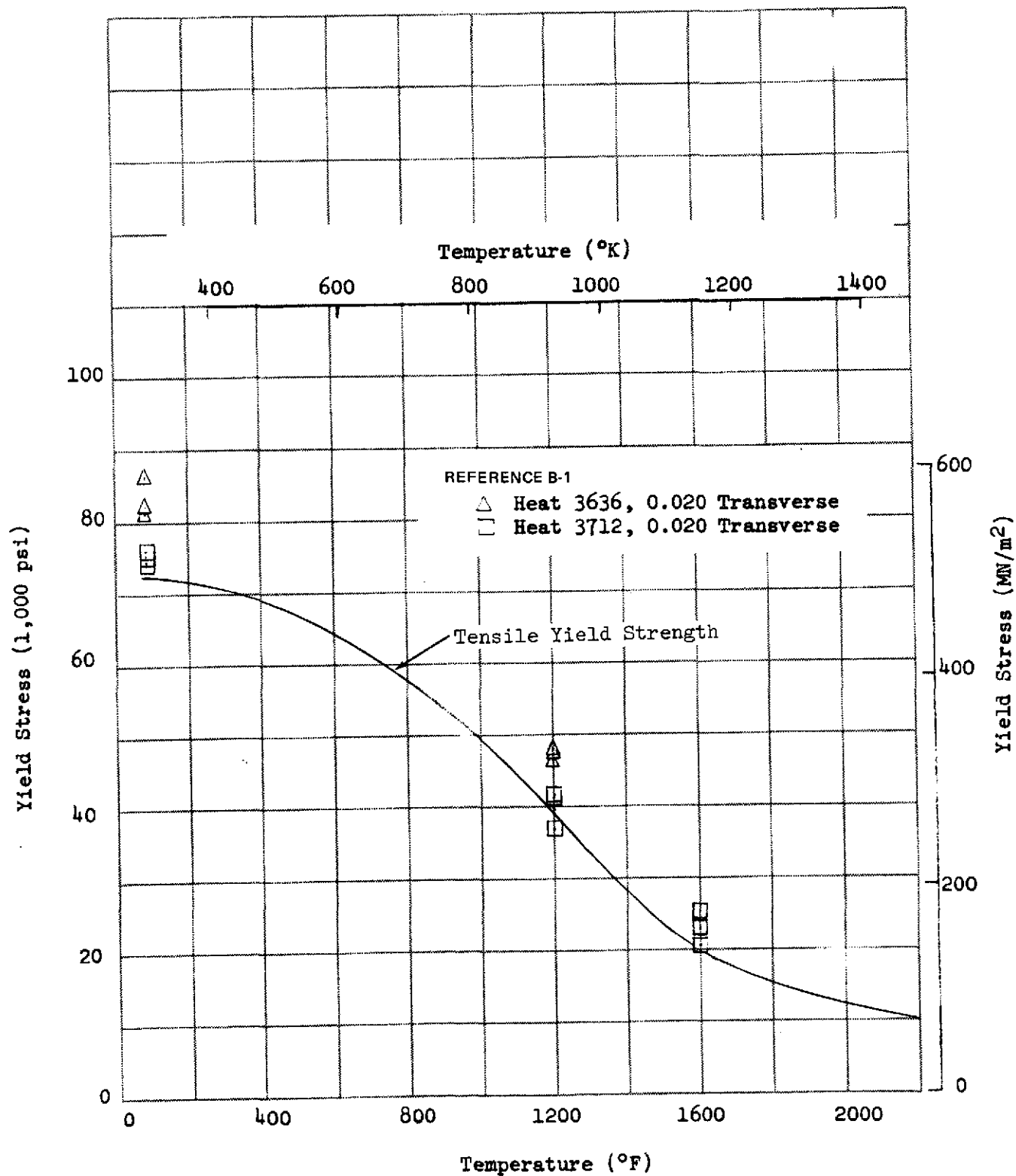
Figure B-7. TD Ni-20Cr Tensile Yield Strength; 0.020-in. to 0.060-in. Sheet Transverse Properties

account for degradation effects from 100 missions, were compared with results from cyclic multiple-parameter tests and other test data from References C-11, C-12, and C-13 (Table C-2, Appendix C).

The values shown in Figures B-5 through B-7 include data from 0.0508-cm (0.020-in.) longitudinal, 0.0508 cm (0.020 in.) transverse, and 0.0254-cm (0.010-in.) longitudinal samples. Transverse 0.0254-cm (0.010-in.) samples generally failed before the 0.2-percent offset strain was reached at temperatures of $924^{\circ}K$ ($1200^{\circ}F$) and above.

Elongation at Failure

The values of elongation at failure are plotted in Figures B-8 through B-10 as a function of temperature. A comparison (Figure B-9) was made between values obtained from Reference B-1 and average elongations recorded in earlier tests (Reference B-3) on similar gages of TD Ni-20Cr sheet. This comparison shows the generally lower elongations recorded in tests of recently produced material.

Poisson's Ratio.

Values of Poisson's ratio reported in Reference B-1 are 0.334 and 0.368 respectively for longitudinal and transverse specimens. These values show close agreement with those developed in Reference B-7, the latter data being 0.333 for longitudinal specimens and 0.338 for transverse specimens.

Modulus of Elasticity.

Static modulus of elasticity is shown in Figure B-11 as a function of temperature. Data used in this plot were obtained from References B-3, B-4, and B-8. The data from Reference B-8 show good consistency and fall near the average of previous data obtained in the temperature range of 1,035 to $1,477^{\circ}K$ (1,400 to $2,200^{\circ}F$). This shows that recently produced TD Ni-20Cr sheet has modulus properties similar to earlier material.

Anisotropy Characteristics

The anisotropy of TD Ni-20Cr sheet has been studied in previous investigations (Reference B-7), and the test program of NAS 3-15558 included strength tests at 0, 45, and 90 degrees, with respect to the sheet rolling direction.
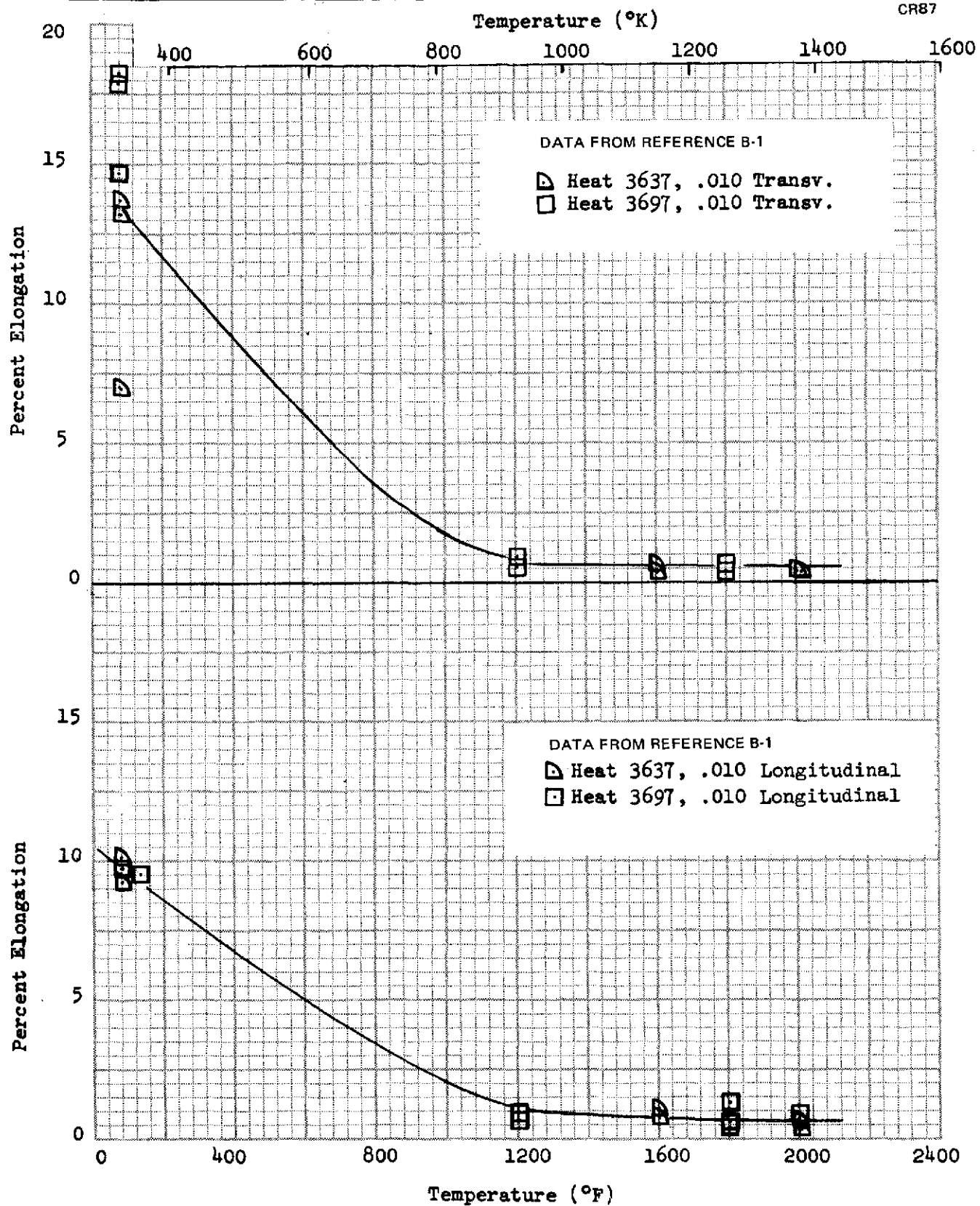
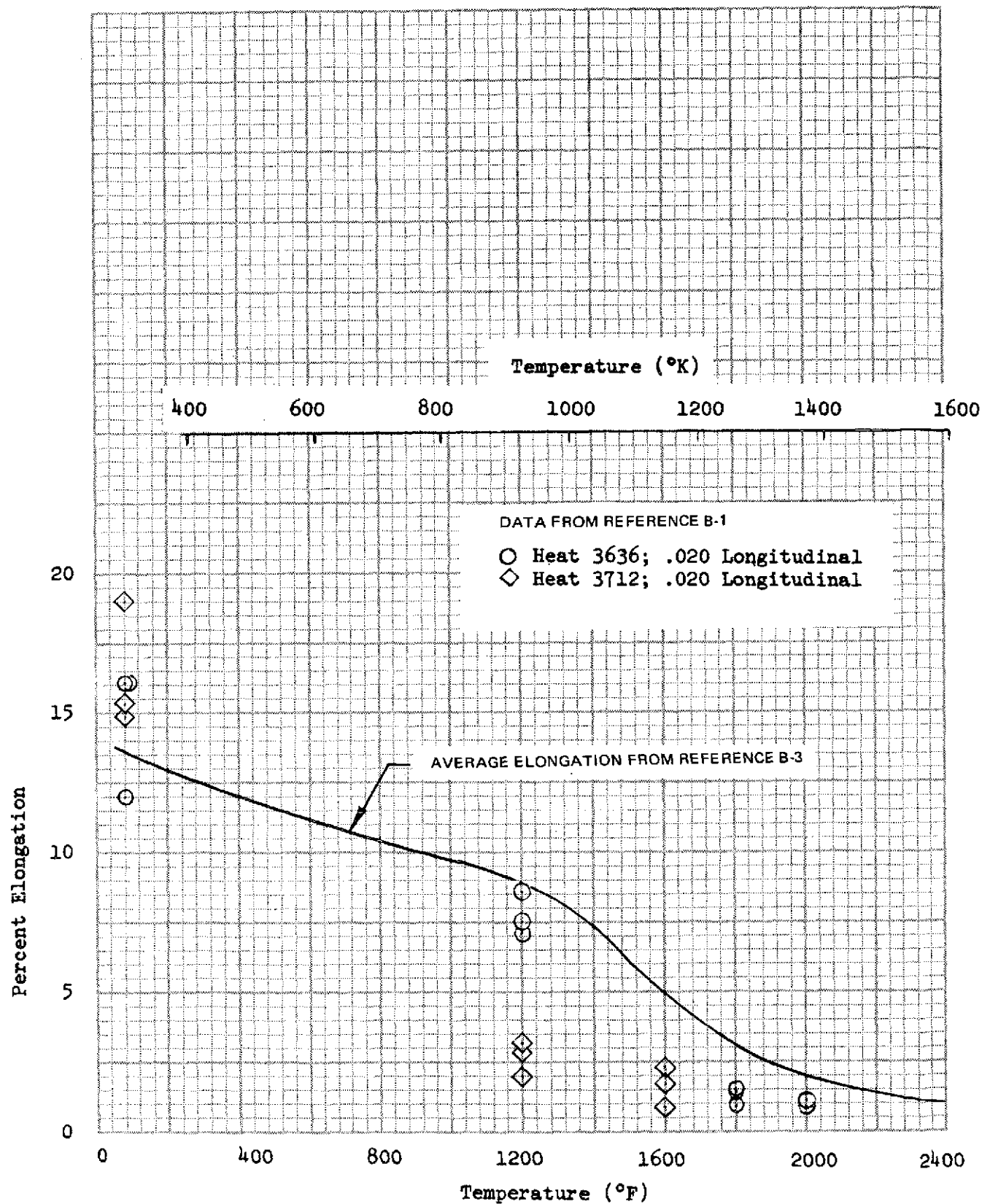Figure B-8. Elongation at Failure; 0.010-in. Sheet Properties

Figure B-9. Elongation at Failure; 0.020-in. to 0.060-in. Longitudinal Properties
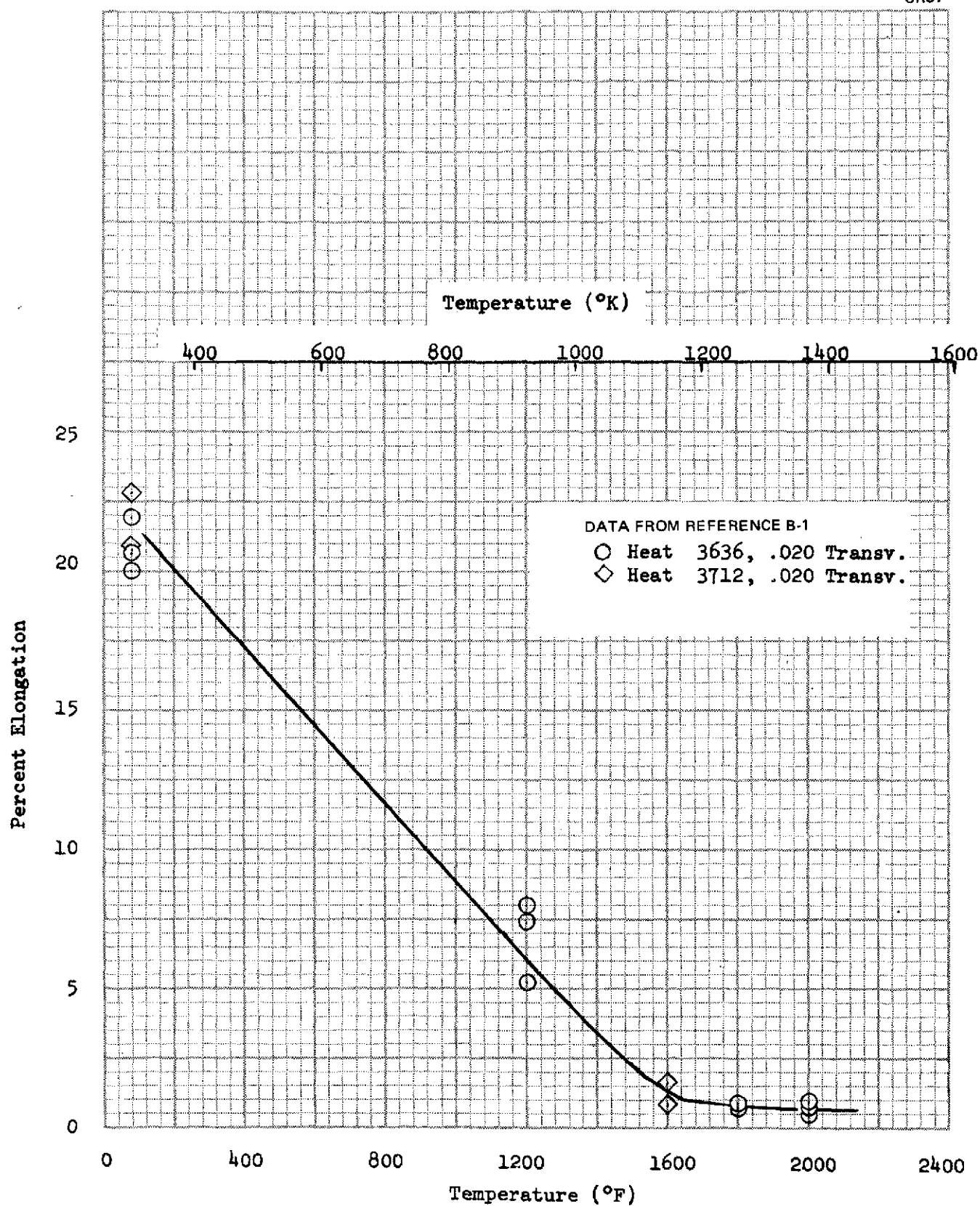
Figure B-10. Elongation at Failure; 0.020-in. to 0.060-in. Transverse Properties
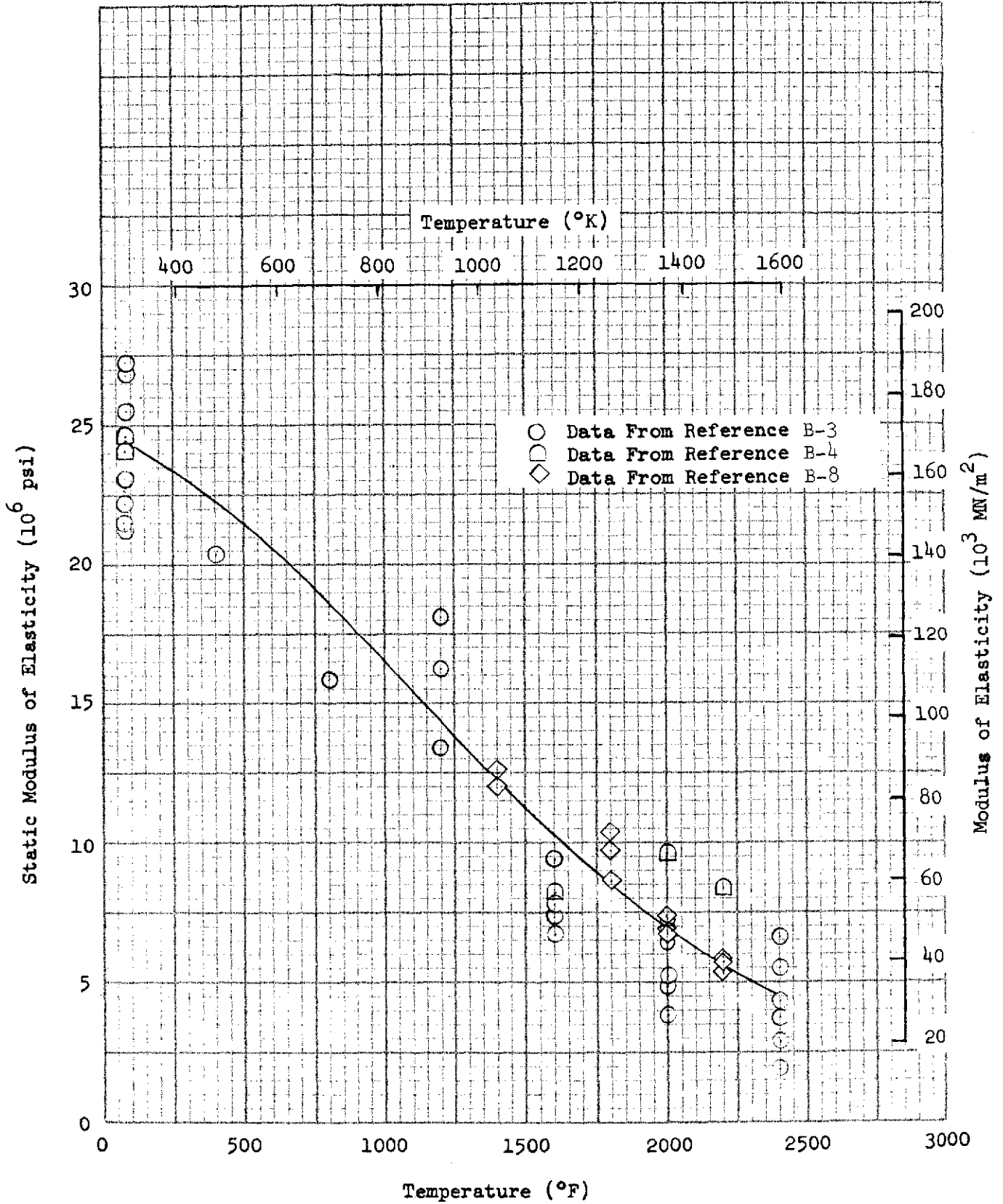
Figure B-11. TD Ni-20Cr Static Modulus of Elasticity

Figure B-12 presents data from Reference B-1 showing the variation of room-temperature ultimate tensile strength with angle from the sheet rolling direction. Comparisons are also made in Figure B-12 with data reported in Reference B-7, and good agreement is shown between the two sets of data. The dip in strength at 45 degrees is an indication that the cube texture, which contributes to the tensile strength and creep resistance of TD Ni-20Cr sheet, is present in the current material.

Compressive Stress Allowables. Local compressive crippling allowables, shown in Figure B-13 as a function of sheet element width-to-thickness ratio, were derived from test data of Reference B-3. As previously noted with tensile properties, the average test data were reduced to account for strength degradation from elevated-temperature, low-pressure environments. The oxidation effects on TD Ni-20Cr strength presented in Appendix C were used to provide a calculated reduction in compressive allowables.

Shear Strength. The ultimate shear strength for TD Ni-20Cr 0.0508 - 0.152-cm (0.020 - 0.060-in.) sheet material at room temperature and 1,368°K (2,000°F) are shown in Figures B-14 and B-15. The average tensile strength of Heat 3712 material is also shown for longitudinal (Figure B-14) and transverse (Figure B-15) properties for comparison with the shear values. The transverse shear strength is lower than the longitudinal strength by about 2 percent at room temperature and by about 7 percent at 1368°K (2,000°F). Strength decreases of that level fall in the range of tensile property differences between longitudinal and transverse samples in tests reported in References B-1, B-2, B-3, B-4, and B-7.

Fatigue Strength. Figure B-16 presents room-temperature fatigue properties for TD Ni-20Cr sheet while properties at 1,368°K (2,000°F) are shown in Figure B-17. The data of Figure B-16 were obtained primarily from Reference B-1, with a few test points being taken from Reference B-4. The data from both references agree reasonably well, but no clear trend of difference between longitudinal and transverse properties is shown. The data of Figure B-16 were used as a discrete loading base from which reduced fatigue allowables were developed for random loading conditions in acoustic fatigue
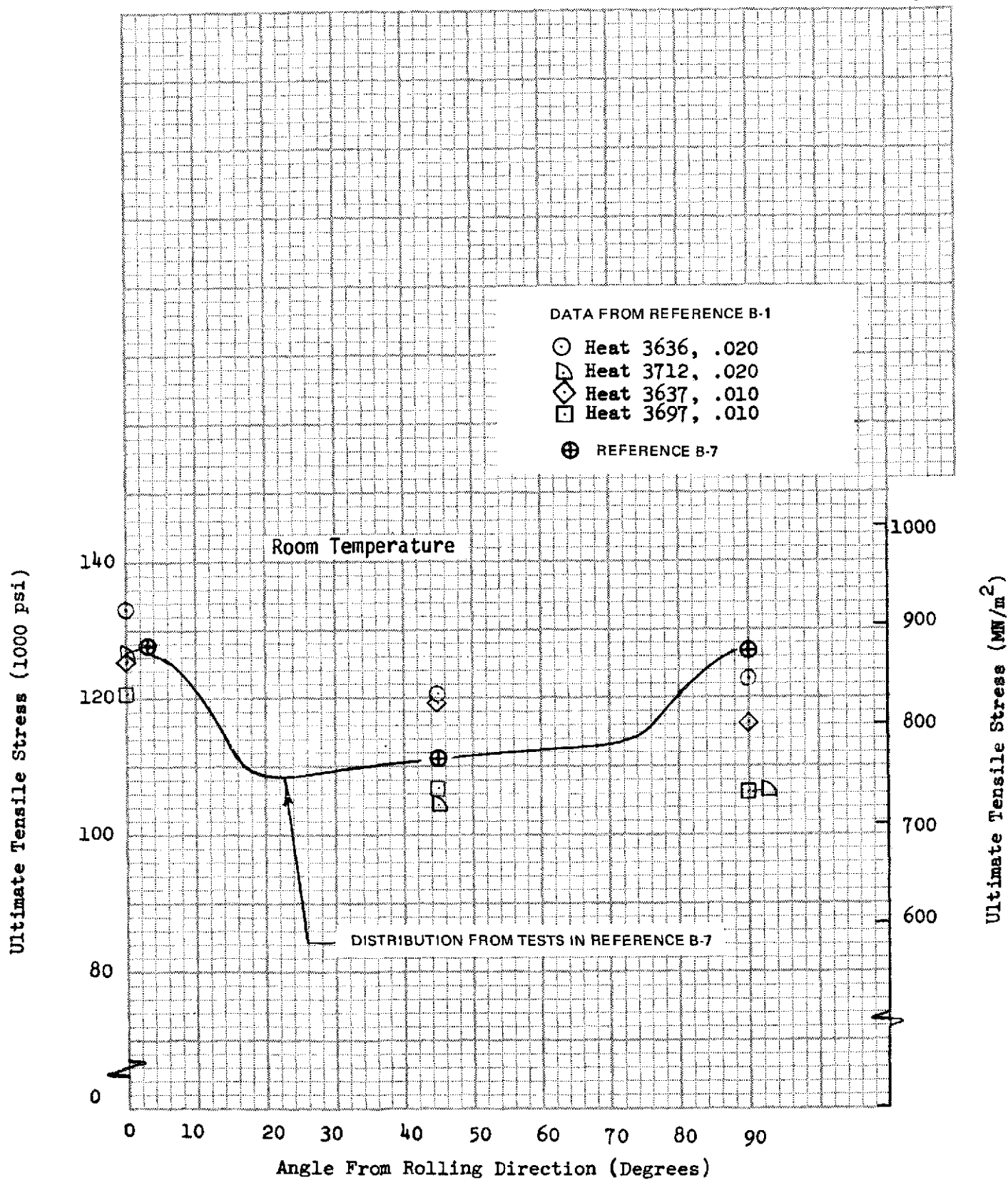
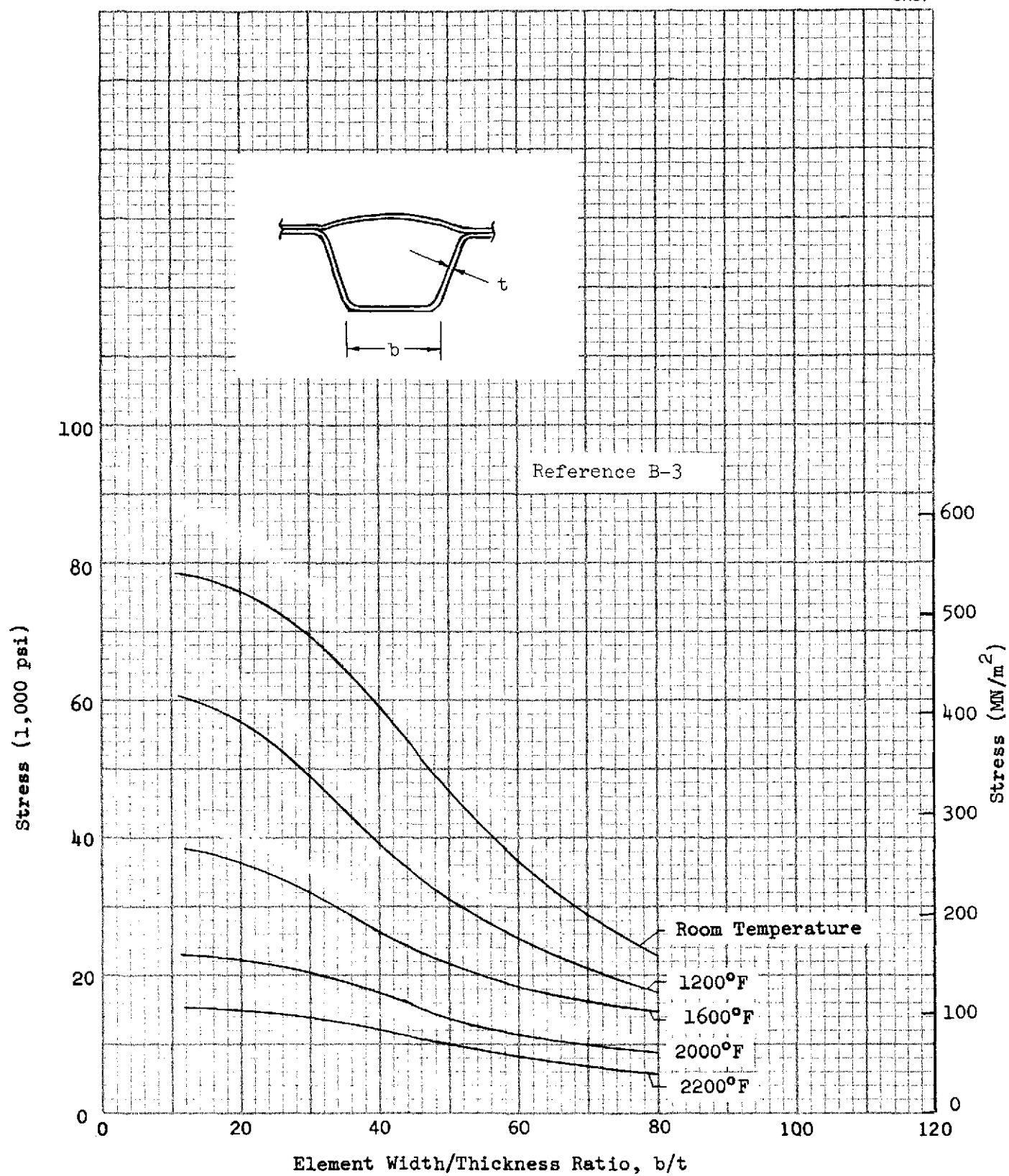Figure B-12. Anisotropic Characteristics of TD Ni-20Cr Sheet

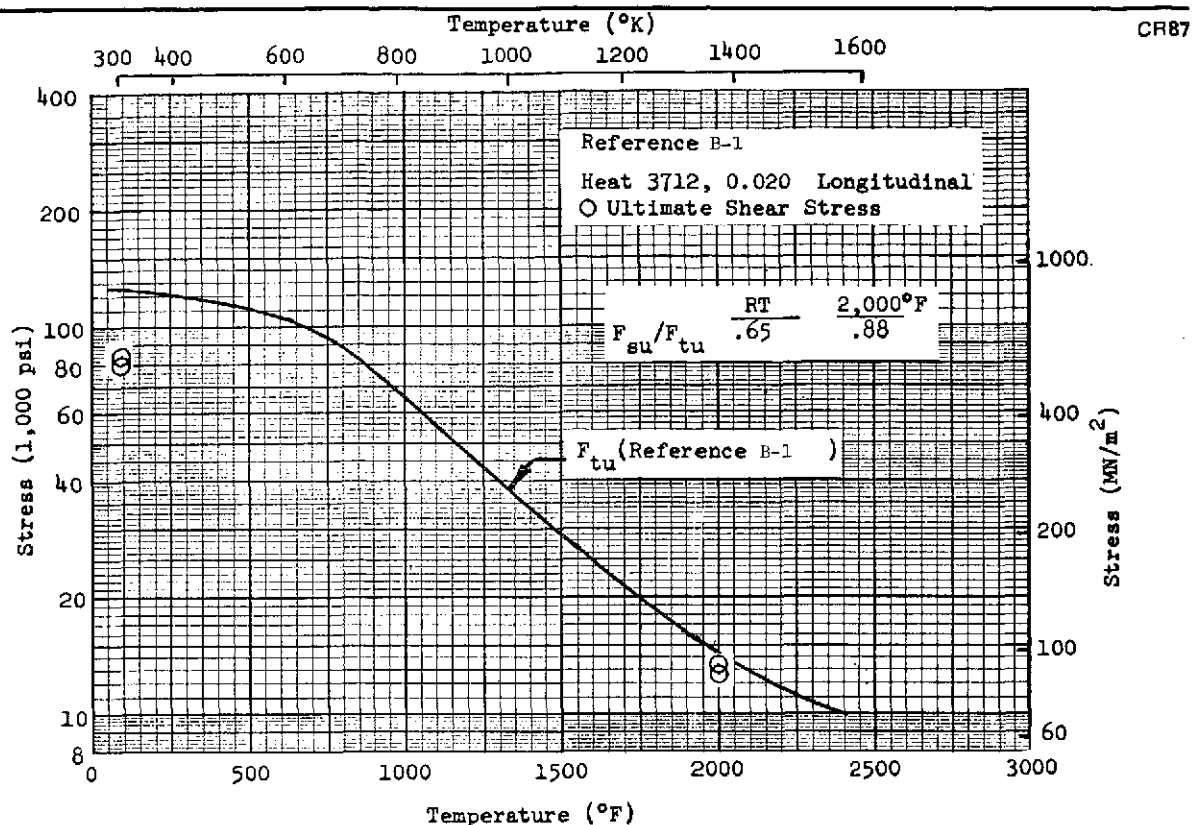Figure B-13. Short Time Compressive Crippling Allowables for Formed Sheet Components

Figure B-14. Comparison of Ultimate Shear and Tensile Longitudinal Strengths for TD Ni-20Cr Sheet
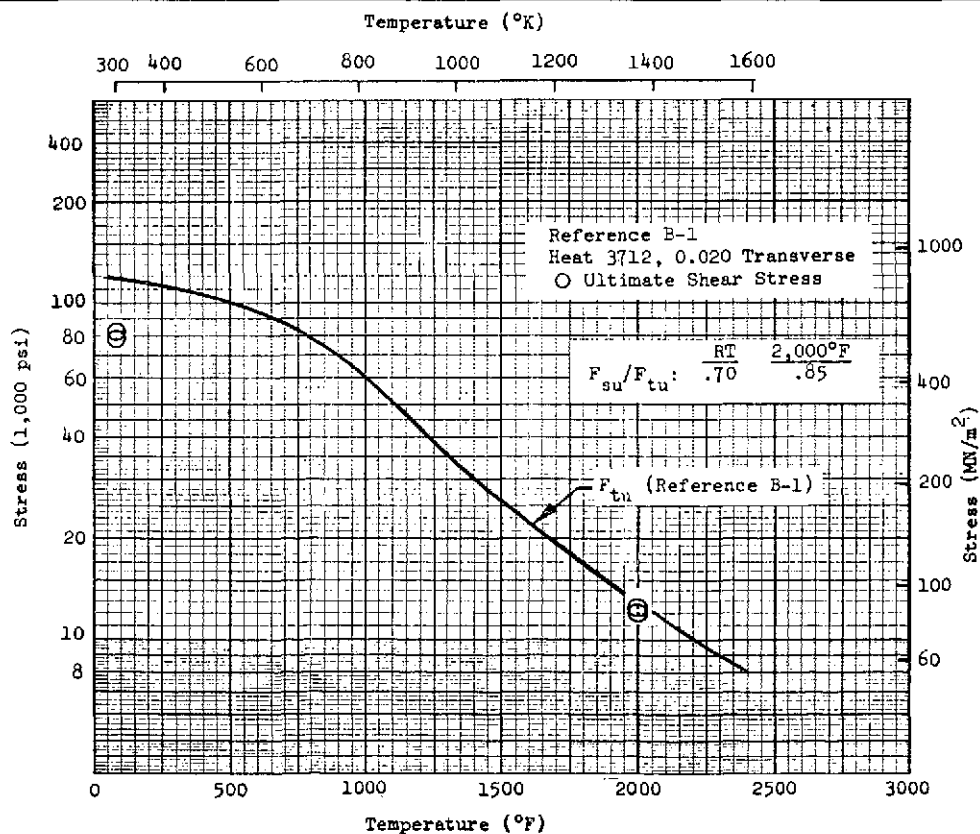

Figure B-15. Comparison of Ultimate Shear and Tensile Transverse Strengths for TD Ni-20Cr Sheet
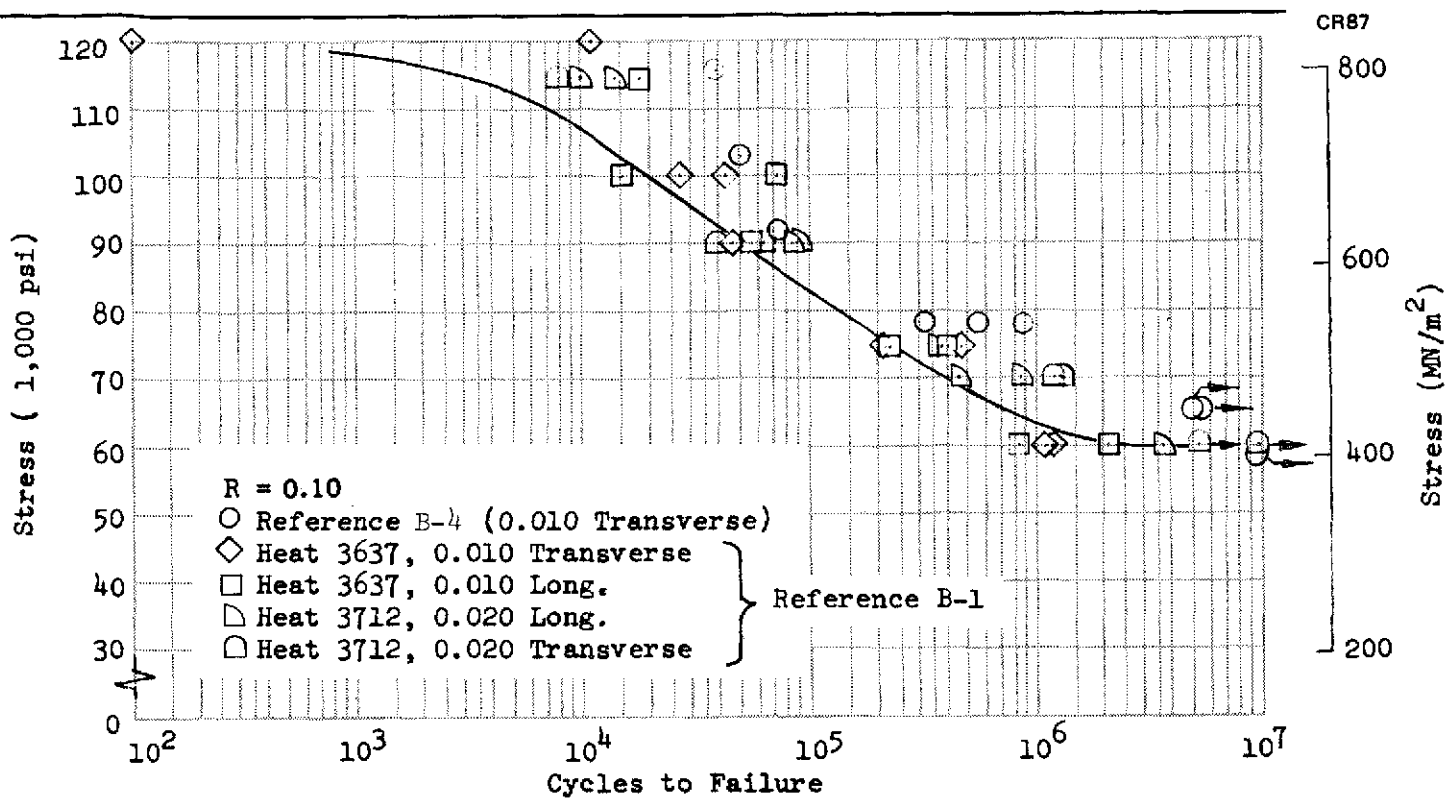
Figure B-16. TD Ni-20Cr Room Temperature Fatigue Strength; Tension-Tension Discrete Loading Tests
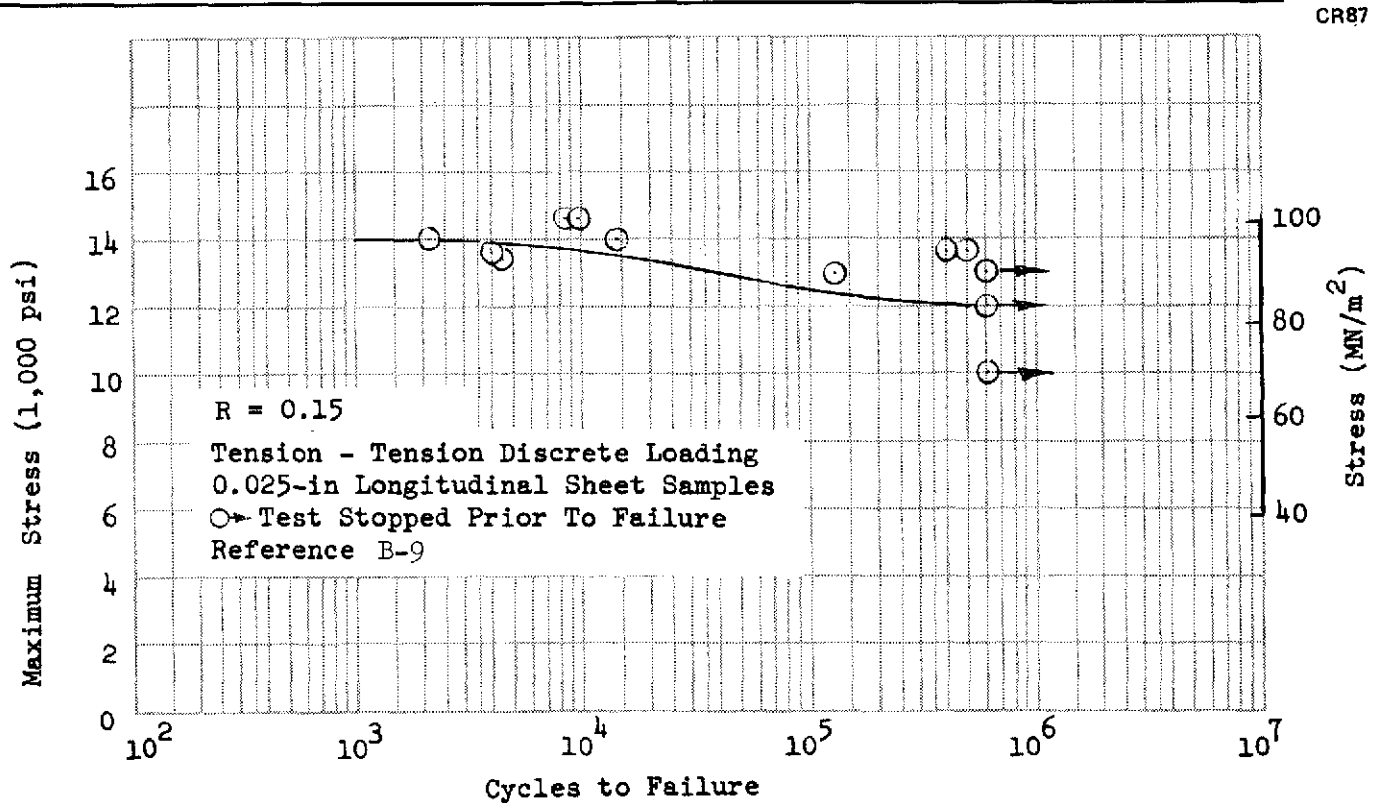

Figure B-17. TD Ni-20Cr Fatigue Strength at 2,000°F

analyses (Appendix D). The fatigue data shown for 1,368°K (2,000°F) were taken from Reference B-9.

Stress Rupture Strength. TD Ni-20Cr sheet stress-rupture strength data are presented in Figures B-18 through B-25. These data cover longitudinal and transverse sample test results ranging from 1,146°K to 1,588°K (1,600°F to 2,400°F) and show constant stress to produce rupture in the time range of 1 to 1,000 hours. As with tensile strength data (Figures B-1 through B-4) the stress rupture data were separated by sheet thickness since it has been noted in previous TD Ni-20Cr tests that the stress rupture properties of 0.0254 cm (0.010-in.) material are slightly lower than those for gages of 0.0508 to 0.152 cm (0.020 to 0.060 in.).

A majority of the data in Figures B-18 through B-25 were taken from Reference B-1. Comparisons at 1146°K (1,600°F) (Figure B-21) with data from Reference B-3 show good agreement.

Creep Strain. Creep strain data for a test time of 100 hours are shown in Figures B-26 through B-29. Data shown were obtained from Reference B-1 and they reflect the cumulative strain at 100 hours for various stress levels. Tests were conducted at 1,143°K (1,600°F), 1,255°K (1,800°F), 1,368°K (2,000°F), and 1,477°K (2,200°F). Longitudinal and transverse sample orientations were used in a majority of the tests; as expected from a review of previous TD Ni-20Cr stress-rupture tests, the transverse samples reached given cumulative strain levels at lower stresses when compared with the longitudinal samples.

The plots of Figures B-26 through B-29 also show the TD Ni-20Cr characteristic in which little or no creep strain is evident until a critical stress level is applied. When the critical stress level is reached, the creep strain increases rapidly with small increases in stress. This nonlinearity in plots of creep strain versus stress for a given time increment is believed to result from the initiation of grain boundary damage when critical stress levels are reached in the material. Grain boundary separation has been observed in posttest microstructure examinations of stress-rupture specimens (Reference B-3), and
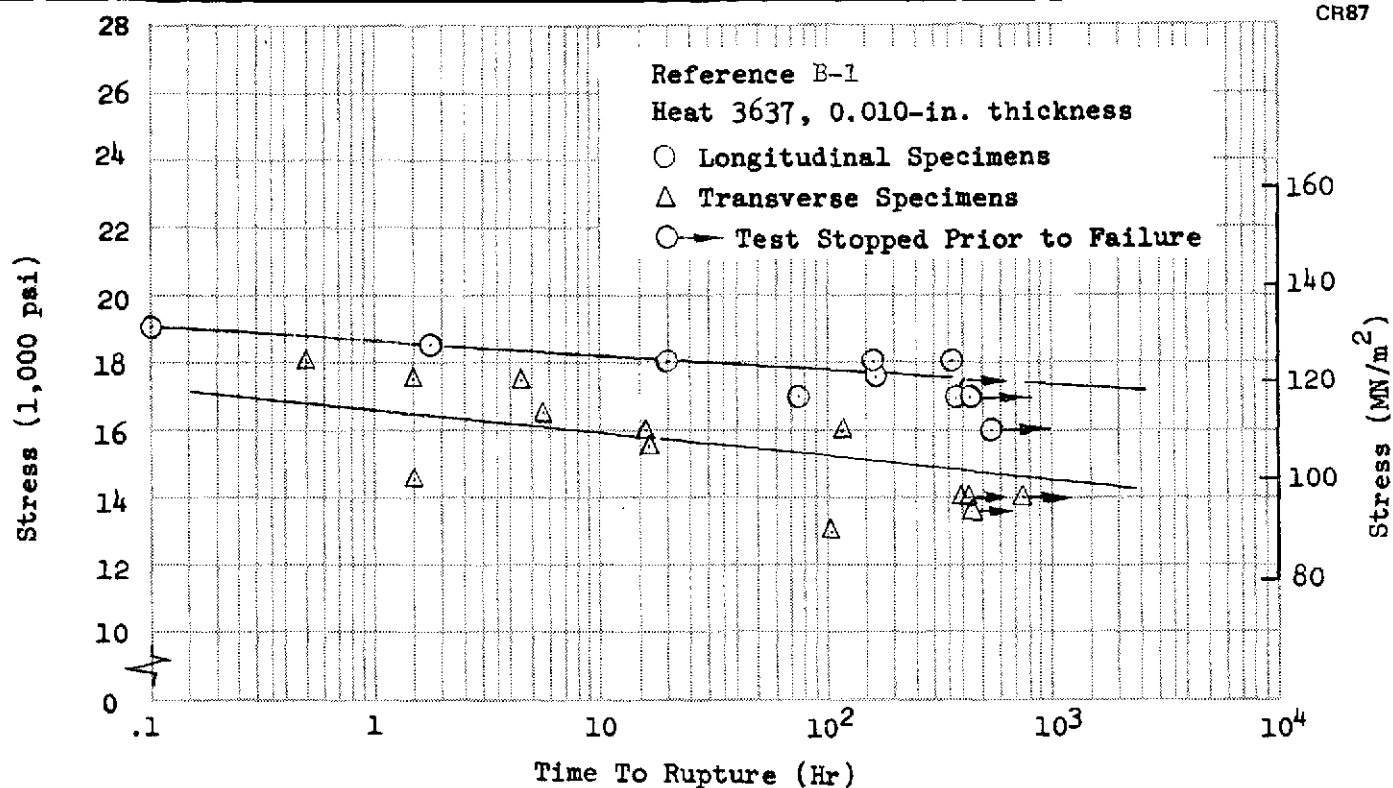
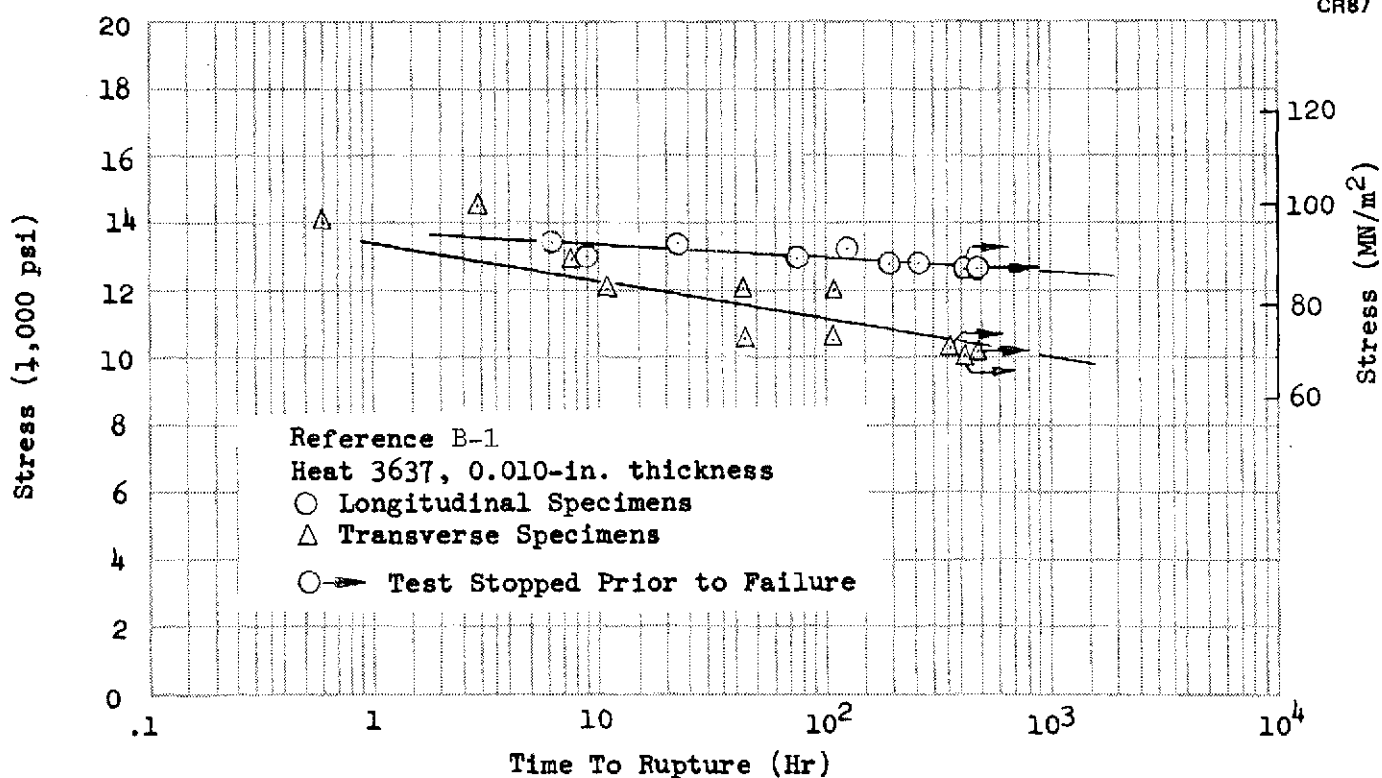Figure B-18. TD Ni-10Cr Stress Rupture Tests; 1,600°F

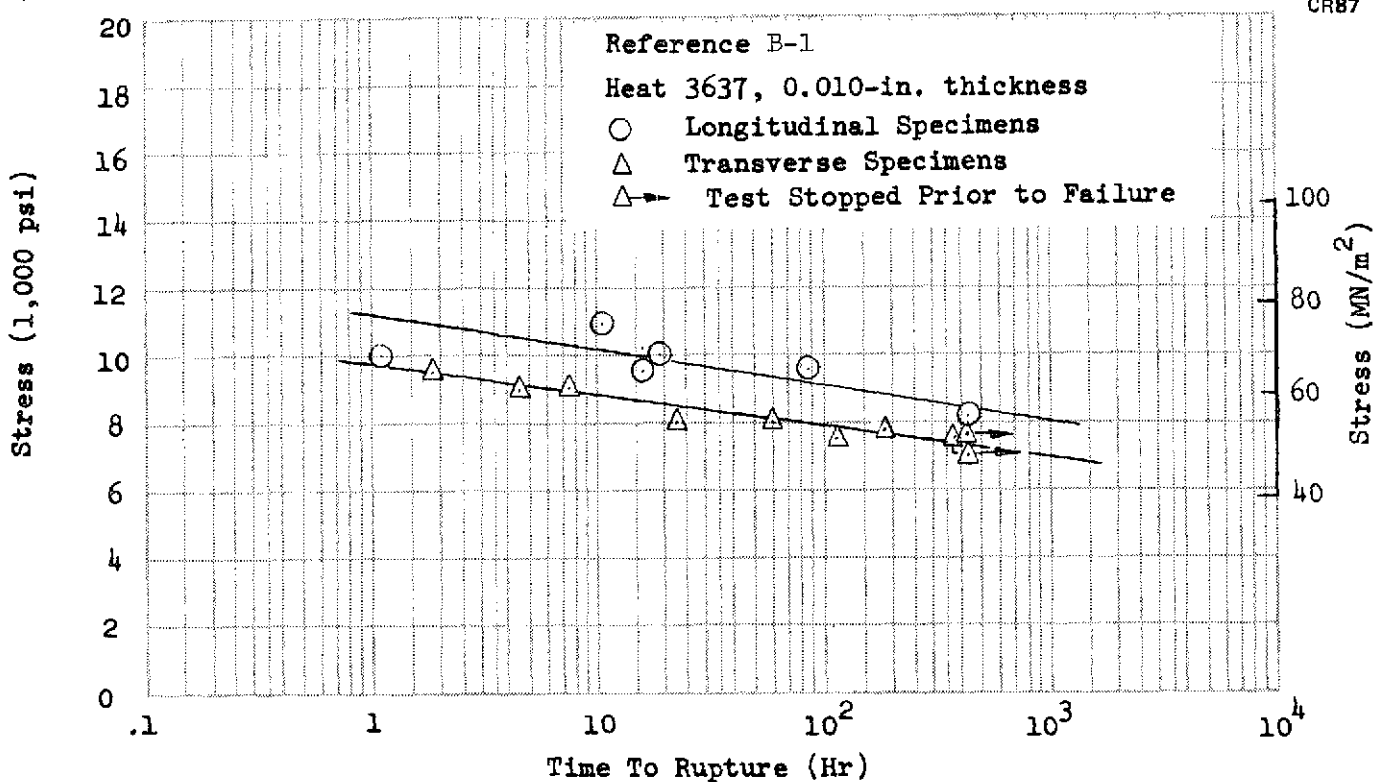Figure B-19. TD Ni-20 Cr Stress Rupture Tests; 1,800°F

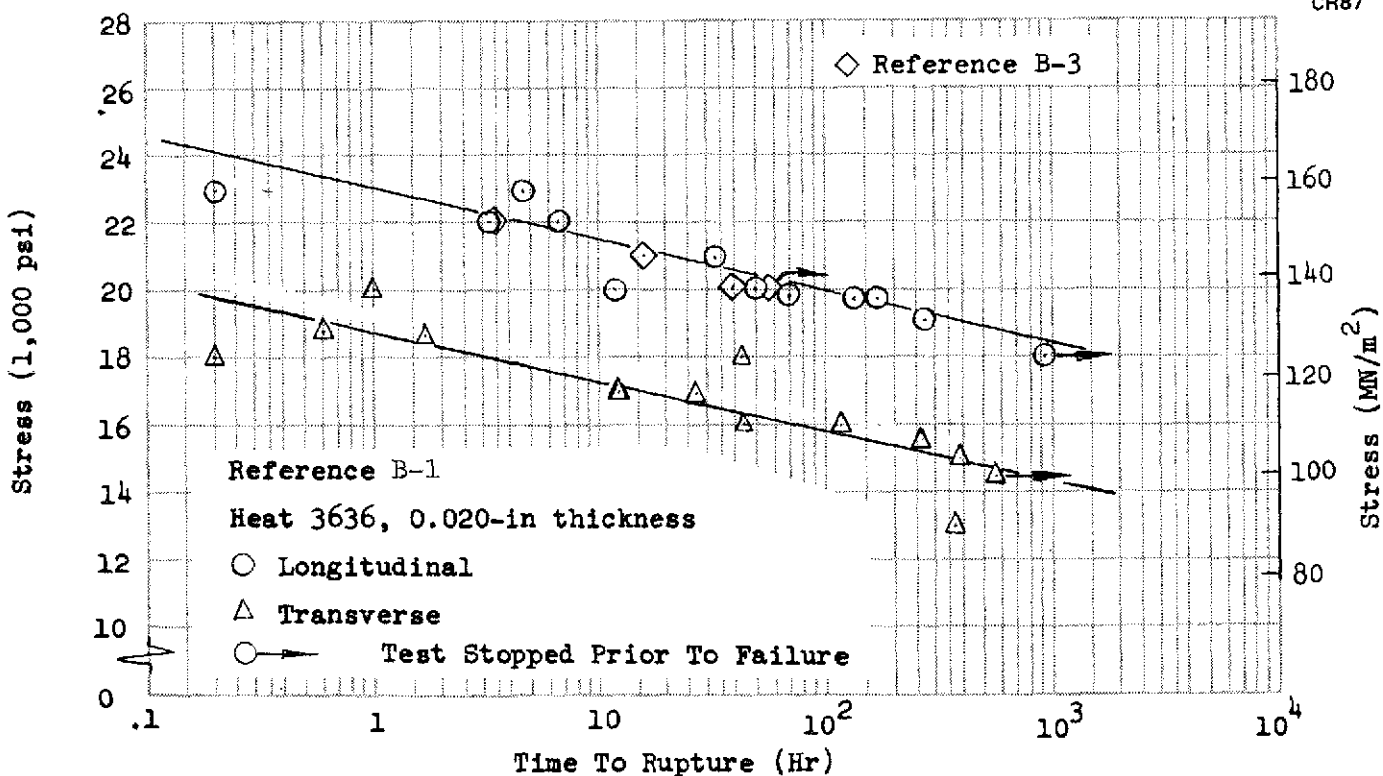Figure B-20. TD Ni-20Cr Stress Rupture Tests; 2,000°F

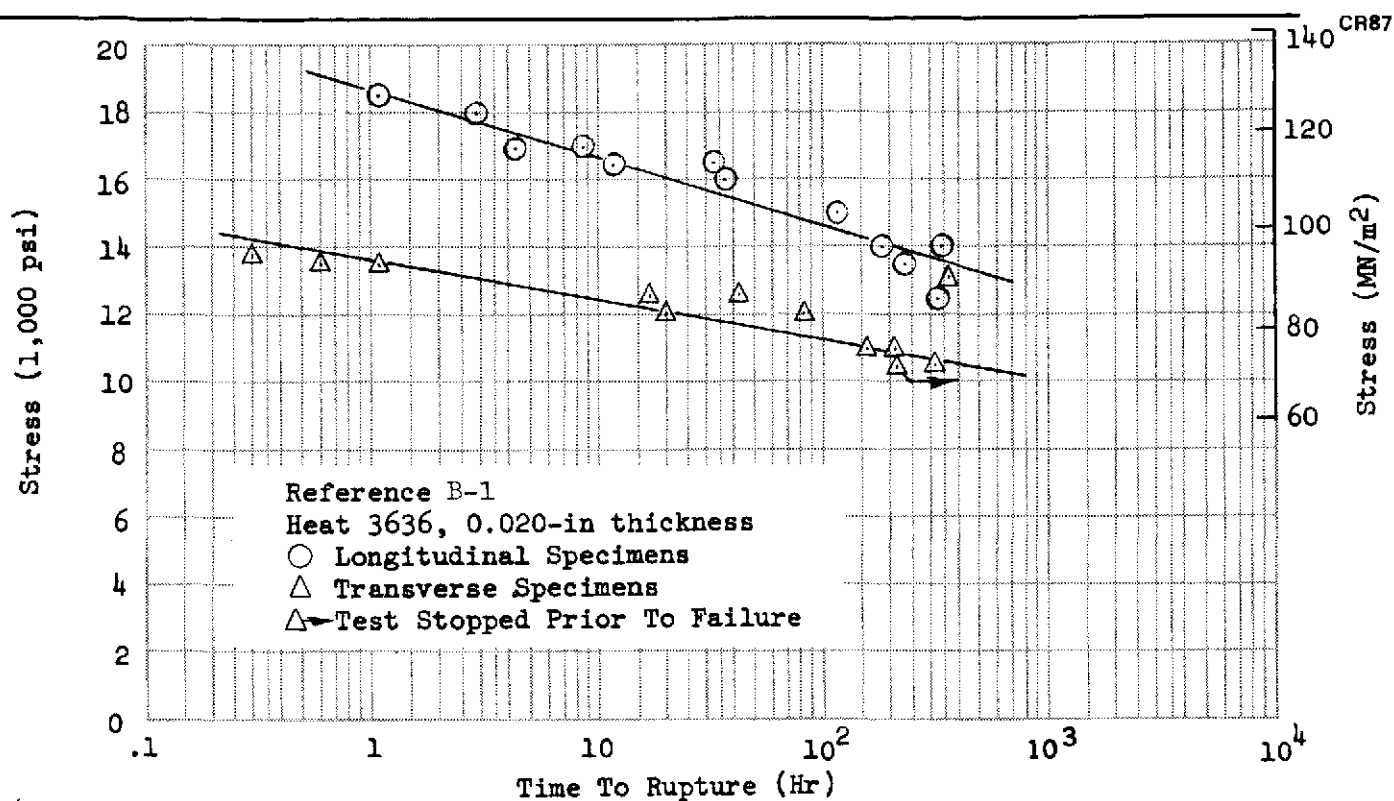Figure B-21. TD Ni-20Cr Stress Rupture Tests; 1,600°F

Figure B-22. TD Ni-20Cr Stress Rupture Tests; 1,800°F
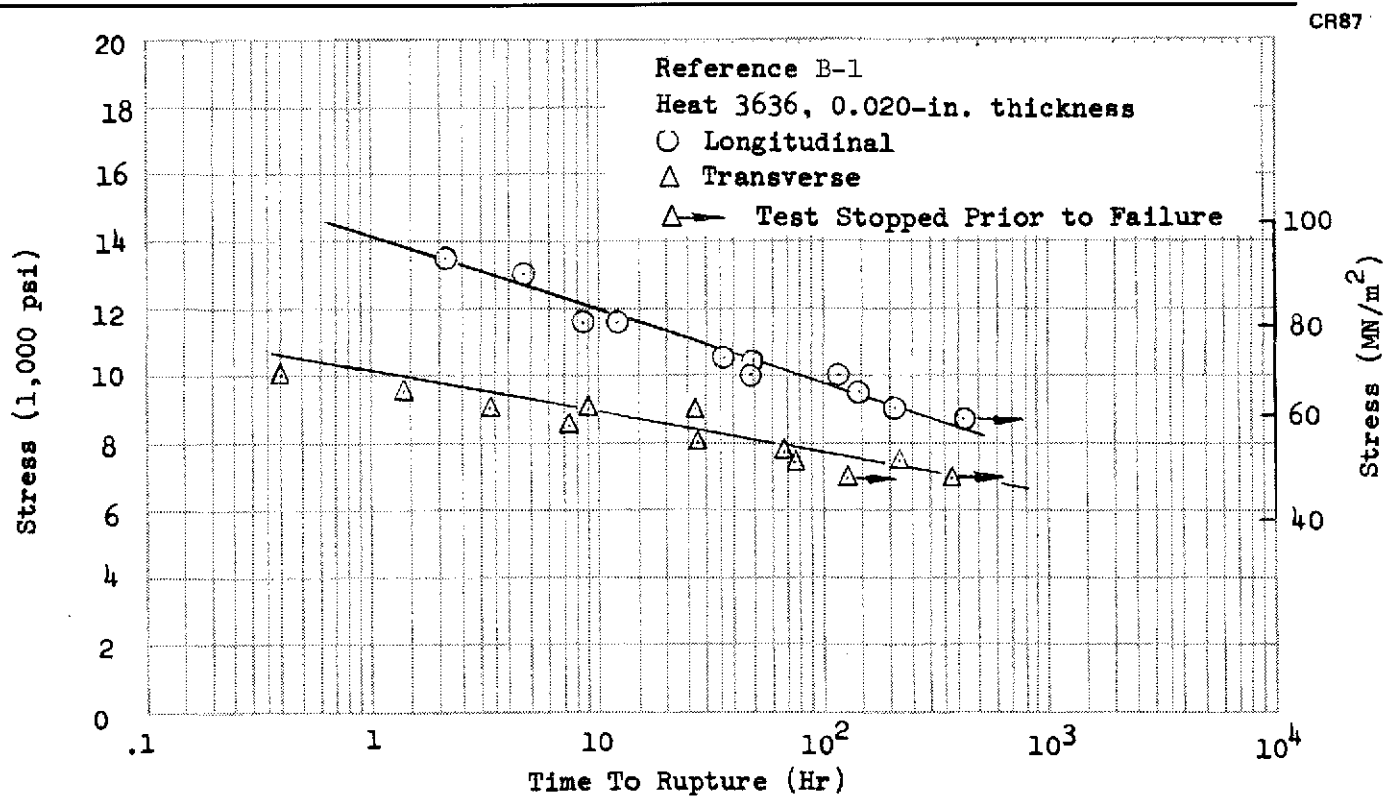

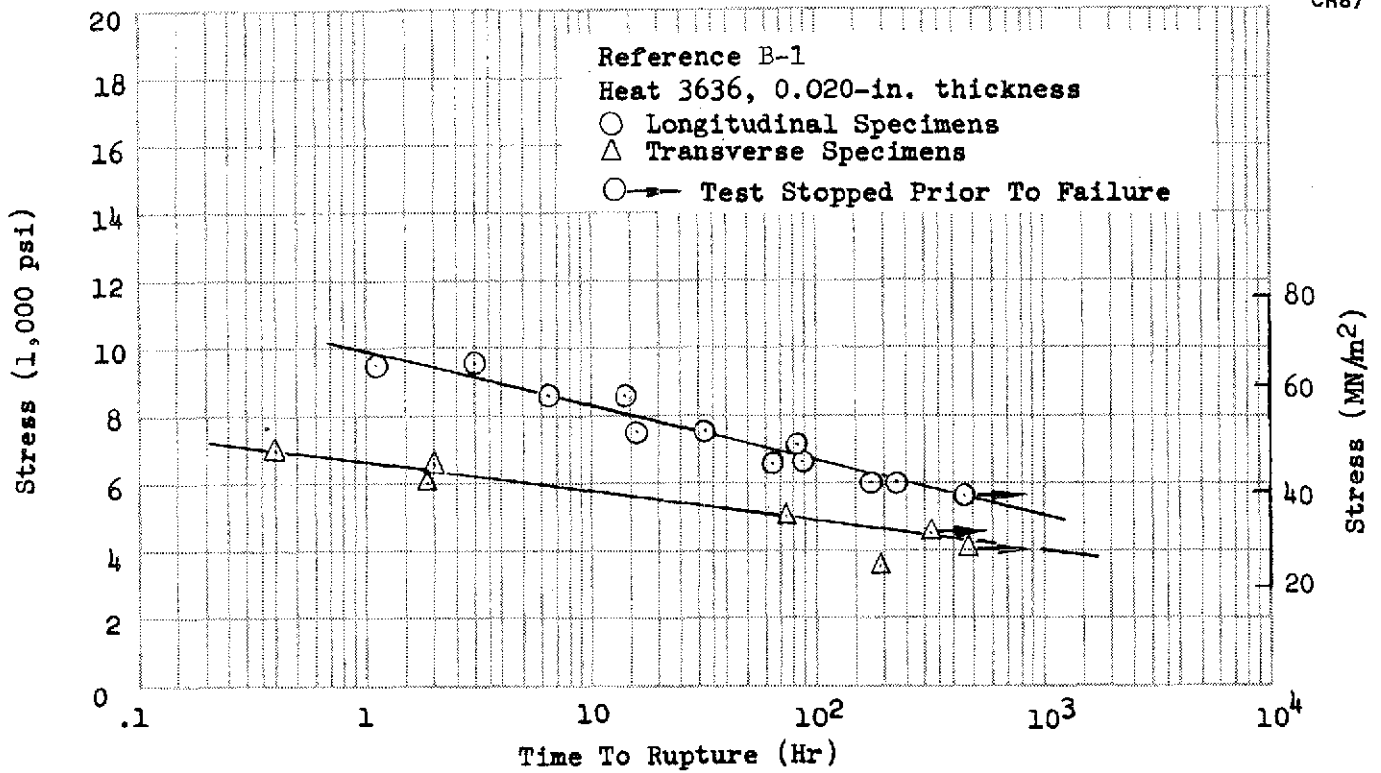Figure B-23. TD Ni-20Cr Stress Rupture Tests; 2,000°F
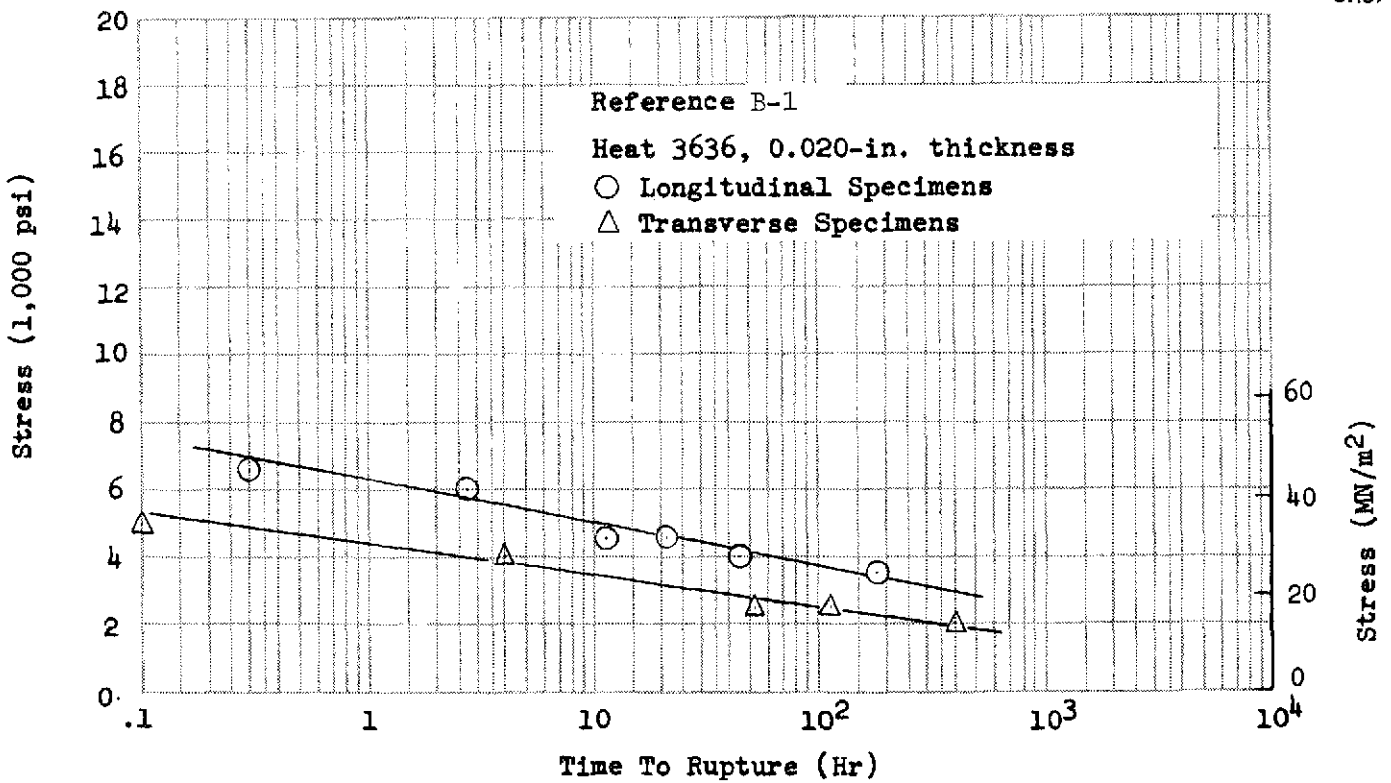
Figure B-24. TD Ni-20Cr Stress Rupture Tests; 2,200°F

Figure B-25. TD Ni-20Cr Stress Rupture Tests; 2,400°F
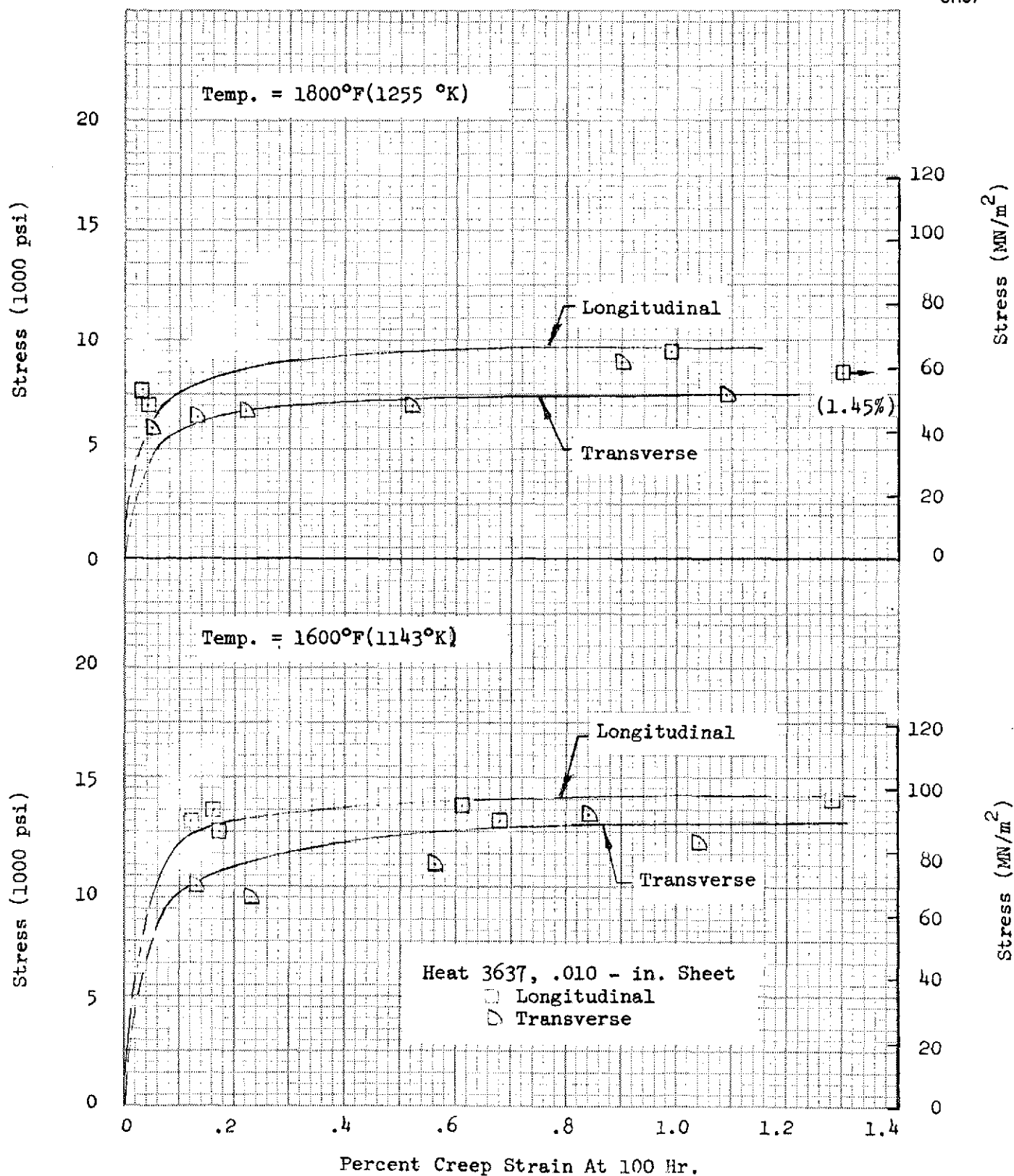
174

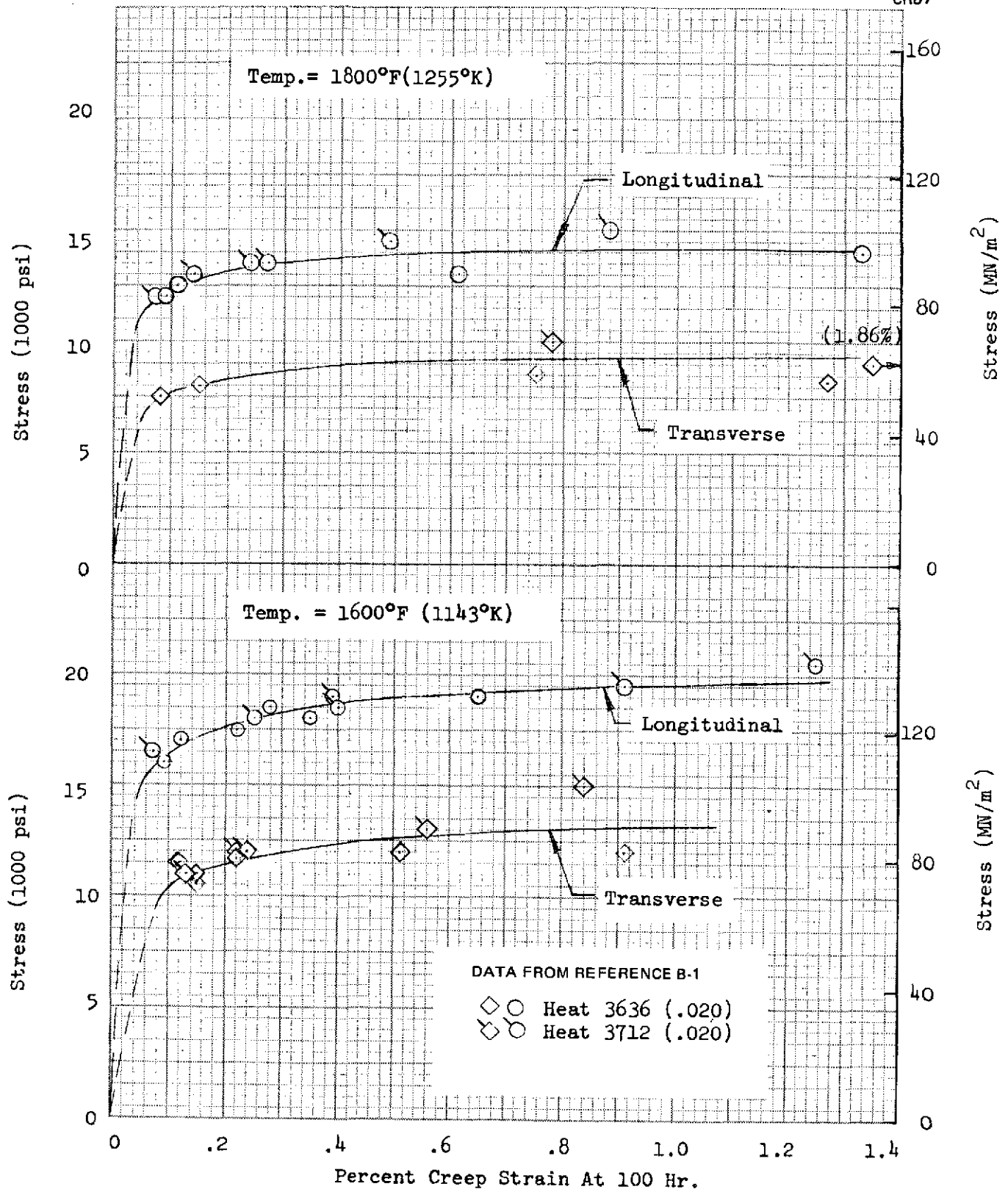Figure B-26. Percent Creep Strain at 100 Hours as Function of Stress

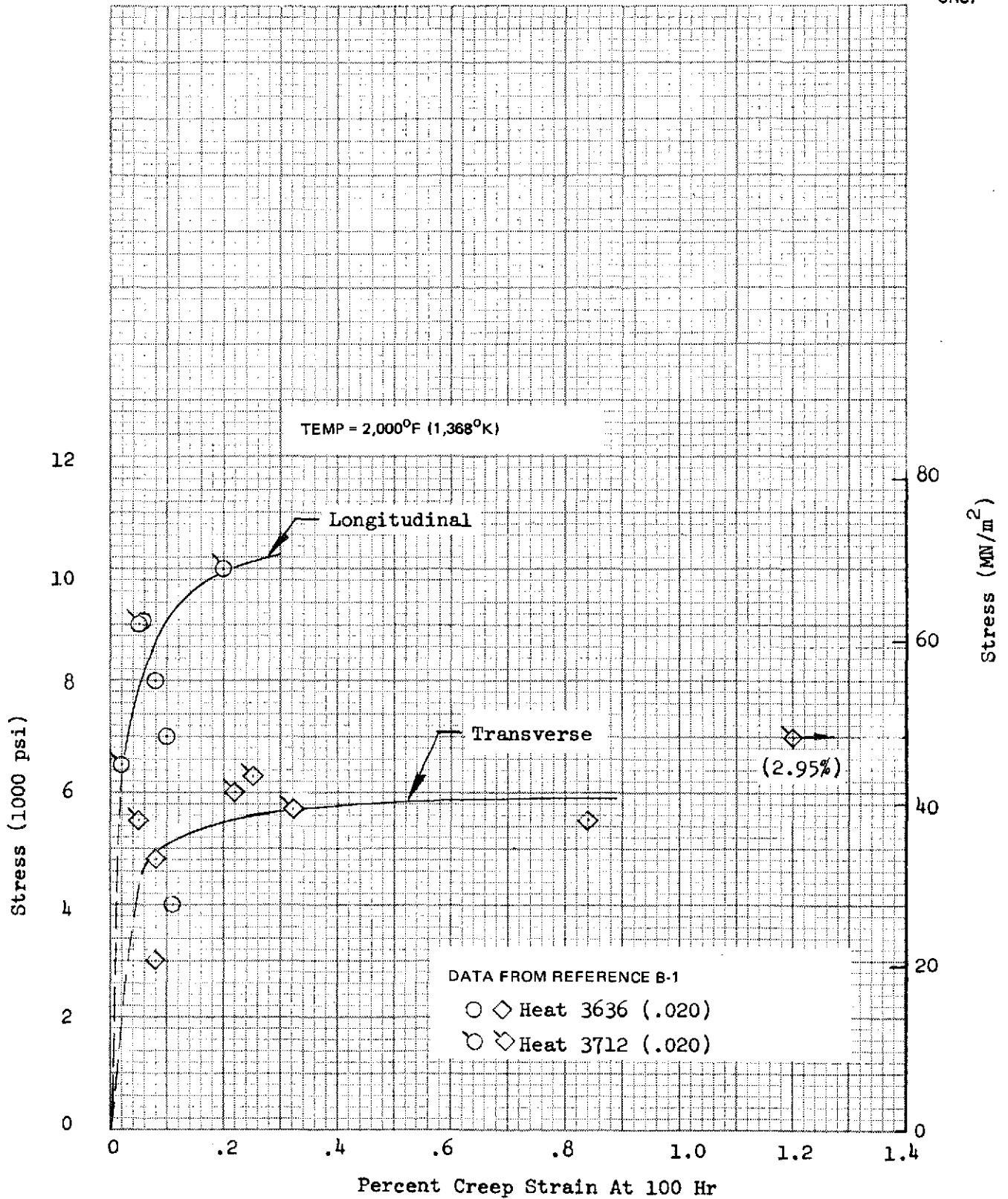Figure B-27. Percent Creep Strain at 100 Hours as Function of Stress

Figure B-28. Percent Creep Strain at 100 Hours as Function of Stress
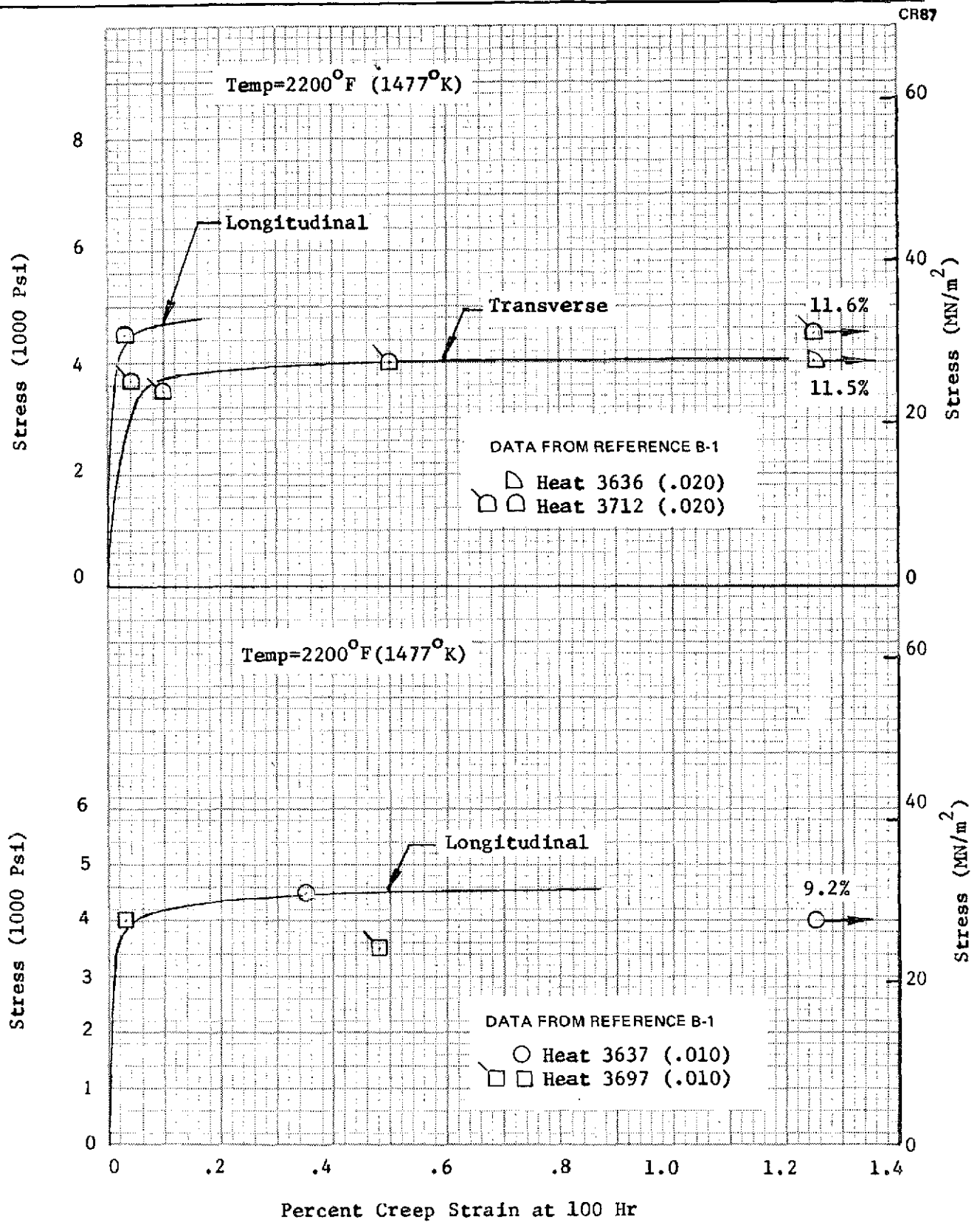
Figure B-29. Percent Creep Strain at 100 Hours as Function of Stress

oxidation at grain boundaries of creep samples has been reported in Reference B-12. The data of Figures B-26 through B-29 indicate that creep from tensile stresses will be minimum for a 100-mission life, provided that the critical stress levels are not exceeded for the service temperatures expected.

Creep strain curves as a function of time are shown in Figures B-30 and B-31 for several levels of stress at $1,255^{\circ}K$ ($1,800^{\circ}F$) and $1,368^{\circ}K$ ($2,000^{\circ}F$). The inherently weaker strength of transverse samples is again apparent in Figure B-31 where the transverse sample, stressed at a lower level, shows larger creep strains than the longitudinal sample.

Linear Thermal Expansion. Linear thermal expansion data for TD Ni-20Cr sheet material between room temperature and $1,588^{\circ}K$ ($2,400^{\circ}F$) is shown in Figure B-32. Test data from Reference B-1 cover a slightly higher range of temperature and were obtained with recently produced material, while data from Reference B-10 are included for comparison. Both sets of data show reasonable agreement, but the curve for use in this program was based upon the data of Reference B-1 since it represents the latest production TD Ni-20Cr sheet material.

Thermal Conductivity. Data from thermal conductivity tests conducted as a part of contract NAS 3-15558 (Reference B-1) are presented in Figure B-33.

Specific Heat. Test data for specific heat values, shown in Figure B-34, were taken from the work conducted under Contract NAS 3-15558, (Reference B-1). Data for Ni-20Cr material (Reference B-11) showed good agreement with the values shown in Figure B-34.

Total Hemispherical Emittance. Data for total hemispherical emittance as a function of temperature are shown in Figure B-35 from two sources, References B-1 and B-3. The data from Reference B-3 are considered more applicable to structures that will be produced in this program since the preliminary processing by use of light-grit impingement is the preferred process and produces a higher emittance.
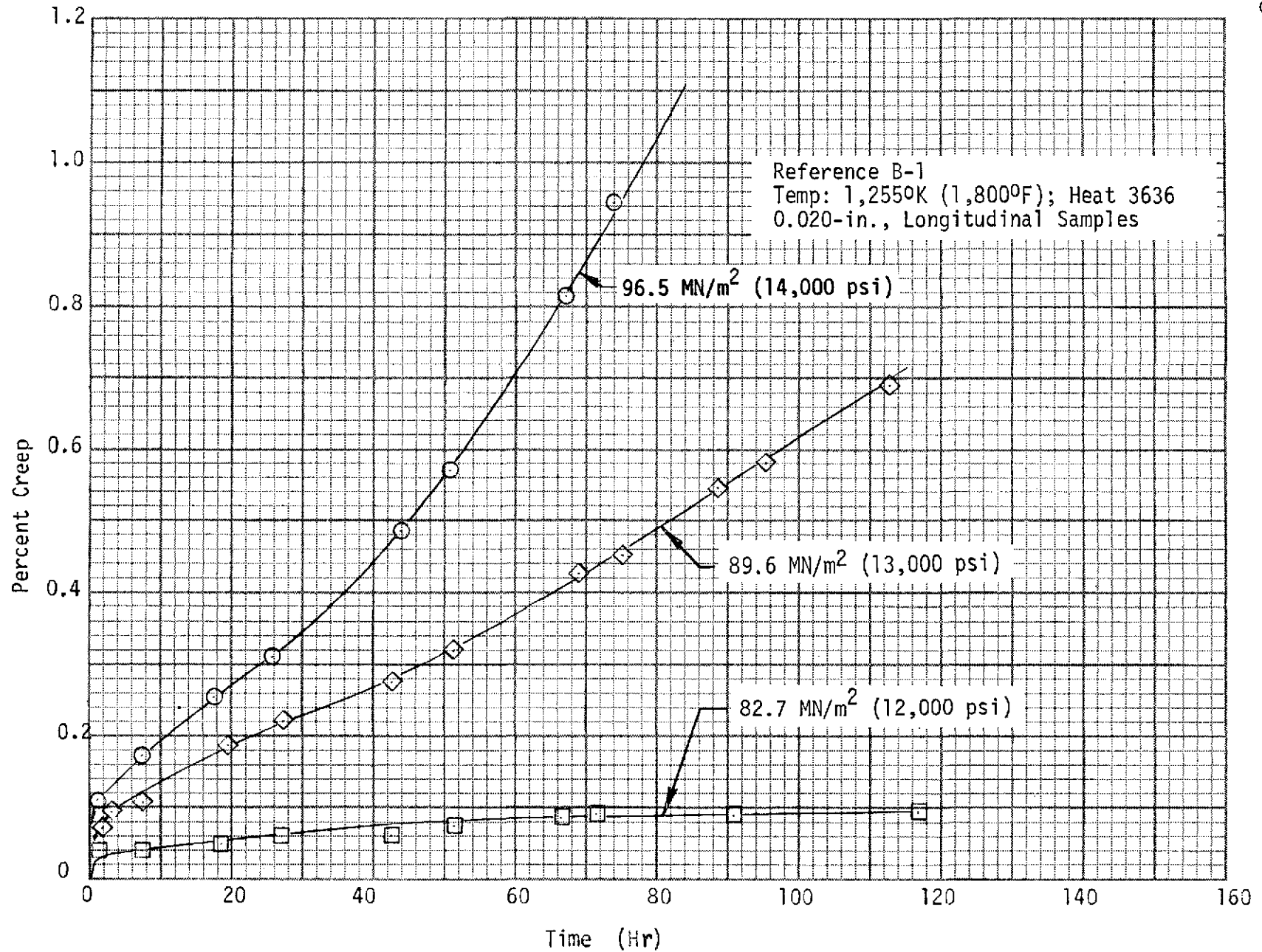
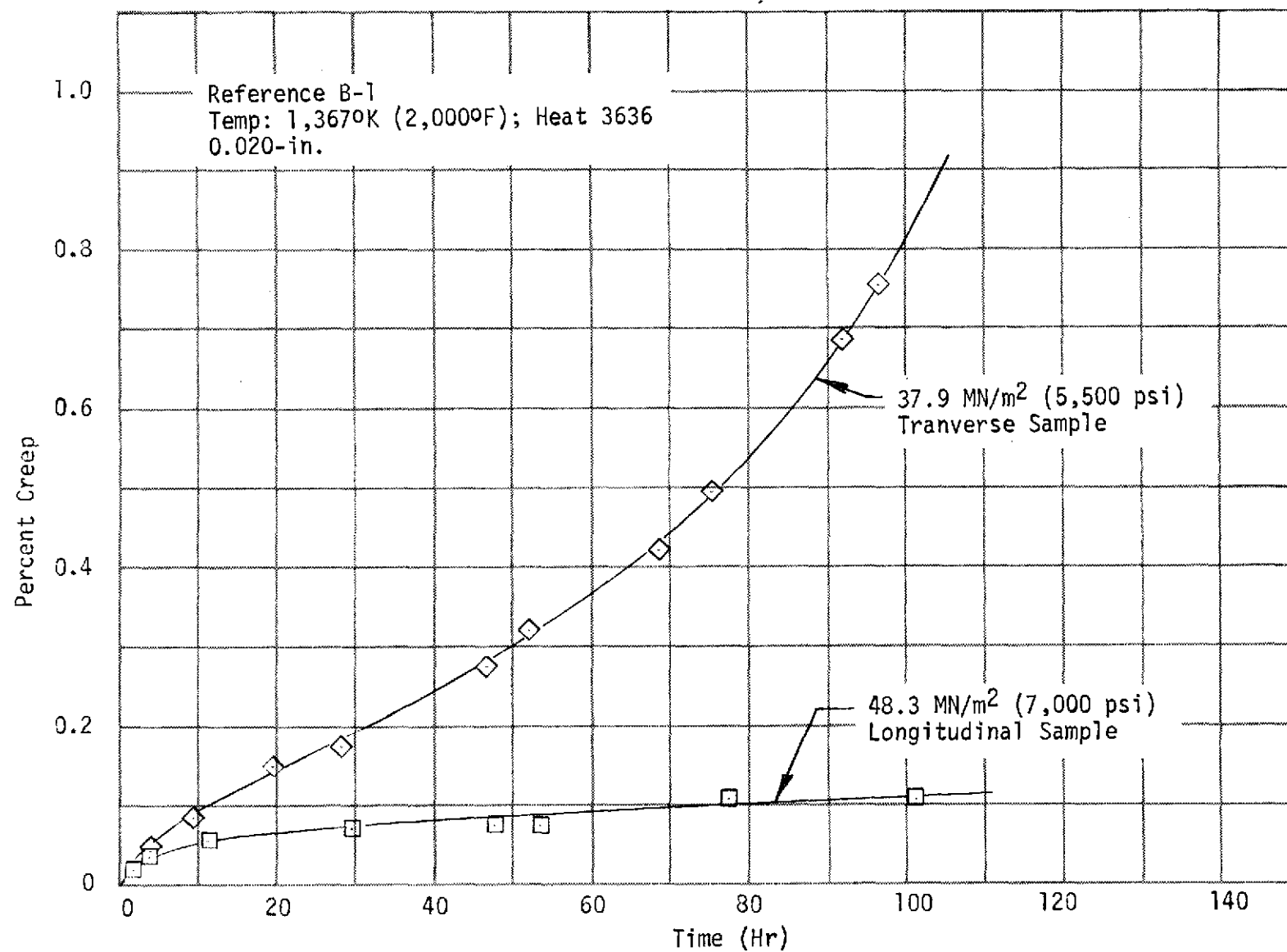Figure B-30. Creep Strain Versus Time for TD Ni-20Cr Sheet

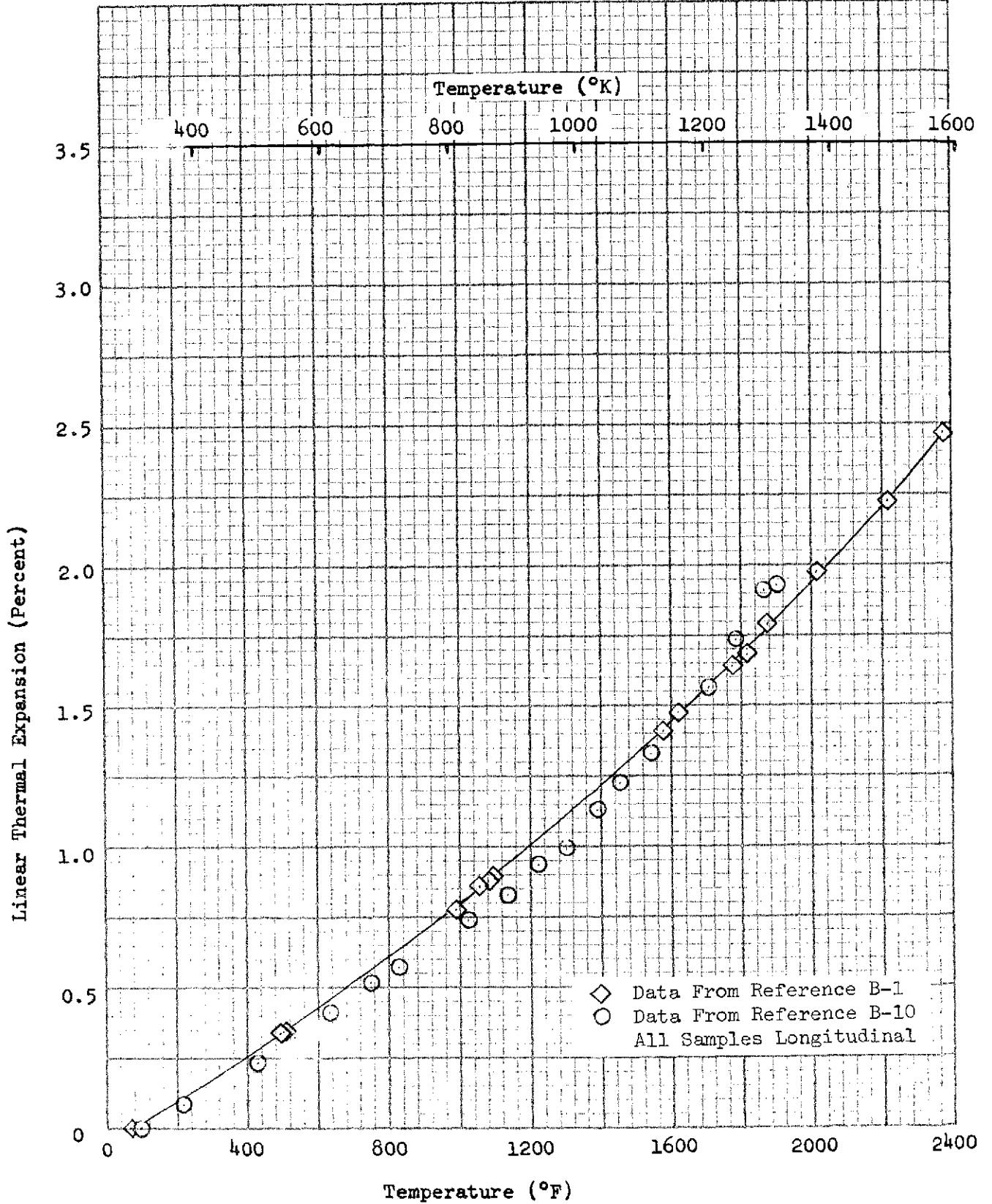Figure B-31. Creep Strain Versus Time for TD Ni-20Cr Sheet

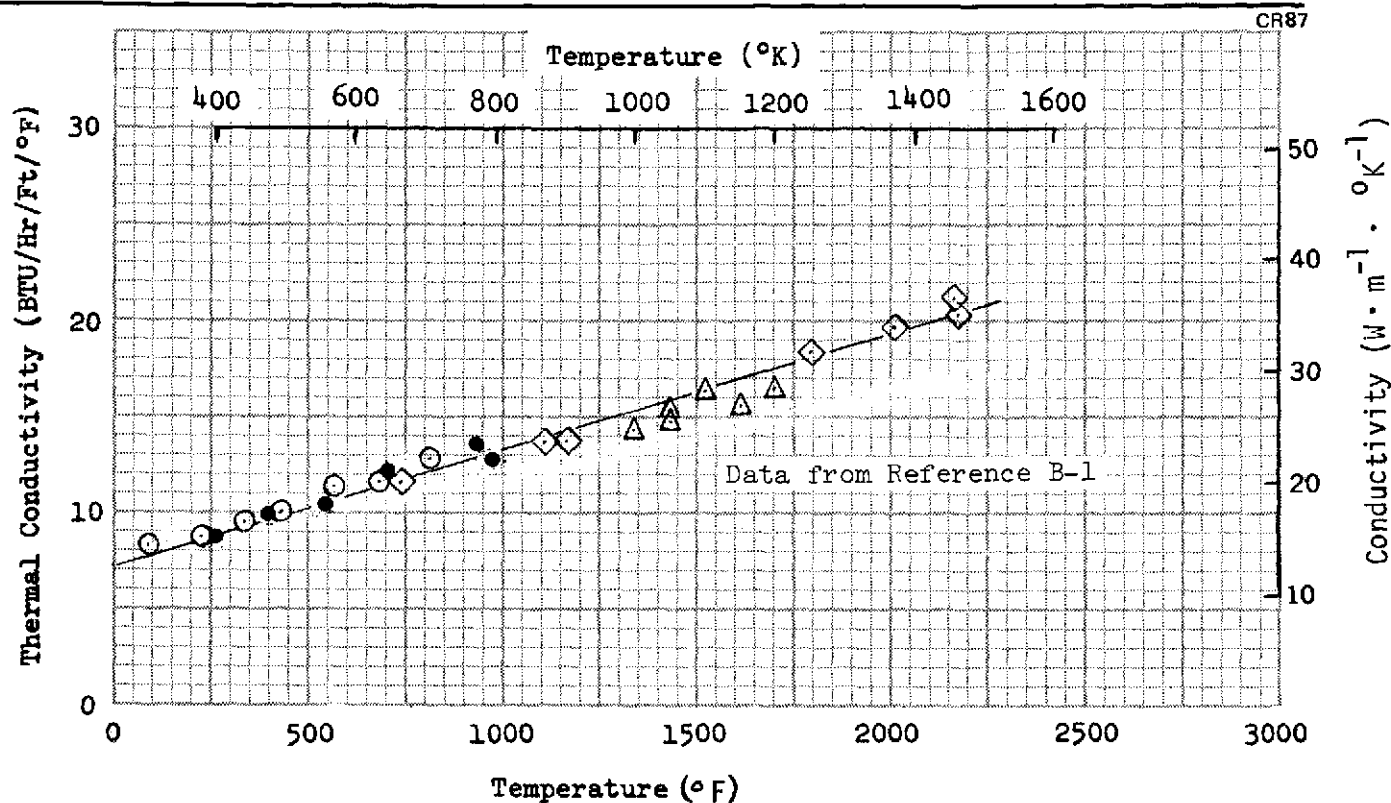Figure B-32. Linear Thermal Expansion of TD Ni-20Cr
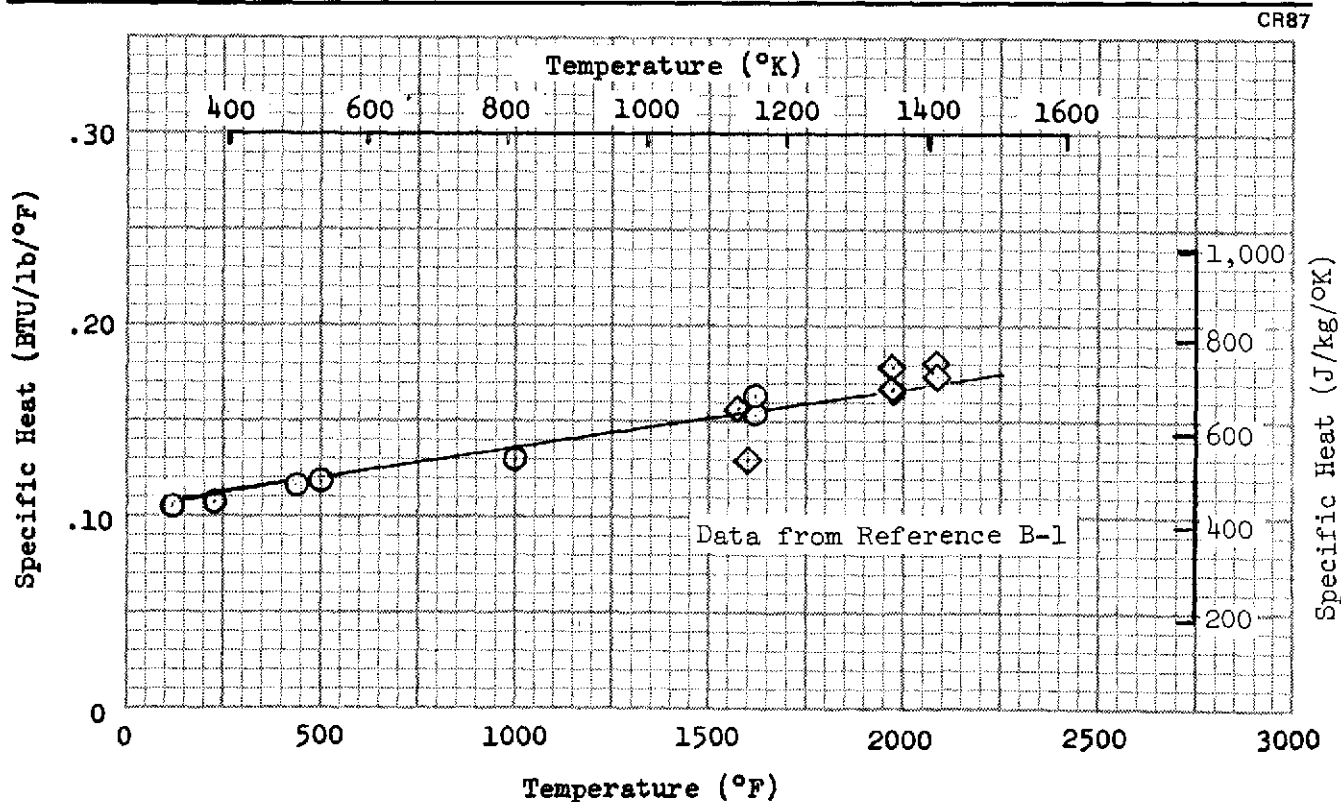
Figure B-33. Thermal Conductivity of TD Ni-20Cr
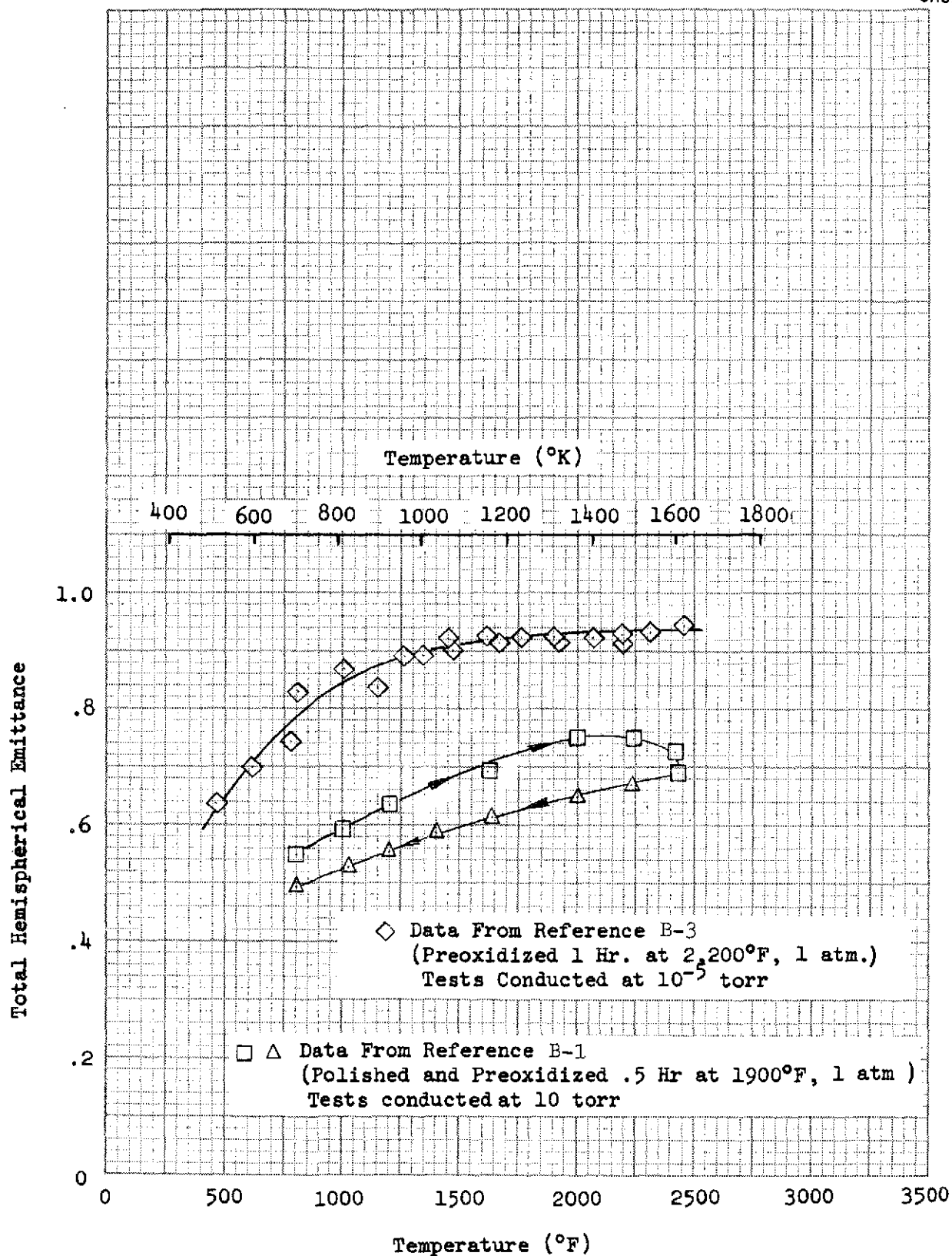

Figure B-34. Specific Heat of TD Ni-20Cr

Figure B-35. Total Hemispherical Emittance of TD Ni-20Cr

Appendix B

REFERENCES

B-1.   Fritz, L. J. Characterization of the Mechanical and Physical
        Properties of TD Ni-Cr (Ni-20Cr-2ThO$_2$) Alloy. Contract
        NAS 3-15588, Monthly Report Nos. 1 through 15, 7 July 1971-
        1 October 1972.

B-2.   Johnson, R. Jr. Dispersion-Strengthened Metal Structural Develop-
        ment. Air Force Contract F33615-67-C-1319, R&D Status Summary
        Report No. 26, 1 April 1970.

B-3.   Johnson, R. Jr., and Killpatrick, D. H. Dispersion-Strengthened
        Metal Structural Development. AFFDL TR-68-130 Part 1,
        October 1968.

B-4.   Malik, R. K., and Stetson, A. R. Evaluation of Superalloys for
        Hypersonic Vehicle Honeycomb Heat Shields AFML-TR-68-292,
        October 1968.

B-5.   Yount, R. E., Kutchera, R. E., and Keller, D. L. Development of
        Joining Techniques for TD Nickel Chromium. AFML-TR-68-224
        (1967).

B-6.   Hocker, R. G., and Killpatrick, D. H. Preliminary Evaluation of
        Dispersion Strengthened Nickel-Chromium Alloy for Heat Shield
        Applications, Douglas Report DAC 59534 (1966).

B-7.   Killpatrick, D. H. and Young, J. D. Texture and Room Temperature
        Mechanical Properties of Dispersion-Strengthened NiCr Alloys.
        Met. Trans. 1955-1961 (1970).

B-8.   Dotson, C. L. Crack Propagation and Tensile Tests of TD NiCr
        Sheet. Contract NAS 8-21781, Interim Report dated 14 December
        1971.

B-9.   Unpublished Test Data. Test conducted by McDonnell Douglas
        Astronautics Company, 1970.

B-10.   Gaz, R. A. Linear Thermal Expansion of Dispersion-Strengthened
        Nickel-Chromium Alloy. Report MP 50363, McDonnell Douglas
        Astronautics Company, February 1967.

B-11.   Douglas, T. B. and Victor, A. C. Enthalpy and Specific Heat of
        Nine Corrosive-Resistant Alloys at High Temperature, Journal
        of Research of NBS. 65C, 65-69 (1961).

B-12.   Whittenberger, J. D. Diffusional Creep and Creep-Degradation
        in the Dispersion-Strengthened Alloy TD-NiCr. NASA TN D-7079,
        December 1972.

APPENDIX C

TD Ni-20Cr STRENGTH REDUCTION FROM OXIDATION EFFECTS

Appendix C
TD Ni-20Cr STRENGTH REDUCTION FROM
OXIDATION EFFECTS

Decreases in the strength of TD Ni-20Cr have been observed after exposure to reduced pressure conditions. In applications such as Space Shuttle an estimate of this decrease is required. This estimate can be done either experimentally or theoretically. In this appendix the theoretical approach is described; sample computed strength degradations are shown for specific temperature and pressure conditions; and comparisons between analyses and tests are presented. Computed degradation values were applied to the TD Ni-20Cr strength allowables, and strength decreases in tensile samples subjected to cyclic tests in a modified Astrofurnace facility were compared with the computed degradation.

In this study, loss of chromium is proposed as the basic method by which the strength of TD Ni-20Cr is degraded upon exposure to elevated-temperature, low-pressure environments. This loss of strength is attributed to two different causes which are considered to be additive. The first is the loss of solid solution strengthening due to the loss of average chromium concentration in the sample. The second is loss in cross section due to the loss in mass.

The loss of chromium can be attributed to two different mechanisms, oxidation and vaporization. In this calculation only one of the mechanisms is considered to be operative in a given environmental condition. At a given temperature the method of chromium loss can be separated into three pressure regions.

In the low pressure region, where the partial pressure of chromium vapor over the TD Ni-20Cr is greater than the ambient pressure over the alloy, sublimation occurs. The concentration of the chromium is reduced to that concentration at which the vapor pressure of chromium is equal to the ambient pressure. The loss of chromium is then diffusion controlled.

At high pressures (near one atmosphere) the chromium is oxidized to Cr_2O_3. The Cr_2O_3 further oxidizes to CrO_3 which is volatile. As the pressure is

reduced, the rate of volatilization of CrO_3 increases. This will occur until the rate of loss of chromium by the volatilization of CrO_3 is faster than the rate of diffusion of chromium to the surface. Below this pressure and above the pressure at which chromium is volatilized directly, the loss of chromium is by the volatilization of CrO_3 but is diffusion controlled. In this region, it is assumed that the surface concentration of chromium in a nickel-chromium alloy which is in equilibrium with Cr_2O_3 is about 5 percent chromium. This is based upon the observations that below about 5 percent chromium, only NiO is formed (Reference C-1). In this reduced pressure region, sufficient oxygen is present to oxidize chromium (Reference C-2).

Thus the fraction loss of chromium can be determined as a function of exposure condition. Using this value the strength loss can then be calculated. The strength loss will be made up of two parts. The part due to loss of cross section due to loss of chromium is calculated directly. The second portion is due to the loss of solid solution strengthening by the loss of chromium. For this portion the strengthening effect of chromium in the dispersion-strengthened alloys is assumed to be parabolic similar to that observed in dispersion free nickel-chromium alloys by Pelloux and Grant (Reference C-3). The calculation is based on an average concentration in the final alloy, i.e., if the Ni-20Cr alloy has lost 25 percent of the chromium, the strength calculation is based on a 15 percent chromium alloy.

In the following sections values are computed for the various parameters necessary to calculate the strength loss and sample calculations are shown for the expected loss from several exposure conditions.

Volatilization

The pressure of chromium vapor over pure chromium has been determined (Reference C-4). Using data from Reference C-4 and assumming that Raoult's Law applies in the case of nickel-chromium alloys the partial pressure of chromium vapor P_{Cr} average, the alloy is just equal to

$$P_{Cr} = (P_{Cr}°)(X_{Cr}) \qquad (1)$$

where P_{Cr}° is the vapor pressure over pure chromium and X_{Cr} is the atomic percent of chromium in the alloy. Using this relationship and the data from Reference C-4, values for the pressure at which chromium vapor is in equilibrium with nickel-chromium alloys with different amounts of chromium have been calculated and are plotted in Figure C-1.

Oxidation

The values for loss of chromium published by Hagen (Reference C-5) were used. The values for the loss of weight due to CrO_3 volatilization at a pressure of 0.1 atm oxygen are computed from the equation

$$\frac{\Delta M}{A} = -\beta K_v t \tag{2}$$

where β is weight fraction of chromium in Cr_2O_3, t is time in seconds, K_v is the volatilization-rate constant for loss of Cr_2O_3 by CrO_3 formation and is given by

$$K_v^{Cr_2O_3} = 0.214e^{-(48,800 \pm 3000/RT)} \; g/cm^2\text{-sec} \tag{3}$$

However, in the case of interest the loss of chromium is not necessarily at 0.1 atmosphere. In entry the pressure may vary from between about 0.01 torr and 760 torr. Consequently the pressure dependance of K_v must be determined. No information is available for the pressure dependance of K_v for Cr_2O_3, but Dushman (Reference C-6) shows that:

$$K_v \propto \frac{1}{P} \tag{4}$$

Using this relationship and equation 2, the rate of Cr_2O_3 loss by conversion to CrO_3 may be determined. In the present problem, the rate of loss of Cr would be:

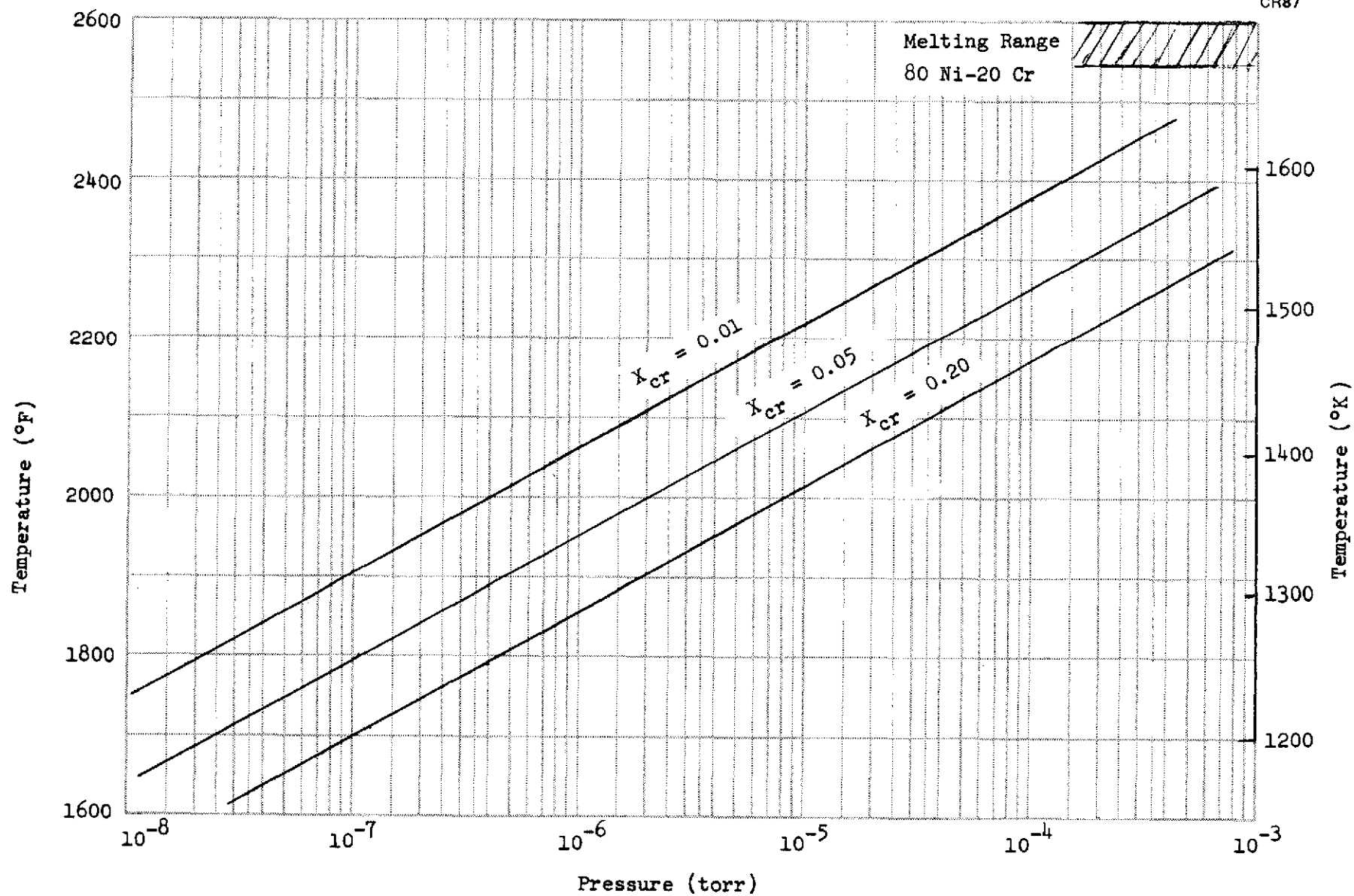$$K_v^{Cr_2O_3} = 1.52 \; K_v^{Cr} \tag{5}$$

Figure C-1. Critical Pressure for Evaporation of Chromium from Nickel-Chromium Alloys

Thus for chromium loss at 0.1 torr oxygen

$$K_V^{Cr} = 0.143 e^{-(48,800 \pm 3000/RT)} \ g/cm^2\text{-sec} \tag{6}$$

This is assumed to be equivalent to 0.5 atmosphere air. Using equations 5 and 3 a family of curves for the rate of loss of chromium by the volatilization of CrO_3 can be calculated. These curves are shown in Figure C-2. Using the value of K_V^{Cr} from Figure C-2 the amount of chromium can be calculated using the relationship

$$\frac{M_t}{M_\infty} = \frac{K_V t}{C_o \ell} \tag{7}$$

The relationship is plotted in Figure C-3, for 20 percent chromium. In equation (7) and in subsequent equations utilizing mass loss relationships, the term "ℓ" is half the sheet thickness.

Diffusion

Since the chromium loss is being controlled by a diffusion process during either low pressure oxidation or direct vaporization, the basis of the calculation of this loss will be the calculation of the amount of chromium leaving the material by diffusion to the surface. To calculate the chromium loss, the chromium composition at the surface will be assumed to go to zero immediately upon the start of oxidation or vaporization. Also, it is assumed that there is no buildup at the surface to prevent further volatilization of the chromium. The solution of the diffusion equation for the amount of material leaving a thin sheet for these conditions is a standard solution listed by Crank (Reference C-7). This solution is:

$$\frac{M_t}{M_\infty} = 1 - \sum_{n=0}^{\infty} \frac{8}{(2n+1)^2 \pi^2} e^{-D(2n+1)^2 \pi^2 t / 4 \ell^2} \tag{8}$$
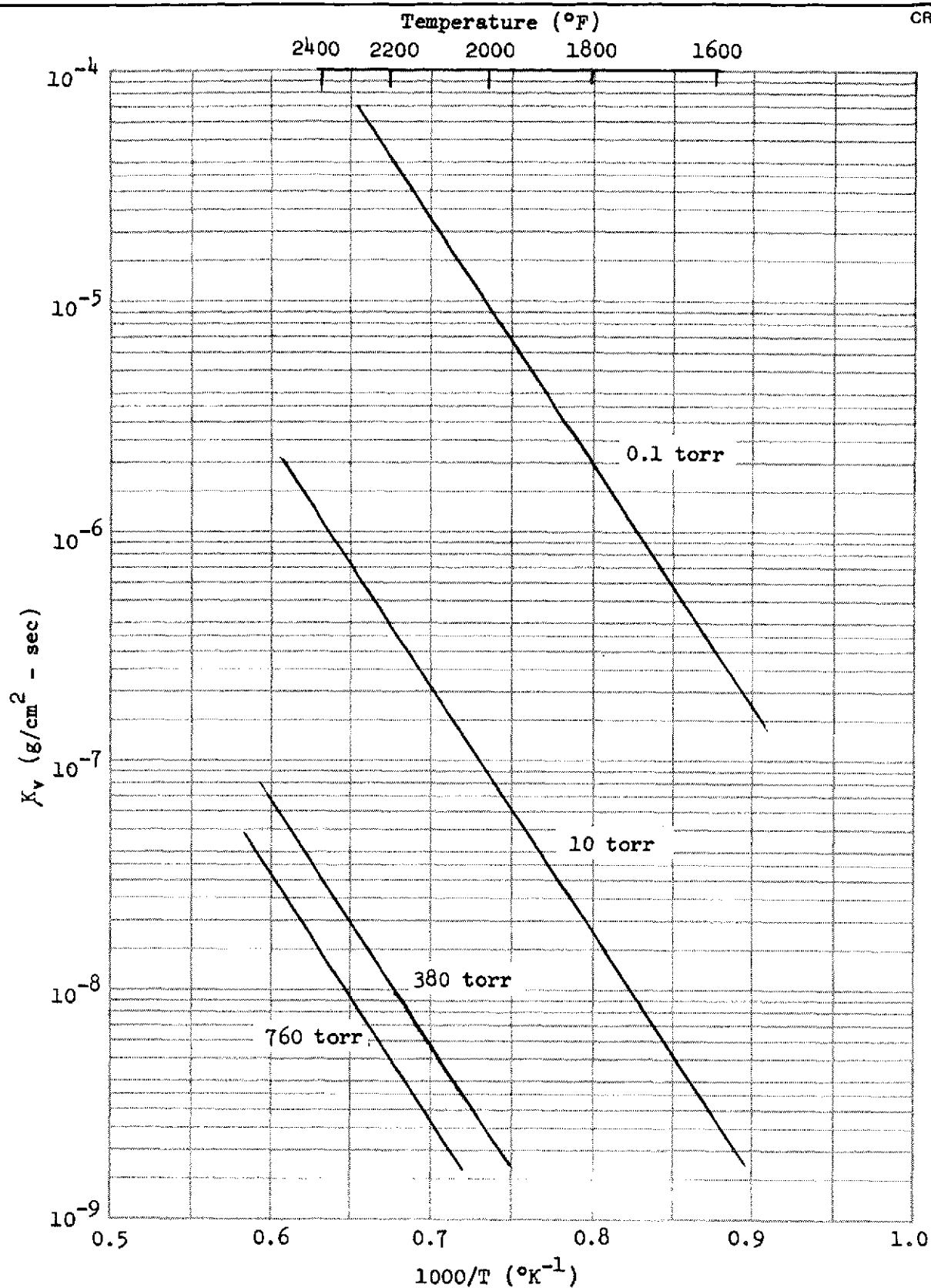
193

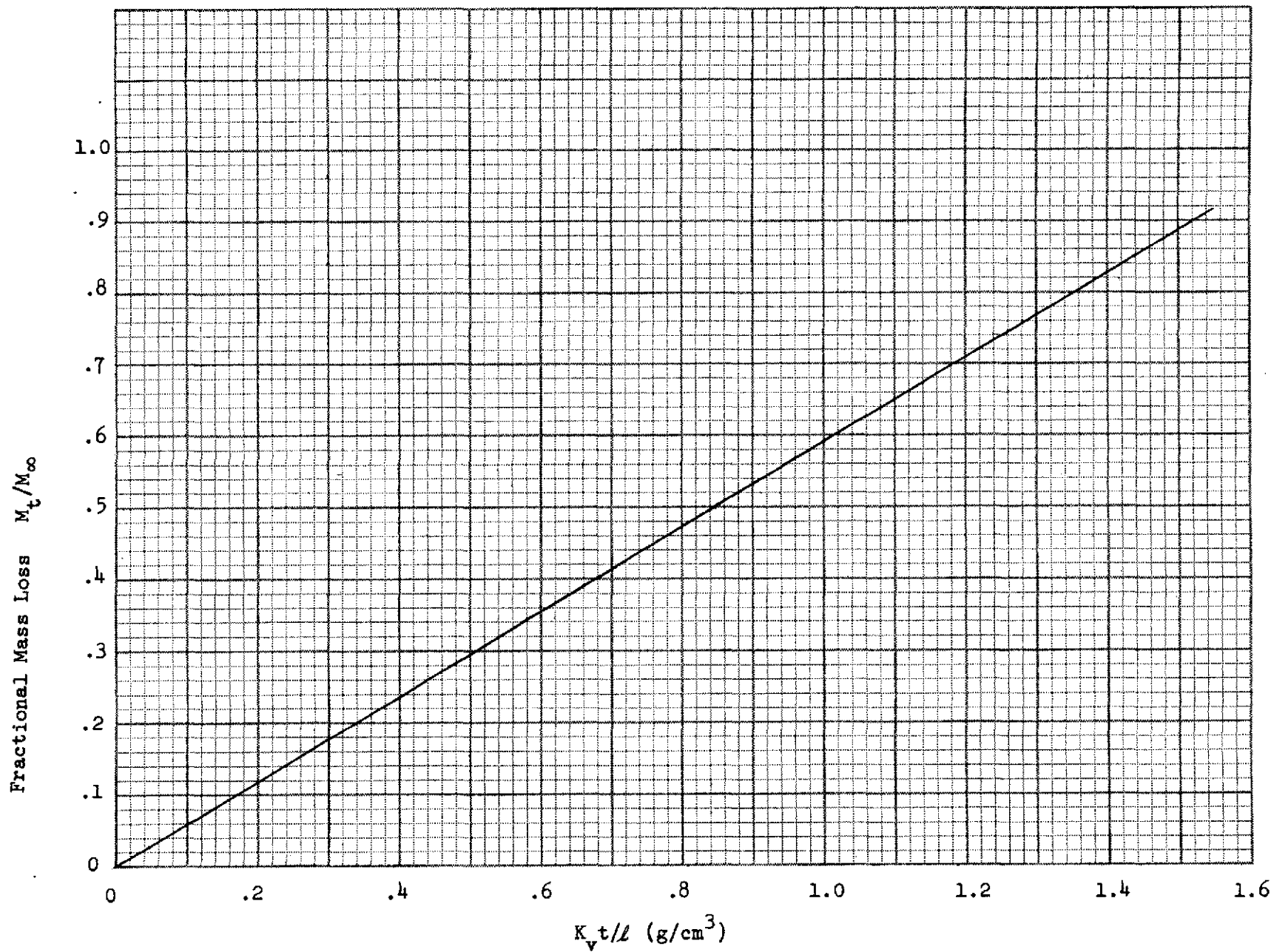Figure C-2. Rate of Loss of Chromium by Volatilization of CrO_3

Figure C-3. Fractional Mass Loss of Chromium Due to Oxidation

For a thick sheet the solution for a semi-infinite solid can be used. This solution is also given by Crank and is

$$\frac{M_t}{M_\infty} = 2\left(\frac{Dt}{\pi \ell^2}\right)^{1/2} \tag{9}$$

where

M_t = amount of chromium leaving in time, t

M_∞ = the amount of chromium leaving in infinite time

D = the diffusion coefficient at the temperature of interest

ℓ = half the sheet thickness

The solutions of these equations are plotted in Figures C-4 and C-5.

These curves are plotted assuming that the surface concentration goes to zero at zero time. If however, the surface concentration goes to some higher value, the value of M_t/M_∞ should be reduced proportionally, e. g., if the surface concentration is 5 percent chromium then the values of M_t/M_∞ would be multiplied by 0.75 to find the fractional loss of chromium.

The diffusion rate of chromium in nickel has been measured (References C-8 and C-9). The values for the diffusion coefficient from these studies are plotted in Figure C-6.

Strength Loss

The strength loss is due to two factors. The first of these is the loss of cross-section. This is calculated simply by assuming if all of the chromium is lost, then twenty percent of the cross-section is lost. This loss of cross-section can be as either Kirkendal voids or measurable thickness or both. For the purpose of this calculation, a fraction loss in thickness, $\Delta \ell / \ell$, was computed from the mass loss.

The plot of fractional cross-section loss as a function of mass loss, M_t/M_∞, is given in Figure C-7. Since the cross-section loss was assumed to be
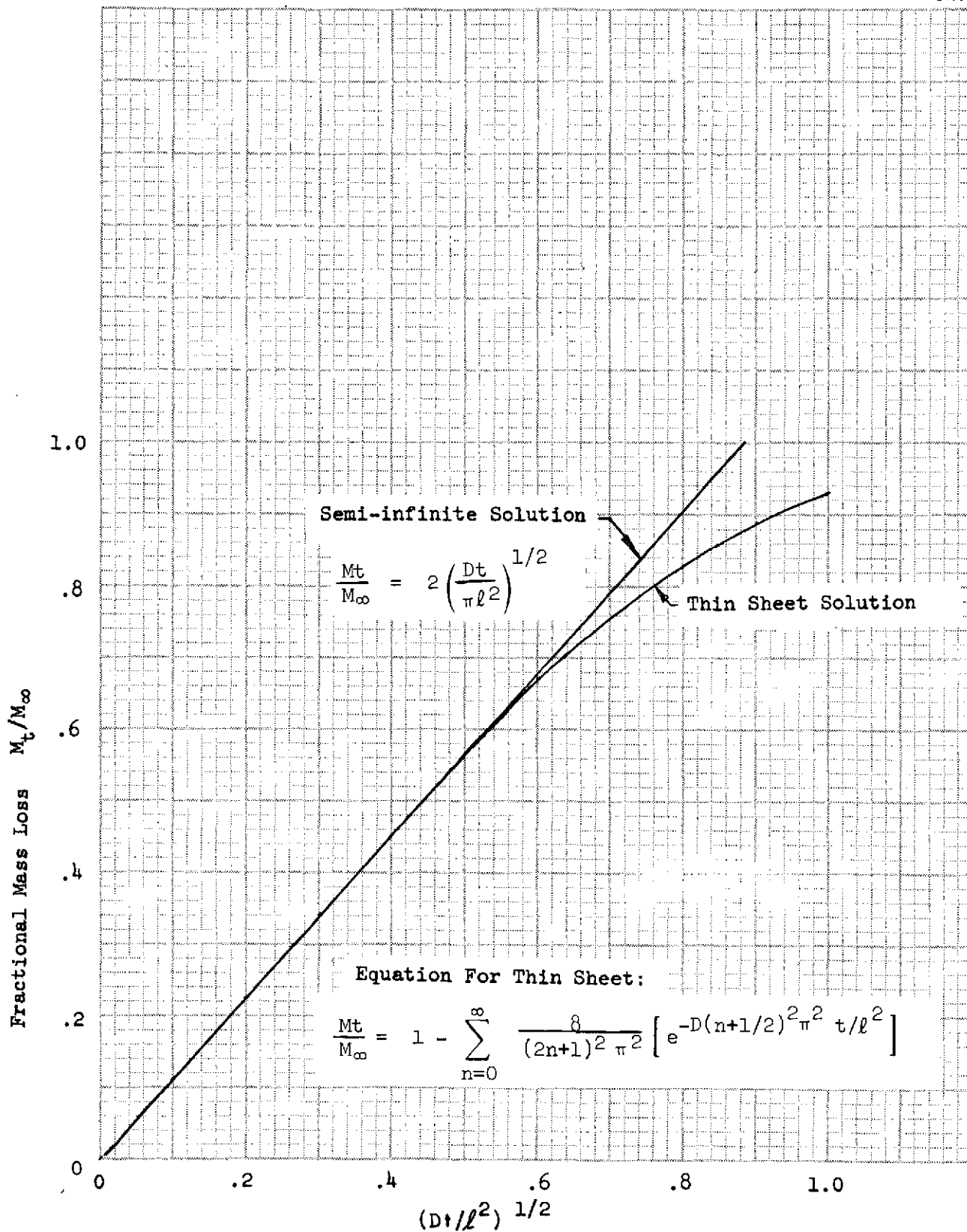
196

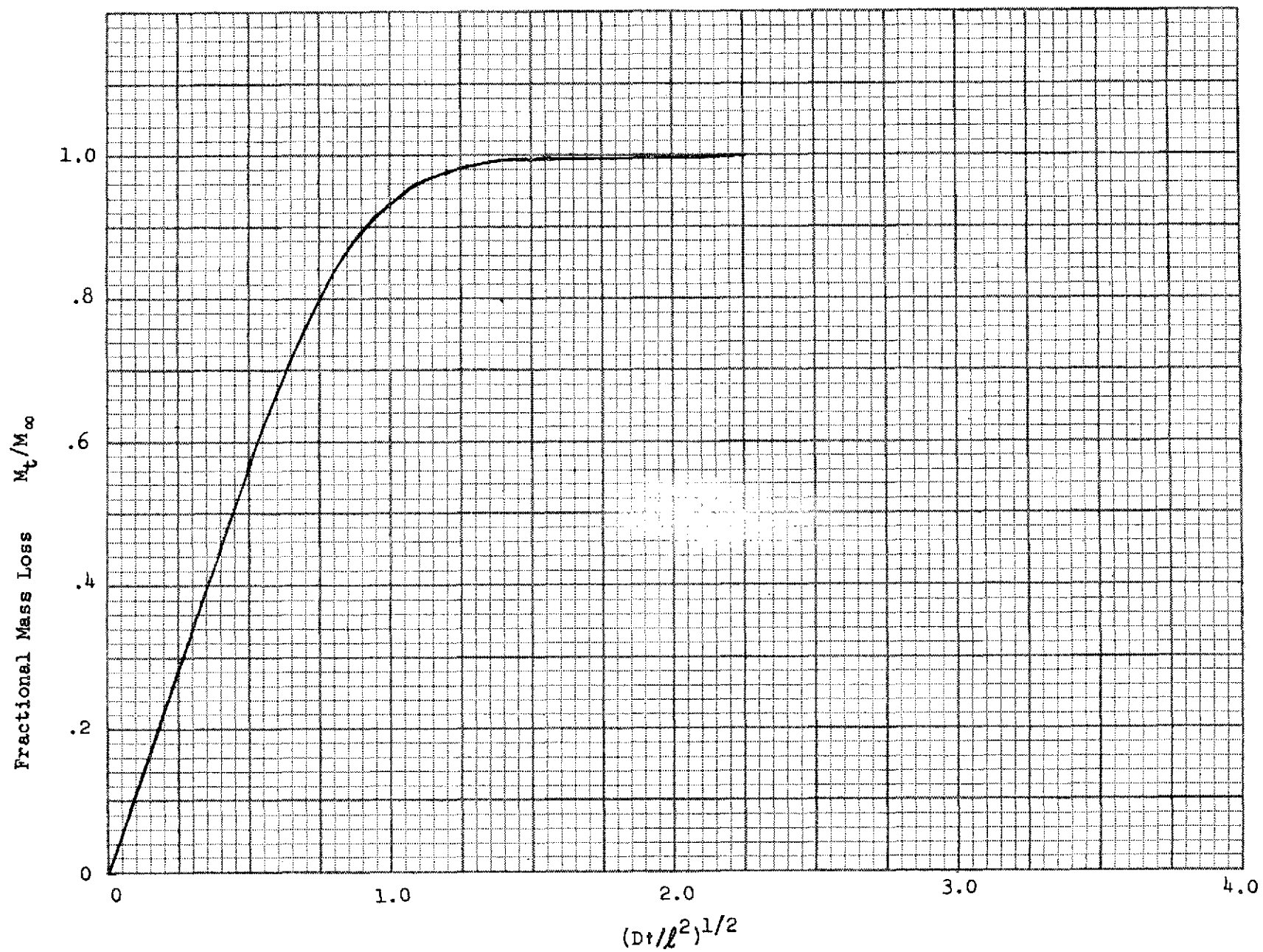Figure C-4. Loss of Chromium from 80Ni-20Cr by Diffusion

The axes and annotations of the figure:

- Vertical axis: Fractional Mass Loss M_t/M_∞, with gridlines at 0, .2, .4, .6, .8, 1.0
- Horizontal axis: $(Dt/\ell^2)^{1/2}$, with gridlines at 0, .2, .4, .6, .8, 1.0

Semi-infinite Solution

$$\frac{M_t}{M_\infty} = 2\left(\frac{Dt}{\pi \ell^2}\right)^{1/2}$$

Thin Sheet Solution

Equation For Thin Sheet:

$$\frac{M_t}{M_\infty} = 1 - \sum_{n=0}^{\infty} \frac{8}{(2n+1)^2 \pi^2} \left[e^{-D(n+1/2)^2 \pi^2 t/\ell^2}\right]$$

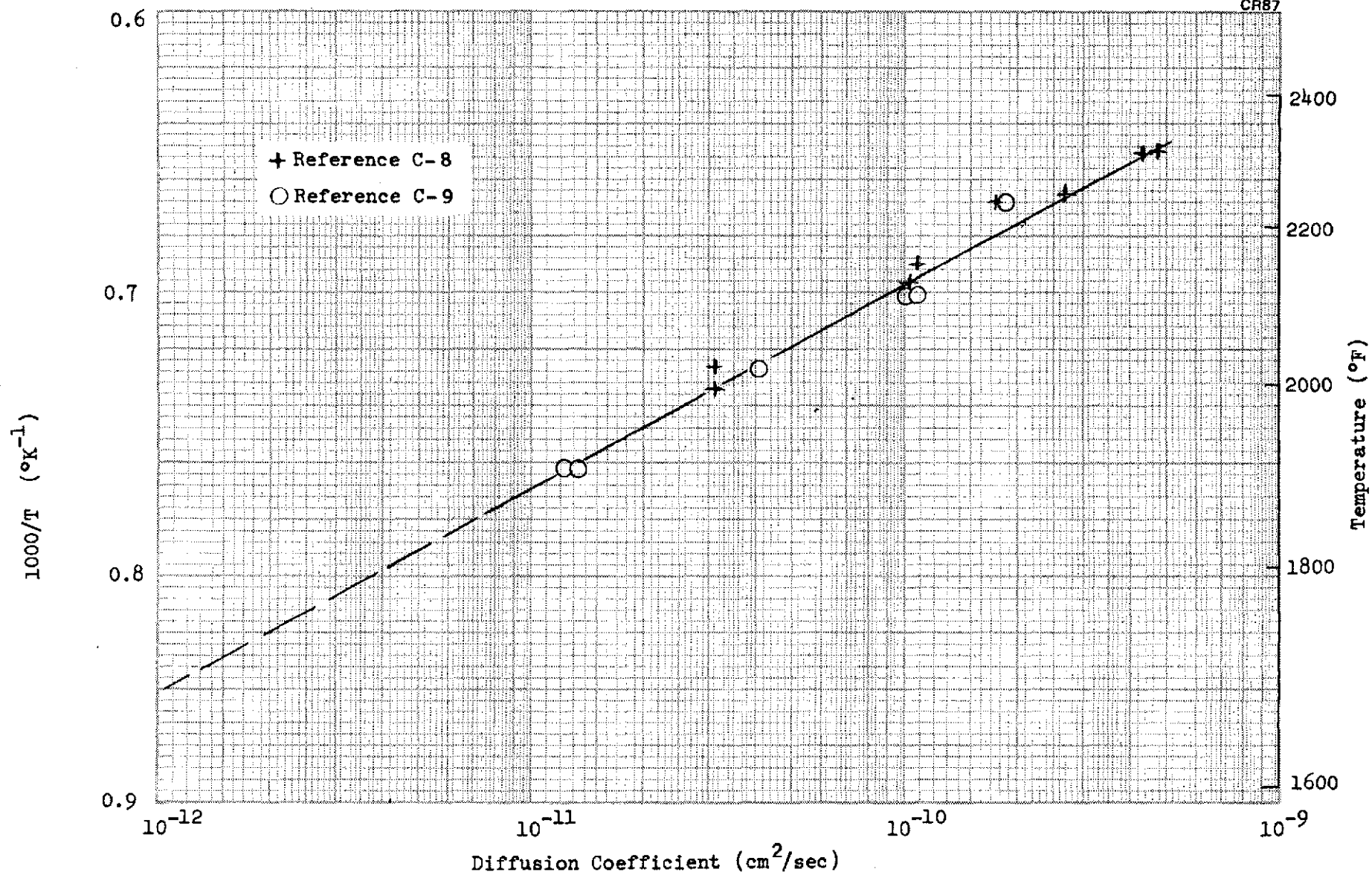Figure C-5. Loss of Chromium from Ni-20Cr by Diffusion

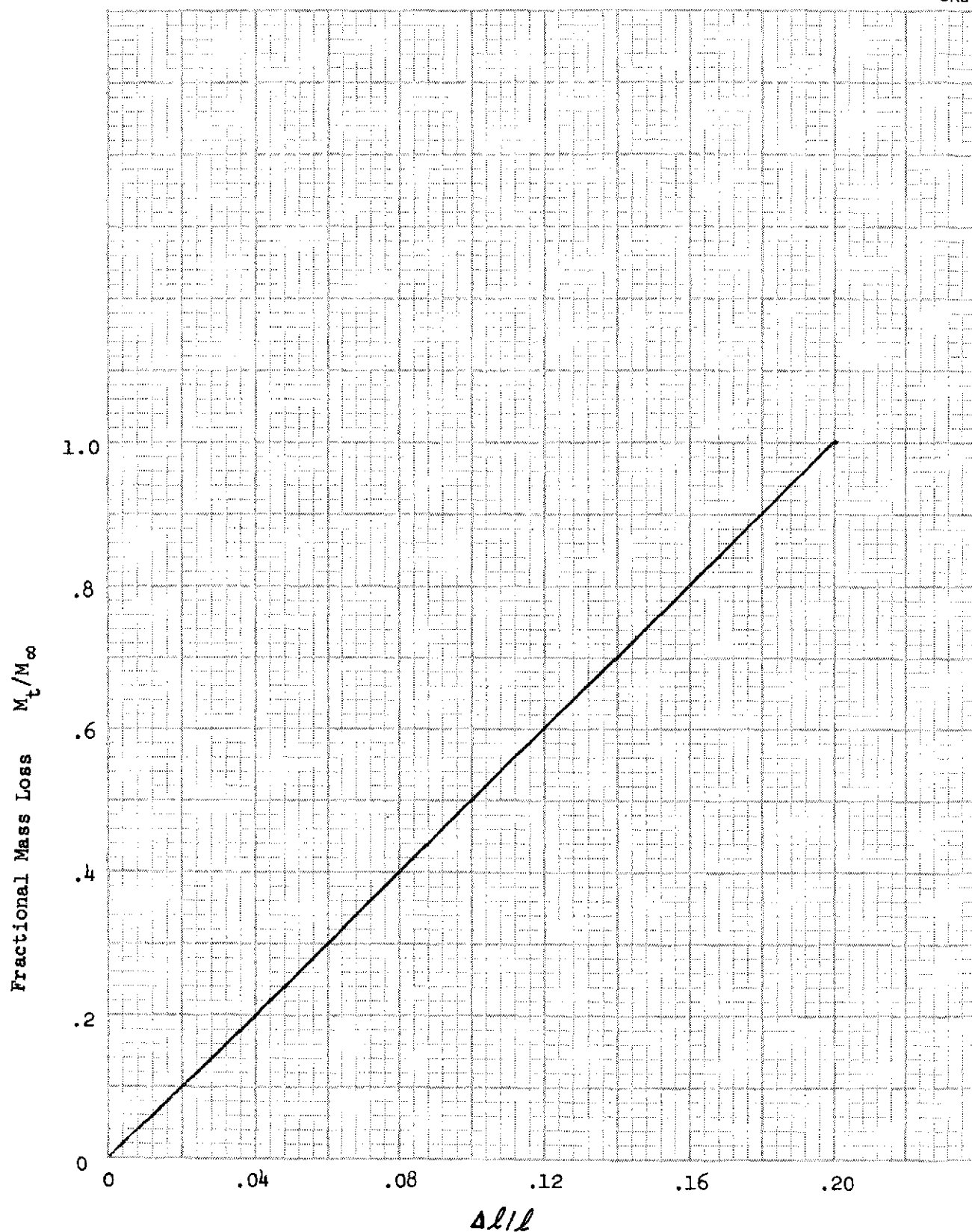Figure C-6. Diffusion Constant for Chromium in Ni-20Cr

199

Figure C-7. Loss of Cross-Section Due to Chromium Loss

only in the thickness direction, the fraction thickness loss, $\Delta \ell / \ell$, was equivalent to cross-section area loss. Calculation of area loss in this manner gave an effective cross-section loss that was equivalent to the sum of the losses due to voids and surface recession.

The strength loss due to the loss of solid solution strengthening of the chromium is accomplished by assuming a parabolic strengthening relationship of chromium in Ni-Cr-ThO$_2$ alloys. The strengthening of chromium in dispersion free nickel-chromium alloys has been studied and this type of non-linear strengthening was observed (Reference C-3). The room temperature ultimate strength of TDNi (Ni-2ThO$_2$) was assumed to be about 80 ksi based on the results of Reference C-10. The strength of TD Ni-20Cr (Ni-20-Cr-2ThO$_2$) was assumed to be 895 MN/m^2 (130 ksi) from the results of Reference C-11.

The assumed curve for the ultimate strength as a function of chromium content is shown in Figure C-8. Similar curves can be calculated for other temperatures and for the yield strength.

Calculation of Strength Loss

To calculate the strength loss of a given sheet thickness for a given exposure condition, the data generated in the preceding paragraphs are used as follows:

(1) The sheet thickness, exposure time, and temperature are defined as:

    (a) The thickness $w = 2\ell$

        $w = 0.015$ in. $= 0.0381$ cm

        $\ell = 0.0075$ in. $= 0.0190$ cm

    (b) The exposure time

        $t = 100$ hrs $= 3.6 \times 10^5$ sec.

    (c) Temperature
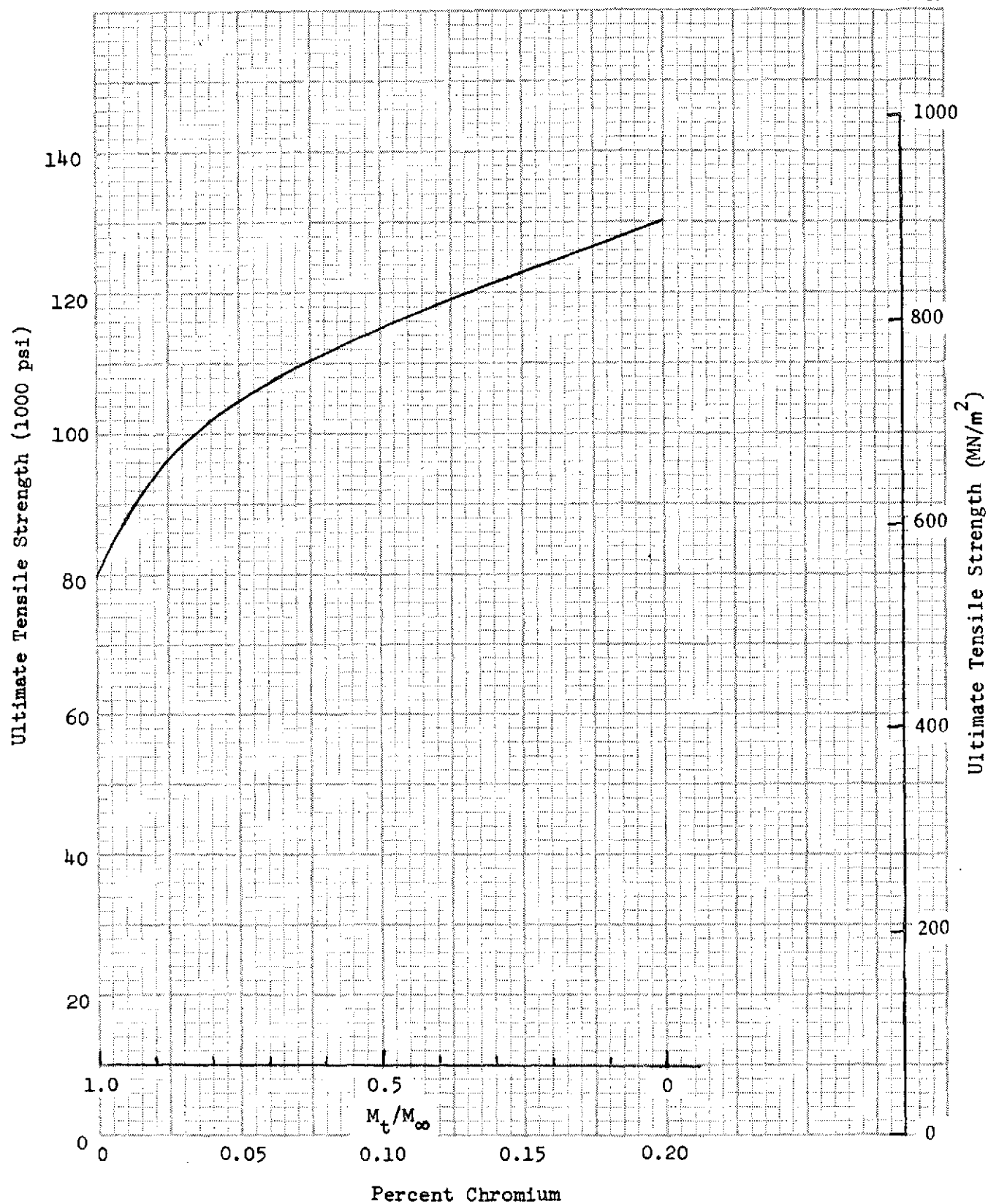
        $t = 1800°F = 1255°K$

Figure C-8. Calculated Strength of Ni-Cr-ThO$_2$ Alloys with Respect to Percent Chromium

(2) The diffusion constant from Figure C-6 is:

$$D = 4.2 \times 10^{-12} \ cm^2/sec$$

(3) The oxidation rate constants, K_v, are taken from Figure C-2. These are shown in the following table:

Table C-1

DATA FOR CALCULATING MASS LOSS DUE TO OXIDATION

K_v	P (torr)	$K_v \, t/\ell$	M_t/M_∞
2.38×10^{-10}	760	4.51×10^{-3}	2.67×10^{-3}
4.77×10^{-10}	380	9.03×10^{-3}	5.33×10^{-3}
1.81×10^{-8}	10	3.43×10^{-1}	2.03×10^{-1}
1.81×10^{-6}	0.1	3.43×10	— — —

(4) The critical pressures for evaporation of chromium are taken from Figure C-1. From these values, i.e., less than 10^{-7} torr, this mode of chromium loss will not enter into the present calculation.

(5) Using the above values and Figures C-3, and C-4 or C-5 the value of M_t/M_∞ as a function of exposure pressure can be determined. For the oxidation controlled portion of the curve the values of M_t/M_∞ from Figure C-3 are used directly. These are shown in Table C-1, and are plotted on Figure C-9.

(6) As pressure decreases, the volatilization rate of chromium becomes sufficient for the rate of chromium loss to be controlled by the diffusion of chromium. In this case, the M_t/M_∞ is determined from Figure C-4 or C-5 and is 0.070. But, since the surface concentration for oxidation has been fixed at 5 percent chromium, this value should be reduced by 25 percent to 0.052. This value is also plotted in Figure C-9 as the curve labeled Diffusion Controlled Chromium Loss.
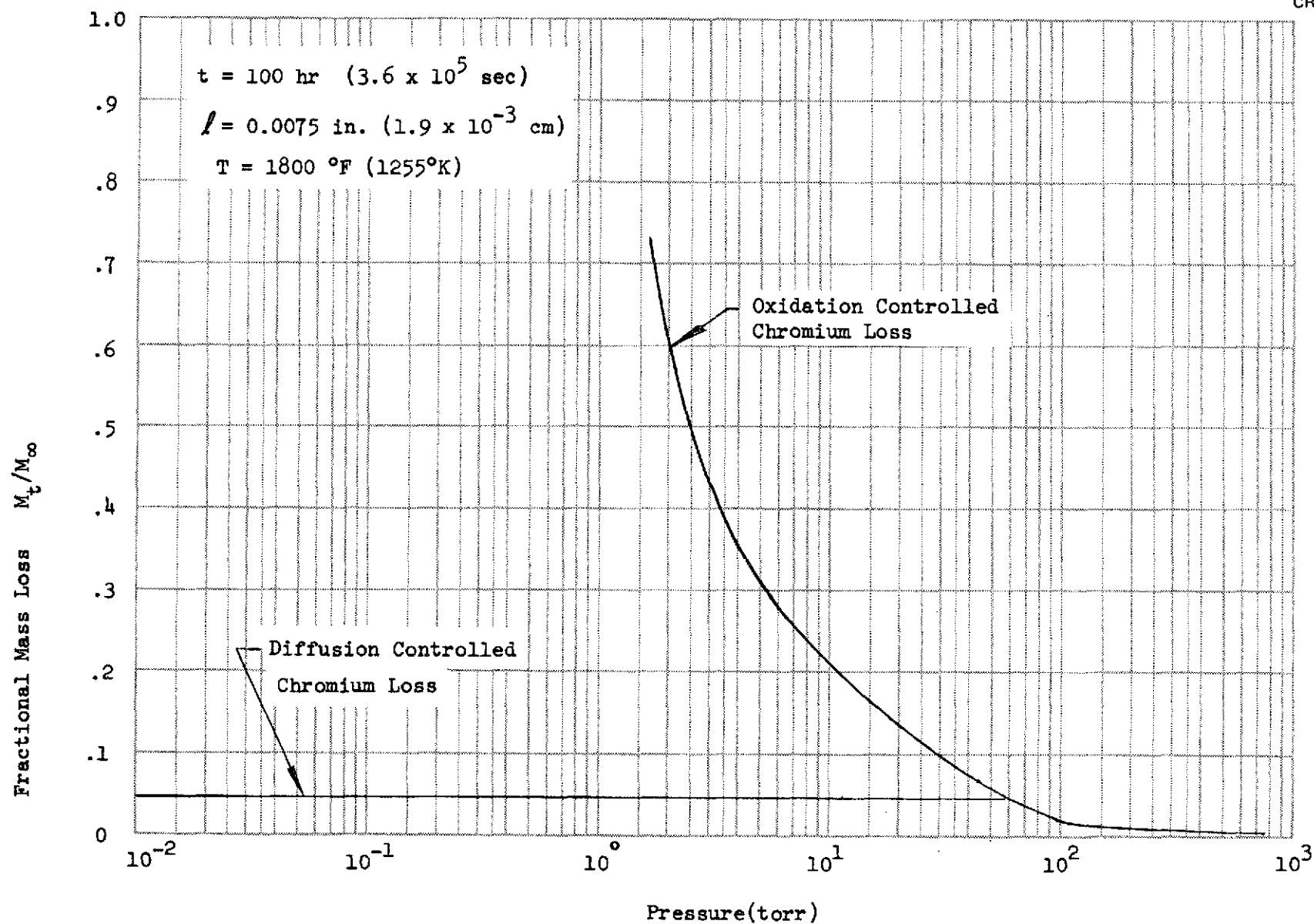
Figure C-9. Calculated Mass Loss of Chromium After Exposure

(7) Using Figures C-7 and C-8, the strength loss can be determined from the values of M_t/M_∞ in Figure C-9. These results are plotted in Figure C-10. In a similar manner, strength losses can be calculated for other temperatures. The losses at 1,368°K (2,000°F) and 1,477°K (2,200°F) are also plotted in Figure C-10.

Using the analytical technique described above, the strength loss was calculated for several samples which had been exposed to elevated temperatures at reduced pressures. The results of the calculations are shown in Table C-2, which also compares computed strength losses with strength losses observed in residual strength tests conducted with the various samples. The agreement between measured and calculated values is considered reasonable for samples exposed to temperatures of 1,368°K (2,000°F) or higher. The relatively good agreement at exposure conditions of 1,368°K (2,000°F) or higher is important since a majority of the strength degradation for TD Ni-20Cr heat shields is expected to occur in that temperature regime. Also, the noted agreement lends confidence to predicting degradation from pressure and temperature effects by the analytical approach presented herein. The assumptions and approximations utilized in the analytical approach should be experimentally verified, but such verification was beyond the scope of the current program. The assumption considered to be most sensitive to error is that the surface between the oxide and the alloy has a concentration of approximately 5 percent chromium.

The results of multiparameter cyclic creep tests (see Section 3.1) were also reviewed and compared with predicted strength degradations developed from the methods presented in this appendix. Such comparisons are summarized in Table C-3. In making the comparisons, calculated values of strength reductions were based on the time the samples were at or above 1,339°K (1,950°F) in the test profile shown in Figure 3-1. Somewhat greater degradation was exhibited by the cyclic creep samples; the more severe degradation was judged to be caused by the application of cyclic stresses on the samples, as well as the pressure and temperature profiles. The greater degradation of transverse samples is also evident from the data of Table C-3. Since the analytical predictions of degradation developed in this appendix considered
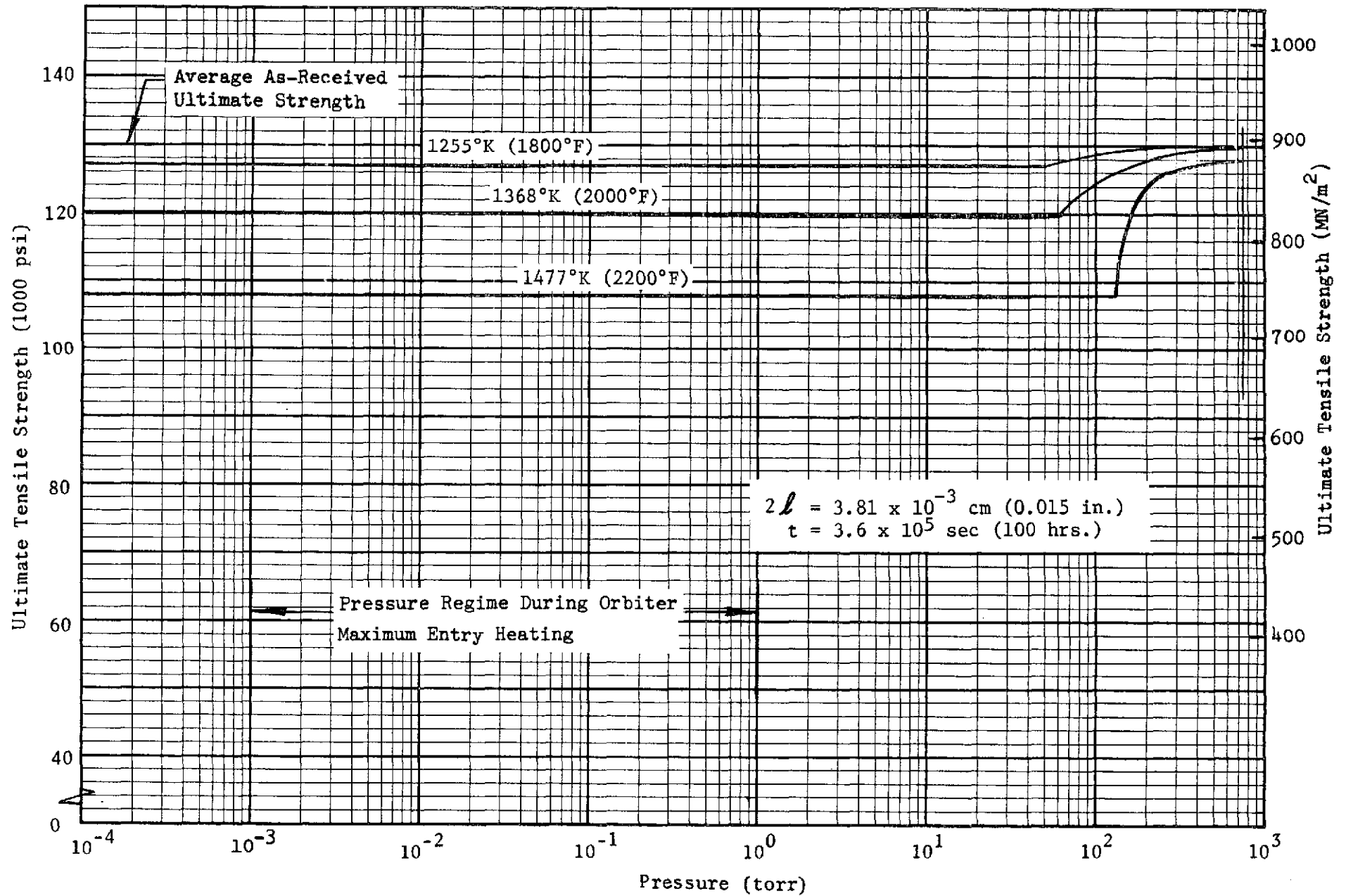
Figure C-10. TD Ni-20Cr Strength Degradation as a Function of Exposure Temperature and Pressure For 100-Hr Exposure

pressure and temperature effects only, the agreement between calculated degradation and that experienced by the cyclic creep samples was relatively poor in a majority of the comparisons.

Table C-2

ROOM-TEMPERATURE STRENGTH LOSS DURING OXIDATION

Thickness in./cm	Temperature °F/°K	Pressure torr	Time (hrs)	Measured Strength Reduction (Percent)	Calculated Strength Reduction (Percent)	Ref
0.025/0.0635	1,900/1311	0.15	24	9.8	1.5	C-12
0.025/0.0635	1,900/1311	0.15	24	13.3	1.5	C-12
0.025/0.0635	1,900/1311	0.15	96	8.4	3.2	C-12
0.025/0.0635	1,900/1311	0.15	96	8.6	3.2	C-12
0.025/0.0635	2,200/1477	0.15	24	6.2	5.1	C-12
0.025/0.0635	2,200/1477	0.15	24	8.6	5.1	C-12
0.025/0.0635	2,200/1477	0.15	96	22.5	10.2	C-12
0.025/0.0635	2,200/1477	0.15	96	24.0	10.2	C-12
0.020/0.0508	2,000/1368	10	10	0	2.8	C-11
0.020/0.0508	2,000/1368	10	10	0	2.8	C-11
0.020/0.0508	2,000/1368	0.1	98.7	3.6	5.2	C-11
0.020/0.0508	2,000/1368	0.1	98.7	1.3	5.2	C-11
0.015/0.0381	2,200/1477	10^{-6}	72	31.0	21.4	–
0.015/0.0381	2,200/1477	10^{-6}	72	26.0	21.4	–
0.010/0.0254	2,400/1588	0.18	100	15.1	33.8	C-13

Table C-3

ROOM-TEMPERATURE STRENGTH LOSS COMPARISON
OF CYCLIC CREEP SAMPLES

Specimen Number (See Table 3-2)	Speci-men Orien-tation	Thickness, cm (in.)	Maximum[3] Stress at 1,368 °K MN/m^2 (psi)	Maximum[3] Temperature, °K (°F)	Pressure[3] (torr)	Time[3] (hr)	Measured Strength Reduction (%)	Calculated Strength Reduction (%)
1	L[1]	0.0259 (0.0102)	34.4 (5,000)	1,477 (2,200)	5 x 10^{-2}	13.3	26.9	9.8
3	T[2]	0.0260 (0.0103)	27.6 (4,000)			13.3	55.7	9.8
5	L	0.0260 (0.0103)	31.0 (4,500)			13.3	39.4	9.8
7	T	0.0272 (0.0107)	24.1 (3,500)			13.3	70.2	9.8
9	L	0.0267 (0.0105)	27.6 (4,000)			10.0	11.0	8.5
11	T	0.0264 (0.0104)	24.1 (3,500)			10.0	38.4	8.5

[1]Longitudinal

[2]Transverse

[3]See Figure 3-1. Average value of pressure was used, and time corresponds to total period samples were above 1,339 °K (1,950 °F).

Appendix C

REFERENCES

C-1. Douglass, D. L., "Literature Search and Evaluation of the Oxidation Behavior at High Temperatures of Thoria-Dispersed Nickel-Chromium and Related Unthoriated Alloys" Report to NASA Ames Research Center, September 1971.

C-2. Richardson, F. D. and Jeffes, J. H. E., "The Thermodynamics of Substances of Interest in Iron and Steel Making from 0°C to 2400°C" J. Iron and Steel Inst. 160, 261-270 (1948).

C-3. Pelloux, R. M. N. and Grant, N. J., "Solid Solution and Second Phase Strengthening of Nickel Alloys at High and Low Temperatures" Trans TMS-AIME 218, 232-237 (1960).

C-4. Kelley, K. K., "Contributions to the Data on Theoretical Metallurgy, XV" U. S. Bureau of Mines Bulletin 604 (1962).

C-5. Hagen, W. C., "Factors Controlling the High-Temperature Oxidation of Chromium" Trans ASM 56, 583-599 (1963).

C-6. Dushman, S., Scientific Foundation of Vacuum Technique, J. Wiley and Sons, New York (1949).

C-7. Crank, J. - The Mathematics of Diffusion Oxford at the Clarenden Press, London (1956).

C-8. Momma, K., Suto, H. and Oikawa, H., "Diffusion of Ni^{63} and Cr^{51} in Nickel Chromium Alloys" J. Jap. Inst. of Metals 28, 188-191 (1964).

C-9. Seltzer, M. S., Wilcox, B. A. and Jaffee, R. I., "Development of Oxidation Resistance in Thoriated Nickel-Chromium Base Alloys" NASA CR-120880 (1971).

C-10. Leggett, H., Cook, J. L., Schwab, D. E., and Powers, C. T. "Mechanical and Physical Properties of Super Alloy and Coated Refractory Alloy Foils" AFML-TR-65-147 (1965).

C-11. Johnson, R. Jr., and Killpatrick, D. H., "Dispersion-Strengthened Metal Structural Development" AFFDL-TR-68-130 Part I (1968).

C-12. Wurst, J. C., et al. The Evaluation of Materials for Aerospace Applications. AFML-TR-67-165 (1967).

C-13. Malik, R. K. and Stetson, A. R. Evaluation of Superalloys for Hypersonic Vehicle Honeycomb Heat Shields. AFML-TR-68-292 (1968).

APPENDIX D

TPS PARAMETRIC STUDIES

# APPENDIX D
TPS PARAMETRIC STUDIES

Parametric studies of TPS configurations were conducted to evaluate several TPS designs and select two configurations for use in Phase I full-scale sub-size panel tests. Areas investigated in the parametric studies included weight, thermal studies to define insulation thicknesses, costs, and qualitative evaluations of fabricability, refurbishability, reliability, and overall design efficiency. The configurations reviewed are shown in Figure D-1.

D.1 THERMAL EVALUATIONS

Thermal analyses were conducted to determine the insulation thickness required to maintain design temperatures on the internal structures. Initially, a typical thermal model was developed with representative masses, thermal properties, and dimensions for the TPS and substructure. The convective heating rate time-history at $X/L = 0.35$ (Appendix A) on the lower surface centerline was applied to the model, and internal structure temperatures were determined as a function of insulation thickness. Typical spacings between heat shield and insulation package and between the insulation package and the substructure were selected as shown in Figure D-2. View factors, noted in Table D-1, were also selected to account for internal reradiation effects. Subsequent evaluation of internal reradiation effects on the zee-stiffened design showed them to be similar to those of the corrugation-stiffened model. Results of the thermal studies are summarized in Figures D-2 and D-3. Figure D-2 shows the substructure temperature as a function of insulation thickness and Figure D-3 shows the temperature time-histories of three points in the TPS/substructure model during entry, using an insulation thickness of 6.35 cm (2.50 in.). Post-flight cooling of the substructure was assumed in the thermal analysis for all insulation thicknesses shown in Figure D-2. The insulation used in this analysis was Fiberfrax Hi-Fi (SKX) ceramic fiber insulation with a density of 128.2 kg/m^3 (8 lb/ft^3). An ambient pressure of 10 torr was assumed for the thermal analyses that produced the results of Figures D-2 and D-3. Since pressures higher than 10 torr were expected to be required to obtain the desired
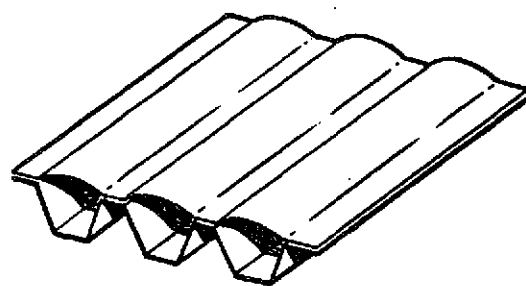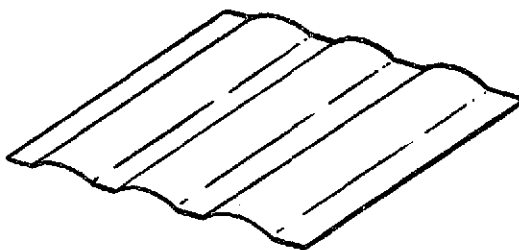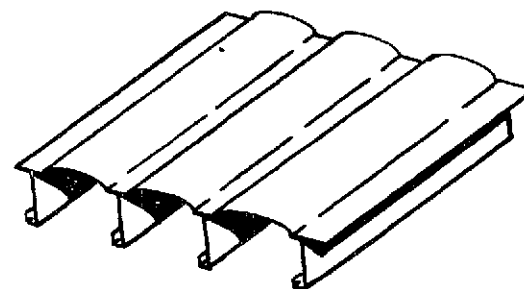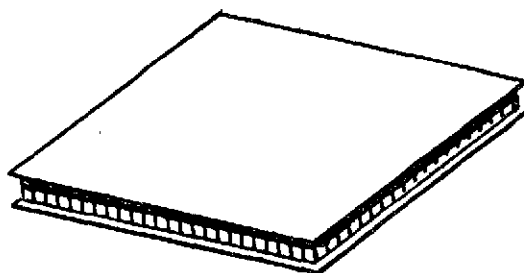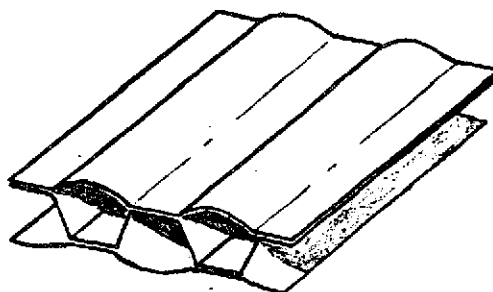
214

1. SINGLE FACE
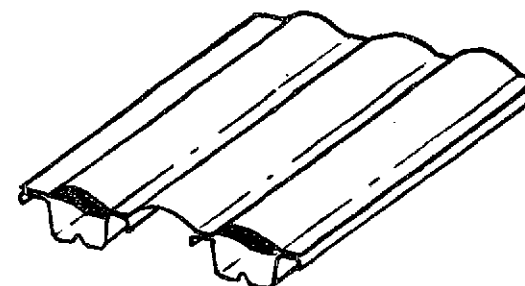CORRUGATION-STIFFENED

2. CORRUGATED SINGLE SHEET

3. ZEE-STIFFENED SHEET

4. HONEYCOMB

5. DOUBLE FACE
CORRUGATION-STIFFENED

6. SINGLE FACE CHANNEL-STIFFENED

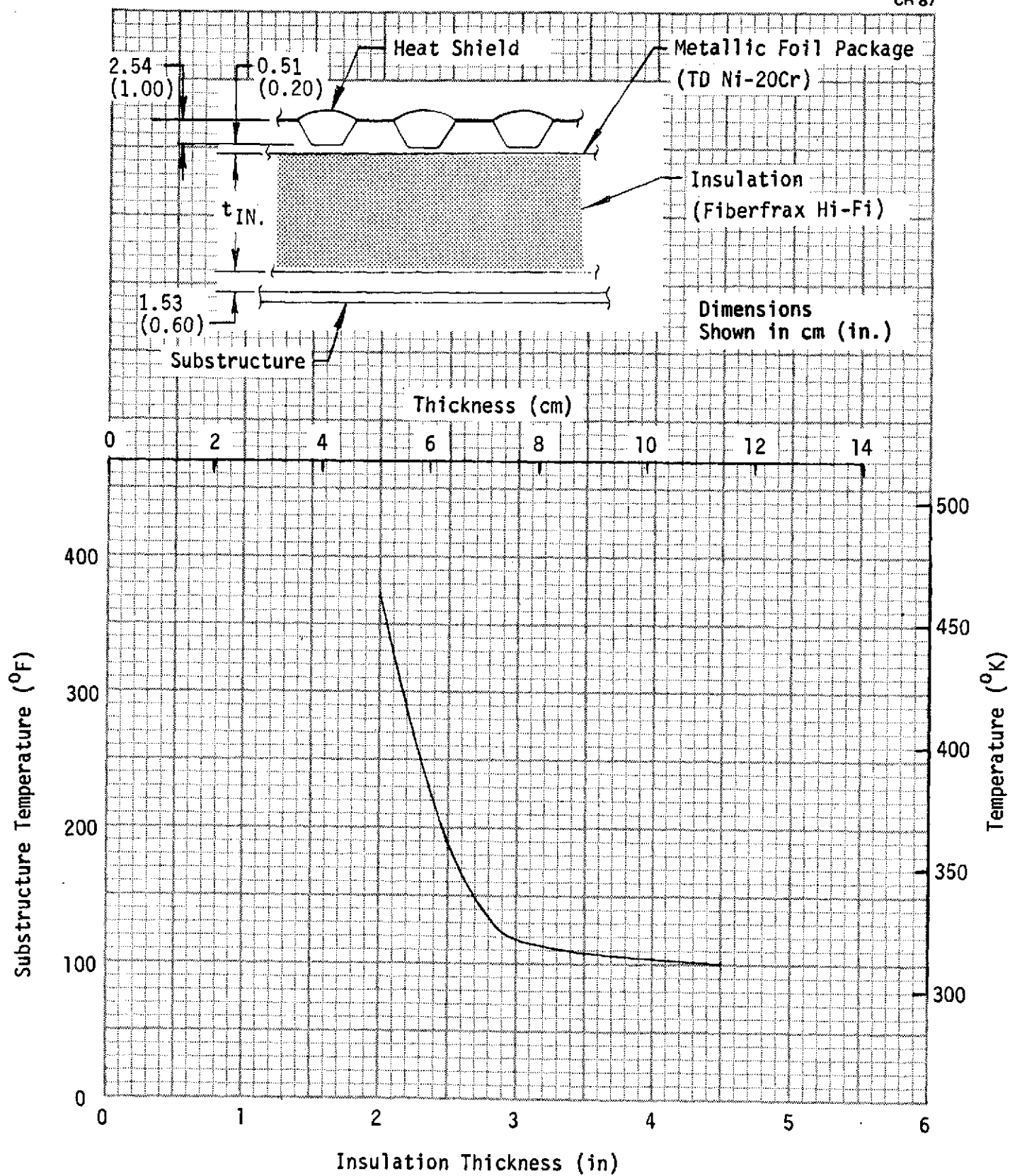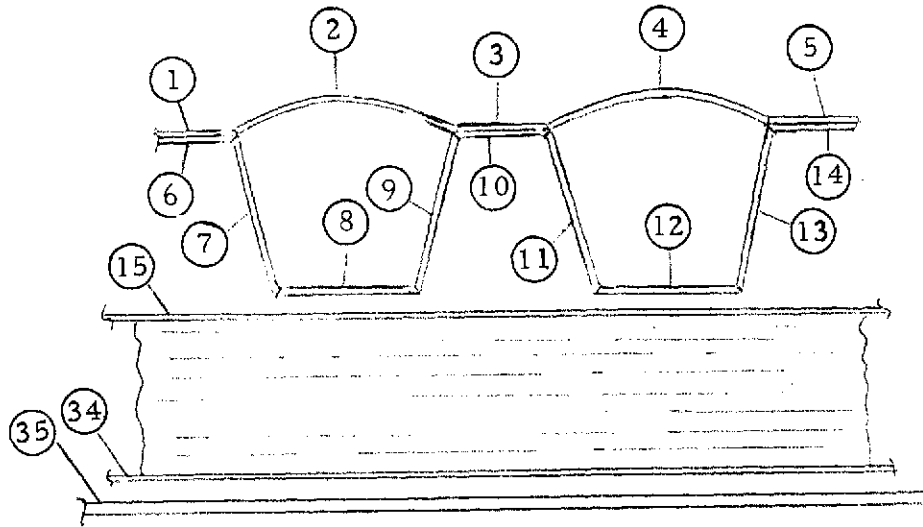Figure D-1. TPS Heat Shield Panel Configurations for Parametric Studies

Figure D-2. Substructure Temperature Variation with Insulation Thickness

THERMAL MODEL GRAY BODY VIEW FACTORS

Radiation		
From Node	To Node	Gray Body View Factor, $\mathcal{F}$
6	7	0.3596
10	11	0.3596
14	13	0.3596
7	8	0.1724
11	12	0.1724
7	9	0.2993
11	13	0.2993
11	9	0.2937
6	15	0.3283
10	15	0.3283
14	15	0.3283
7	15	0.3596
9	15	0.3596
11	15	0.3596
13	15	0.3596
8	15	0.9043
12	15	0.9043
9	10	0.1705
7	2	0.4866
9	2	0.4866
11	4	0.4866
13	4	0.4866
8	9	0.2677
12	13	0.2677
8	2	0.3907
12	4	0.3907
34	35	1.00
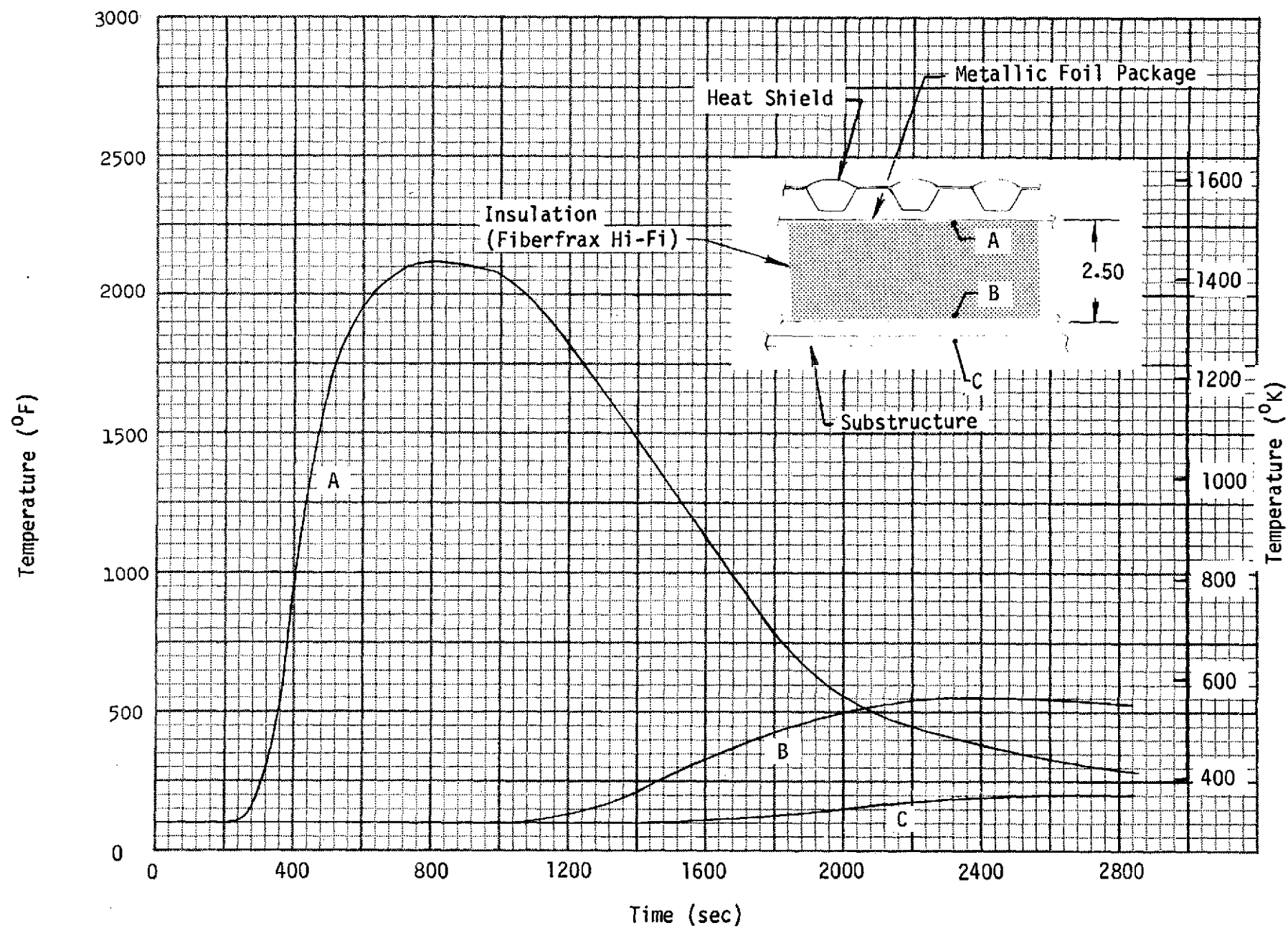
Figure D-3. Substructure and Insulation Temperature Time Histories

differential pressure profile in tests, the insulation thickness was increased to 6.99 cm (2.75 in.) in the full-scale subsize TPS design.

Specific heat and thermal conductivity for TD Ni-20Cr were taken from Figures B-33 and B-34 (Appendix B). TD Ni-20Cr emittance values were taken from Figure B-35, using the curve for preoxidized panels. Specific heat and thermal conductivity values used for the Fiberfrax Hi-Fi insulation are given in Figures D-4 and D-5. Values in Figures D-4 and D-5 were obtained from Reference D-1. An aluminum substructure was assumed for the thermal analysis, the specific heat and conductivity values being shown in Figures D-6 and D-7.

After the selection of the zee-stiffened and corrugation-stiffened designs for use in Phase I tests, a final thermal check was made to determine if significant differences existed between the zee-stiffened panel TPS and the initial model using a corrugation-stiffened design. No significant differences in thermal performance were found for the zee-stiffened panel, and the same insulation package thickness was therefore used for both the zee-stiffened design and the corrugation-stiffened heat shield in Phase I tests.

D.2 WEIGHTS

Structural analyses were conducted to develop typical panel and support system weights based on static loadings. The most promising configurations were then checked for fatigue and flutter to determine their suitability for dynamic loading conditions.

Equivalent weight thicknesses (smeared thicknesses) were determed during both ascent and entry conditions for varying panel depths. These weight thicknesses were then plotted as a function of maximum panel bending stresses (tension and compression) at boost flight temperatures and entry temperatures. The selected panel limit differential pressures are as follows:

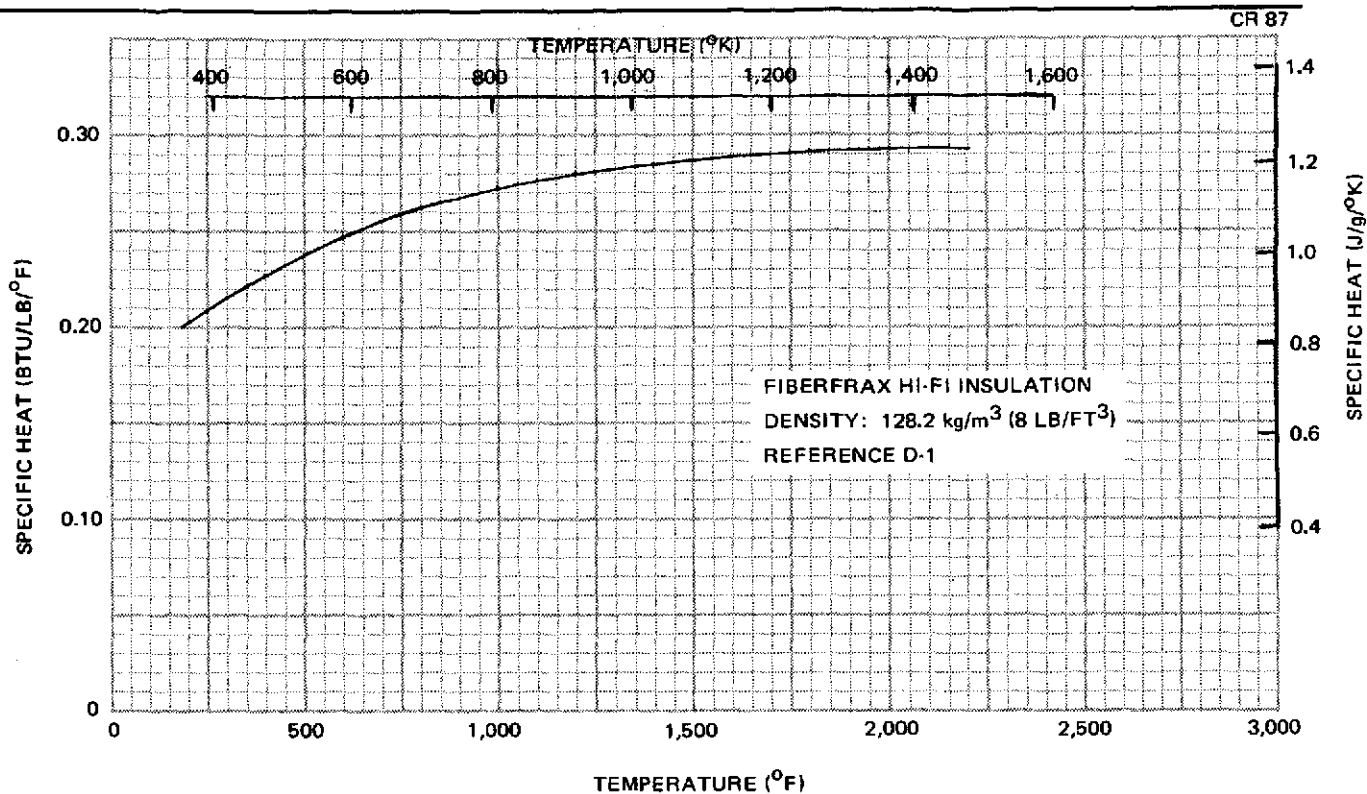| Flight Phase	Differential Pressure (psi)
Boost	+3.3 (collapse)
Boost	-1.0 (burst)
Entry	+0.50 (collapse)
Entry	-0.50 (burst)

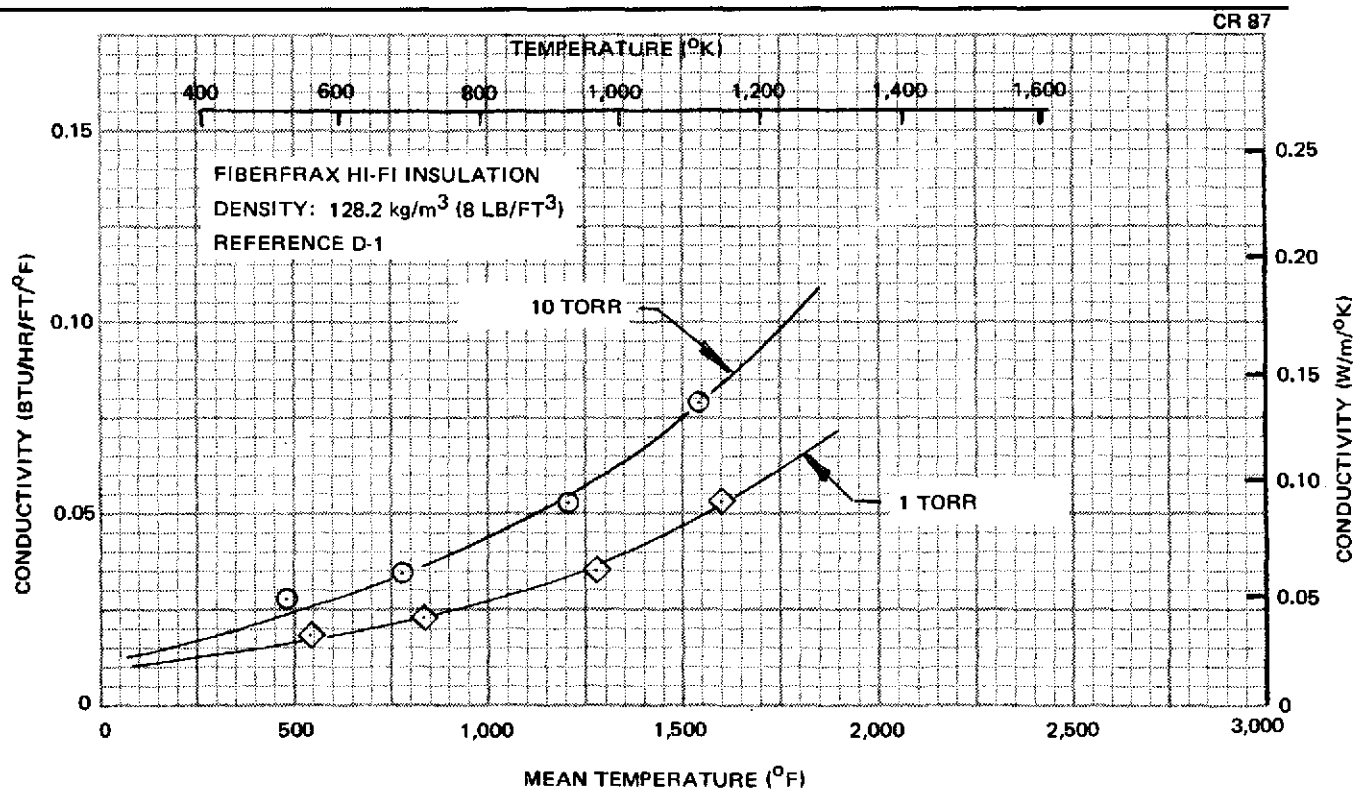Figure D-4. Insulation Specific Heat

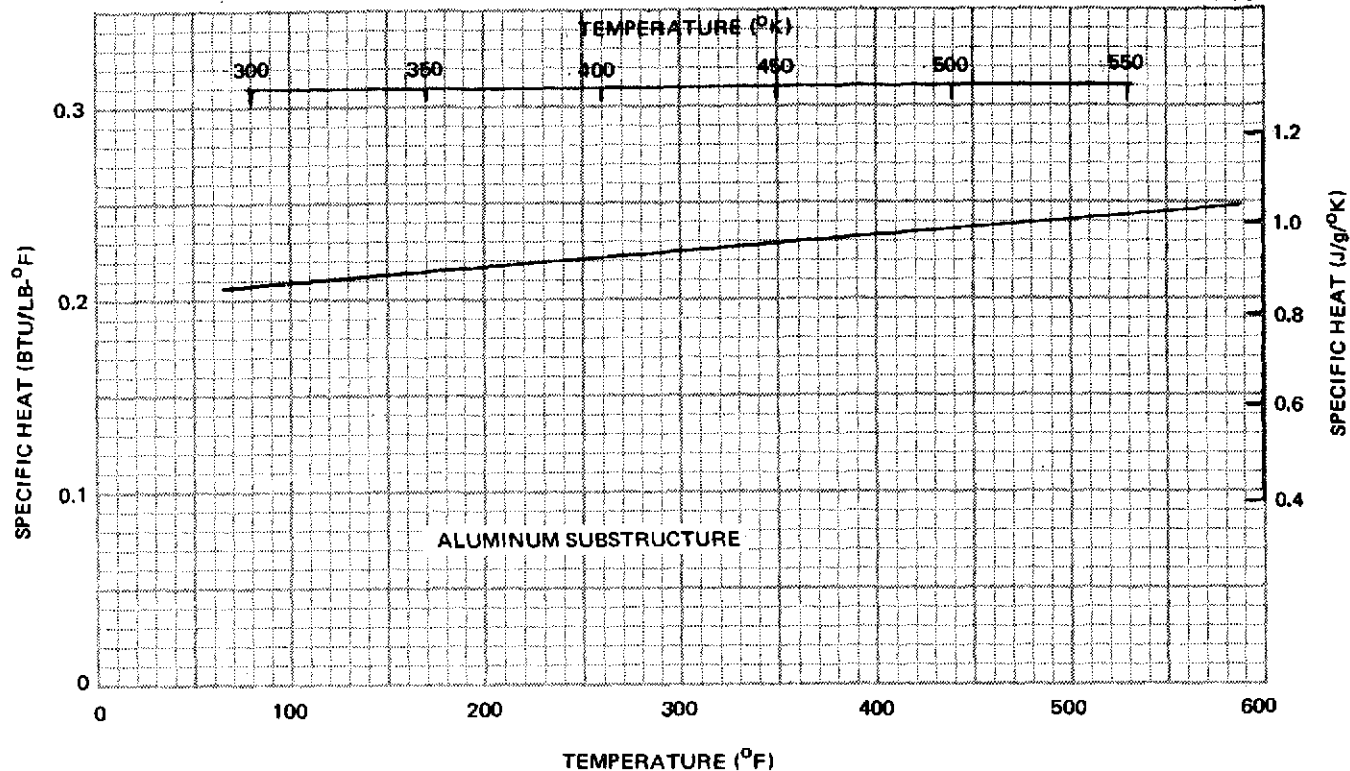Figure D-5. Insulation Conductivity
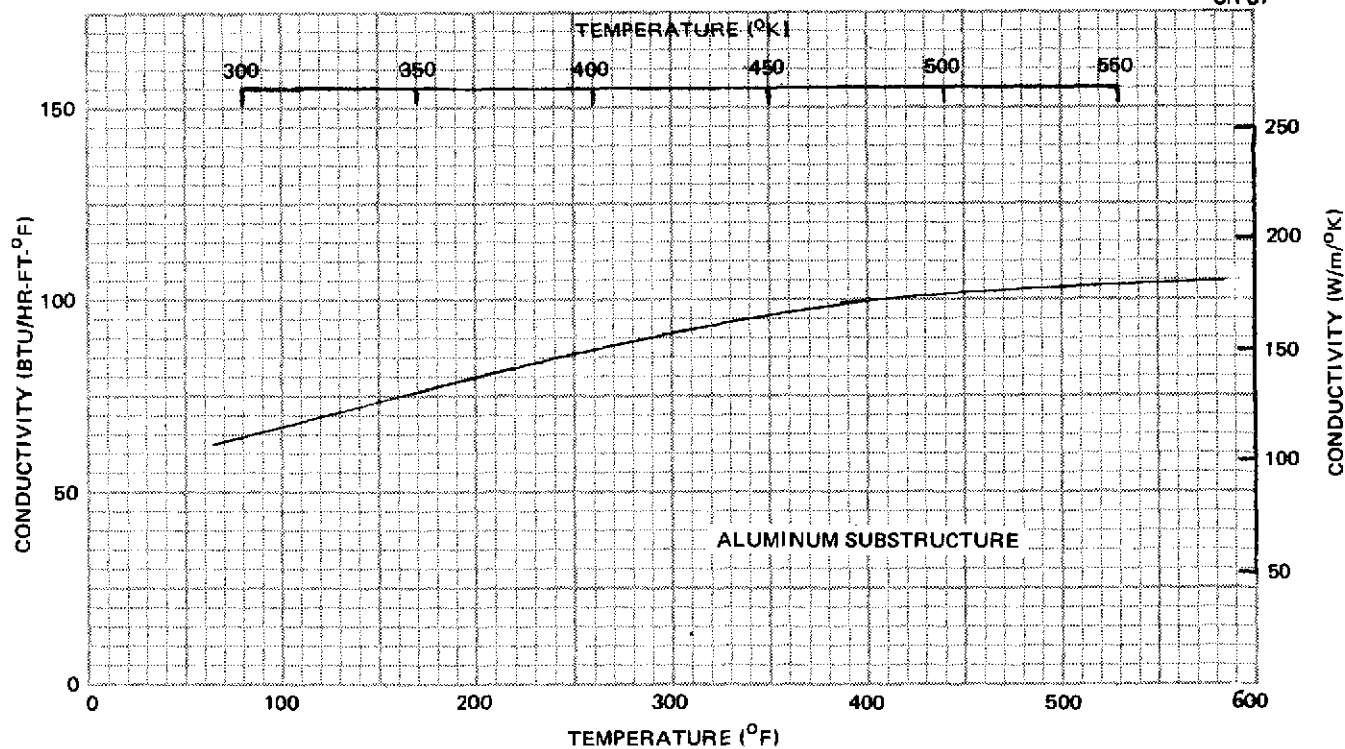
Figure D-6. Specific Heat of Substructure

Figure D-7. Substructure Conductivity

The above differential pressures were selected from computed surface pressures, from vent-lag considerations during boost flight, and from considerations of minimum design burst pressures required during entry flight.

Typical variations of equivalent thickness with maximum stress are shown in Figure D-8 for several panel configurations. Allowable stresses for tension and compressive crippling were determined for each configuration; critical stresses were used to select the minimum equivalent thickness panel for each configuration. Weight penalties for braze-reinforcement were added to configurations using this technique of assembly. Also, weights were computed for panel edge members and doublers, support structure, attachments, and packaged insulation. Detailed weight breakdowns are presented in Table 4-2 (Section 4), while the total unit weights of the designs investigated are presented here. The various heat shield configurations and their total unit weights are given below, the highest rank being equivalent to the lowest weight TPS.

| Rank	Configuration	Unit Weight kg/m^2 (lb/ft^2)
1.	Double face, corrugation-stiffened	22.1 (4.52)
2.	Corrugated Sheet, Post Supports	21.1 (4.33)
3.	Honeycomb	20.5 (4.20)
4.	Single face, corrugation-stiffened (Spotwelded plus braze-reinforced)	20.4 (4.18)
5.	Single face, zee-stiffened (Spotwelded plus braze-reinforced)	20.3 (4.17)
6.	Single face, corrugation-stiffened (Spotwelded only)	20.0 (4.10)
7.	Single face, zee-stiffened (Spotwelded only)	19.9 (4.09)
8.	Single face, channel-stiffened	19.7 (4.03)
9.	Corrugated Sheet (Transverse beam supports)	19.2 (3.94)
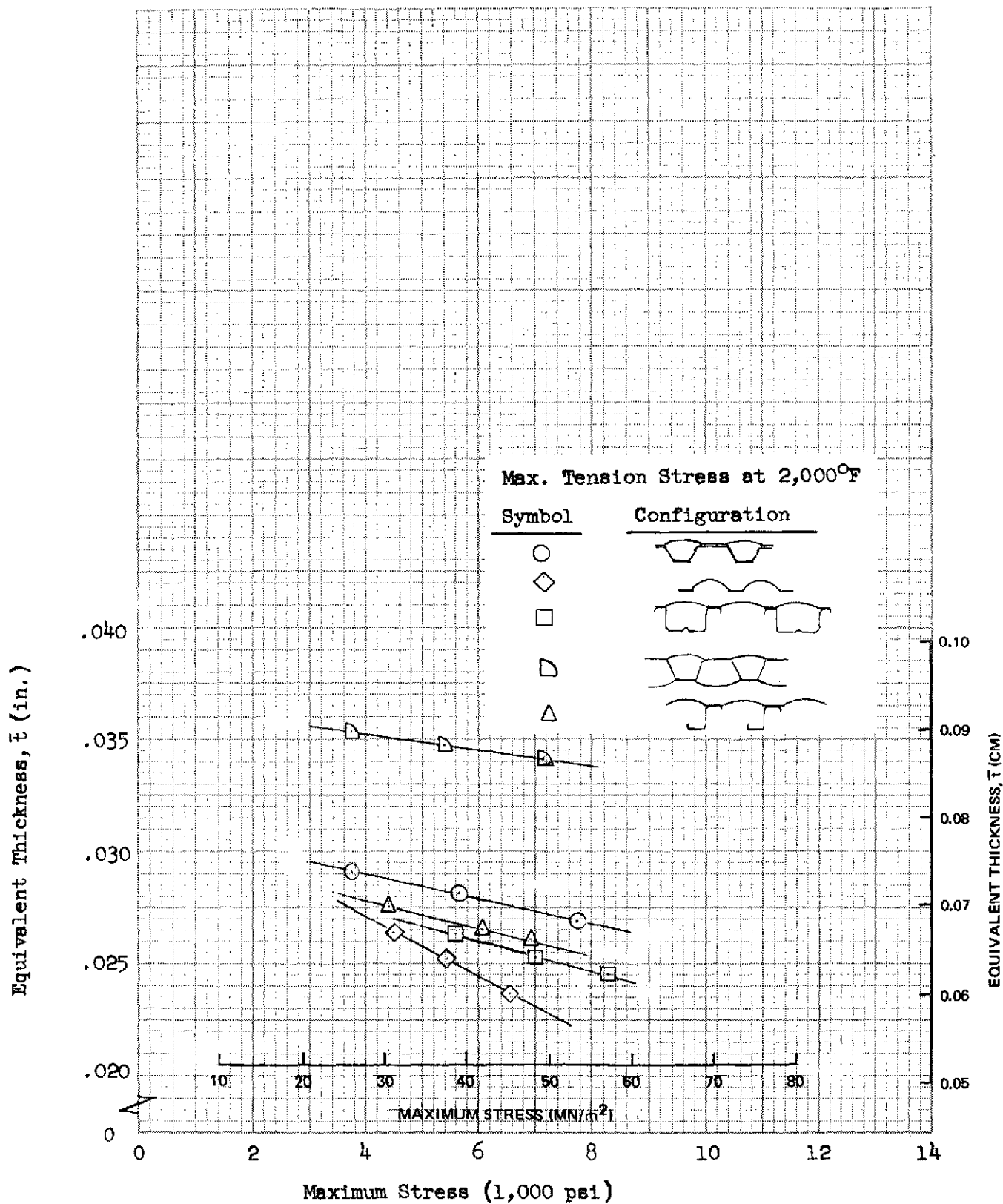
Figure D-8. Panel Equivalent Weight Thickness vs Maximum Stress

D.3 FATIGUE AND FLUTTER EVALUATIONS

The most promising condidate configurations were also checked for fatigue and flutter as a part of the structural evaluation. The four configurations selected for fatigue analysis were the single-faced, corrugation-stiffened design; the zee-stiffened design; the single-faced, channel-stiffened configuration; and the corrugated-sheet design. Acoustic loads during boost flight produced the critical fatigue environment for the surface panels. The fatigue analysis utilized was based upon evaluation of panel equivalent design stresses and comparison of such stresses with a random loading S-N curve. In this analysis method, the panel damping ratio in the first normal mode is first estimated for the frequency ranges where maximum acoustic sound intensities (and maximum fatigue damage) occur. For the liftoff acoustic field (Figure 2-7) experienced in the area used to analyze TD Ni-20Cr heat shields, the frequency ranges of 44.7 to 89.2 Hz, 89.2 to 178 Hz, and 178 to 335 Hz were selected as those of primary interest. For the selected designs, the first natural frequencies all fell in the range of 178 to 335 Hz, and a damping ratio of 0.01 was selected as most appropriate.

The second step in the analysis was the establishment of an equivalent rms differential pressure for the panel designs as a function of acoustic level (in this case, distance from booster nozzle plane) and panel damping ratio. An equivalent rms differential pressure of 9.32 kN/m^2 (1.35 psi) was used to develop equivalent panel stresses for each design.

After the equivalent design pressure was established, the number of stress cycles was determined for the 100-mission life as a function of the panel's natural frequency. The computed number of cycles versus frequency is plotted in Figure D-9 for 100 missions using a life factor of 1.0. The first natural frequency of each panel design was used to determine the total number of cycles for 100 missions.

Equivalent acoustic loading design stresses are compared in Figure D-10 with a random loading S-N curve developed for TD Ni-20Cr sheet material. This S-N curve was developed from the discrete-loading room temperature fatigue
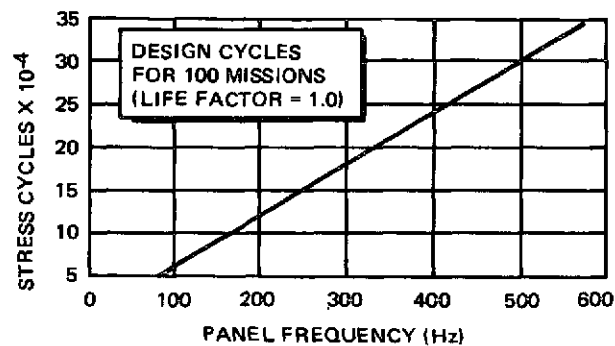
Figure D-9. Panel Stress Cycles vs Frequency

curve presented in Appendix B. A life factor of 10 was applied to the number of cycles computed for the panels (based on 100 missions); the resulting points in Figure D-10 are seen to be below the random loading S-N curve for TD Ni-20Cr sheet. This indicates satisfactory fatigue life for the panels shown in Figure D-10.

Panel flutter investigations included an examination of results presented in Reference D-2, plus evaluations based on flutter design checks used for TPS surface panels during shuttle Phase B efforts.

Data in Reference D-2 were examined since they pertained directly to the single corrugated-sheet design evaluations. Figure D-11 shows the severe decrease in panel flutter resistance of a single corrugated-sheet design when only a small flow angularity occurs with respect to the panel's corrugations. Even with rigid end supports ($K_D = \infty$) the single corrugated sheet falls below the estimated Shuttle trajectory band and thus is predicted to be unstable in flutter.
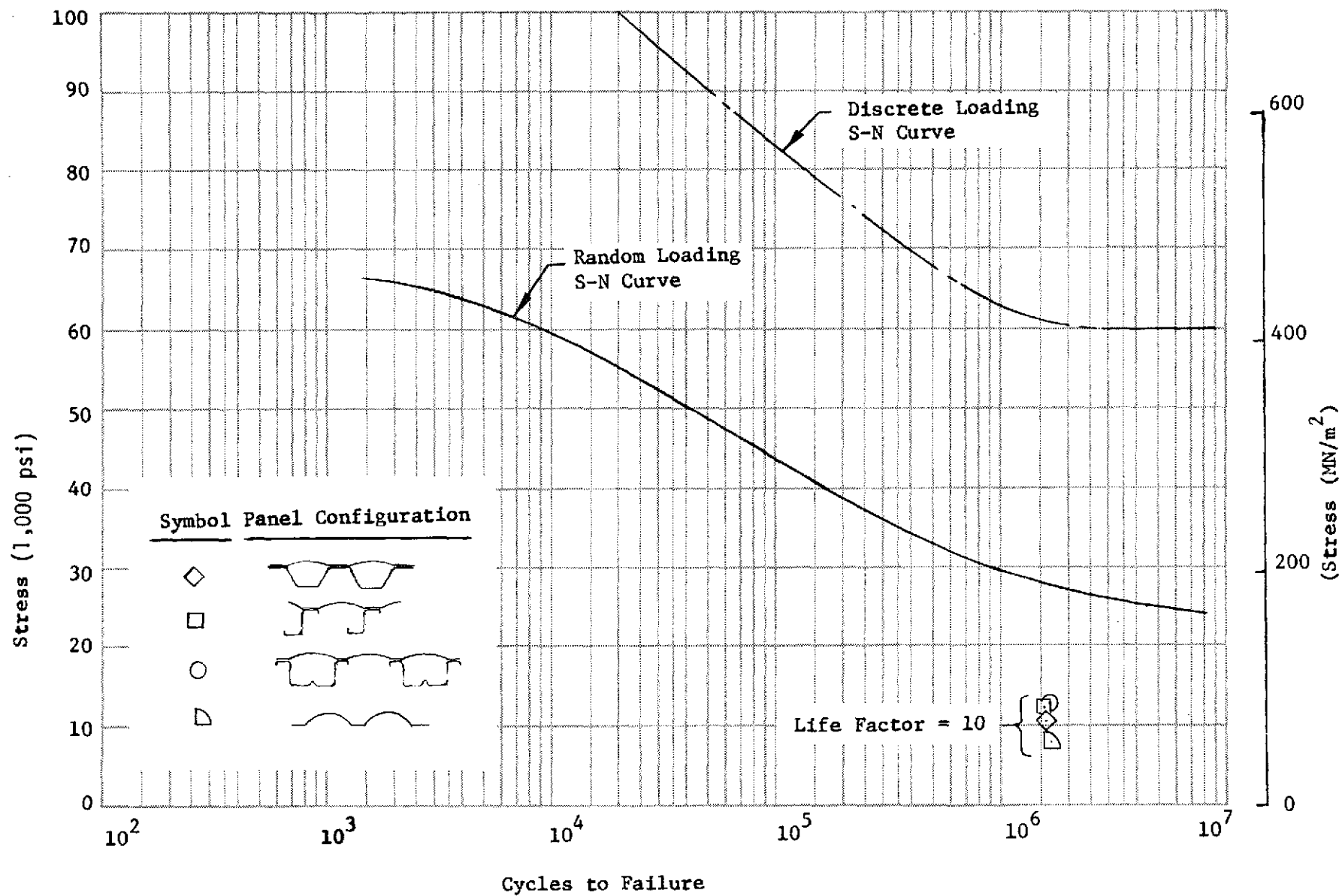
Figure D-10. Heat Shield Fatigue Stresses From Acoustic Loads
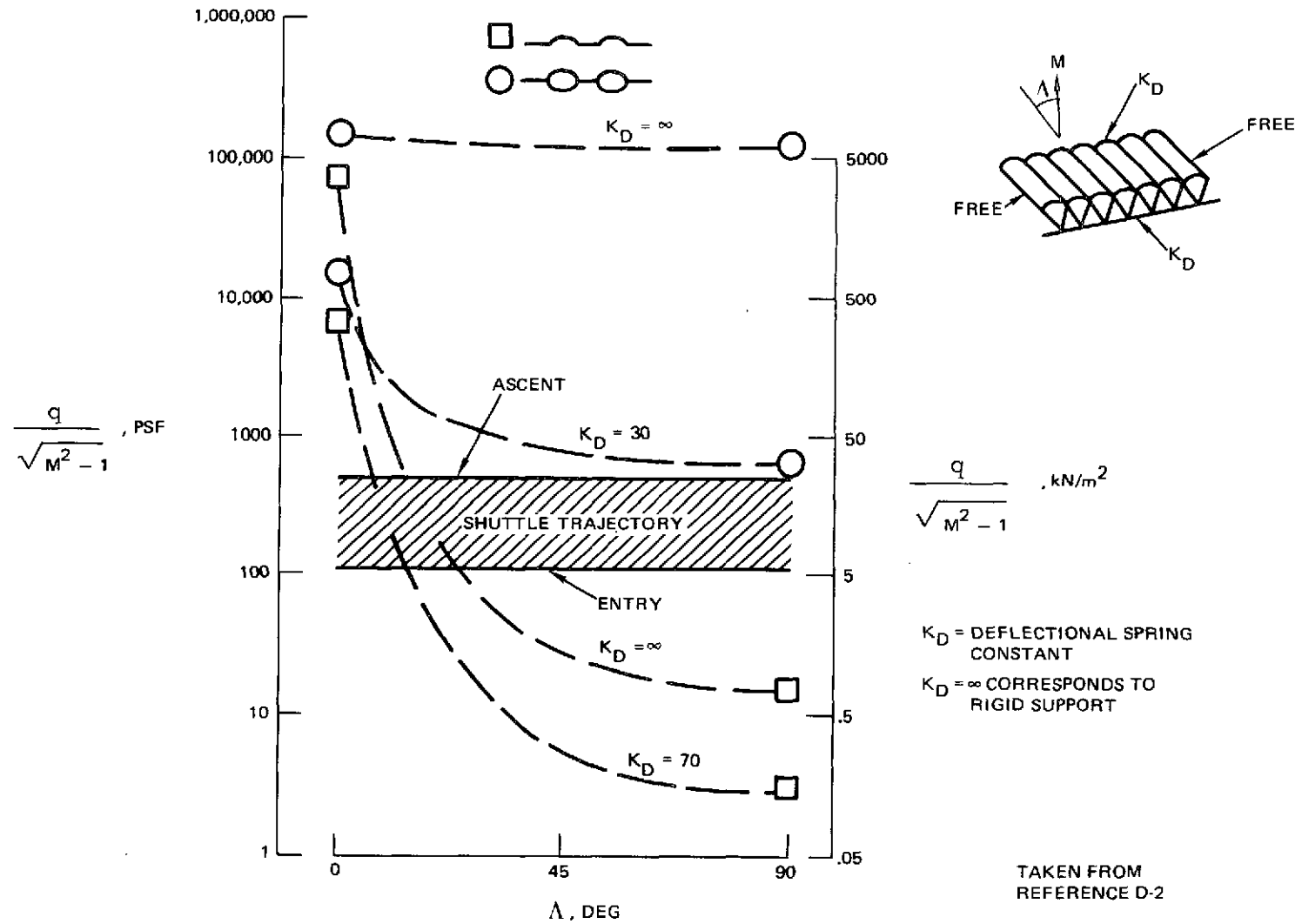
Figure D-11. Flutter Comparison of Shuttle Surface Structure

The lack of flutter resistance of the single corrugated sheet caused low ratings in terms of panel reliability and overall efficiency. Further evaluations of the single corrugated sheet were made using MDAC panel flutter boundary curves as discussed below.

The four most promising candidate designs were evaluated to determine their flutter resistance when compared to MDAC developed flutter boundary curves. The method used in the MDAC analysis accounts for edge-support stiffness effects and for flow angularity effects in the case of orthotropic panels. Panel and flow notations are shown in Figure D-12, and the corrections for Mach number and flow angularity are presented in Figures D-13 and D-14. The flutter boundaries for two edge conditions are presented in Figure D-15 as a plot of panel geometry parameter versus flutter parameter.

The panel flutter stiffness evaluations made on the heat shield designs are presented in Figure D-15. All four designs fell into the flutter-free region of the design chart, with the single corrugated-sheet showing the lowest flutter resistance. Differences in panel cross-sections and stiffnesses combined with differences in analytical approaches account for the single corrugated sheet being shown as flutter-free in Figure D-15, while it falls in the flutter-prone region in Figure D-11. The single face corrugation-stiffened design, the zee-stiffened design, and the channel-stiffened configuration showed the highest flutter resistance of the four designs evaluated.

D-4. CUMULATIVE CREEP EVALUATIONS

Creep deflections for the two designs selected for Phase I tests, the zee-stiffened and single-faced corrugation-stiffened configurations, were analyzed using the Creep Prediction Computer Program. This program uses a numerical approach to solve for creep deflections in metallic TPS panels. The procedure used in this program is similar to that proposed by MacCullough in Reference D-3. To determine panel deflections after a given number of cycles, the proper cyclic creep stress strain curves are input and stress distributions through the depth and along the length of the beam are determined. Steps used to determine creep deflections are described below and illustrated in Figure D-16.

NOTATION:

a	PANEL WIDTH, CROSS STREAM
b	PANEL LENGTH, STREAMWISE
D_x	FLEXURE STIFFNESS, X-DIRECTION
D_y	FLEXURE STIFFNESS, Y-DIRECTION
D_{xy}	TWISTING STIFFNESS
$D_1 =$	$D_x/(1-\mu_x\mu_y)$
$D_2 =$	$D_y/(1-\mu_x\mu_y)$
$D_{12} =$	$D_{xy} + \mu_x D_2$
q	DYNAMIC PRESSURE
f(M)	MACH NUMBER CORRECTION FACTOR
C $=$	$D_{12}/\sqrt{D_1 D_2}$ PANEL STIFFNESS PARAMETER
K_S	DEFLECTIONAL SPRING CONSTANT, STREAM EDGE
K_{LT}	DEFLECTIONAL SPRING CONSTANT, LEADING AND TRAILING EDGES
$\bar{K}_S =$	$K_s a^3/\pi^3 D_1$
$\bar{K}_{LT} =$	$K_{LT} b^3/\pi^3 D_2$

(b/a) $\sqrt{D_{12}/D_2} \div \sqrt{1 + C^2/\bar{K}_S}$ GEOMETRY STIFFNESS PARAMETER

$D_2 f(M)/qb^3 (1 + \pi^2/\bar{K}_{LT})$, FLUTTER PARAMETER
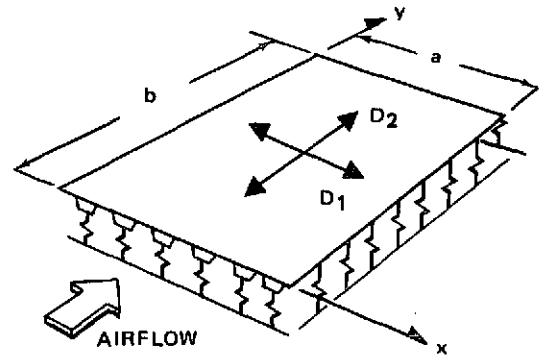
Figure D-12. Panel and Airstream Notation for Flutter Analysis
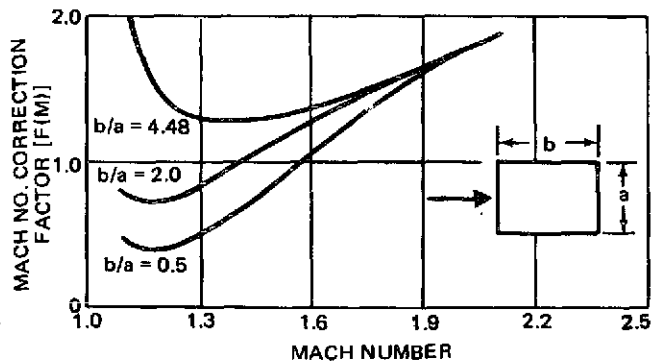
Figure D-13. Mach Number Correction Factor
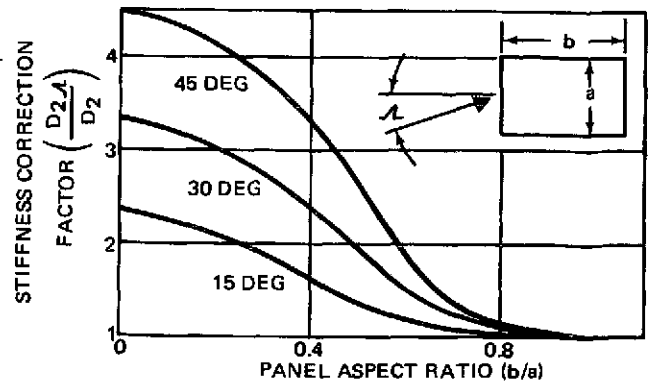
Figure D-14. Stiffness Correction for Flow Angularity
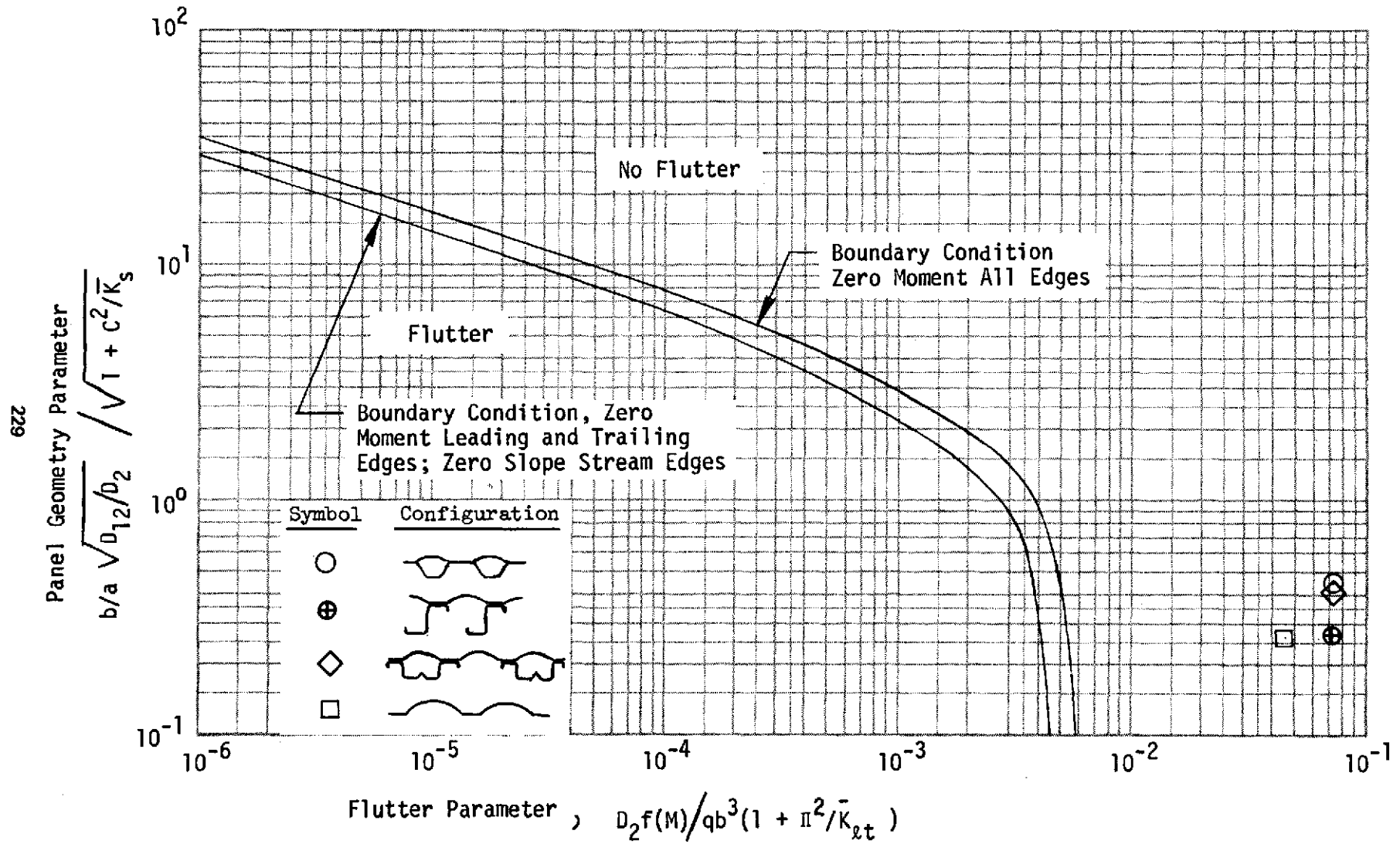
Figure D-15. Panel Flutter Design Boundary
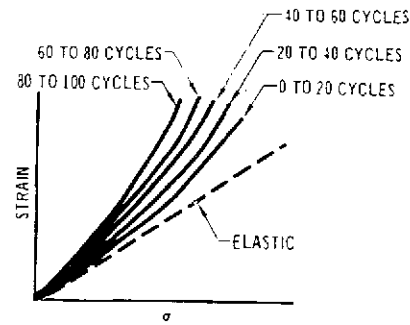
DETERMINE STRESS VERSUS CHANGE
IN STRAIN FOR ASSUMED CYCLE
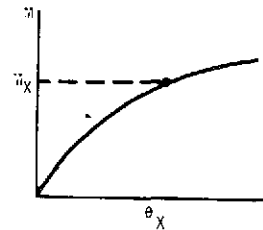INCREMENTS. (20 CYCLE INCREMENTS
SHOWN)
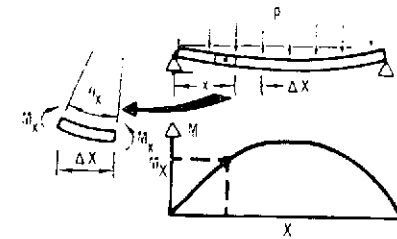
STEP 1 - DIVIDE BEAM INTO FINITE
ELEMENTS OF LENGTH ΔX
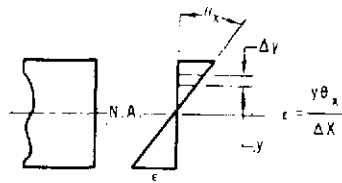
STEP 2 - DIVIDE CROSS SECTION INTO ELEMENTS.
ASSUME NEUTRAL AXIS LOCATION AND
COMPUTE STRAINS FOR ASSUMED
VALUES OF θ_x
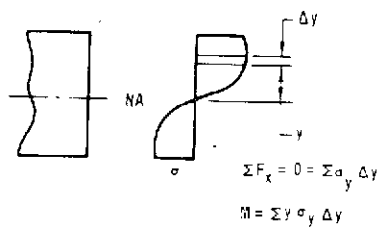
STEP 3 - DETERMINE STRESSES FROM STEP 2 FOR
CALCULATED STRAINS IN STEP 4.
LOCATE CORRECT NEUTRAL AXIS AND
COMPUTE BENDING MOMENT

STEP 4 - PLOT MOMENTS DETERMINED IN
STEP 5 VERSUS θ_x's ASSUMED IN
STEP 4
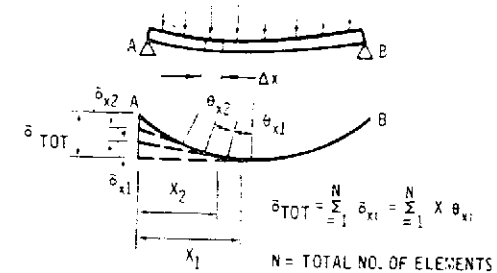
STEP 5 - DETERMINE PANEL DEFLECTION FROM
θ_x's COMPUTED IN STEP 6

Figure D-16. Method for Predicting Panel Deflection

In Step (1), the beam is idealized by dividing the length into segments of length ΔX over which moments are assumed constant. This procedure facilitates computation of beam deflection due to elastic and creep strains.

In Step (2), the beam cross section is idealized by dividing it into increments of thickness ΔY. In this step, it is assumed that plane sections before bending remain plane after bending so strains are proportional to the distance from the neutral axis.

In Step (3), the stress distribution is determined for the strain distribution of Step (4) using the creep stress-strain curves (or analytic functions). The neutral axis is correctly located when the summation of forces over the cross section is zero. Knowing the stress distribution, internal bending moments are determined.
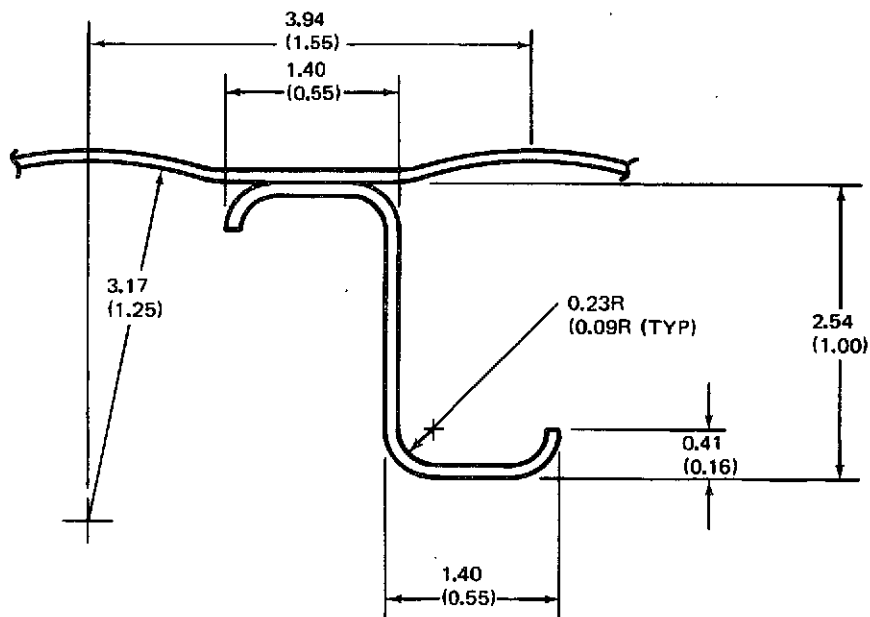
In Step (4), bending moments for various strain distributions (or angular rotations) are determined and related to the actual bending moment distribution along the length of the beam.

In Step (5), bending deflections are computed using angular rotations determined along the length of the beam in Step (4).

A creep deflection analysis was conducted for each of the beam cross-sections shown in Figure D-17 utilizing cyclic creep data presented in Figure D-18. The beam length used for each TPS concept was 39.7 cm (15.62 in.) (Figures 5-17 and 5-18), and an average differential pressure of 2.76 kN/m^2 (0.40 psi) was selected for the panel loading. For the applied pressure of 2.76 kN/m^2 (0.40 psi), maximum outer fiber elastic stresses of 14.98 MN/m^2 (2,170 psi) and 11.52 MN/m^2 (1,670 psi) result for the zee-stiffened and single-faced corrugation-stiffened TPS concepts, respectively. Due to the linear nature of the cyclic stress-strain data in this stress range, the calculation of creep

4.78
(1.88)

3.45
(1.36)

3.17
(1.25)

72°

2.54
(1.00)

1.58
(0.62)
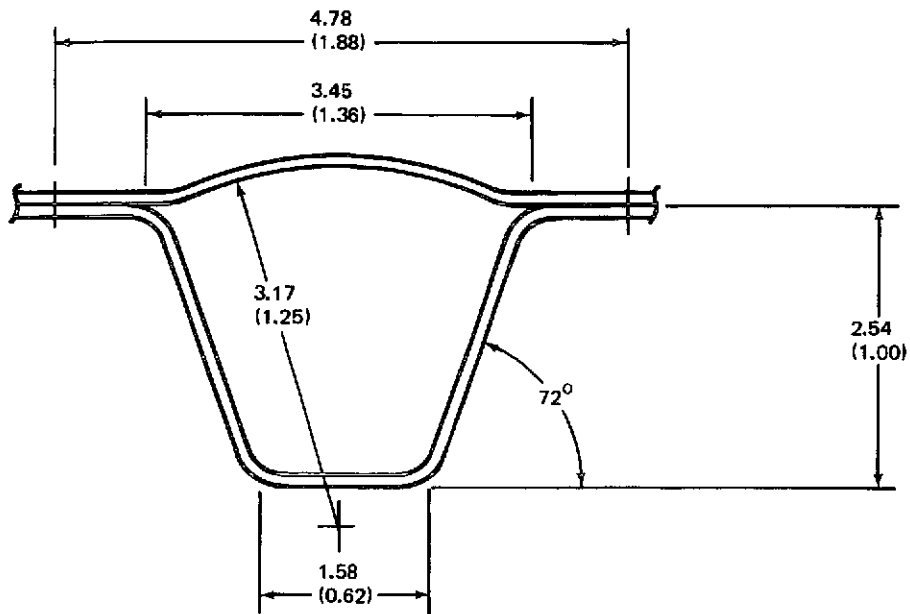
0.010-IN. SHEET THICKNESS
FOR ALL PARTS

3.94
(1.55)

1.40
(0.55)

3.17
(1.25)

0.23R
(0.09R (TYP)

2.54
(1.00)

0.41
(0.16)

1.40
(0.55)

DIMENSIONS ARE IN CM (IN.)

EQUIVALENT STATIC PRESSURE LOAD = 0.40 PSI AT 2,100°F

Figure D-17. Panel Cross-Sections for Panel Creep Analysis

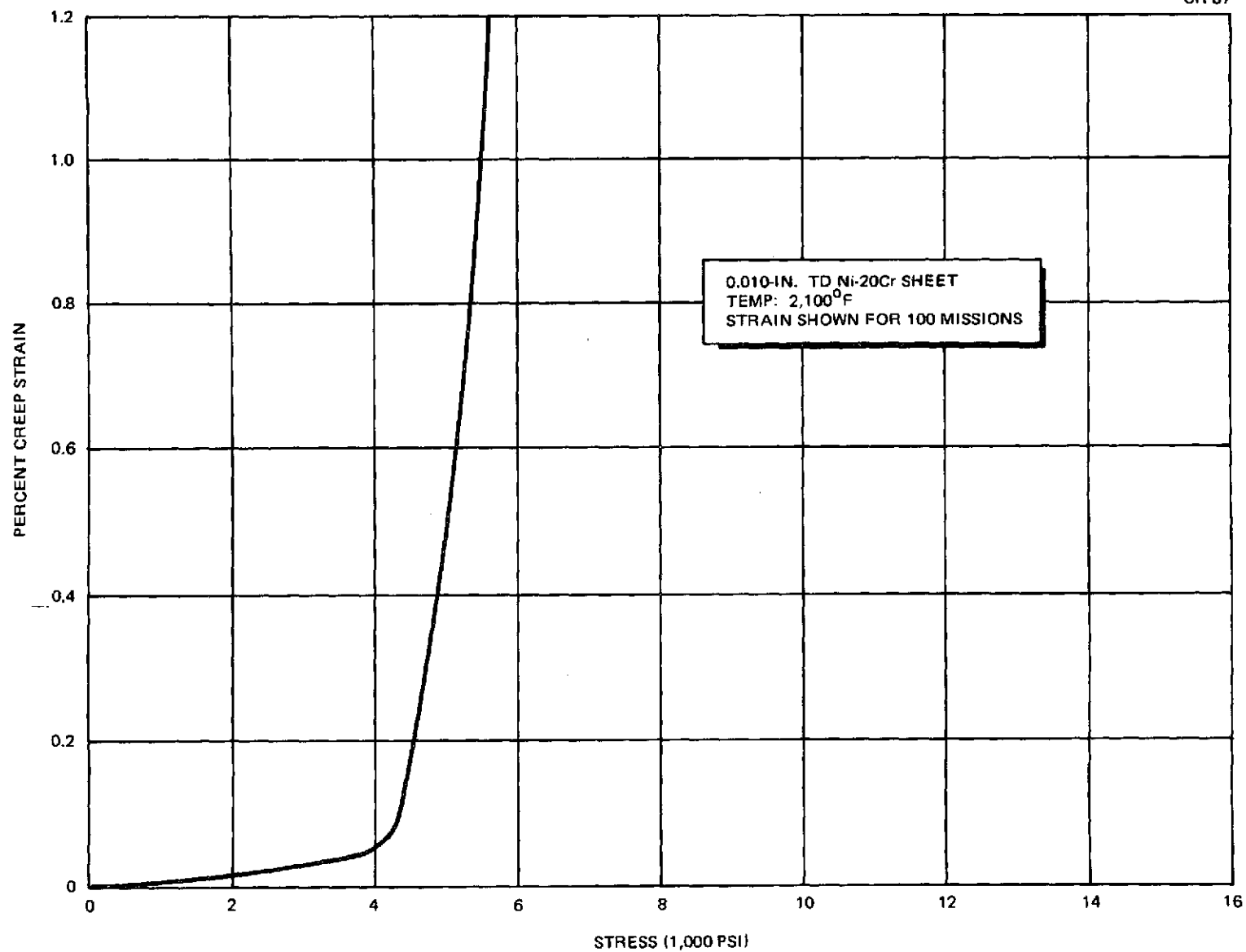Figure D-18. Percent Strain as Function of Stress

deflections based on the total 100-cycle creep data can be checked using linear elastic beam theory. Initial linear elastic stress and strain distributions on the beam sections produce linear creep strains and no residual stresses occur. The analysis assumes that the linear creep stress strain data holds for all cycles and that the data are applicable for both tension and compression. Results of the analysis are presented in Table D-2.

Predicted values of midspan creep deflection as a function of applied pressure for 100 cycles are presented in Figure D-19. Creep deflections of the zee-stiffened concept are higher than the single-face, corrugation-stiffened design due to its lower moment of inertia resulting in higher stresses at a given pressure. Actual panel cumulative mid-span deflections from the 100 test cycles described in Section 5 are also shown in Figure D-19, and, although deflections are very small, reasonable agreement with predicted values was observed.

Table D-2

CUMULATIVE CREEP

|	TPS Concept	
	Zee-Stiffened	Corrugation-Stiffened
Pressure Load	2.76 kN/m^2 (0.40 psi)	2.76 kN/m^2 (0.40 psi)
Beam Length	39.7 cm (15.62 in.)	39.7 cm (15.62 in.)
I/Pitch	0.264 cm^4 (.00635 in^4)	0.404 cm^4 (.00971 in^4)
Maximum Fiber Distance ($\bar{y}$)	1.86 cm (0.7317 in.)	1.80 cm (0.7068 in.)
Maximum Stress	14.98 MN/m^2 (2,170 psi)	11.52 MN/m^2 (1,670 psi)
100-Cycle Midspan Creep Deflection	0.0167 cm (0.00655 in.)	0.0133 cm (0.00524 in.)
Elastic Deflection Under Load (E = 3.5 x 10^6 psi)	0.0549 cm (0.0216 in.)	0.0437 cm (0.0172 in.)

234
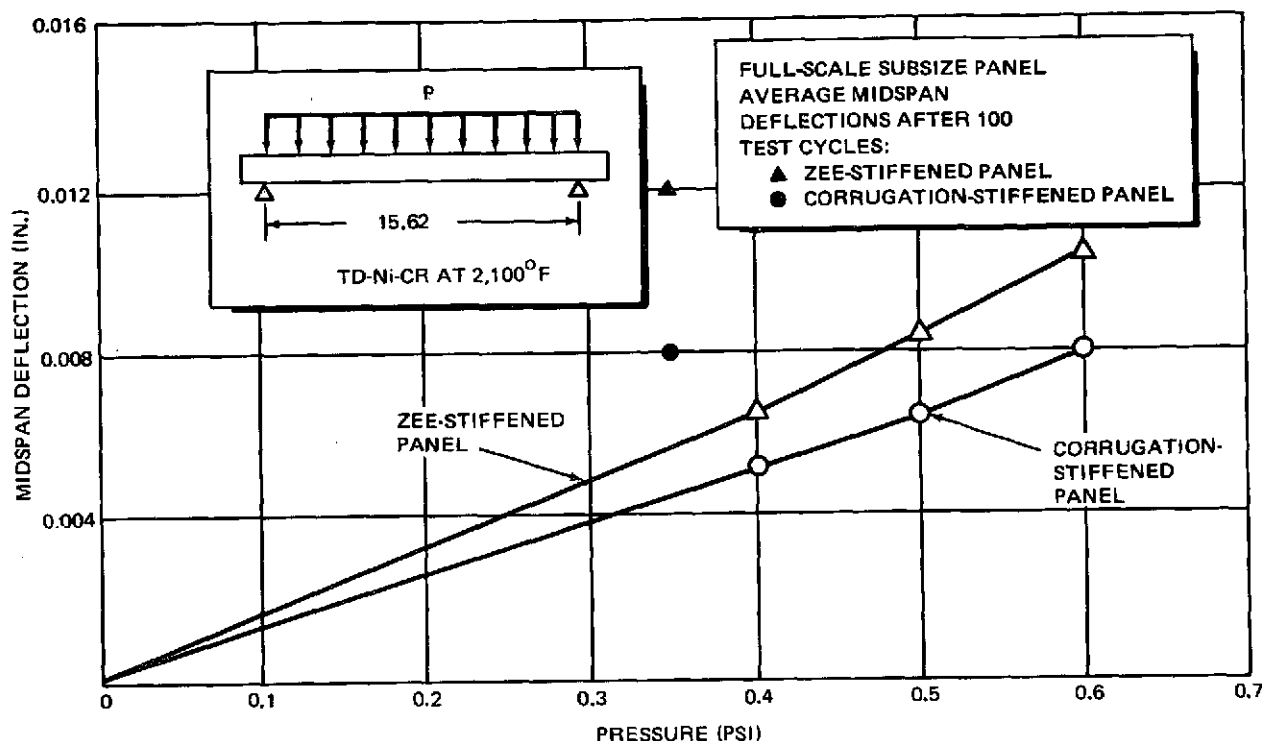
Figure D-19. 100 Cycle Midspan Creep Deflection vs Applied Pressure

D.5 PRODUCTION COSTS

In comparing fabrication costs, configurations 1 and 3 (Figure D-1) were ana-
lyzed for two assembly techniques; one in which simple spotwelding was used
and the second in which the panels were spotwelded and braze reinforced.
Configuration 2, the single corrugated sheet, was analyzed using spotwelding
to attach required edge members and clips. Brazing was the assembly tech-
nique for honeycomb, while spotwelding was used in analyzing panel configu-
rations 5 and 6.

Detailed fabrication procedures were outlined for each configuration to include
all required shop operations such as cutting, forming, trimming, drilling or
punching, inspection of parts, cleaning, and assembly. Tooling required for

each configuration was determined; costs for each configuration were computed based upon manhour and material estimates that included the following operations:

A. Manufacturing Engineering and Tooling
B. Planning
C. Industrial Engineering
D. Manufacturing Operations
E. Quality Assurance
F. Material for tooling and manufacturing.

Cost analyses included full burden for labor and material plus G & A expenses.

As a result of these studies, the configurations shown in Figure D-1 were ranked in order, with the highest rank being associated with the lowest cost. The configuration rankings were

Rank	Configuration	Relative Cost
1.	Honeycomb	Highest
2.	Single face, corrugation-stiffened (Spotwelded plus braze-reinforced)	
3.	Single face, zee-stiffened (Spotwelded plus braze-reinforced)	
4.	Double face, corrugation-stiffened	
5.	Single face, channel-stiffened	
6.	Single face, corrugation-stiffened (Spotwelded only)	
7.	Single face, zee-stiffened (Spotwelded only)	
8.	Corrugated Sheet (Transverse beam supports)	
9.	Corrugated Sheet (Multiple post supports)	Lowest

D.6 SUMMARY OF PARAMETRIC EVALUATIONS

The parametric studies of TPS configurations are summarized in Table D-3. Weighted ratings are given for each design approach in each of the categories evaluated. The TPS weight and cost were given the heaviest weightings, with the other parameters being given equal weight in the evaluations. Experienced design and manufacturing personnel were used to provide qualitative judgements of the various concepts in areas of fabricability, refurbishability, and reliability. Efficiency of each concept was judged in terms of overall performance and simplicity of the design approach. Rating factors from 1 to 10 were assigned; these ratings are shown in the left column under each parameter. The weighted rating was obtained by multiplying the weighting factor by the concept rating. The highest total ratings were shown by the single face, zee-stiffened panel and the single face, corrugation-stiffened designs using spotwelding without braze-reinforcement. These designs were considered to be weight competitive, cost competitive, and were rated highly in the other evaluation categories considered. As a result of this evaluation, the two designs with highest ratings were selected for use in the Phase I full-scale subsize panel tests.

Table D-3

SUMMARY OF HEAT SHIELD PARAMETRIC STUDY

Note: Rating factor shown in left column under each parameter
Weighted rating shown in right column under each parameter

TPS Configuration Summary			TPS Study Parameters and Weighting											Rating Summary	
Heat Shield Configuration	Support System	Panel Joining Method	TPS Weight (0.20)		Cost (0.20)		Fabricability (0.15)		Refurbishability (0.15)		Reliability (0.15)		Efficiency (0.15)		Sum of Weighted Rating	Order of Rating
	Transverse Beams at Panel Ends	Spotwelded	6	1.20	8	1.60	7	1.05	8	1.20	7	1.05	7	1.05	7.15	2
		Spotwelded and Braze Reinforced	4	0.80	5	1.00	5	0.75	8	1.20	8	1.20	8	1.20	6.15	6
	Multiple Post	Spotwelded[1]	3	0.60	10	2.00	7	1.05	7	1.05	4	0.60	2	0.30	5.60	7
	Transverse Beams at Panel Ends	Spotwelded[1]	9	1.80	9	1.80	6	0.90	9	1.35	3	0.45	1	0.15	6.45	4
	Transverse Beams at Panel Ends	Spotwelded	8	1.60	9	1.80	7	1.05	7	1.05	7	1.05	7	1.05	7.60	1
		Spotwelded and Braze Reinforced	5	1.00	6	1.20	5	0.75	7	1.05	8	1.20	8	1.20	6.40	5
	Multiple Post	Brazed	3	0.60	2	0.40	2	0.30	6	0.90	6	0.90	9	1.35	4.45	8
	Transverse Beams at Panel Ends	Spotwelded	2	0.40	6	1.20	4	0.60	5	0.75	5	0.75	3	0.45	4.15	9
	Transverse Beams at Panel Ends	Spotwelded	8	1.60	7	1.40	6	0.90	7	1.05	7	1.05	5	0.75	6.75	3

[1] Edge members and clips spotwelded to panel.

APPENDIX D

REFERENCES

D-1. Hughes, T. A. High Temperature Insulation Materials for Reradiative Thermal Protection Systems. Final Report, Contract NAS 8-26115. McDonnell Douglas Report No. MDC E0666, July 1972.

D-2. Bohon, H. L. and Shore, C. P. Application of Recent Panel Flutter Research to the Space Shuttle, Part II-Influence of Edge Clips and Flow Angularity. NASA TM X-2274, pp. 247-264, April 1971.

D-3. MacCullough, G. H. An Experimental and Analytical Investigation of Creep in Bending. Trans. ASME, Vol. 55, 1933.

APPENDIX E

METEOROID ENVIRONMENT EFFECTS ON HEAT SHIELD GAGES

Appendix E

METEOROID ENVIRONMENT EFFECTS ON
HEAT SHIELD GAGES

This appendix presents calculations for Orbiter heat shield thicknesses required to meet criteria of (1) a 0.95 probability of no puncture during a seven-day mission and (2) a 0.95 probability of one or fewer punctures during a seven-day mission.

The Space Shuttle meteoroid impact requirements (Appendix A) specify that protection shall be provided against loss of functional capability of selected critical items when subjected to the meteoroid flux model as defined in NASA TMX-64627. It is further specified that the probability of no penetration shall be assessed on each item, dependent upon function criticality.

The basic Shuttle requirement stipulated at least a 0.95 probability of no puncture during total mission time (100 to 500 missions). This requirement creates an excessive weight penalty for radiative metallic heat shields, and the requirement may be excessive for external heat shields that can be inspected visually between missions. Thus, a seven-day mission was used as a discrete time span for exposure of the TD Ni-20Cr heat shields to the meteoroid flux, the assumption being made that damaged heat shield panels will be detected and replaced between missions. The other basic assumptions used in the analysis are

A. Average meteoroid velocity = 20 km/s (TMX-64627).

B. Meteoroid mass density = 0.5 g/cm^3 (TMX-64627).

C. Threshold penetration of a thin ductile metallic skin is expressed by the equation

$$t = K_1 \, \rho^{1/6} \, m^{0.352} \, V^{0.875} \tag{1}$$

where

$$t = \text{skin thickness, cm}$$
$$K_1 = \text{material constant} = 0.32$$
$$\rho = \text{meteoroid density, g/cm}^3$$
$$m = \text{meteoroid mass, g}$$
$$V = \text{meteoroid velocity, km/s}$$

(4) The orbital altitude is 100 nm

The probability P, of n or less penetrations occurring is expressed by Poisson's distribution*.

$$P(0, 1, 2, ---n) = \sum_{n=0}^{n} \frac{e^{-\lambda}\lambda^n}{n!} \tag{2}$$

The average number of expected events, λ, can be expressed as

$$\lambda = NFAT \tag{3}$$

where

N = Number of impacts per square meter per second exceeding a particle mass m

F = Shielding factor

A = Exposed area to meteoroid environment, square meters

T = Duration of stay in meteoroid environment, seconds

The basic equation relating meteoroid mass, m, and the meteoroid flux, N, is

$$\log N = -14.37 - 1.213 \log m \tag{4}$$

---

*Burford, J.C., Johnson, C.E., and Ong, C.C. The Effect of the Meteoroid Environment on a Coated Columbium Radiative Heat Shield for a Space Shuttle, Bellcomm Inc. Technical Memorandum TM70-1012-1, April 17, 1970.

Combining equations (3) and (4), the meteoroid mass may be expressed as

$$m = \left[\frac{0.427 \times 10^{-14}}{N}\right]^{0.824}$$

or

$$m = \left[\frac{0.427 \times 10^{-14}(FAT)}{\lambda}\right]^{0.824} \tag{5}$$

The meteoroid mass is determined from equation (5) for the value of λ which corresponds to the selected probability and number of allowable penetrations. This mass is then substituted in equation (1) to determine the skin thickness required.

From TMX-64627 the shielding factor is

$$F = \frac{1 + \cos \theta}{2} \tag{6}$$

where θ is as shown
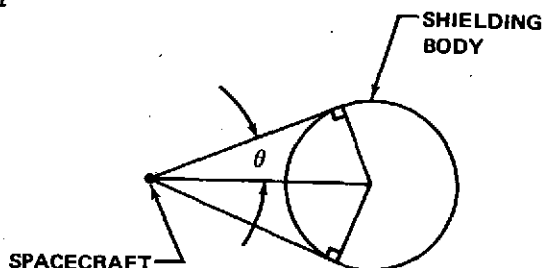
For a spacecraft at 100-nm altitude,

$$F = 0.612$$

As noted previously, the time selected ~~ ~~
or seven days.

$$T = 7 \text{ days} = 6.05 \times 10^5 \text{ s}$$

For a 0.95 probability of no penetrations in the seven-day mission,
P (0, 0) = 0.95 then

$$\lambda = 0.0506$$

and

$$m = 3.44 \times 10^{-5} \text{ g}$$

Using the above meteoroid mass in equation (1), the required heat shield panel thickness is

$$t = 0.106 \text{ cm}$$

or

$$t = 0.0417 \text{ in.}$$

This thickness requirement was considered to be prohibitively heavy, and a criterion of one or less penetrations was investigated. In this criterion, P (0, 1) = 0.95 and the corresponding value of λ from equation (2) is

$$\lambda = 0.35$$

and

$$m = 6.99 \times 10^{-6} \text{ g}$$

246

The required heat shield panel thickness then becomes

$$t = 0.0605 \text{ cm}$$

or

$$t = 0.0238 \text{ in.}$$

This smaller panel thickness was selected as an initial design requirement for the TD Ni-20Cr subsize panels tested in Phase I. Specific tests were conducted to check the damage sustained by test panels when subjected to simulated meteoroid impact followed by simulated entry flow conditions in the Plasma Arc Tunnel (see Section 5).

APPENDIX F

PRELIMINARY ACOUSTIC TESTS OF FULL-SCALE
SUBSIZE PANELS

APPENDIX F

PRELIMINARY ACOUSTIC TESTS OF FULL-SCALE
SUBSIZE PANELS

Preliminary acoustic tests were conducted at four overall sound pressure
levels (150 db, 155 db, 160 db, and 165 db) to determine panel rms stresses
as a function of sound pressure level. Test duration was approximately
one minute at each sound pressure level. The panels had four strain gages
installed, two at the center of each panel. The gage numbers and locations,
shown in Figures 5-17 and 5-18, are repeated here for convenience.

Strain Gage 1 - Center of _Γ̄ stiffener - top skin

Strain Gage 2 - Center of Π̄ stiffener - top skin

Strain Gage 3 - Center of _Γ̄ stiffener - bottom flange

Strain Gage 4 - Center of Π̄ stiffener - bottom flange

The test fixture was bolted to the floor of the progressive wave chamber for
acoustic excitation. The output of the four strain gages were recorded on
magnetic tape at input sound pressure levels of 150, 155, 160, and 165 db.

Octave band spectrum analyses of the four acoustic inputs are presented in
Figures F-1 through F-4. Power spectral density analyses of the four strain
gages are presented in Figures F-5 through F-20. Table F-1 lists the filter
bandwidths and statistical degrees of freedom for the spectrum analyzer used
for the strain gage analyses. Correlation of overall stress level and sound
pressure level for the four strain gages were presented in Figure 5-24.
Stress was calculated using a modulus of elasticity for the panel equal to
168×10^6 kN/m^2 (24.4×10^6 psi) and assuming that the stress was uni-
directional.

The equivalent rms stresses predicted for liftoff acoustic levels were com-
pared to a random loading fatigue curve in Appendix D to assess the panel
designs in terms of fatigue resistance. Strain readings in the preliminary
acoustic tests were also analyzed for rms stress levels. The panel midspan
rms stresses in the preliminary acoustic tests were determined from tape

recordings of the strain gage outputs that were subsequently analyzed by a true rms voltmeter. The rms stresses obtained from the recordings were based on a Gaussian distribution with a 3σ deviation. The tape recordings of strain output were also fed to a Ling ASDE-80 analyzer to obtain the power spectral density distributions shown in Figures F-5 through F-20. The rms stress levels recorded in preliminary acoustic tests (Figure 5-24) were lower than had been predicted in the fatigue analysis (see Appendix D, Figure D-10), the computed stresses being in the range of 55.1 MN/m^2 (8,000 psi) to 75.8 MN/m^2 (11,000 psi). The somewhat lower stresses of less than 20.7 MN/m^2 (3,000 psi) recorded in the preliminary acoustic tests indicated a safe stress level at the center of the panels. However, attach points on the panels showed progressive damage from acoustic tests (see Section 5).
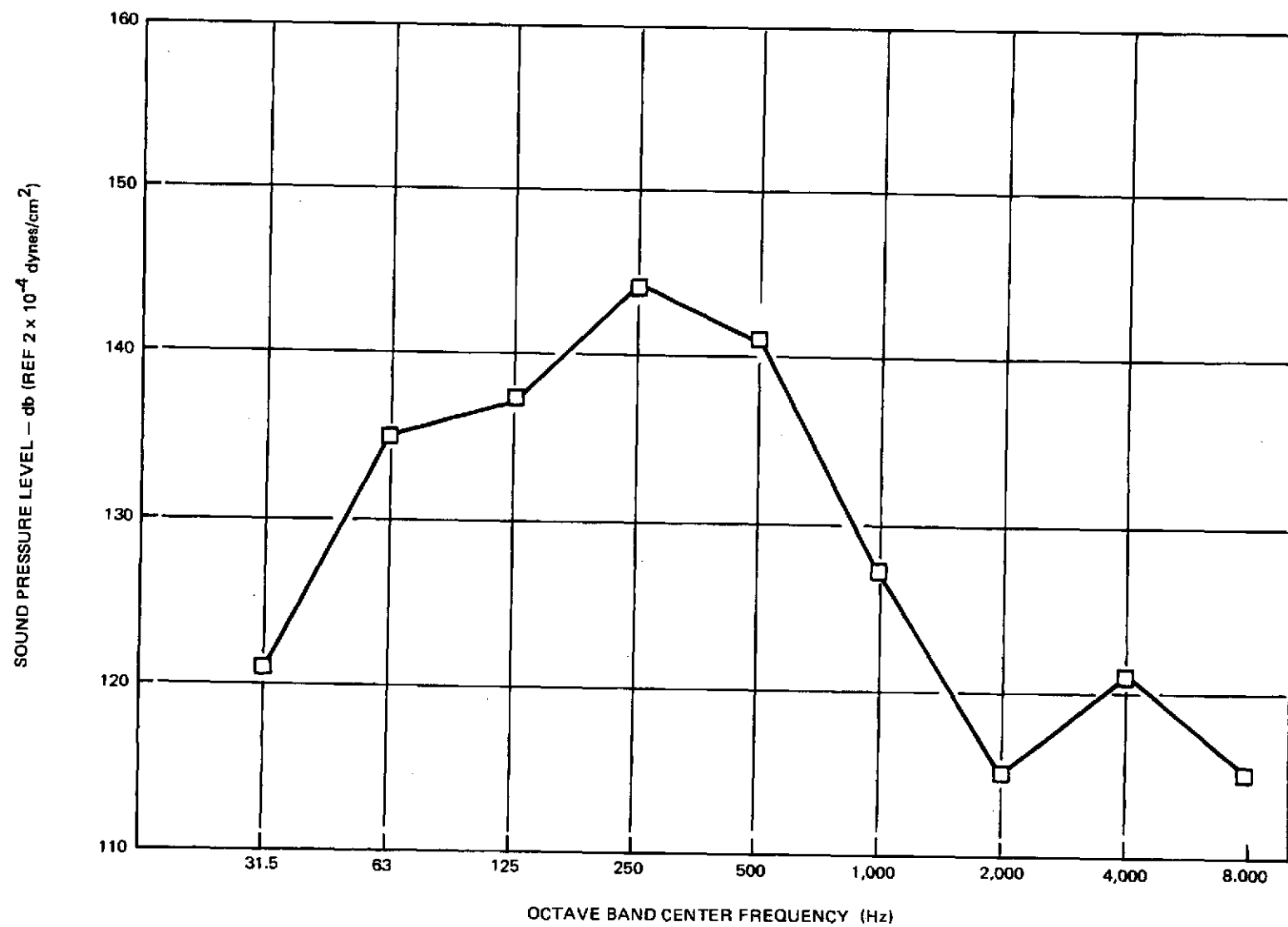
Figure F-1. Octave Band Spectrum Analysis; 150 db OASPL
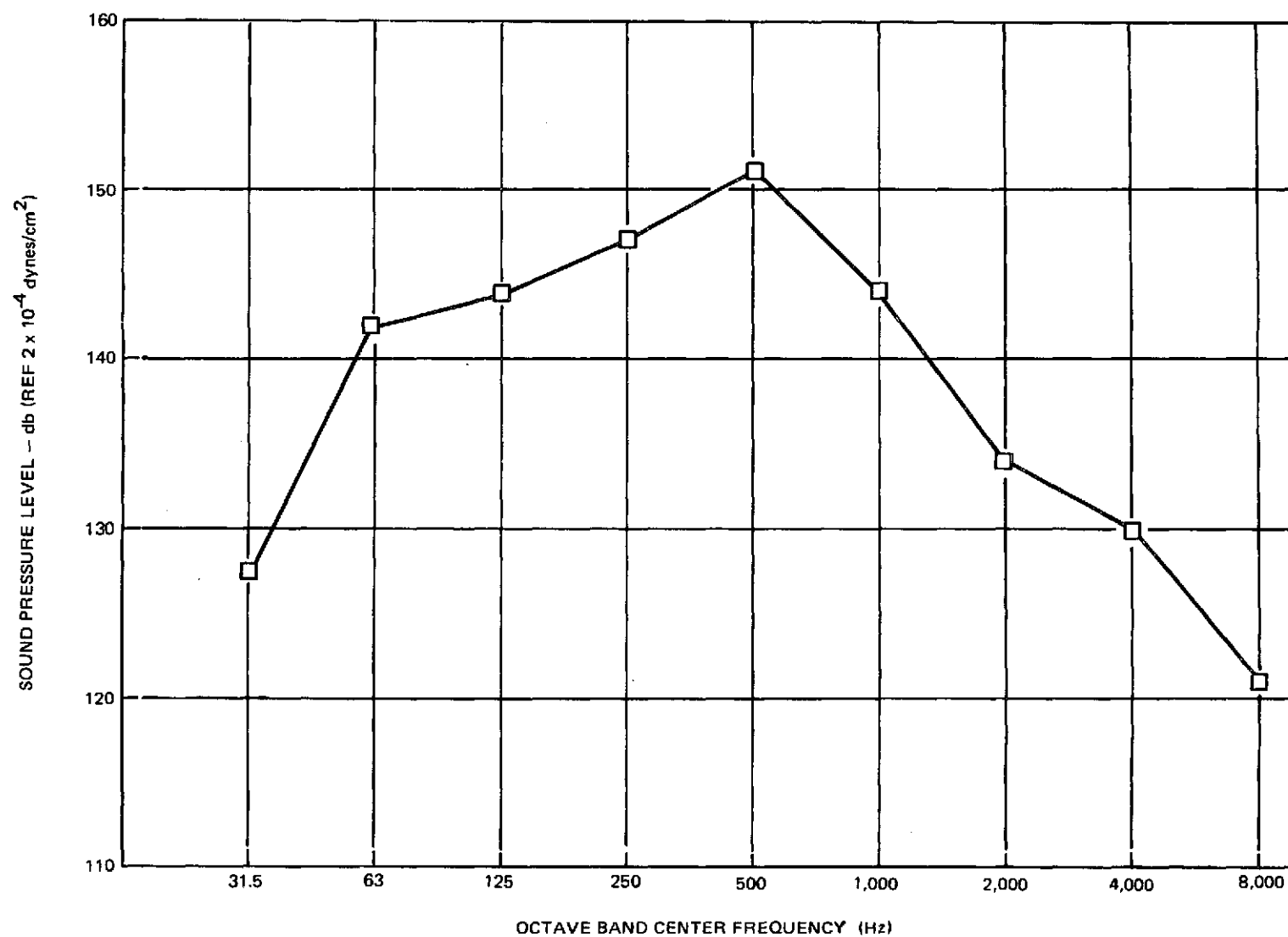
Figure F-2. Octave Band Spectrum Analysis; 155 db OASPL
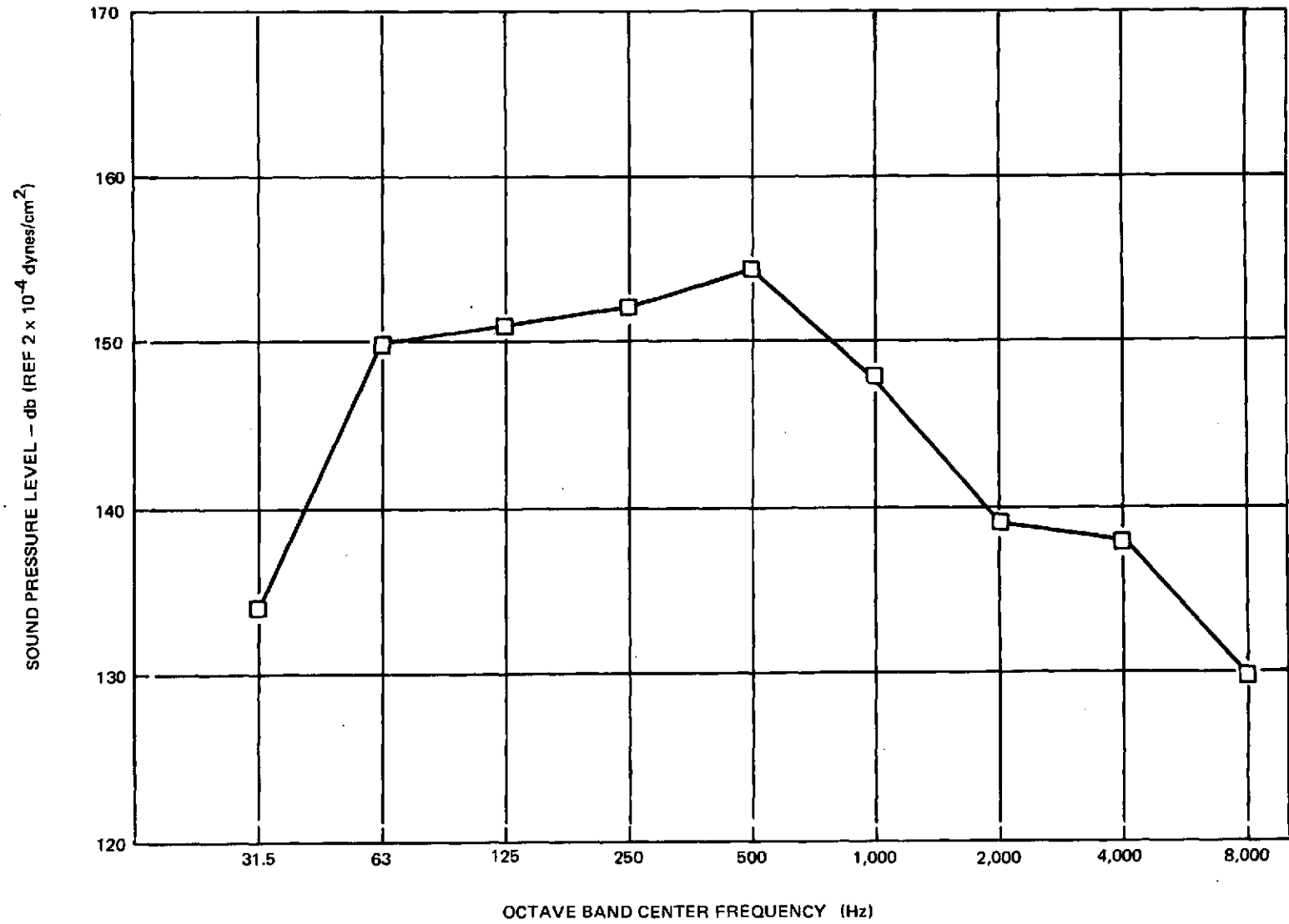
Figure F-3. Octave Band Spectrum Analysis; 160 db OASPL
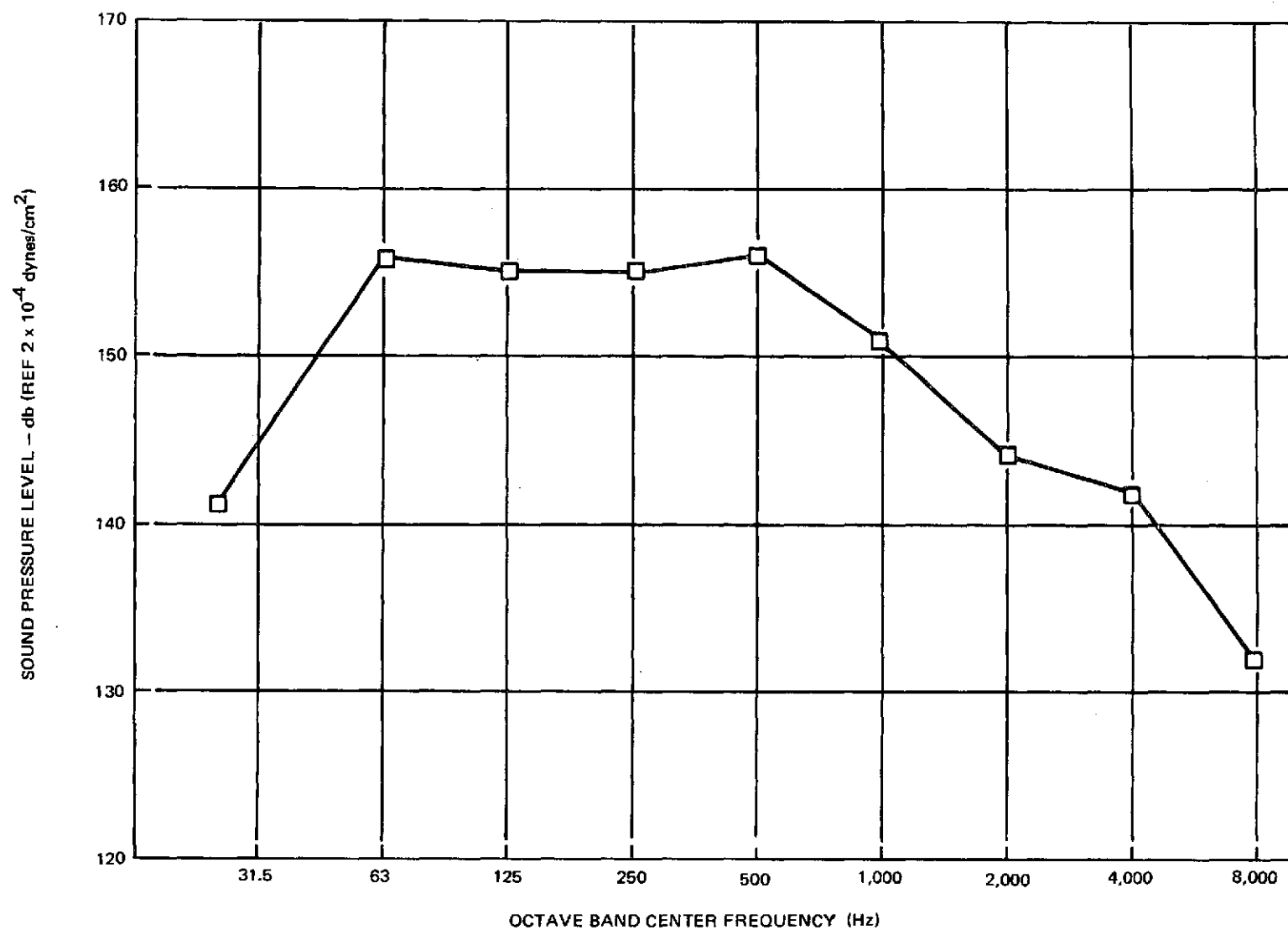
Figure F-4. Octave Band Spectrum Analysis; 165 db OASPL
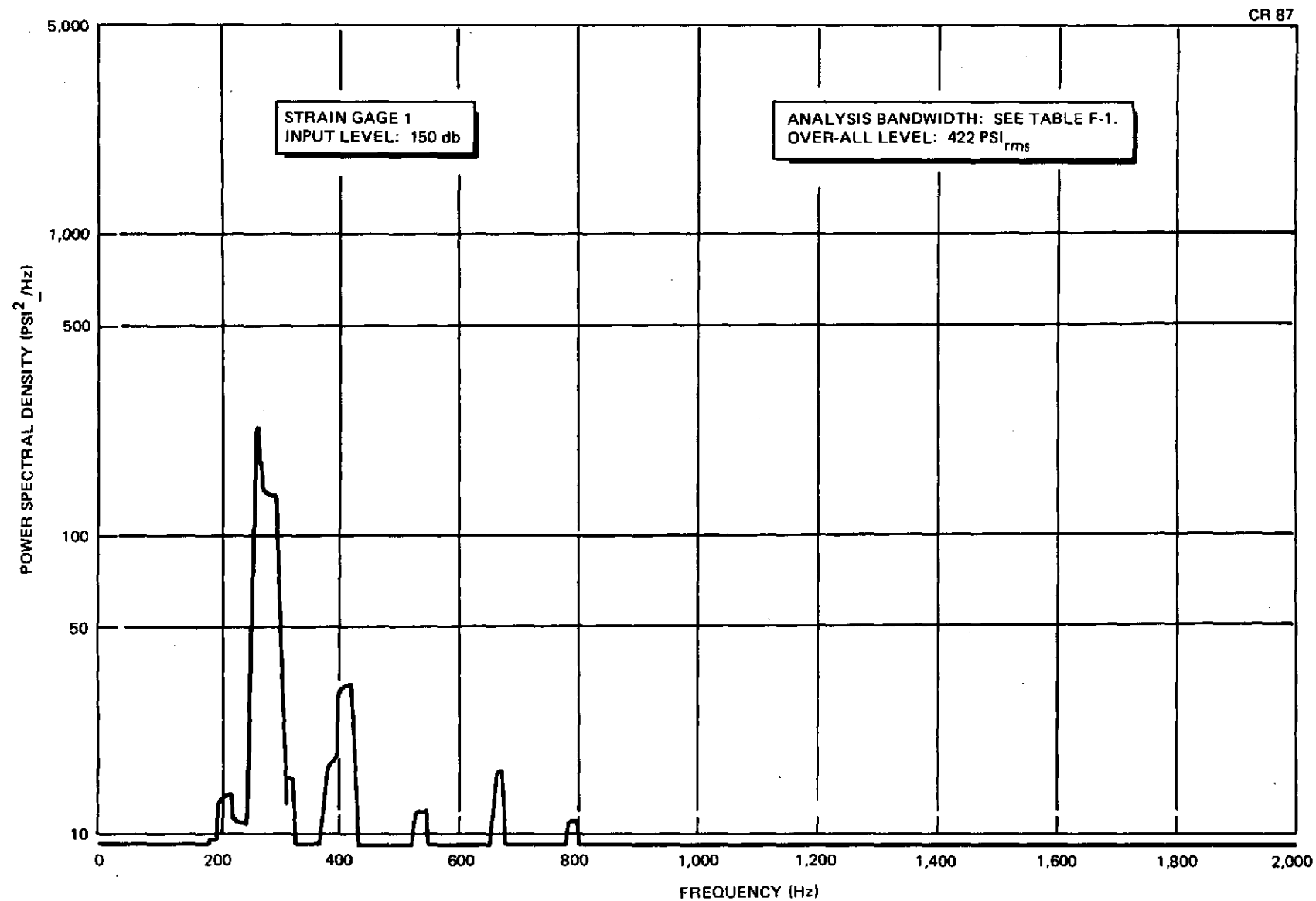
Figure F-5. Power Spectral Density Analysis; SG 1, 150 db
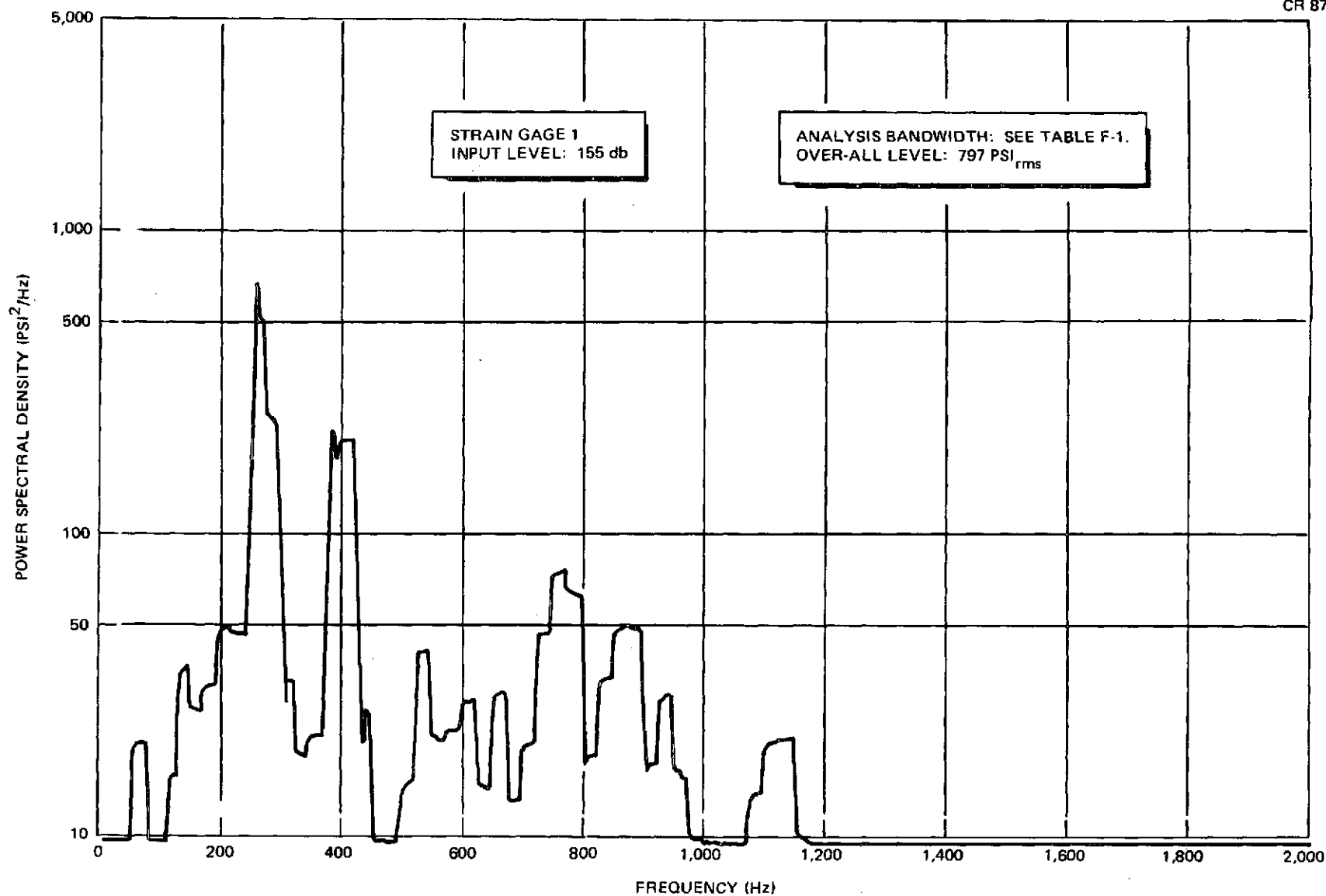
Figure F-6. Power Spectral Density Analysis; SG 1, 155 db
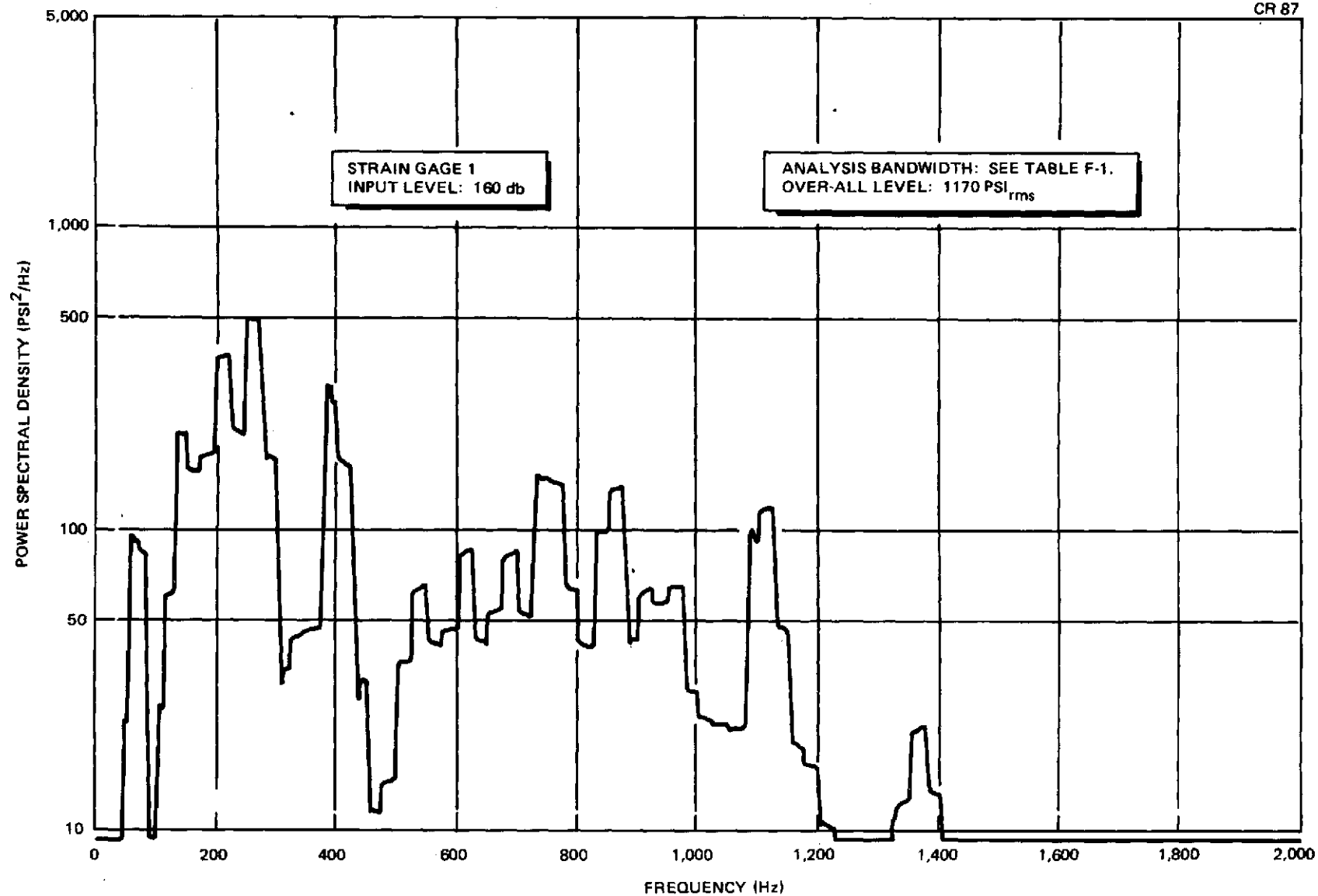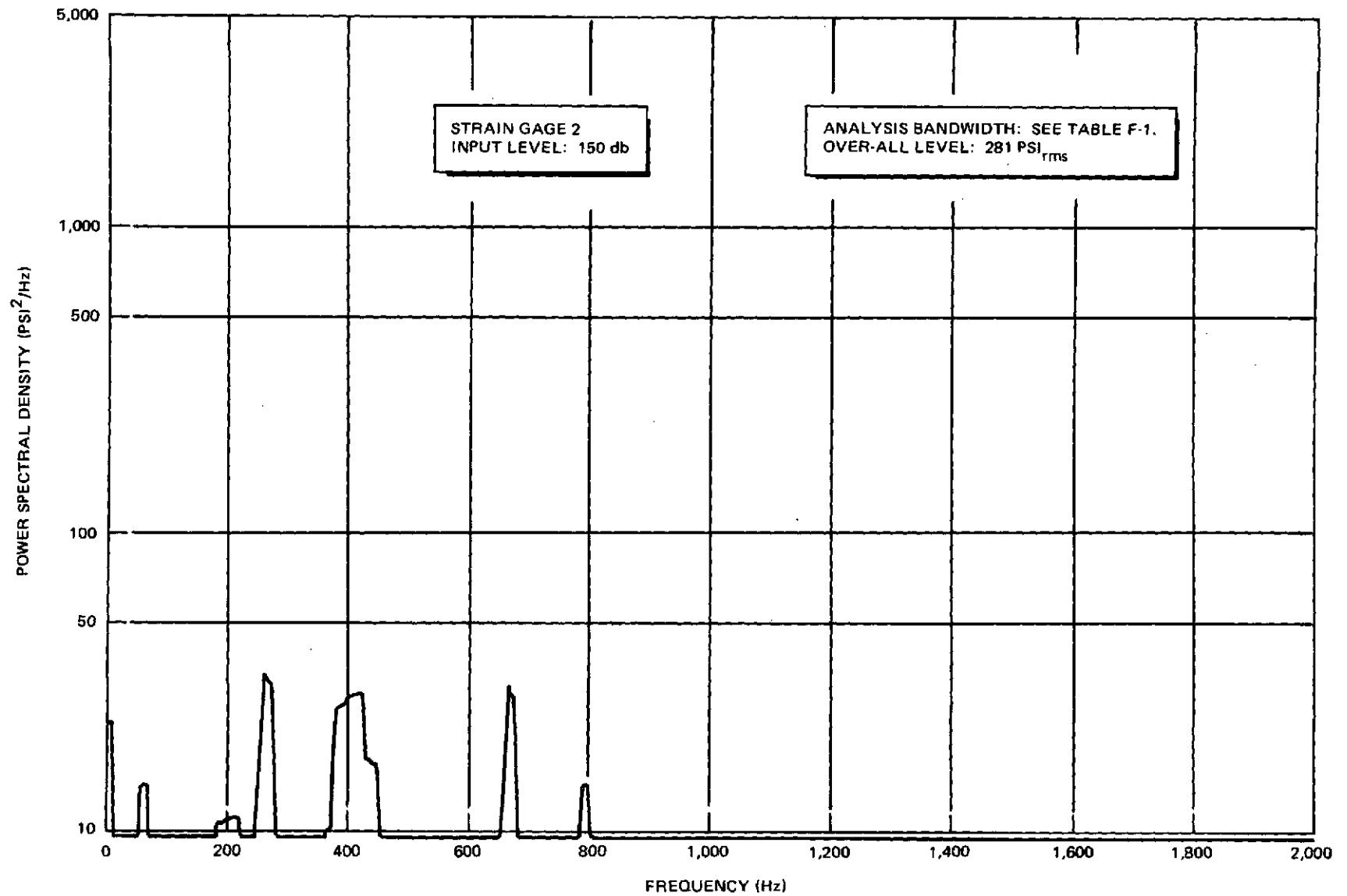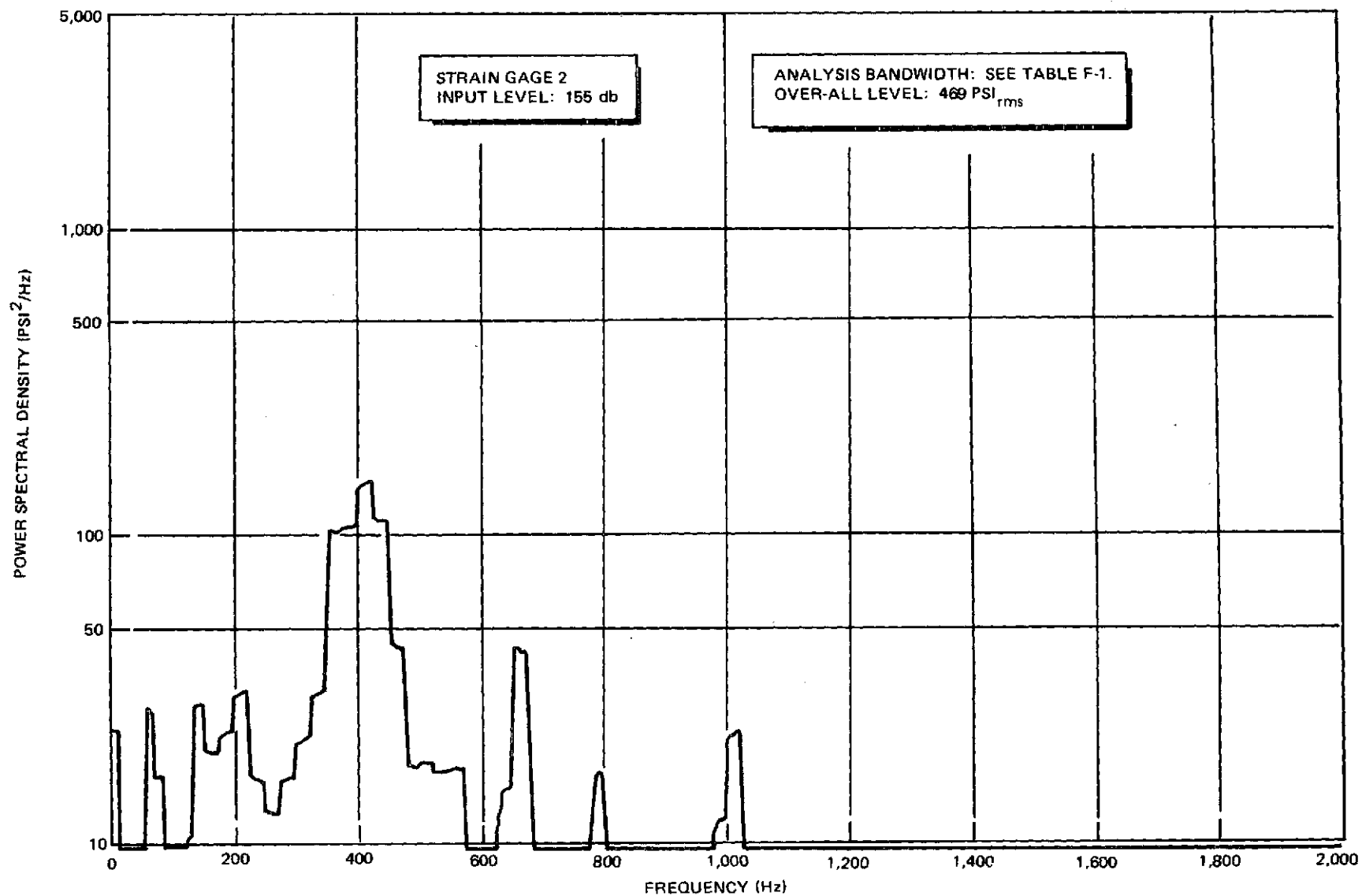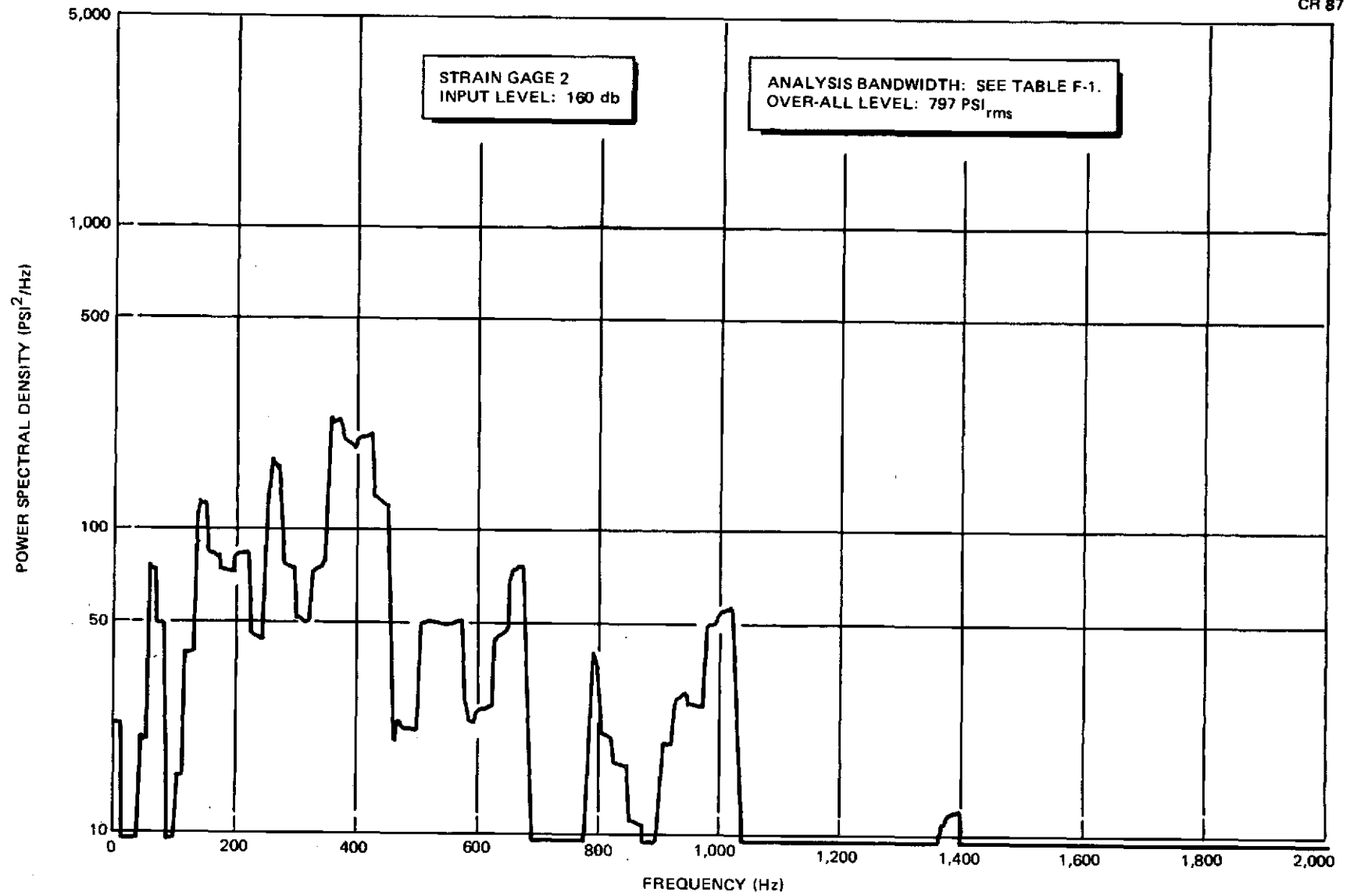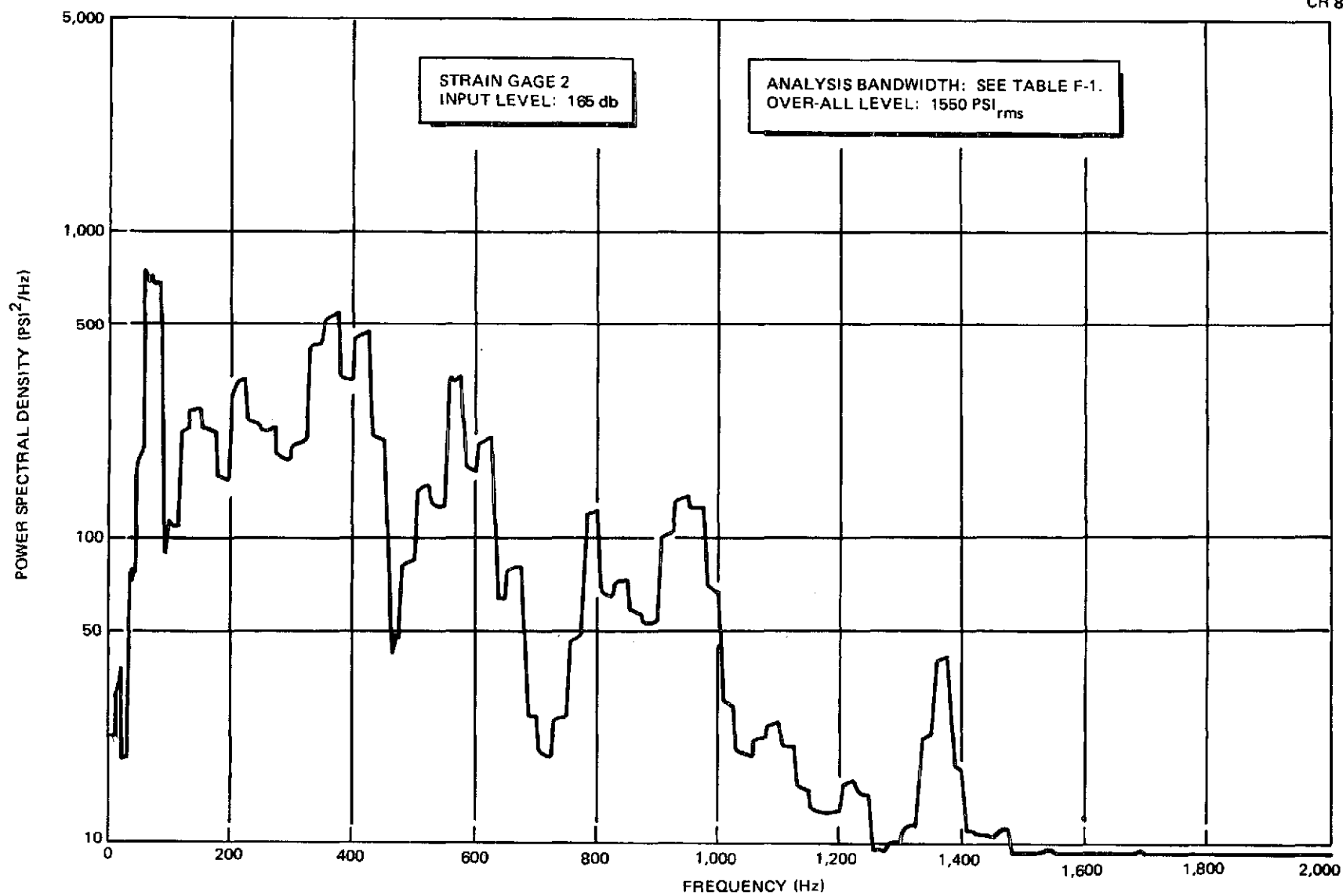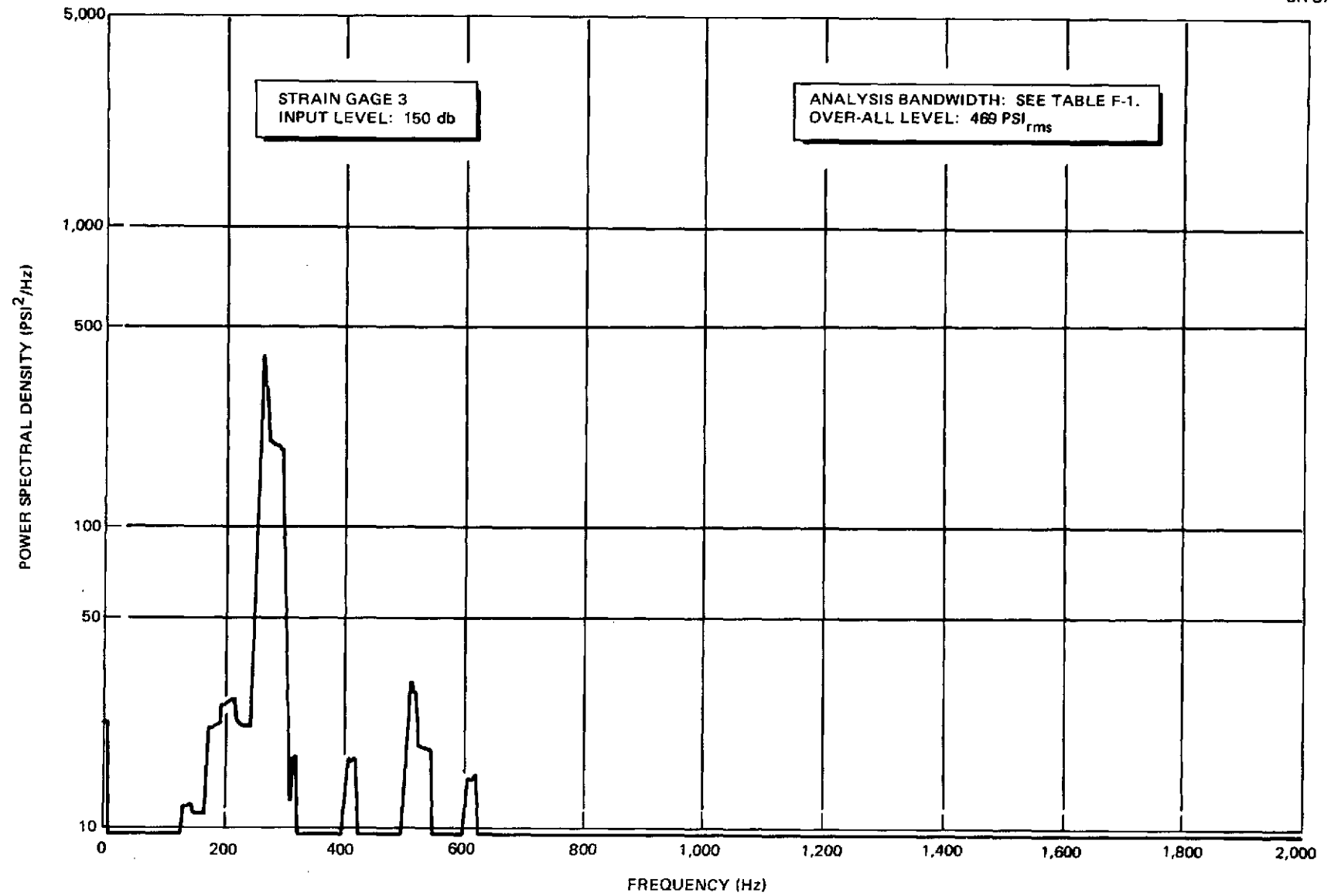
Figure F-7. Power Spectral Density Analysis; SG 1, 160 db
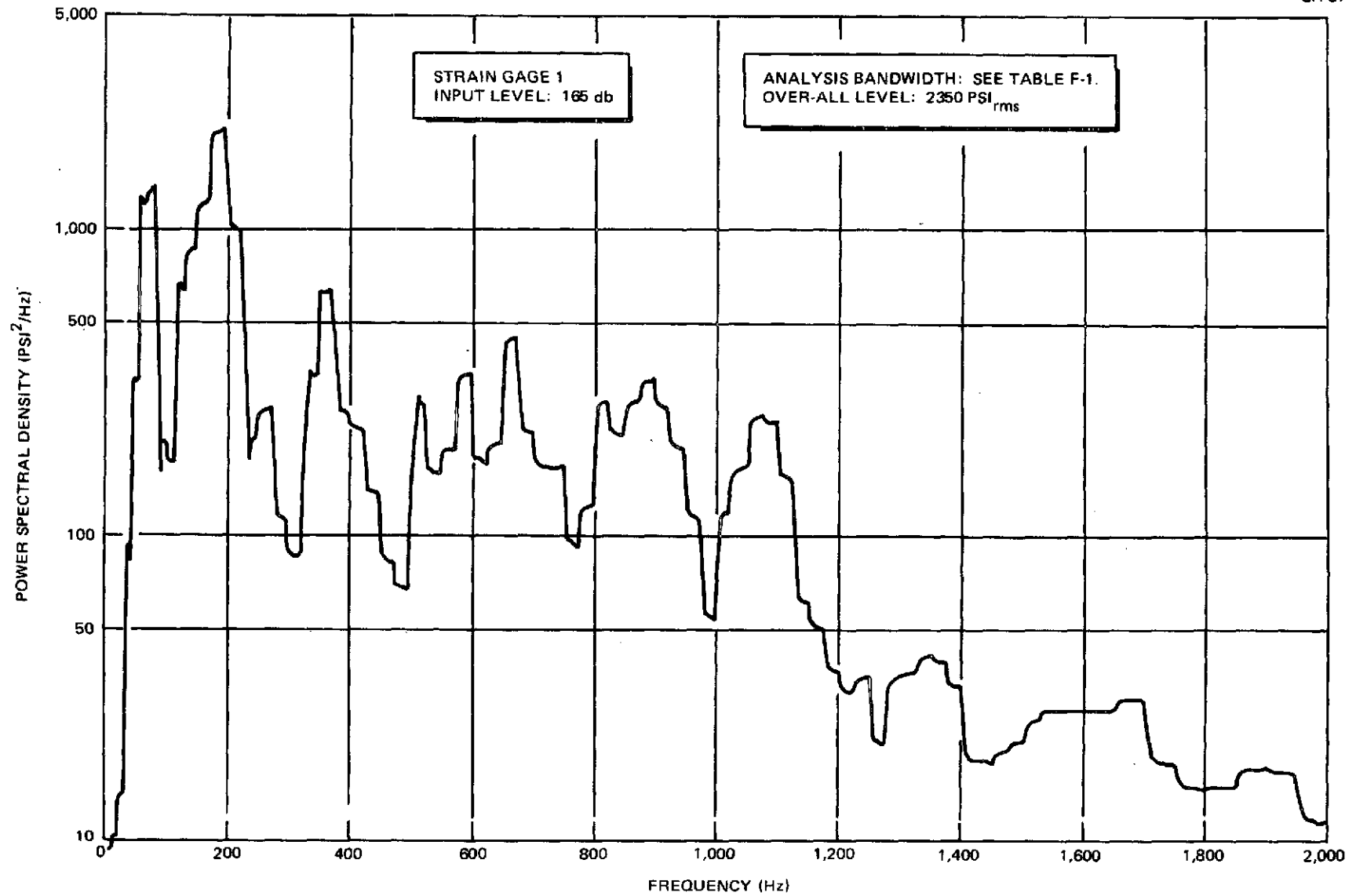
Figure F-8. Power Spectral Density Analysis; SG 1, 165 db
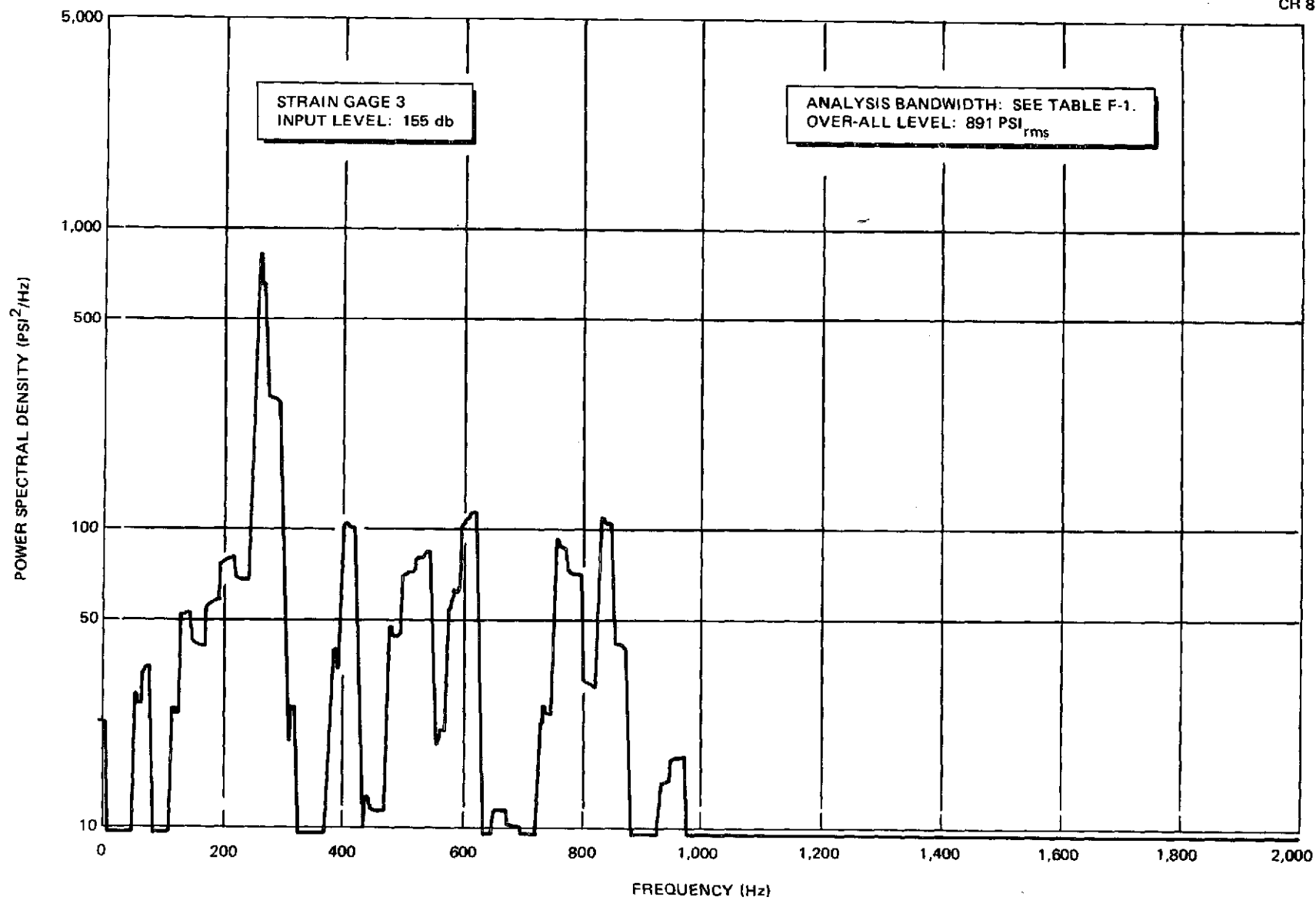
Figure F-9. Power Spectral Density Analysis; SG 2, 150 db
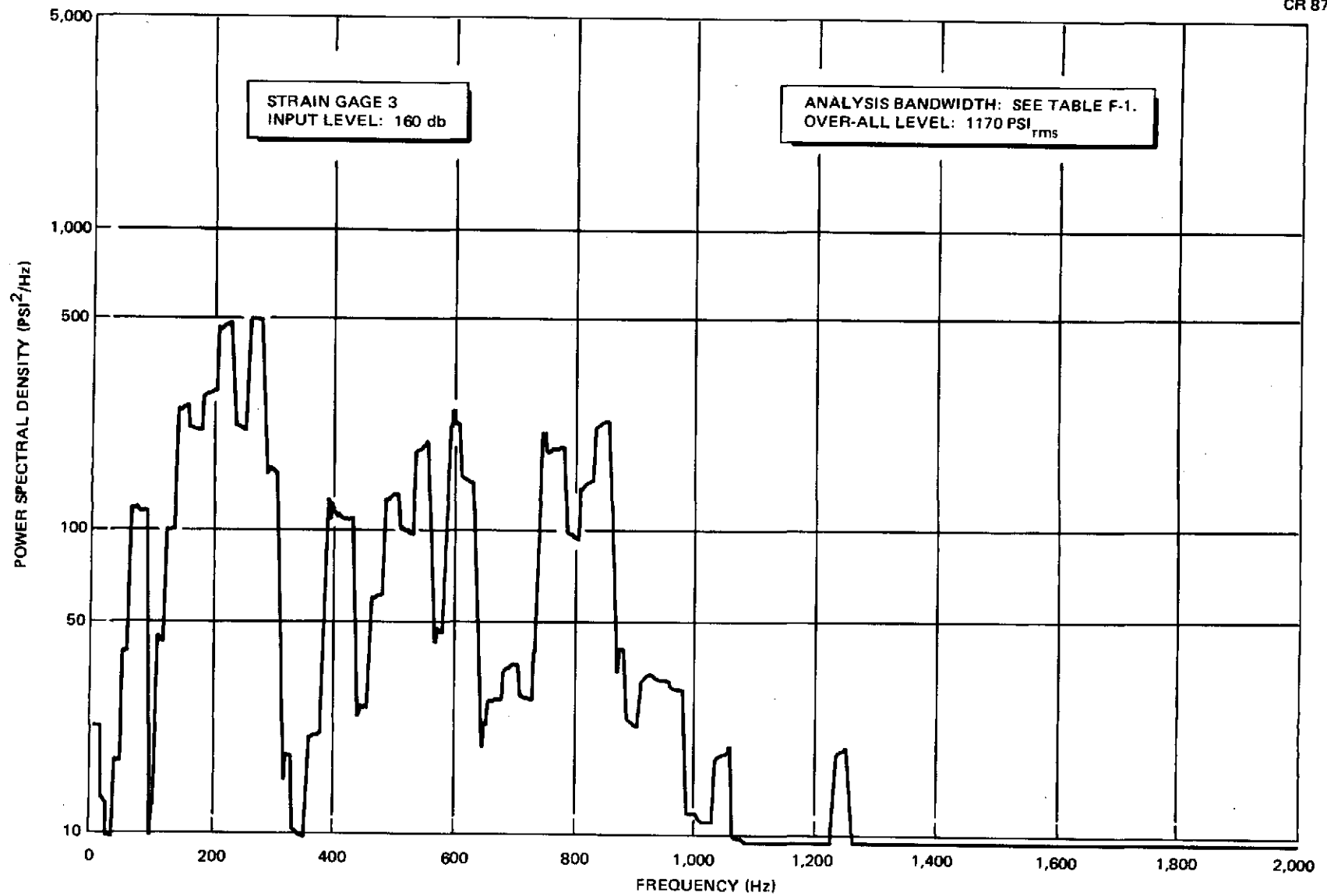
Figure F-10. Power Spectral Density Analysis; SG 2, 155 db

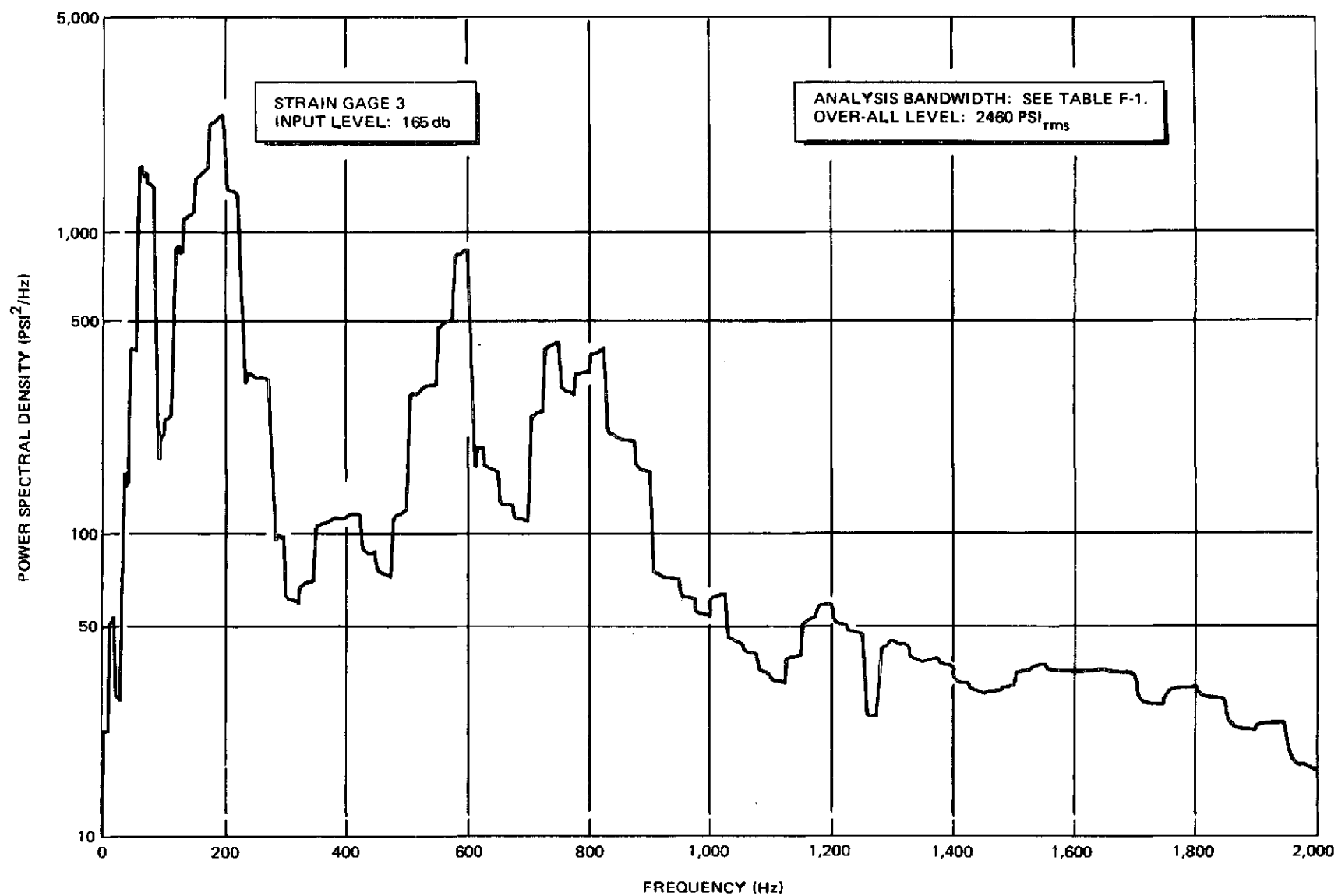Figure F-11. Power Spectral Density Analysis; SG 2, 160 db

Figure F-12. Power Spectral Density Analysis; SG 2, 165 db

Figure F-13. Power Spectral Density Analysis; SG 3, 150 db

Figure F-14. Power Spectral Density Analysis; SG 3, 155 db

Figure F-15. Power Spectral Density Analysis; SG 3, 160 db

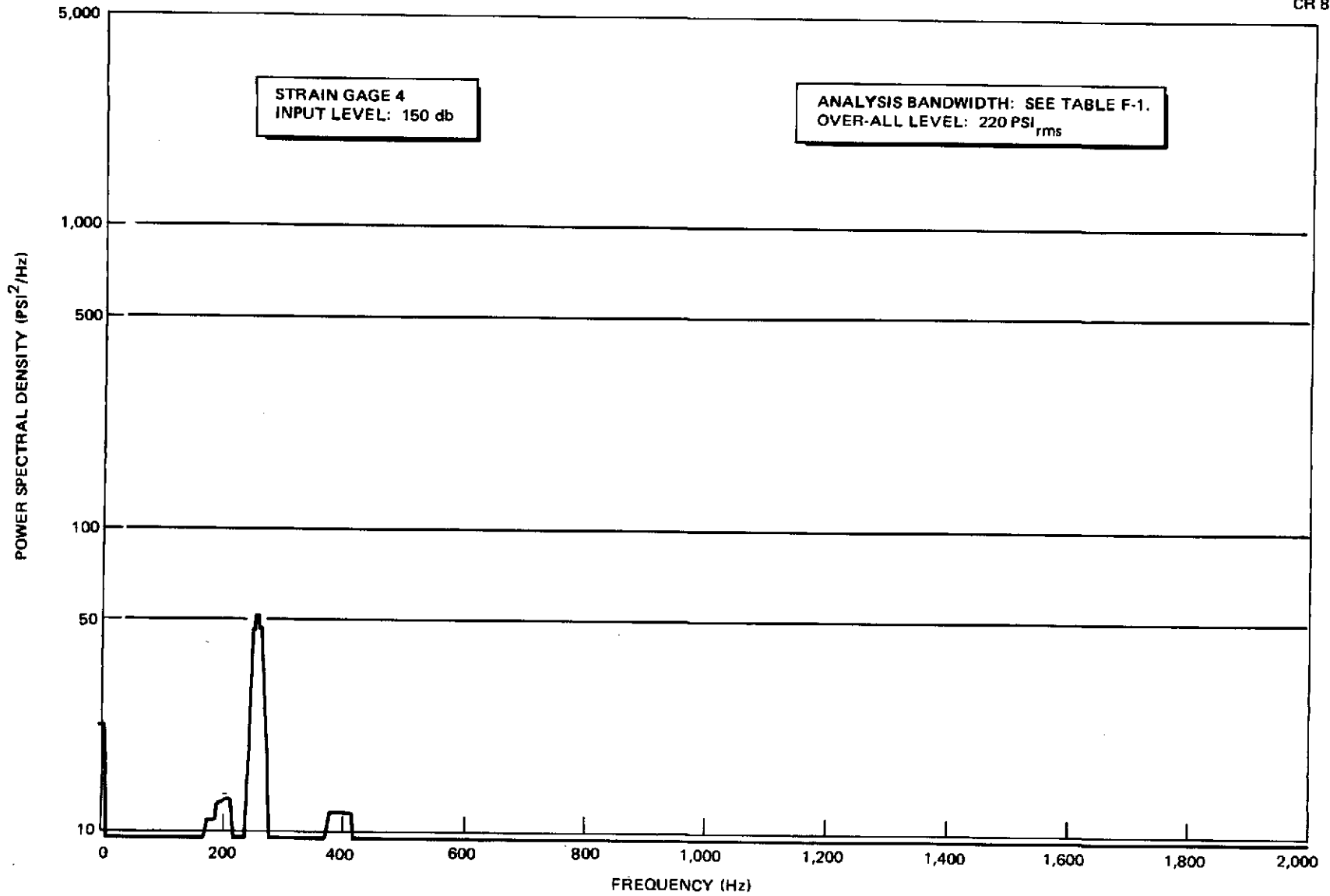Figure F-16. Power Spectral Density Analysis; SG 3, 165 db

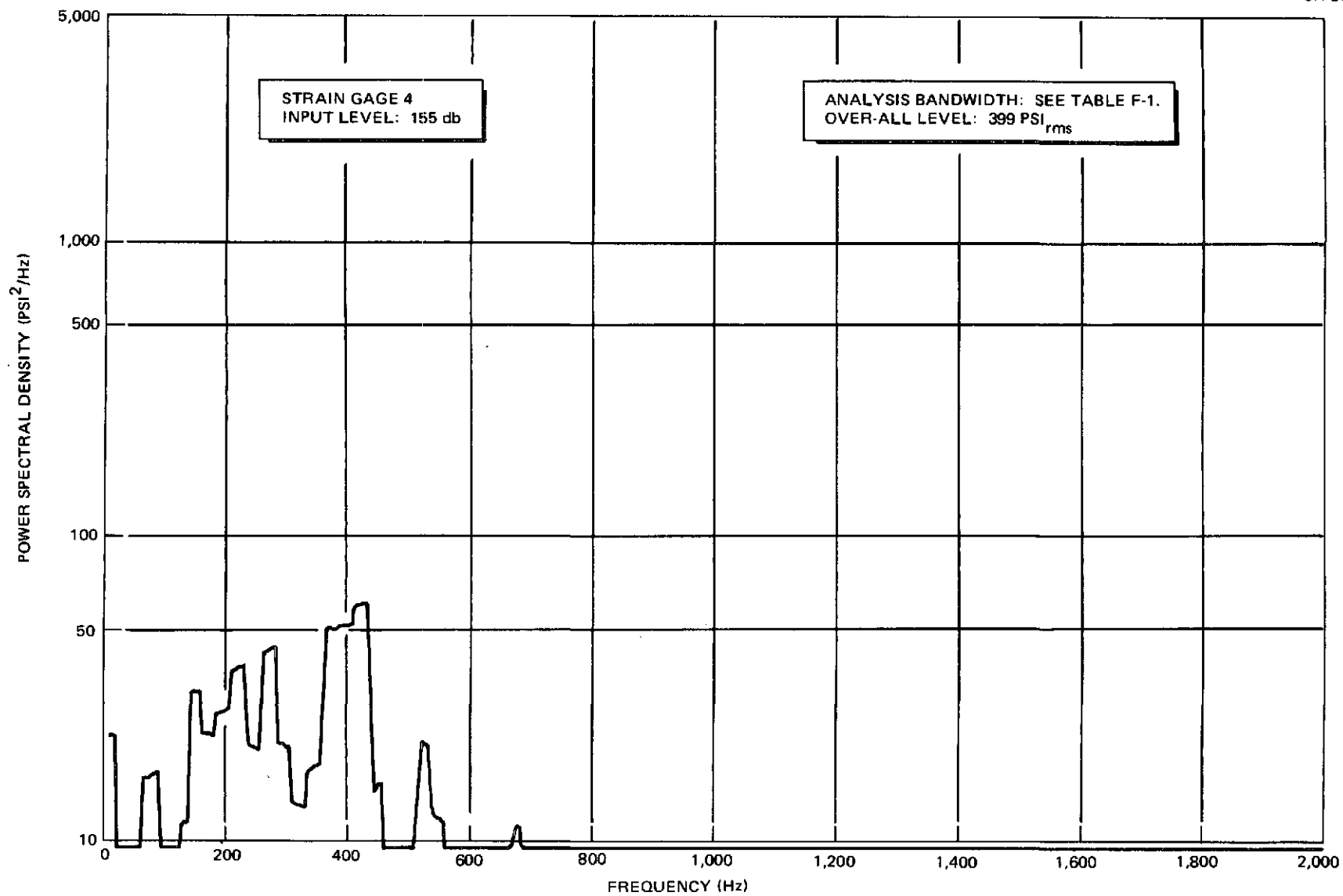Figure F-17. Power Spectral Density Analysis; SG 4, 150 db

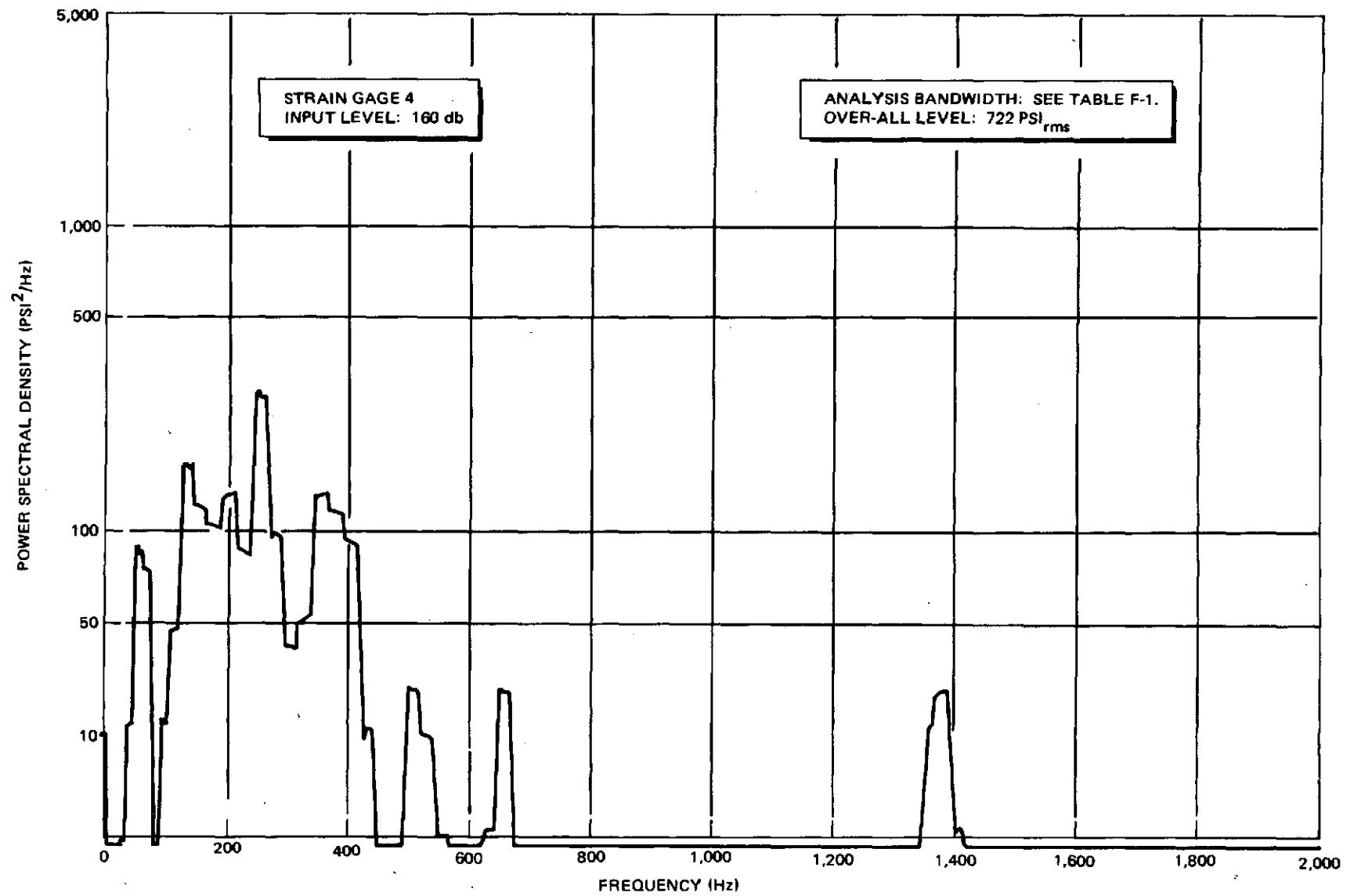Figure F-18. Power Spectral Density Analysis; SG 4, 155 db

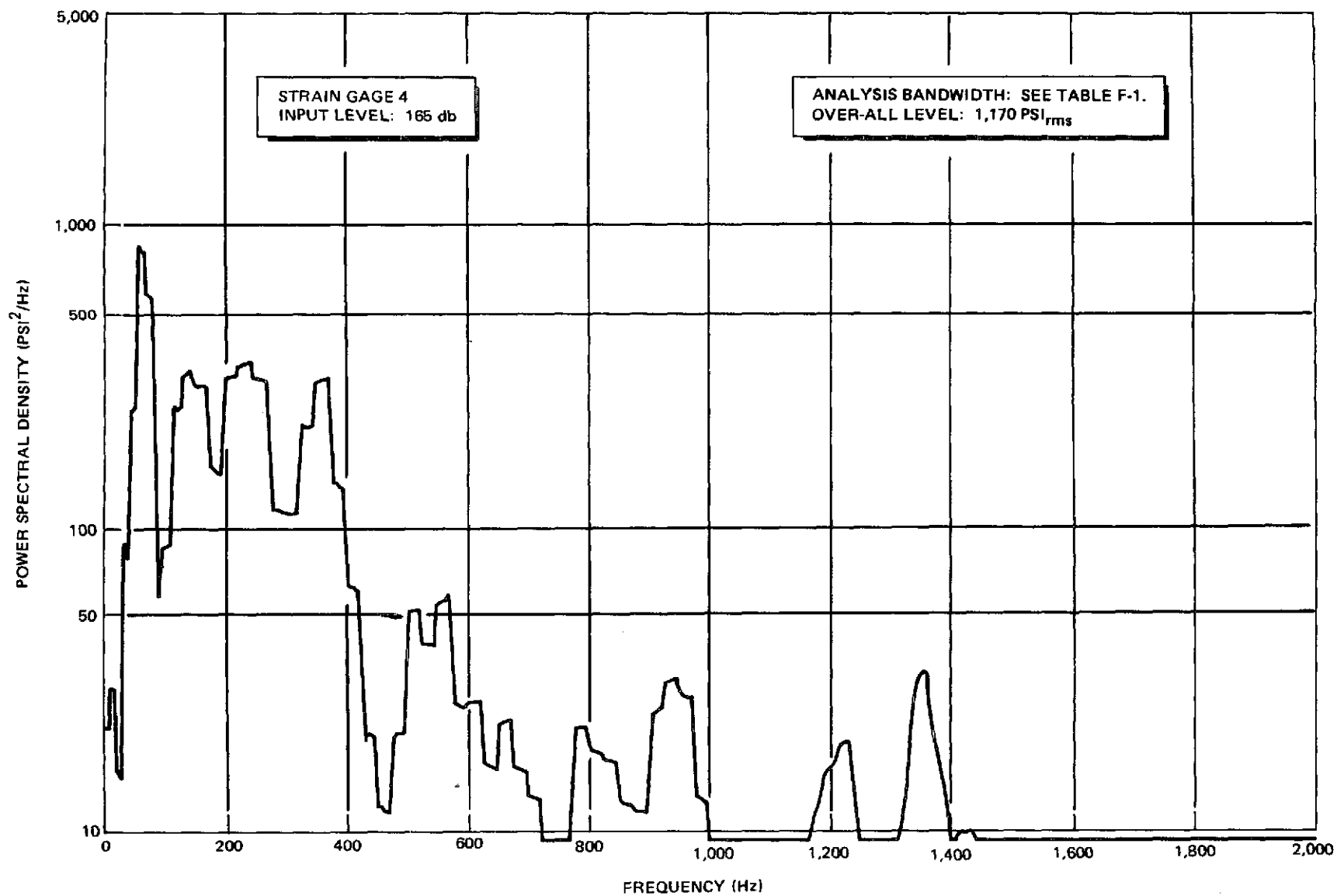Figure F-19. Power Spectral Density Analysis; SG 4, 160 db

Figure F-20. Power Spectral Density Analysis; SG 4, 165 db

Table F-1

LING ASDE-80 ANALYZER FILTER BANDWIDTHS
AND STATISTICAL DEGREES OF FREEDOM

Frequency Range (Hz)	Analysis Filter Bandwidth (Hz)	Number of Statistical Degrees of Freedom (1) (N)
10 - 20	10	240
20 - 31	11	264
31 - 43	12	288
43 - 56	13	312
56 - 84	14	336
84 - 99	15	360
99 - 115	16	384
115 - 132	17	408
132 - 150	18	432
150 - 1550	25	600
1550 - 2000	50	1200

Notes: (1) Where random signals are measured by smoothing the instantaneous squared values with a low-pass RC filter: $N = 4BK$ where,

N = number of statistical degrees of freedom

B = analysis filter bandwidth, Hertz

K = RC time constant for the smoothing filter (six seconds for plotted data using the Ling SSN-100 Scanner) $(K \ll T_r)$

T_r = sample record length, seconds